Carrier Momentum Relaxation in Highly Doped Polar Semiconductors and Semiconductor Heterostructures

Anna Miriam Hauber
DIPL.-PHYS.

Thesis submitted for the degree of Doctor of Philosophy

NATIONAL UNIVERSITY OF IRELAND, CORK

College of Science, Engineering and Food Science

Department of Physics

Tyndall National Institute

October 2016

Head of Department: Prof. J. G. McInerney

Supervisor: Stephen Fahy

Research supported by SFI Science Foundation Ireland

Contents

List of Tables

I, Anna Miriam Hauber, certify that this thesis is my own work and has not been submitted for another degree at University College Cork or elsewhere.

Anna Miriam Hauber

For Kitty and Thomas

Acknowledgements

Working on this thesis for years while wondering whether it would result in a PhD, or in a big, ugly, gaping hole in my CV was probably the hardest thing I've ever done.[1] Now as the first outcome is looking more and more likely, it's time to thank the many people who helped me along the way.

First of all, I would like to thank my supervisor, Stephen Fahy, for giving me the chance to engage in this work in the first place, and the freedom to pursue this project as it moved away somewhat from the one originally envisioned. I am grateful, and especially in hindsight sightly baffled, that I got to work on methodology in semi-classical semiconductor physics, which often meant sitting down with a pencil and piece of paper, or writing simple code from scratch, in a time when one could be forgiven for thinking that all theoretical solid state physics was large-scale high-throughput computation. Stephen saw that this was the kind of physics which appealed to me, encouraged me in it, and devoted hundreds and hundreds of hours to discussions with me, often lasting hours on end. He also dealt quite admirably with certain flaws in my personality. I also have to thank Stephen for securing funding for me from the Science Foundation Irland for the entirety of my PhD.

I also want to thank everybody in the Materials Theory Group (Ivana Savić, Philip Murphy, Éamonn Murray, Martin Vaughan, Masoud Seifikar, Mark Hartnett, John Buckeridge, Ronan Murphy and Shane O'Mahony) for input I received in discussions of my work during group meetings, and general tips and tricks on working in Tyndall and science as a whole, and being welcomed in the group.

I am especially indebted to Martin Vaughan for sharing a piece of code he wrote, which I used to benchmark some of my calculations. I would also like thank Terrance O'Regan to sending me his code to benchmark some of the calculations I did on polar semiconductor heterostructures which did not make it into this thesis.

Thanks also go to my PhD progress committee, Jim Greer, Eoin O'Reilly and Paul Hurley, who not only let me continue with this work, but also had very kind things to say about it, and my PhD mentor Andrew Ellis, for advice.

I also want to thank Massimo Fischetti and Andreas Ruschhaupt for agreeing to be the examiners of this thesis, and to read all of this rather long thesis.

I am thankful for everybody in Tyndall who helped me in any way, or made my experience here enjoyable, if only with some friendly chat over tea, coffee, lunch, or in the pub. The full list would take too much space, but I would like to single out John Kissane, who was always quick and helpful with IT problems.

I particularly need to thank many of the other students and post-docs in the theory department for helping me with my programming, scripting, dealing with the cluster and many other small things, but more importantly for making me feel welcome and becoming friends. (Thank you Siobhán, Irene, Finbarr, Simon, Miguel, Thomas, Mahdi, Mark, Alfonso, Shane, Shane Jr., Gabriel, Marios, Eoin, Tom, Nick, Alfonso, Hadi, Katya, Conor, Pedram and many more)

[1] Yes, I've lived a pretty sheltered, privileged life. Danke Mama und Papa.

I spent many great days in the Irish hills and many evenings climbing in the Mardyke Arena with the UCC Mountaineering Club. These experiences put the PhD in perspective and helped me refuel, thus contributing significantly to this thesis. Thank you Marie, Ellen, Brian, Michelle, Dave, Joe, Anthony, Ruaidhri, Denis, Cormac, Donovan, Sorcha, Darragh, Simon, Kerstin, Anna, Richard, Ger, Mags, Cian, Harry, Damo, Kieran and everybody else!

I also want to thank the many great teachers, lecturers and tutors who have encouraged me through first, second and third level education. I'm lucky that Frau Flämig and Frau Sieber-Döhle not only taught Physics and Maths excellently, but also served as role models of women in physics. I've had too many great tutors and lecturers in university to enumerate here, but knowing people like Wolfgang Limmer, Matthias Freyberger, Michael Bussardt and Sarah and Endre Kajari gave me the idea that being a researcher, or at least an enthusiastically struggling PhD student might be something.

I also need to thank all my friends and family who haven't yet been mentioned for support, encouragement, good conversations, care packages and visits. Danke Alex, Mi, Uli und Micha! I think the way my parents raised me had everything to do with my becoming a physicist, finding myself quite far away from home, and happily struggling through the difficulties associated with all that. Danke Mama und Papa! I want to thank my sister for inspiring me with her general fearlessness. Danke Julia, du Bachkind! I probably wouldn't have finished this thesis if it hadn't been for my boyfriend being there. Thank you, Thomas!

Finally, if you're a student, read some of this thesis, and found any little bit of it helpful, I'm delighted.

Abstract

Highly doped polar semiconductors are essential components of today's semiconductor industry. Most strikingly, transistors in modern electronic devices are polar semiconductor heterostructures. It is important to thoroughly understand carrier transport in such structures. In doped polar semiconductors, collective excitations of the carriers (plasmons) and the atoms (polar phonons) couple. These coupled collective excitations affect the electrical conductivity, here quantified through the carrier mobility. In scattering events, the carriers and the coupled collective modes transfer momentum between each other. Carrier momentum transferred to polar phonons can be lost to other phonons through anharmonic decay, resulting in a finite carrier mobility. The plasmons do not have a decay mechanism which transfers carrier momentum irretrievably. Hence, carrier-plasmon scattering results in infinite carrier mobility. Momentum relaxation due to either carrier–plasmon scattering or carrier–polar-phonon scattering alone are well understood. However, only this thesis manages to treat momentum relaxation due to both scattering mechanisms on an equal footing, enabling us to properly calculate the mobility limited by carrier–coupled plasmon–polar phonon scattering. We achieved this by solving the coupled Boltzmann equations for the carriers and the collective excitations, focusing on the "drag" term and on the anharmonic decay process of the collective modes. Our approach uses dielectric functions to describe both the carrier-collective mode scattering and the decay of the collective modes. We applied our method to bulk polar semiconductors and heterostructures where various polar dielectrics surround a semiconducting monolayer of MoS_2, where taking plasmons into account can increase the mobility by up to a factor 15 for certain parameters. This screening effect is up to 85% higher than if calculated with previous methods. To conclude, our approach provides insight into the momentum relaxation mechanism for carrier–coupled collective mode scattering, and better tools for calculating the screened polar phonon and interface polar phonon limited mobility.

System of units and preferred units of frequency

This thesis uses the Gaussian cgs system of units, e.g. [6], except in plots and tables of quantities which are conventionally expressed in other units in semiconductor physics. For consistency, all equations in this thesis are in Gaussian cgs units. Consequently, they yield the mobility in $cm^2/(statVs)$ and the Seebeck coefficient in $statV/K$. However, the mobility and the Seebeck coefficient are usually expressed in $cm^2/(Vs)$ and $\mu V/K$, respectively. This means that we have to convert the statvolts into volts, replacing 1 statV with exactly 299.792458V. This is done behind the scenes, and all the plots use the conventional units.

We recommend Yu and Cardona's textbook [3] to a reader who is more familiar with SI units, because they give many important quantities in semiconductor physics both in cgs and in SI units.

Different subfields of solid state physics have their own preferred methods of giving "phonon frequencies". In this thesis, we will give the phonon energies $E = \hbar\omega$ in electronvolts in all tables. As discussed above, all equations are strictly in Gaussian cgs, so that phonon energies–as indeed all energies–in equations are in erg.

In spectroscopy, the convention is to characterize phonon frequencies by the wave vector $k^{spectroscopy}$ an electromagnetic wave of the phonon frequency would have in a vacuum. The phonon energy can hence be retrieved as $\hbar\omega = 2\pi\hbar c_{vac} k^{spectroscopy}$, where c_{vac} is the speed of light in a vacuum. This convention is used in most of our sources for phonon frequencies [3] and references therein, and [7, 8, 9], and we have converted them to phonon energies in eV for the tables in this thesis.

Chapter 1

Introduction

Polar semiconductors, such as III-V compounds, and especially Gallium Arsenide (GaAs) have long been materials of interest in semiconductor and device physics, and have a plethora of technological applications [10, 11]. Optically active III-Vs are used in LEDs (light emitting diodes), semiconductor lasers, photo-detectors and solar cells [11]. Heterostructures consisting of layers of different III-V alloys allow the creation of arrays of quantum wells [12], with applications such as the quantum cascade laser [13]. Certain polar semiconductors, like lead telluride (PbTe) alloys, also show thermal properties which are promising for energy harvesting [14].

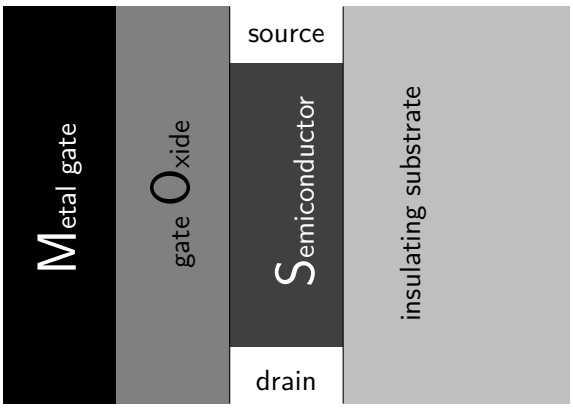

Figure 1.1: Schematic sketch of the main components of a MOSFET.

Metal-oxide-semiconductor field effect transistors (MOSFETs) are the most technologically important polar semiconductor structures today, as they are crucial components in the computer chips without which modern electronic devices would be unthinkable (cf. Fig. 1.1). These MOS structures are even polar when the semiconductor is non-polar (such as silicon), because the oxide layer is a polar material. Traditionally, the oxide layer used to be silicon oxide (SiO_2 or silica), but in current MOSFETs, SiO_2 has been replaced by "high-κ" oxides, where κ stands for the

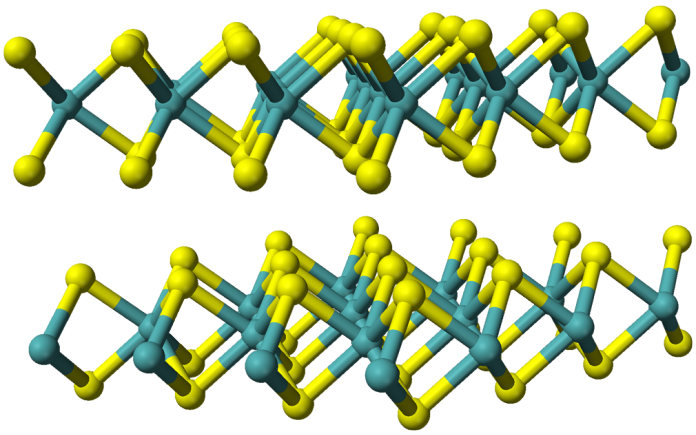

Figure 1.2: Stick and ball model of the atomic structure of MoS_2. The yellow balls symbolize sulfur atoms and the green balls stand for molybdenum atoms. The picture shows two monolayers offset against each other as they are in bulk MoS_2. [7]. This plot was created from data from the American Mineralogist Crystal Structure Database [20] by Ben Mills (Own work) [Public domain], via Wikimedia Commons [21].

relative dielectric constant, and "high-κ" means that the dielectric constant is higher than that of SiO_2. The reason for this development is that a high-κ–MOSFET of the same capacitance as a SiO_2–MOSFET has a thicker oxide layer, thus reducing leakage currents. Importantly for this thesis, this means that today's high-κ MOSFETs are more strongly polar then former SiO_2-MOSFETs, with dielectrics such as hafnia (HfO_2). Even tomorrow's more futuristic MOSFETs cannot forgo the polar dielectric. Recent MOSFETs consisting of just a single layer of molybdenite (MoS_2), cf. Figure 1.2 [15], lying on silica [16], or a monolayer of MoS_2 on SiO_2 with a HfO_2 top gate [17], are mainly polar heterostructures because of the silica and hafnia. MoS_2 itself is only barely polar [18, 19].

The understanding of carrier transport in highly doped polar semiconductor structures which will be developed in this thesis is applicable to all the applications discussed above.

Polar semiconductors are often highly doped in order to increase the carrier concentration, so that the high number of charge carriers (electrons or holes, though we will mainly be concerned with electrons in this thesis) delocalized throughout the semiconductor form a plasma. In non-polar semiconductors, natural, unforced longitudinal oscillations of this plasma occur at the plasma frequency. At this frequency, the electrical displacement is zero, because the polarization of the carrier plasma compensates any uniform external electric field. Plasma waves were first studied in classical plasmas by Langmuir and Tonks [22]. In quantum mechanics, these collective excitations of the electron gas are described as plasmons [23].

In undoped, polar semiconductors, the lattice causes a polarization field when the

different species of atoms oscillate out of phase. Similarly to the case of the plasma discussed just above, this can give rise to natural collective oscillations, at frequencies where the polarization compensates for any external electric field. These collective excitations are called longitudinal optical (LO) phonons, and the natural oscillation frequencies are called the LO-phonon frequencies [24, 25, 3, 26]. Phonons in general are quantized collective excitations of the semiconductors, see, e.g. [24, 25]. These phonons are called "optical", because the out of phase oscillation of different species of atoms gives rise to an oscillating electrical dipole moment, so that these phonons can couple to infrared radiation and light. In fact, the optical phonon frequencies used as parameters in this thesis have been determined from infrared and Raman spectroscopy [7, 8, 3]. Both the plasmons and LO-phonons are longitudinal excitations, that is, the collective mode oscillation is in the direction of the electric field, the polarization, and the wave vector. [1]

Highly doped polar semiconductor have both a carrier plasma, and optically active lattice excitations. Hence, their natural oscillations occur at frequencies where the polarization due to the lattice and the carrier plasma together compensate the external electric field. We will call these coupled collective excitations of the lattice and the carrier plasma "coupled modes" throughout this thesis. In highly doped polar semiconductors, the plasma frequency can be large enough to be comparable to the LO-phonon frequencies, and the coupled mode frequencies differ significantly from both the plasma and LO-phonon frequencies, as has been measured, e.g., for bulk PbTe and GaAs [27, 28, 29], following calculations by Varga [30].

We describe the collective excitations entirely through their dielectric functions, cf. [6, 31]. Dielectric functions capture how the electric displacement in a material depends on the external electric field. In Fourier space, the dielectric displacement is simply the product of the dielectric function and the electric field, and all three quantities are functions of wave vector and frequency. The natural oscillation of a collective motion, where the electric displacement field vanishes, occurs at the zeros of the dielectric function. These zeros are usually parametrized through the wave vector, so that one speaks of the natural oscillation frequencies as a function of wave vector. In the simplest case, like for a single undamped LO-phonon or plasmon mode in the bulk long-wavelength limit, the natural oscillation frequency is a single real number independent of wave vector. Yet, some polar materials are better described with several different optical phonon modes, like HfO_2 or SiO_2 [1]. In the semiconductor heterostructures consisting of MoS_2 sandwiched between different polar dielectrics, which we investigate in this thesis, each of the constituent layers on its own has at least one longitudinal optical phonon mode. They all couple with each other and with

[1] This holds without qualification in isotropic bulk materials. In anisotropic materials, the direction of the electric field to the crystal axes is also important, and in heterostructures, only the in–plane contribution of the wave vector, polarization and electric field will be parallel.

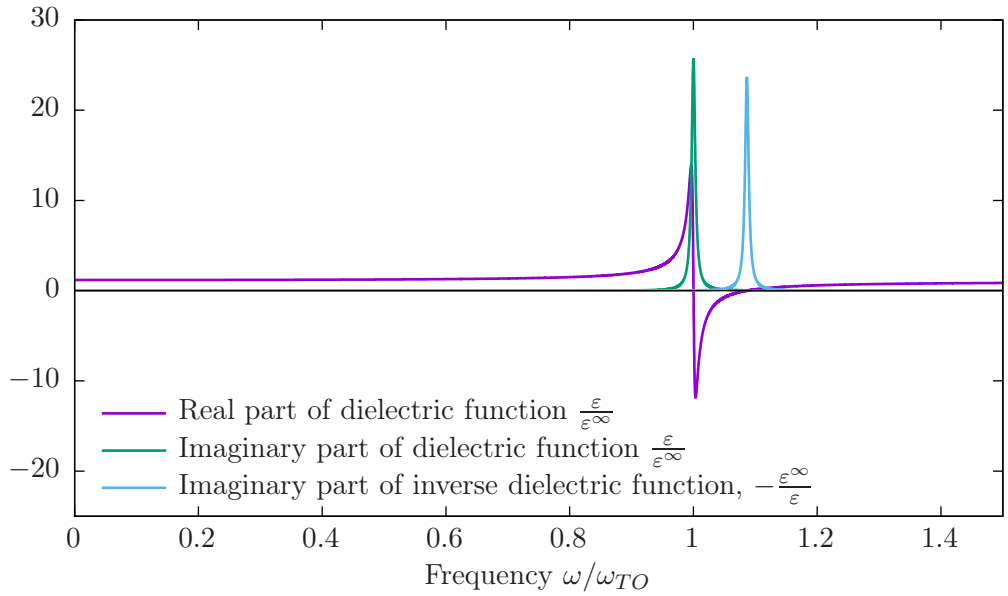

Figure 1.3: Real part and imaginary part of the dielectric function, and imaginary part of the inverse of the negative dielectric function as a function of frequency. The dielectric function describes undamped optical phonons in GaAs in the long-wavelength limit, cf. section 2.1. The dielectric function ε is scaled by its high-frequency limit ε^∞, and the frequency ω by the transverse-optical phonon frequency ω_{TO}.

the carriers in MoS_2-monolayer, yielding a complicated set of coupled modes. In general, natural oscillations will be damped, that means the zeros of the dielectric functions have an imaginary contribution, the damping rate. Both the natural oscillation frequencies and the damping rates usually depend on wave vector. In this thesis, we consider anharmonic damping of the LO-phonons, and Landau damping [2] for the plasmons. The coupled modes will in general be damped due to a mixture of those two mechanisms.

Keeping track of the multiple coupled modes, each with a wave vector dependent frequency and damping rate seems quite daunting and requires conscientious bookkeeping. As we will see in the course of this thesis, it will be advantageous to describe the coupled mode excitations in terms of the inverse dielectric function as a function of wave vector and a real frequency. Real zeros of the dielectric function, or undamped collective excitations correspond to poles in the inverse dielectric function, or delta-peaks in the imaginary part of the inverse dielectric function as a function of wave vector and real frequency [32]. Damped collective excitations correspond to poles in the inverse dielectric function off the real frequency axis. They show as peaks of finite width and height in the imaginary part of the inverse dielectric function as a function of wave vector and real frequency. A simple example are damped LO-phonons in the long wavelength limit (whose dielectric function is plotted in Figure 1.3 and which will be discussed in detail in chapter 3): The imaginary part of their inverse dielectric function can be expressed through Lorentzians, whose width

depends on the damping rate. In the limit of undamped LO-phonons, the Lorentzians become delta-peaks at the LO-phonon frequencies. The imaginary part of the inverse dielectric function as a function of wave vector and real frequency is a crucially important quantity throughout this thesis. Its magnitude shows how strong the collective excitation is for a certain wave vector and frequency. The position of its peaks gives the dispersion of the collective excitations, and their width indicates their damping.

As the LO-phonons and the plasmons in highly doped polar semiconductors are coupled, carrier–coupled mode scattering in such materials cannot be described accurately by independent carrier–LO-phonon scattering and carrier–carrier scattering. Carrier-LO-phonon scattering [33, 34] is known to have an important effect on the carrier momentum relaxation, and the hence the carrier mobility (For a comparison of the different scattering mechanisms in GaAs see, e.g., [35]). Carrier–carrier scattering, which, in our collective excitation picture will be described as carrier–plasmon scattering (similarly to carrier–LO-phonon scattering), is usually assumed to have a negligible effect on momentum relaxation and mobility, see, e.g., the discussion in Ziman's textbook [25]. Loosely speaking, this difference in momentum relaxation occurs because the damping of the LO-phonons is due to coupling to an external "bath" (of other phonons), so that some of the momentum transferred between the carriers and the phonons is lost to the environment. The damping of the plasmon is due to Landau damping [2], i.e., an interaction of the carrier gas amongst itself.[2] No external bath is involved. Consequently, none of the carrier momentum can be transferred to the environment. The momentum relaxation due to carrier–coupled mode scattering falls somewhere in between these to limiting cases. It cannot be assumed *a priori* that either carrier LO-phonon or carrier plasmon scattering describe it accurately. Therefore, carrier scattering with the coupled modes needs to be investigated carefully.

In this thesis, we develop a method which treats the scattering of carriers by coupled excitations in a generalized way, thus treating carrier–carrier scattering and carrier–LO-phonon scattering on an equal footing. We achieve this conceptual simplicity by expressing the relevant properties of the coupled collective excitations, (the scattering rate between the carriers and the coupled modes and the damping rates of coupled modes) in terms of dielectric functions. Our treatment includes LO-phonon scattering and carrier–carrier scattering as limiting cases.

We also want this thesis to help the reader to attain an intuition for the momentum relaxation due to carrier–coupled collective mode scattering. Therefore, we discuss a quantity, which we shall call the "phonon dissipation weight factor", the ratio of the

[2] In quantum mechanical language, Landau damping means that the lifetime of the plasmon is due to its ability to decay into quasi-particle–quasi-hole pairs, which are again excitations of the carrier gas. Hence, none of the carrier momentum is lost in such a process.

imaginary part of the dielectric function for the optical phonons alone and the imaginary part of the total dielectric function, and which follows naturally from our description. The phonon dissipation weight factor characterizes how strongly scattering with a coupled excitation of a certain wave vector and energy contributes to degrading an electric current - on a scale from zero to one. Zero - no degradation of the current - corresponds to the conventional description of carrier–carrier scattering, and one characterizes the LO-phonon scattering limit.

It has long been known that LO-phonons and plasmons in doped polar semiconductors are coupled, but the effect of this coupling on momentum relaxation has been less clear. Varga [30] gave the frequencies of the resulting coupled excitations in the long-wavelength limit, and also defined their phonon content - the part of the total kinetic energy which is due to atomic motion. Ridley used the phonon content to derive the scattering rate of the coupled modes in the long wavelength limit [26]. He also commented that this was equivalent to the expression of Kim et al. [36], where the scattering rate is calculated from the dielectric function of the coupled plasma-lattice system. While Kim's long-wavelength expression is satisfactory for a description of energy relaxation, this is not true for momentum relaxation. A calculation of the momentum relaxation time for carrier–coupled modes scattering in strict analogy to the calculation of the momentum relaxation time for carrier–LO-phonon scattering, cf. [37], leads to inaccurate results in most parameter ranges.

Fischetti et al. [1] alleviated this issue by taking into account what they called "an approximate treatment of Landau damping".[3] They used the long-wavelength limit expression for the coupled mode momentum relaxation rate only up to a certain cut-off wave vector, and the LO-phonon momentum relaxation rate for larger wave vectors. This provided a patch to the problem, and was suitable for the realistic device-physics application they studied. Incidentally, the desire to fully understand the reasons behind, and the validity of this approximation by Fischetti et al. [1] was one of the major motivations for this work originally. We will carefully analyse this approximation, apply it to polar semiconductors in the simplest conceivable case, and then carry out a careful comparison with our own approach.

Kim et al. [36] describe the energy relaxation of a carrier due to scattering with a coupled mode in terms of the imaginary part of the inverse dielectric function [38]. Unlike the approaches by Varga and Ridley, which are based on discrete modes characterising the long wavelength limit rather than a spectrum of excitation frequencies, Kim et al.'s approach can be applied to nonzero wave vectors directly – simply by using a wave vector dependent dielectric function. Using the zero-temperature random-phase approximation (RPA) [39, 23, 40] dielectric

[3] Note that Landau damping was originally introduced in the classical limit [2] and not in the extreme quantum limit, as used in [1].

function [41] for the electronic dielectric function and a Lyddane-Sachs-Teller [42] type lattice dielectric function as suggested by Varga [30], Kim et al. [36] could calculate the changes in the coupled mode excitation frequencies as a function of wave vector [36]. Kim el al. [36] did not calculate the energy relaxation time for this case, but other authors have, using this method, e.g., [43, 44]. Drawing on work by Maslov[45] and Stern [46], we can apply Kim et al.'s treatment of the carrier-coupled mode scattering in terms of the imaginary part of the dielectric function to carrier–interface phonon scattering. This requires solving a Poisson equation to find an effective scalar dielectric function for the investigated semiconductor heterostructure.

Sanborn [47] expands on the method by Kim et al. [36] by using scattering rates calculated from the dielectric function in a Boltzmann transport equation to calculate momentum relaxation rates. A variety of scattering mechanism enter Sanborn's numerical calculations of momentum relaxation rates in GaAs [48], and Sanborn's aim was not to track the effect of carrier-coupled mode scattering specifically. However, her carrier–carrier collisional integral reproduces the textbook result [49] that carrier–carrier scattering in parabolic bands does not degrade an electric current (in the absence of Umklapp processes). Sanborn's carrier–carrier scattering model can be extended to the case of carrier - coupled mode scattering. Yet, Sanborn did not do this, and instead used an approximate treatment of the carrier coupled mode scattering in another collisional integral in the Boltzmann equation. The present work generalizes Sanborn's approach to include carrier-coupled mode scattering.

Our contribution, the critical step for the generalization of the description of momentum relaxation due to carrier–carrier scattering to momentum relaxation due to carrier-coupled mode scattering, is to emphasize the importance of the collective mode decay mechanism for momentum relaxation. We formulate a Boltzmann equation for the carriers - including a term due to the external electric field, and a Boltzmann equation for the coupled excitations, including the anharmonic decay of the LO-phonons. All these terms are expressed through dielectric functions. We find that the details of the anharmonic phonon decay determines how far the coupled excitations are out of equilibrium. [4] This in turn affects the carrier contribution to the momentum relaxation, and hence the carrier mobility. The same non-equilibrium term in the Boltzmann equation is responsible for the "phonon drag effect" [25] on the thermal conductivity and the Seebeck coefficient [50].

We first apply our approach to a series of bulk polar semiconductors where electron–LO-phonon scattering is well described with electrons in a single spherical, parabolic conduction band interacting with a single LO-phonon resonance. We investigate in detail how our approach compares to other treatments, and how the

[4] Sanborn [47] implicitly assumed that the LO-phonon distribution function, not the coupled mode distribution function, is in equilibrium.

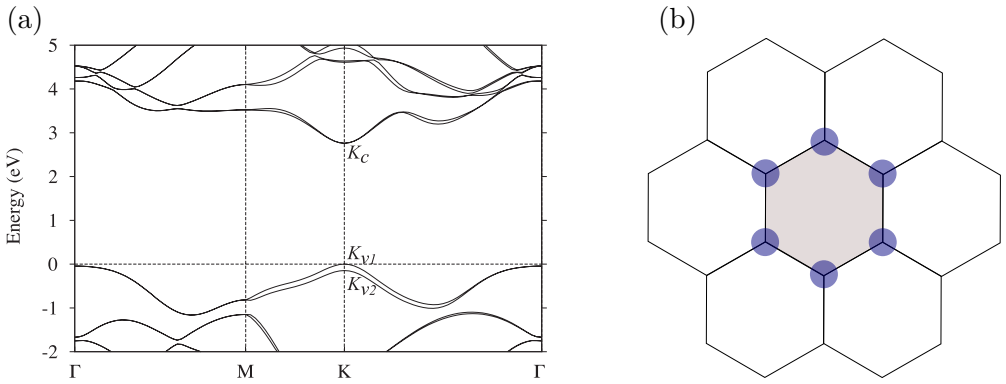

Figure 1.4: (a) Band structure of monolayer MoS_2. (b) The hexagonal lattice spanning the reciprocal space of monolayer MoS_2. The first Brillouin zone is shaded. The K-points are at the vertices of the hexagons. The six K-points shared between the first and subsequent Brillouin zones are marked with circles. Reprinted figure (a) with permission from [T. Cheiwchanchamnangij and W. R. L. Lambrecht, *Phys. Rev. B*, vol. 85, p. 205302, 2012.] Copyright 2012 by the American Physical Society [52]

inclusion (screened LO-phonon scattering) or neglect (unscreened LO-phonon scattering) of the carrier gas affects the mobility. We also explain in detail how we iterate the solution of the coupled Boltzmann equations to self-consistency, and how the self-consistent solution differs from relaxation time approximation (RTA) solution. The comparatively simple case of carrier-coupled mode scattering in bulk polar semiconductors allows us to develop qualitative understanding of momentum relaxation due to coupled collective mode scattering, which we can carry over to our investigation of screened interface phonon scattering (also called "remote phonon" or "surface optical phonon" scattering)[51, 1] in polar semiconductor heterostructures.

MoS_2 has attracted great interest in the last few years, because single atomic layers of it can be exfoliated and manipulated [15]. As a semiconductor, a gap is already present in its band structure [53, 52], (Figure 1.4a shows a quasi-particle GW calculation of the band structure of monolayer MoS_2 [52]) and does not have to be painstakingly introduced before it comes suitable for electronic applications. Field effect transistors with one or few layers of MoS_2 as the channel material have already been realised [16, 17]. Such devices have the advantage (at least in principle) of eliminating carrier scattering due to surface roughness, cf. [54].

The conduction band minima in MoS_2-monolayers lie at the K-points, cf. Figure 1.4a [52]. Figure 1.4b shows the six equivalent K-points within the first Brillouin zone. As each K-point is shared equally between three hexagonal cells, MoS_2 has two equivalent K-points per cell, and hence two equivalent valleys in the band structure governing low-field transport, e.g. [24, 25]. Due to the two equivalent valleys with quite high effective mass in monolayer MoS_2, screening effects are important [52, 5, 54]. If defects in the MoS_2 layers, which presently limit the carrier mobility through large charged impurity scattering[55, 56], can be decreased, higher

carrier mobilities could be reached. Therefore a careful investigation of dynamically screened interface polar phonon scattering is of interest, since this scattering might ultimately limit the carrier mobilities that can be achieved in certain ideal heterostructures. We will discuss this in chapter 6.

As the conduction band minima in monolayer MoS_2 are well described by spherical parabolic bands and well separated in energy from the next lowest conduction band extrema,[52, 57], we will follow [54, 57, 57, 55] in treating transport in MoS_2 with effective mass theory.

At a computational level, transport in semiconducting monolayers is simpler than in traditional MOSFET channels [58], because it can reasonably be approximated as truly two-dimensional. This relieves us from worrying about carrier wave functions in the directions perpendicular to the direction of transport, and the associated eigenvalues, which give rise to so-called subbands, e.g. [3], which, in turn would affect the carrier dielectric function. Finally, heterostructures with polar dielectrics surrounding a non-polar or weakly polar semiconductor like MoS_2 (Imagine the MOSFET from Figure 1.1 with a MoS_2-monolayer as the semiconductor and various dielectrics as the gate oxide and substrate.) are ideal to study the effects of screening on carrier-optical phonon scattering, because changing the dielectrics allows us to change the background dielectric function in a way that would be impossible in a bulk polar semiconductor.

The rest of this thesis is organized as follows: In chapter 2, we review the dielectric functions for the phonons, plasmons and coupled collective modes. In chapter 3, we discuss how carrier-coupled mode scattering can be expressed in terms of these dielectric functions. In section 3.1, we focus on bulk polar semiconductors, and in section 3.2 on polar semiconductor heterostructures. In chapter 4, we lay out our method of treating the momentum relaxation due to carrier-coupled mode scattering. We apply this method to the momentum relaxation in bulk polar semiconductors in chapter 5 and to the momentum relaxation in polar semiconductor heterostructures, consisting of sandwiches of various dielectrics around a monolayer of MoS_2, in chapter 6. The material presented in section 3.2, chapter 4, chapter 5 and chapter 6 has been submitted for publication. We summarize and give a brief outlook in chapter 7.

Chapter 2

Dielectric functions

In this chapter, we discuss the dielectric functions which we need to describe the collective excitations throughout this thesis. As discussed in chapter 1, the zeros of the dielectric functions correspond to the natural oscillation frequencies, and we describe the collective excitations in terms of the imaginary part of the inverse dielectric function. We start by deriving the dielectric functions in the long wavelength limit from the equations of motions for the normal coordinates of the phonons or plasmons, because this gives some intuitive insight. These dielectric functions will be used for the LO-phonons throughout this thesis, and we give material parameters for the various polar semiconductors and polar dielectrics we treat in this thesis at this point.

In section 2.2, we discuss the carrier dielectric function. In subsection 2.2.2 we treat this dielectric function in the random phase approximation (RPA) [39, 23, 40], which we will use to describe the dielectric response of the plasma excitation in this thesis. The RPA captures certain important properties, like the existence of two clearly divided regimes where plasmons are either damped, or undamped at zero temperature. In general, we will use temperature dependent RPA dielectric functions with a full wave vector and frequency dependence [59, 60].

Landau damping [2] is reviewed in detail in Appendix A. Besides providing an illuminating picture of the damping of collective oscillations in a classical electron gas, this appendix provides background information on the Landau contour and how it relates to the computation of the real and imaginary part of the dielectric functions in section 2.2.

As mentioned in chapter 1, the imaginary part of the inverse dielectric function will prove to be an important quantity for this thesis. In subsection 2.2.3, we discuss some of its properties, its temperature dependence, and how it differs in two and in three dimensions.

In section 2.3, we piece the phonon and the carrier dielectric function together to form the total dielectric function, which we can then use to describe the collective excitation in a polar semiconductor.

2.1 Lattice dielectric function for a polar material in the long-wavelength limit

In our derivation of the dielectric function of the lattice, we follow [3, section 6.4]. Polar materials are optically active, because there is an ionic contribution to the bonds. Say there are two ions of different polarity in the unit cell, as in Gallium Arsenide, which crystallizes in the rock salt structure. As the two ions oscillate, the charge distribution changes, giving rise to an electric field. In the center of mass reference frame we can describe the coupled oscillation of the two ions as an oscillation of a single oscillator which has their reduced mass M, their effective charge Q, and their relative displacement, $\boldsymbol{u}$:

$$M\ddot{\boldsymbol{u}} - M\gamma\dot{\boldsymbol{u}} + M\omega_{TO}^2\boldsymbol{u} = Q\boldsymbol{E}. \tag{2.1}$$

Here, ω_{TO} is the transverse natural oscillation frequency of the coupled ionic oscillators and γ is their damping rate. $\boldsymbol{E}$ is an external electrical field.

The Fourier components of the displacement and the electric field obey

$$\boldsymbol{u}_\omega = \frac{Q}{M}\frac{\boldsymbol{E}_\omega}{\omega_{TO}^2 - \omega^2 - i\omega\gamma}. \tag{2.2}$$

The polarization due to the motion of the ions is

$$\boldsymbol{P_\omega}^{ion} = \frac{N}{V}Q\boldsymbol{u}_\omega = \frac{NQ^2}{VM}\frac{\boldsymbol{E}_\omega}{\omega_{TO}^2 - \omega^2 - i\omega\gamma}, \tag{2.3}$$

when there are N unit cells in the sample of volume V.

Our model does not take electronic motion into account yet. The contribution to the polarization and displacement field from the electrons in filled bands is usually treated as a constant and lumped into the ionic dielectric function. As the ionic polarization vanishes in the high frequency limit, this so-called valence electron polarization is the only high-frequency contribution. Therefore, the valence electron contribution to the dielectric function is called ε^∞. The polarization field due to the valence electrons is

$$\boldsymbol{P}_\omega^{\text{e-valence}} = \frac{\varepsilon^\infty - 1}{4\pi}\boldsymbol{E}_\omega. \tag{2.4}$$

The displacement field due to the ionic motion and the valence electrons hence follows

as

$$\boldsymbol{D}_{\omega}^{ph} = \boldsymbol{E}_{\omega} + 4\pi \left(\boldsymbol{P}_{\omega}^{\text{e-valence}} + \boldsymbol{P}_{\omega}^{ion} \right) = \varepsilon_{\omega}^{ph} \boldsymbol{E}_{\omega} \tag{2.5}$$

with the dielectric function

$$\varepsilon_{\omega}^{ph} = \varepsilon^{\infty} + \frac{4\pi NQ^2}{VM} \frac{1}{\omega_{TO}^2 - \omega^2 - i\omega\gamma} \tag{2.6}$$

We marked the displacement and the dielectric function with a superscript "ph" for "phonon", to stress that the dielectric response is due to the optical phonons in the polar material.

Lyddane-Sachs-Teller relations It is customary to express the ionic dielectric function through its high- and low-frequency limit

$$\varepsilon_{\omega=0}^{ph} = \varepsilon^{\infty} + \frac{4\pi NQ^2}{VM\omega_{TO}^2} = \varepsilon^{0}, \tag{2.7}$$

and the longitudinal natural oscillation frequency, ω_{LO} in the undamped limit. The latter is the frequency for which the dielectric function

$$\varepsilon_{\omega_{LO},\gamma=0}^{ph} = \varepsilon^{\infty} + \frac{4\pi NQ^2}{VM} \frac{1}{\omega_{TO}^2 - \omega_{LO}^2} = 0 \tag{2.8}$$

so that

$$\omega_{LO}^2 = \omega_{TO}^2 + \frac{4\pi NQ^2}{VM\varepsilon^{\infty}}. \tag{2.9}$$

It can be verified easily that the longitudinal and the transverse natural oscillation frequencies are connected to the high and low frequency dielectric constants by the Lyddanne-Sachs-Teller relation [42]

$$\frac{\omega_{LO}^2}{\omega_{TO}^2} = \frac{\varepsilon^{0}}{\varepsilon^{\infty}}. \tag{2.10}$$

Replacing N, V, Q and M by ω_{LO}, ω_{TO} and ε^{∞}, we can write

$$\varepsilon_{\omega}^{ph} = \varepsilon^{\infty} + \frac{\varepsilon^{0} - \varepsilon^{\infty}}{1 - \frac{\omega^2}{\omega_{TO}^2} - i\frac{\omega\gamma}{\omega_{TO}^2}}. \tag{2.11}$$

2.1.1 Dielectric functions for polar semiconductors

We use the model lattice dielectric function Eq. (2.11) for all the bulk semiconductors discussed in this thesis. The parameters in Eq. (2.11) are given for room temperature GaAs in Tab. 2.1, and for the other bulk semiconductors considered, InAs, InP, InSb, ZnSe, PbTe and ZnS in Tab. 2.2. The assumption of constant optical phonon frequencies is well justified on the length scales of an inverse Fermi wave vector (See

Table 2.1: Material parameters for GaAs [3]. m_e is the electron mass. For simplicity, we assume that these parameters do not change with temperature or carrier concentration.

Quantity	symbol	value
LO-phonon energy	$\hbar\omega_{LO}$	36.14 meV
TO-phonon energy	$\hbar\omega_{TO}$	33.25 meV
High frequency dielectric	ε^{∞}	11.1
Static dielectric constant	ε^{0}	13.1
Optical phonon damping rate	γ	0.007 ω_{TO}
Conduction band effective mass	m^*	0.067 m_e
LA phonon scattering Volume deformation potential	a_c	6 eV
crystal density	ρ	$5.31\frac{g}{cm^3}$
LA phonon velocity	v_s	$5.22\times10^5\frac{cm}{s}$

Table 2.2: Material parameters for coupled collective mode scattering. Parameters from [3] unless indicated otherwise.

	GaAs	InAs[1]	InP	InSb[2]	ZnSe	PbTe[3]	ZnS[4]
$\hbar\omega_{LO}$(meV)	36.14	30.2	43.1	23.6	31.9	13.65	36.9
$\hbar\omega_{TO}$(meV)	33.25	27.1	38.1	22.2	26.2	3.97	28.40
ε^{∞}	11.1	11.8	9.52	15.7	5.9	32.8	4.9
m^*/m_e	0.067	0.026	0.073	0.014	0.134	0.038	0.34
γ/ω_{TO}	0.007	0.01	0.01	0.016	0.01	0.65	0.01
$n_C(10^{17}cm^{-3})$	7.04	2.02	9.36	0.89	5.82	1.68	16.5

definition in section 2.2), which is relevant for mobility calculations. Even for very highly doped GaAs at $n = 5 \times 10^{19}cm^{-3}$, the Fermi wave vector $k_F = 1.14 \times 10^7 cm^{-1}$ is still about a factor of five smaller than $\frac{\pi}{a} = 5.56 \times 10^7 cm^{-1}$, the width of the Brillouin zone in [100] direction.

The real and imaginary part of the dielectric function Eq. (2.11) were already plotted in chapter 1 for GaAs, using the parameters in Table 2.1, see Figure 1.3.

2.1.2 Dielectric functions for polar materials

We use a phenomenological model for the ionic dielectric response of the different dielectric materials surrounding the MoS_2-monolayer in our calculations of the carrier mobility in (dielectric 1)-MoS_2-(dielectric 2) structures. We account for two damped optical phonon modes.

$$\varepsilon_\omega = \varepsilon^{\infty} + \frac{(\varepsilon^0 - \varepsilon^i)\omega_{TO,1}^2}{\omega_{TO,1}^2 - \omega^2 + i\omega\gamma_1} + \frac{(\varepsilon^i - \varepsilon^{\infty})\omega_{TO,2}^2}{\omega_{TO,2}^2 - \omega^2 + i\omega\gamma_2} \tag{2.12}$$

[1] Experimental value for γ is an upper limit
[2] Effective mass from [61]
[3] Effective mass from [36], other parameters from [62]. PbTe bands are highly anisotropic and anisotropic, but have been approximately described with a single effective mass before [36].
[4] Parameters from [61], set $\gamma = \gamma_{ZnSe}$ due to lack of γ_{ZnS} in the literature.

A dielectric response of this kind can be parametrized in many equivalent ways (compare [8] with Eq. (2.12)) - we use a parametrization of the scattering strength in terms of an intermediate dielectric constant ε^i, as [1], but with nonzero damping rates for the optical modes. Here, ε^0 is the static and ε^∞ the high-frequency dielectric constant, $\omega_{TO,1}$ is the lower frequency transverse optical mode frequency and γ_1 the corresponding damping rate, and $\omega_{TO,2}$ is the lower frequency transverse optical mode frequency and γ_2 the corresponding damping rate. Setting $\varepsilon^i = \varepsilon^0$ or $\varepsilon^i = \varepsilon^\infty$ recovers Eq. (2.11) a dielectric response with just one optical resonance.

Some of the polar materials discussed here have strongly anisotropic dielectric functions [8, 7]. These are layered materials, where the in-plane dielectric function differs strongly from the out-of-plane dielectric function. As the structures discussed, if anisotropic at all, are stacks of monolayers, the crystal axes of the various materials align with the interfaces between the layer (x-y-plane) and the axes perpendicular to it (z-axis, see Fig. 3.4). Consequently, the dielectric function parallel to the hexagonal c-axis, $\varepsilon^\parallel$ as used by [8, 7], is equal to ε^{zz}, and the dielectric function perpendicular to the c-axis, $\varepsilon^\perp$ is the same as ε^{xx}.

All parameters relative to ionic dielectric response used can be found in Tab. 2.3.

Table 2.3: Material parameters for model dielectric functions

Material		ε^∞	ε^i	ε^0	$\omega_{TO,1}$ (meV)	γ_1(meV)	$\omega_{TO,2}$(meV)	γ_2(meV)
MoS_2[5]	ε^{xx}	15.2		15.4	47.61	0.12		
	ε^{zz}	6.2		6.23	58.27	0.29		
BN[6]	ε^{xx}	4.95	6.82	7.04	95.10	4.34	169.49	3.60
	ε^{zz}	4.10	4.56	5.09	97.08	0.99	187.22	9.92
SiO_2[7]	$\varepsilon^{xx} = \varepsilon^{zz}$	2.5	3.05	3.9	55.6	0.56	138.1	1.38
HfO_2[8]	$\varepsilon^{xx} = \varepsilon^{zz}$	5.03	6.58	22.0	12.4	0.124	48.35	0.4835

2.2 Carrier dielectric functions

2.2.1 Electronic dielectric function in the long wavelength limit

We discuss the carrier dielectric function in great detail in section 2.2. The present treatment serves only to give an intuitive understanding of its short wavelength limit. In that case, the only conceptual difference between the plasma oscillation and those of the ions is the lack of a restoring force and a damping in the former. Hence, we

[5] Ref. [7]

[6] Ref. [8]

[7] Dielectric constants and TO mode frequencies from Ref. [1].Ref. [9] has a review of measurements of these TO modes and their damping rates. The damping rates vary between measurements, but all have roughly $\gamma_1/\omega_{TO,1} = \gamma_2/\omega_{TO,2} = 0.01$, which we use.

[8] Dielectric constants and TO mode frequencies from Ref. [1]. Damping rates set to $\gamma_1/\omega_{TO,1} = \gamma_2/\omega_{TO,2} = 0.01$, because we could not find these values extracted previously.

skip the equation of motion for the electrons and jump straight to the polarization $\boldsymbol{P}^e$ (We use the superscript "e" for "electron") due to the plasma oscillations,

$$\boldsymbol{P_\omega}^e = ne\boldsymbol{u}^e_\omega = -\frac{nq^2}{m^*}\frac{\boldsymbol{E}_\omega}{\omega^2} \tag{2.13}$$

where m^* and e are the effective mass and charge of an electron, n is the electron concentration, and $\boldsymbol{u}^e_\omega$ is the displacement of an electron. We see that this equation bears a strong similarity to Eq. 2.3.

The contribution $\boldsymbol{P}^e_\omega$ to the polarization is only from the free carriers in the conduction bands. Corresponding expressions can be found for the hole plasma in p-type semiconductors, in particular for the polarization $\boldsymbol{P}^h$ due to the free holes of concentration p in the highest valence band. We will not give explicit expressions for the hole plasma, because we treat n-type semiconductors throughout this thesis, which are usually better described by parabolic bands. In principle, however, the formalism developed in this thesis applies to the holes in parabolic valence bands just as well as to the electrons in parabolic conduction bands, and we will use the term carrier throughout the remainder of this thesis to account for both scenarios.

The polarization due to the electrons in all the lower lying bands, the valence band electrons, is already taken into account, see Eq. 2.4. The total polarization for a non-polar n-type semiconductor therefore is the sum of the two, and its total displacement field is

$$\boldsymbol{D}^e_\omega = \boldsymbol{E}_\omega + 4\pi\left(\boldsymbol{P}^{\text{valence electrons}}_\omega + \boldsymbol{P}^e_\omega\right) = \varepsilon^e_\omega \boldsymbol{E}_\omega \tag{2.14}$$

with the dielectric function

$$\varepsilon^e_\omega = \varepsilon^\infty - \frac{4\pi ne^2}{m^*\omega^2} \tag{2.15}$$

Plasma frequency The plasma frequency ω_P, the natural oscillation frequency of the plasma excitations in the long wavelength limit, is the frequency at which the dielectric function ε^e_ω vanishes:

$$\varepsilon^e_{\omega_P} = \varepsilon^\infty - \frac{4\pi ne^2}{m^*\omega_P^2} = 0 \tag{2.16}$$

This determines ω_P as

$$\omega_P^2 = \frac{4\pi ne^2}{m^*\varepsilon^\infty}. \tag{2.17}$$

Similarly to the ionic case above, we will replace the material parameters n, e and m^* by the plasma frequency ω_P, and we can write the electronic dielectric function in the

long wavelength limit as

$$\varepsilon_\omega^e = \varepsilon^\infty - \varepsilon^\infty \frac{\omega_P^2}{\omega^2} = \varepsilon^\infty \left(1 - \frac{\omega_P^2}{\omega^2}\right). \tag{2.18}$$

Again, keep in mind that we have included the contribution from the valence band electrons in the electronic dielectric function.

2.2.2 Dielectric function in the random phase approximation

We use carrier dielectric functions in the random phase approximation (RPA) throughout this thesis. The name RPA stems from a sum over exponential terms which are neglected in the derivation with the argument that the phases in the exponentials vary randomly [32]. The RPA has historically been derived in different equivalent ways, see the discussion in [32, 22, 63]. Originally, the focus was to understand the behaviour of the collective excitations of an electron liquids, or plasmons [39, 23, 40].

In 1957, the ground state energy of the electron liquid was calculated from a sum over certain pertubation theoretic terms [64, 65], in an approximation which was later proved to be equivalent to the RPA [66, 67]. There are a multitude of equivalent derivations of the RPA [68, 69], including a quantum-mechanical equivalent of Landau's derivation (cf. appendix A)[70].

The radius r_S of a sphere whose volume contains on average one carrier, measured in units of the Bohr radius a_0 [63],

$$r_s = \left(\frac{4\pi}{3} n a_0\right)^{-\frac{1}{3}} \tag{2.19}$$

has been used as a measure for the applicability of the RPA. The RPA holds better for high-density carrier gases, or smaller r_S, and is quite accurate for $r_S \ll 1$ [22]. Pines puts the breakdown of the RPA at densities with $r_S \approx 1$ [22, Chapter 3].

When we apply the RPA to semiconductors, the effective Bohr radius

$$a_0^* = \frac{\hbar^2 \varepsilon^\infty}{e^2 m^*} = \varepsilon^\infty \frac{m_e}{m^*} a_0, \tag{2.20}$$

which is much larger than a Bohr radius for many semiconductors, because the high frequency dielectric function usually fulfills $\varepsilon^\infty \gg 1$ and the effective mass m^* is usually much smaller than the electron mass m_e, enters into the effective r_S^*

$$r_s^* = \left(\frac{4\pi}{3} n a_0^*\right)^{-\frac{1}{3}} = r_s \frac{m^*}{\varepsilon^\infty m_e}. \tag{2.21}$$

This means that the RPA has higher applicability for semiconductors than for metals, and can even be applied at quite low carrier concentrations [63, 36]. In GaAs at $n = 5 \times 10^{17} cm^{-3}$, $r_S^* \approx 0.89$ with the parameters from Tab. 2.1 but $r_s \approx 150$.

We employ a Lindhard-type or RPA carrier dielectric function [41, 22], but for nonzero temperatures [59, 60]. The nonzero temperature dielectric functions allow us to consider any point of the sliding scale between the classical and the extreme quantum limit.

The real part of the temperature dependent RPA dielectric functions has to be evaluated numerically, but its imaginary part can be expressed analytically. See, for example, [63, chapter 5.5] for the imaginary part of the three-dimensional temperature dielectric function. Arista and Brandt [59] calculated the real part of the temperature dependent dielectric function in three dimensions numerically, and Flensberg and Hu [60] calculated its two-dimensional equivalent.

The zero and high temperature limits of the real and imaginary parts of the dielectric function can also be expressed analytically. The three-dimensional zero temperature dielectric function was found by Lindhard [41]. The high temperature expressions for the three-dimensional dielectric function is discussed in the context of Landau damping in appendix A.

Stern gives an analytical expression for the zero temperature limit of the two-dimensional dielectric function [46]. There are also analytical expressions for the high temperature limit [71]. Maldague gives a semi-analytical formula for the temperature dependence of the static susceptibility [72], which is commonly used for capturing static screening.

All these expressions for the dielectric functions depend on a parabolic dependence of carrier energy on wave vector, because they were originally envisioned with either free electrons or effective mass theory in mind. We will assume thoughout this thesis that the kinetic energy of a carrier of wave vector $\boldsymbol{p}$

$$E_{\boldsymbol{p}} = \frac{\hbar^2 \boldsymbol{p}^2}{2m^*} \tag{2.22}$$

unless it is explicitly specified otherwise. Here m^* is the effective mass, and $\hbar$ is the reduced Planck constant.

In this section, we derive the expressions for the 2d and 3d dielectric functions alongside each other. In the process, we also introduce important quantities which will be used throughout this thesis, like the Fermi-Dirac distribution function, and the carrier density, and the Fermi wave vector and energy.

Distribution functions and carrier concentration We are interested in the dielectric function for a system with N carriers, which are all in equilibrium. Such a carrier is described by the Fermi-Dirac distribution function

$$f^0_{\boldsymbol{p}} = \frac{1}{1 + e^{E_{\boldsymbol{p}}\beta - \tilde{\mu}\beta}} \tag{2.23}$$

where $\tilde{\mu}$ is the chemical potential. $\beta = \frac{1}{k_B T}$ with the Boltzmann constant k_B. $E_{\boldsymbol{p}}$ is the energy of a carrier of wave vector $\boldsymbol{p}$, cf. Eq. (2.22).

The carrier concentration $n^{d=3}$ in three dimensions is

$$\begin{aligned} n^{d=3} &= \sum_{\boldsymbol{p},\sigma} f^0_{\boldsymbol{p}} = \frac{2}{(2\pi)^3} \int \mathrm{d}^3\boldsymbol{p}\, f^0_{\boldsymbol{p}} = \frac{8\pi}{(2\pi)^3} \int \mathrm{d}p \, \frac{p^2}{1 + \exp\left[(\frac{\hbar^2 p^2}{2m} - \tilde{\mu})\beta\right]} \\ &= \frac{\sqrt{2}}{\pi^2} \left(\frac{m}{\hbar^2\beta}\right)^{\frac{3}{2}} \Gamma(\frac{3}{2}) \mathfrak{F}_{\frac{1}{2}}(\tilde{\mu}\beta) = 2\left(\frac{m k_B T}{2\pi\hbar^2}\right)^{\frac{3}{2}} \mathfrak{F}_{\frac{1}{2}}(\tilde{\mu}\beta) \end{aligned} \tag{2.24}$$

The summation over the spin σ can be carried out, because $f^0_{\boldsymbol{p}}$ does not depend on spin. We also used the Fermi-Dirac integrals $\mathfrak{F}_j$

$$\mathfrak{F}_j(x) = \frac{1}{\Gamma(j+1)} \int_0^\infty \mathrm{d}t \, \frac{t^j}{e^{t-x} + 1}, \quad \text{with the Gamma-function } \Gamma(x), \tag{2.25}$$

and $\Gamma(\frac{3}{2}) = \frac{\sqrt{\pi}}{2}$ [4].

Similarly, the carrier concentration $n^{d=2}$ in two dimensions is

$$\begin{aligned} n^{d=2} &= \sum_{\boldsymbol{p},\sigma} f^0_{\boldsymbol{p}} = \frac{2}{(2\pi)^2} \int \mathrm{d}^2\boldsymbol{p}\, f^0_{\boldsymbol{p}} = \frac{4\pi}{(2\pi)^2} \int \mathrm{d}p \, \frac{p}{1 + \exp\left[(\frac{\hbar^2 p^2}{2m} - \tilde{\mu})\beta\right]} \\ &= \left(\frac{m}{\pi\hbar^2\beta}\right) \Gamma(1) \mathfrak{F}_0(\tilde{\mu}\beta) = \left(\frac{m}{\pi\hbar^2\beta}\right) \ln(1 + e^{\tilde{\mu}\beta}) \end{aligned} \tag{2.26}$$

Here we used the analytic expression for the $\mathfrak{F}_0$ Fermi-Dirac integral, and $\Gamma(1) = 1$.

Fermi wave vector and energy The chemical potential at zero temperature is called the Fermi energy E_F. At $T = 0$, all states with $E_{\boldsymbol{p}} < E_F$ are occupied, and all states with $E_{\boldsymbol{p}} > E_F$ are unoccupied. In the present case, where we have a spherical, parabolic band of effective mass m^*, the Fermi wave vector is defined by

$$E_F = \frac{\hbar^2 k_F^2}{2m^*}. \tag{2.27}$$

This means that the $T = 0$ Fermi-Dirac distribution reads

$$f^0_{\boldsymbol{p}} = \begin{cases} 1 & E_{\boldsymbol{p}} < E_F \\ 0 & E_{\boldsymbol{p}} > E_F. \end{cases} = \begin{cases} 1 & |\boldsymbol{p}| < k_F \\ 0 & |\boldsymbol{p}| > k_F. \end{cases} \tag{2.28}$$

This carrier configuration is sometimes called the "Fermi-sea". It is sketched in Fig. 2.1.

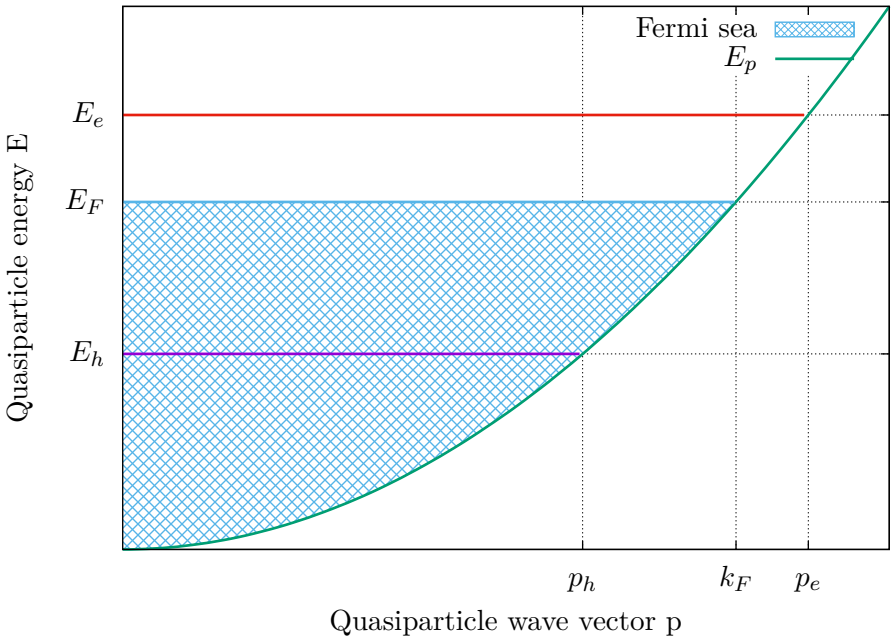

Figure 2.1: Energy E_p (Eq. (2.22)) as a function of wave vector p. The region marked Fermi-sea indicates all occupied states at $T = 0$. E_e and E_h are the quasi-particle and hole energy, p_e and p_h are the quasi-particle and hole wave vector. The Fermi energy and wave vector, E_F, k_F are also marked.

The carrier concentration at $T = 0$ thus becomes[9]

$$n^d = \sum_{\boldsymbol{p},\sigma} f^0_{\boldsymbol{p}} = \frac{2}{(2\pi)^d} \int\limits_{|\boldsymbol{p}|<k_F} \mathrm{d}^d\boldsymbol{p} = \frac{k_F^d}{\pi^{d-1} d} \tag{2.29}$$

Fermi-Energy scaling In order to investigate the effects of temperature on the dielectric functions, scales for both energy and wave vector which are independent of temperature can be useful. We will use the Fermi wave vector and energy as a wave vector or energy scale, even when the temperature is nonzero:

$$k_F^{d=2} = \sqrt{2\pi n^{d=2}} \qquad k_F^{d=3} = \sqrt[3]{3\pi^2 n^{d=3}} \tag{2.30}$$

The Fermi wave vector k_F is only determined by the density of carriers. Using Eq. (2.26) and Eq. (2.24), we can express how the Fermi energy is connected to the

[9] In chapter 5 and chapter 6, we will not include the superscript, because chapter 5 only deals with the 3-d case and chapter 6 only with the 2-d case. However, we explicitly use $n_S \equiv n^{d=2}$ for the two-dimensional sheet density in chapter 6 to distinguish it from a volume density.

chemical potential at a given temperature $k_B T = \frac{1}{\beta}$: For three dimensions, we have

$$E_F^{d=3}\beta = \left[\frac{3\sqrt{\pi}}{4}\mathfrak{F}_{\frac{1}{2}}\left(\tilde{\mu}^{d=3}\beta\right)\right]^{\frac{2}{3}} = \left[\frac{3}{2}\int_0^\infty \mathrm{d}x\, \frac{x^{\frac{1}{2}}}{1+e^{x-\tilde{\mu}^{d=3}\beta}}\right]^{\frac{2}{3}} \tag{2.31}$$

and for two dimensions the analytical expression

$$E_F^{d=2}\beta = \ln\left(1+e^{\tilde{\mu}^{d=2}\beta}\right) \tag{2.32}$$

holds. Figure 2.2 shows that the Fermi energy is positive for all chemical potentials, with $E_F\beta \to 0$ as $\tilde{\mu}\beta \to -\infty$. This makes it useful for scaling energies with it. One can also see that for low temperatures, $\tilde{\mu} \gg k_B T$, $E_F \to \tilde{\mu}$ as expected.

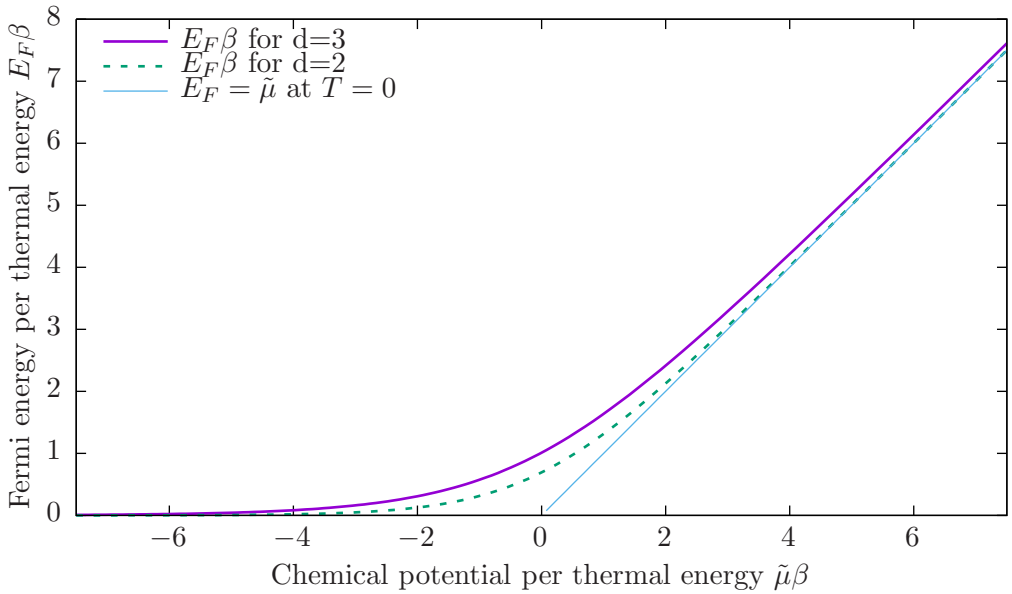

Figure 2.2: Fermi energy E_F as a function of chemical potential $\tilde{\mu}$ in two and three dimensions, both in units of the thermal energy $k_B T = \frac{1}{\beta}$. The limit for $T = 0$, where $\tilde{\mu} \to E_F$ is also shown.

Dielectric function and polarizability in two and three dimensions In this section, we derive the RPA carrier dielectric function

$$\varepsilon^c_{\boldsymbol{k},\omega} = \varepsilon^\infty + \chi^c_{k,\omega} \tag{2.33}$$

with the susceptibility $\chi^c_{k,\omega}$.[10] In the literature, the dielectric function is often defined as $\varepsilon = 1 + \chi$, when the context is a free electron model, so that $\varepsilon^\infty = 1$. As we apply the RPA to semiconductors described with effective mass theory, we always have $\varepsilon^\infty \neq 1$. As the carrier susceptibility $\chi^c_{k,\omega}$ is the same in both cases, we focus on this

[10] The polarizability and susceptibility are not defined consistently throughout our references. If in doubt, the reader should work back to the dielectric function for comparisons with the literature.

quantity. We also drop the superscript "c" in this section, to make room for a superscript indicating the dimension d.

The carrier susceptibility is

$$\chi^d_{k,\omega} = \nu^d_k \alpha^d_{k,\omega} \tag{2.34}$$

in a 3-d or 2-d system, where d marks the number of degrees of freedom.

$$\nu_k = \begin{cases} \frac{2\pi e^2}{k} & d = 2 \\ \frac{4\pi e^2}{k^2} & d = 3 \end{cases} \tag{2.35}$$

is the Fourier transform of the Coulomb potential and $\alpha^d_{k,\omega}$ is the polarizability.

In the random phase approximation (RPA), the polarizability is [22]

$$\alpha^d_{k,\omega} = -\lim_{\gamma\to 0} \sum_{\boldsymbol{p},\sigma} \frac{n_{\boldsymbol{p}+\boldsymbol{k},\sigma} - n_{\boldsymbol{p},\sigma}}{E_{\boldsymbol{p}+\boldsymbol{k}} - E_{\boldsymbol{p}} - \hbar\omega - i\hbar\gamma}. \tag{2.36}$$

γ is a positive damping rate used for regularizing the summation and will be discussed further later. $n_{\boldsymbol{p},\sigma}$ is the occupation density of a state with wave vector $\boldsymbol{p}$ and spin σ

The dielectric function is defined by Eq. (2.34) through Eq. (2.36) in two and in three dimensions [46]. The definitions of the polarizability change between authors.
Stern [46], e.g., includes part of the Fourier transform of the Coulomb potential in his definition of the polarizability. Our definition of the polarizability differs from Stern's in order to highlight the similarities between the 2d and the 3d case. These different exact definitions of the polarizability yield the same dielectric function.

At this point, we can already directly derive the expression for the imaginary part of the dielectric function in the RPA, which will be of use extensively latter in this thesis. Using

$$\lim_{\gamma\to 0} \mathfrak{Im}\left\{\frac{1}{x - i\gamma}\right\} = \lim_{\gamma\to 0} \frac{\gamma}{x^2 + \gamma^2} = \pi\delta(x), \tag{2.37}$$

where $\delta(x)$ is the Dirac delta function, and exchanging the order of the summation and the limit in Eq. (2.36), we find

$$\mathfrak{Im}\left\{\varepsilon_{k,\omega}\right\} = \pi\nu_k \sum_{\boldsymbol{p},\sigma} \left(n_{\boldsymbol{p},\sigma} - n_{\boldsymbol{p}+\boldsymbol{k},\sigma}\right) \delta\left(E_{\boldsymbol{p}+\boldsymbol{k}} - E_{\boldsymbol{p}} - \hbar\omega\right) \tag{2.38}$$

After substituting $n_{\boldsymbol{p},\sigma} = \frac{f^0_{\boldsymbol{p}}}{L^d}$ where, $L^2 = A$ is the area of the 2d system, and $L^3 = V$ is the volume of the 3d system, into Eq. (2.36), we can carry out the spin summation.

Moreover turning the summation over $\boldsymbol{p}$ into an integration, we find

$$\alpha^d_{k,\omega} = -2\lim_{\gamma\to 0} \int_{\boldsymbol{p}} \frac{f^0_{\boldsymbol{p}+\boldsymbol{k}} - f^0_{\boldsymbol{p}}}{E_{\boldsymbol{p}+\boldsymbol{k}} - E_{\boldsymbol{p}} - \hbar\omega - i\hbar\gamma}. \tag{2.39}$$

Here, we have used the notation

$$\int\limits_{\boldsymbol{p}} \equiv \frac{1}{(2\pi)^d} \int \mathrm{d}^d \boldsymbol{p} \tag{2.40}$$

for wave vector integrals which hold for both two and three dimensions. This notation will prove particularly useful in chapter 4, where many long equations will be discussed. The imaginary part of the RPA dielectric function thus now reads

$$\mathfrak{Im}\left\{\varepsilon_{k,\omega}\right\} = 2\pi\nu_k \int\limits_{\boldsymbol{p}} \left(f^0_{\boldsymbol{p}} - f^0_{\boldsymbol{p}+\boldsymbol{k}}\right) \delta\left(E_{\boldsymbol{p}+\boldsymbol{k}} - E_{\boldsymbol{p}} - \hbar\omega\right). \tag{2.41}$$

It will turn out to be advantageous to make the substitution $\boldsymbol{p} \to \boldsymbol{p}' = \boldsymbol{p} - \frac{\boldsymbol{k}}{2}$, so that Eq. (2.39) will take on the symmetric form

$$\alpha^d_{k,\omega} = -2 \lim_{\gamma\to 0} \int\limits_{\boldsymbol{p}} \frac{f^0_{\boldsymbol{p}+\frac{\boldsymbol{k}}{2}} - f^0_{\boldsymbol{p}-\frac{\boldsymbol{k}}{2}}}{E_{\boldsymbol{p}+\frac{\boldsymbol{k}}{2}} - E_{\boldsymbol{p}-\frac{\boldsymbol{k}}{2}} - \hbar\omega - i\hbar\gamma}. \tag{2.42}$$

We assume that the carriers are all in one spherical, parabolic band characterized by the effective mass m^*, cf. Eq. (2.22). We scale all wave vectors with the Fermi wave vector k_F and all energies with the Fermi energy E_F from Eq. (2.27). We use capital letters for the scaled wave vectors P and K and the scaled frequencies and damping rates Ω and Γ:

$$P = \frac{p}{k_F} \quad K = \frac{k}{k_F} \qquad \text{and} \qquad \Omega = \frac{\hbar\omega}{E_F} \quad \Gamma = \frac{\hbar\gamma}{E_F} \tag{2.43}$$

The carrier energies fulfill $E_{\boldsymbol{p}} = E_F P^2$. In this notation, Eq. (2.42) becomes

$$\alpha^d_{k,\omega} = -\lim_{\Gamma\to 0} \frac{2k_F^d}{(2\pi)^d E_F} \int \mathrm{d}^d \boldsymbol{P}\, \frac{f^0_{\boldsymbol{P}+\frac{\boldsymbol{K}}{2}} - f^0_{\boldsymbol{P}-\frac{\boldsymbol{K}}{2}}}{2P_x K - \Omega - i\Gamma}. \tag{2.44}$$

In the last step, we aligned the x-axis of the P-coordinate system with $\boldsymbol{K}$, so that $\boldsymbol{P}\cdot\boldsymbol{K} = P_x K$. We can now simplify Eq. (2.44) by carrying out the integration over the other $d-1$ Cartesian axes. Defining the quantities

$$F^d_P = \begin{cases} \int\limits_{-\infty}^{\infty} \mathrm{d}P_y\, f^0_{\boldsymbol{P}=P_x\boldsymbol{e}_x+P_y\boldsymbol{e}_y} & d=2 \\ \int\limits_{-\infty}^{\infty} \mathrm{d}P_y \int\limits_{-\infty}^{\infty} \mathrm{d}P_z\, f^0_{\boldsymbol{P}=P_x\boldsymbol{e}_x+P_y\boldsymbol{e}_y+P_z\boldsymbol{e}_z} & d=3, \end{cases} \tag{2.45}$$

which will be evaluated explicitly shortly, Eq. (2.44) can be written as a scalar integral,

$$\alpha^d_{k,\omega} = -\frac{2k_F^d}{(2\pi)^d E_F} \frac{1}{2K} \lim_{\Gamma\to 0} \int\limits_{-\infty}^{\infty} \mathrm{d}P\, \frac{F^d_{P+\frac{K}{2}} - F^d_{P-\frac{K}{2}}}{P - \frac{\Omega}{2K} - i\frac{\Gamma}{2K}}. \tag{2.46}$$

Finally, introducing the dimensionless quantities $z = \frac{K}{2}$ and $u = \frac{\Omega}{2K}$ used by Lindhard [41] for easy reference, we write

$$\alpha^d_{k,\omega} = -\frac{A^d}{2\pi}\frac{1}{4z}\lim_{\Gamma\to 0}\int_{-\infty}^{\infty} \mathrm{d}P\, \frac{F^d_{P+z} - F^d_{P-z}}{P - u - iD}, \tag{2.47}$$

with the additional constant $A^d = \frac{2k_F^d}{(2\pi)^{(d-1)}E_F}$ and $D = \frac{\Gamma}{2K}$.

Real and imaginary part of α The real and imaginary parts of $\alpha^d_{k,\omega}$ from Eq. (2.47) read

$$\mathfrak{Re}\left\{\alpha^d_{k,\omega}\right\} = \frac{A^d}{4z}\lim_{D\to 0}\int_{-\infty}^{\infty}\frac{\mathrm{d}P}{2\pi}\,\frac{P-u}{(P-u)^2+D^2}\left(F^d_{P-z} - F^d_{P+z}\right) \tag{2.48}$$

$$\mathfrak{Im}\left\{\alpha^d_{k,\omega}\right\} = \frac{A^d}{4z}\lim_{D\to 0}\int_{-\infty}^{\infty}\frac{\mathrm{d}P}{2\pi}\,\frac{D}{(P-u)^2+D^2}\left(F^d_{P-z} - F^d_{P+z}\right) \tag{2.49}$$

When we exchange the limit and the integration, we find

$$\mathfrak{Re}\left\{\alpha^d_{k,\omega}\right\} = \frac{A^d}{4z}\mathfrak{P}\int_{-\infty}^{\infty}\frac{\mathrm{d}P}{2\pi}\,\frac{F^d_{P-z} - F^d_{P+z}}{P-u} \tag{2.50}$$

$$\mathfrak{Im}\left\{\alpha^d_{k,\omega}\right\} = \frac{A^d}{4z}\frac{1}{2}(F^d_{u-z} - F^d_{u+z}) \tag{2.51}$$

Here, we have used the Poisson representation of the Dirac delta function,

$$\delta(P-u) = \lim_{D\to 0}\frac{1}{\pi}\frac{D}{(P-u)^2+D^2}. \tag{2.52}$$

We denote the Cauchy principal value of an integral with $\mathfrak{P}$.

Note that Eq. (2.50) and Eq. (2.51) can equivalently be obtained from

$$\alpha^d_{k,\omega} = \frac{A^d}{2\pi}\frac{1}{4z}\int_{\Gamma_L}\mathrm{d}P\,\frac{F^d_{P-z} - F^d_{P+z}}{P-u}, \tag{2.53}$$

with a Landau Contour Γ_L for real valued singularities u. Such a Landau Contour is shown in Fig. A.2 in appendix A. The Cauchy principal value yielding the real part of the polarizability is the contribution from the integration along the real axis. The imaginary part of the polarizability stems from the integration off the real axis, the residue contribution in Landau's formalism.

After defining the Cauchy principal values

$$I^d_x = \frac{1}{\pi}\mathfrak{P}\int_{-\infty}^{\infty}\frac{\mathrm{d}y}{y}\,F^d_{x+y} = \frac{1}{\pi}\lim_{\varepsilon\to 0}\int_{\varepsilon}^{\infty}\frac{\mathrm{d}y}{y}\,\left(F^d_{x+y} - F^d_{x-y}\right), \tag{2.54}$$

we can write the real part of the polarizability as

$$\mathfrak{Re}\left\{\alpha^d_{k,\omega}\right\} = \frac{A^d}{4z}\frac{1}{2}\left(I^d_{u-z} - I^d_{u+z}\right), \tag{2.55}$$

similar to Eq. (2.51).

The integral I_x Eq. (2.54) has certain properties independent of the precise choice of distribution function. As the energy only depends on the magnitude, and not one direction of the wave vector, Eq. (2.22), the expressions F_x Eq. (2.45) have to be even functions of x, and the I_x are consequently odd functions of x. This entails $I_{x=0} = 0$.

The integrand of I^d_x fulfills

$$\lim_{y\to 0}\frac{1}{\pi}\frac{F^d_{x+y} - F^d_{x-y}}{y} = \frac{2}{\pi}\frac{\partial}{\partial x}F^d_x, \tag{2.56}$$

i.e., the singularity in the integrand of I^d_x is removed.

The polarizability α, and hence the carrier dielectric function ε can be evaluated explicitly in the classical limit and in the degenerate limit. The classical limit yields the expression due to Landau [2] discussed in appendix A. We will now discuss the general case for nonzero temperature, and afterwards the degenerate, or $T = 0$ limit.

2.2.2.1 Nonzero temperature dielectric function

For the evaluation of the nonzero temperature dielectric functions, we first evaluate the quantities F^d_P, Eq. (2.45). In 2d, this yields

$$F^{d=2}_P = \sqrt{\frac{\pi}{E_F\beta}}\mathfrak{F}_{-\frac{1}{2}}\left(\tilde{\mu}\beta - P^2E_F\beta\right), \tag{2.57}$$

with the Fermi-Dirac-integral from Eq. (2.25). In 3d, an integration best carried out in polar coordinates yields,

$$F^{d=3}_P = \frac{\pi}{E_F\beta}\mathfrak{F}_0\left(\tilde{\mu}\beta - P^2E_F\beta\right) = \frac{\pi}{E_F\beta}\ln\left(1 + e^{\tilde{\mu}\beta - P^2E_F\beta}\right), \tag{2.58}$$

which can even be expressed in closed form. Consequently, the imaginary part of the three dimensional dielectric function is expressed through the simple expression [63, chapter 5.5]

$$\mathfrak{Im}\left\{\varepsilon^{d=3}_{k,\omega}\right\} = \frac{\nu^{d=3}_k A^{d=3}}{8z}\frac{\pi}{E_F\beta}\ln\left(\frac{1 + e^{\tilde{\mu}\beta - (u-z)^2E_F\beta}}{1 + e^{\tilde{\mu}\beta - (u+z)^2E_F\beta}}\right) \tag{2.59}$$

The imaginary part of the two-dimensional dielectric function still features Fermi-Dirac integrals:

$$\mathfrak{Im}\left\{\varepsilon_{k,\omega}^{d=2}\right\} = \frac{\nu_k^{d=2} A^{d=2}}{8z}\sqrt{\frac{\pi}{E_F\beta}}\left[\mathfrak{F}_{-\frac{1}{2}}\left(\tilde{\mu}\beta - (u-z)^2 E_F\beta\right) - \mathfrak{F}_{-\frac{1}{2}}\left(\tilde{\mu}\beta - (u+z)^2 E_F\beta\right)\right] \tag{2.60}$$

We do not give the real part of the dielectric functions explicitly, because there is no closed form expression for them. They are obtained by substituting the expressions F_P^d Eq. (2.45) into into the Cauchy Principal integrals I_P^d Eq. (2.54), evaluating the Cauchy Principal integrals numerically and substituting them into the polarizability Eq. (2.55). The dielectric function is determined by Eq. (2.34).

Numerical evaluation of $\varepsilon_{k,\omega}^{d=3}$ As an example, we give some detail of the numerical evaluation of the three dimensional dielectric function $\varepsilon_{k,\omega}^{d=3}$.

Using Eq. (2.33), Eq. (2.34) and Eq. (2.55), we find

$$\mathfrak{Re}\left\{\varepsilon_{k,\omega}^{d=3}\right\} = \varepsilon^{\infty} + \frac{\nu_k^{d=3} A^{d=3}}{8z}\left(I_{u-z}^{d=3} - I_{u+z}^{d=3}\right) \tag{2.61}$$

with

$$I_x^{d=3} = \frac{1}{E_F\beta}\lim_{\delta\to 0}\int_{\delta}^{\infty}\frac{\mathrm{d}y}{y}\ln\left(\frac{1+e^{\tilde{\mu}\beta-(x+y)^2E_F\beta}}{1+e^{\tilde{\mu}\beta-(x-y)^2E_F\beta}}\right) \tag{2.62}$$

$I_x^{d=3}$ will have to be calculated numerically and tabulated for every value of $\tilde{\mu}\beta$ (i.e.,

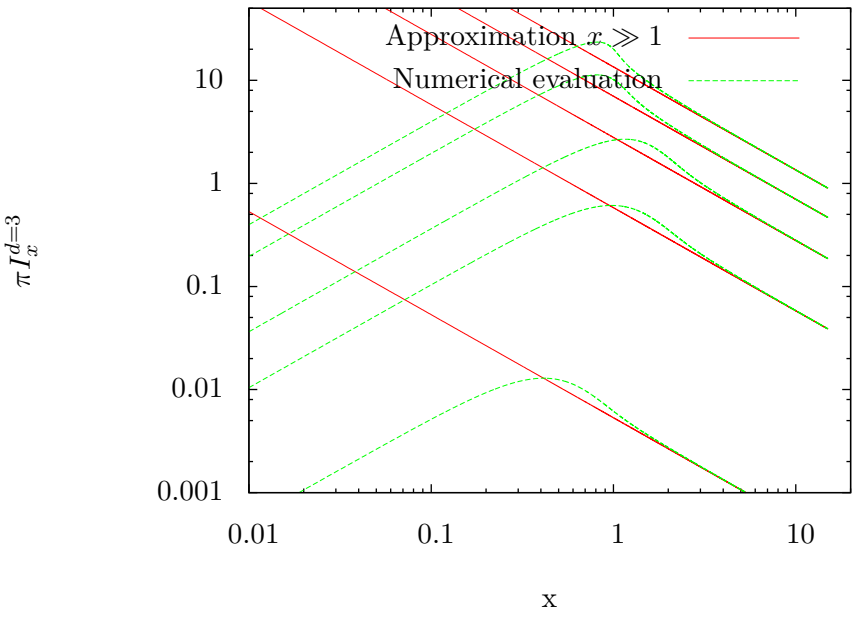

Figure 2.3: Plot of $\pi I_x^{d=3}$ from Eq. (2.62) against x for $\tilde{\mu}\beta \in \{-5, -1, 1, 5, 10\}$ from bottom to top. Also plotted are the approximations for large x for the same values of $\tilde{\mu}\beta$.

every carrier density) and x. However, the asymptotic behavior for large x can be calculated more easily. For $x \gg 1$, $e^{-2E_F\beta yx} \ll e^{2E_F\beta yx}$, so that $I_x^{d=3} \approx -\int_0^\infty \frac{\mathrm{d}y}{y} \ln\left[1+\exp\left(\tilde{\mu}\beta - E_F\beta(y-x)^2\right)\right]$. If, moreover, the width of the Gaussian is much smaller than x we can approximate further

$$I_x^{d=3} \approx -\frac{1}{x}\int_0^\infty \mathrm{d}y\, \ln\left[1+\exp\left(\tilde{\mu}\beta - E_F\beta(y-x)^2\right)\right] = -\frac{2}{\sqrt{E_F\beta}x}\int_0^\infty \mathrm{d}y\, \ln\left[1+\exp\left(\tilde{\mu}\beta - y^2\right)\right].$$

The last expression has the advantage that it only contains an integral which is independent of x. Figure 2.3 shows the numerically calculated $I_x^{d=3}$ for several choices of $\tilde{\mu}\beta$, and the approximation for large x.

2.2.2.2 Highly degenerate or zero temperature dielectric function

The expressions for the polarizability $\alpha_{k,\omega}$ above can be evaluated explicitly in the zero temperature limit. The corresponding dielectric function in three dimensions was first found by Lindhard [41], and is hence called the Lindhard dielectric function. The two-dimensional zero temperature electronic dielectric function was later calculated by Stern [46].

The zero temperature dielectric functions have one very striking difference with the classical dielectric functions: They are real for a large region of the wave-vector vs frequency region, while the classical dielectric functions are generally complex valued for nonzero wave vectors. This means that the natural oscillation frequencies of the carrier plasma will be real, i.e., undamped, for certain wave vectors and frequencies at zero temperature, where they were damped due to Landau damping at higher temperature. That means that Landau damping at $T = 0$ is restricted to certain regions of $k-\omega$ space, the single pair excitation region.

2.2.2.2.1 Single pair excitation region The single pair excitation region is the region in a wave vector – energy plane where energy and quasi-momentum conservation allow the plasma excitation to decay into an electron-hole pair. Due to energy conservation, the plasmon energy has to be the difference between the electronic energy E_p at the electron wave vector $\boldsymbol{p}_e$, $E_{\boldsymbol{p}_e} = E_e$, and at the hole wave vector $\boldsymbol{p}_h$, $E_{\boldsymbol{p}_h} = E_h$. The former has to lie above the Fermi sea, the latter below. This is is illustrated in Fig. 2.1. Momentum conservation means that $\boldsymbol{p}_e = \boldsymbol{p}_h + \boldsymbol{k}$, where $\boldsymbol{k}$ is the plasmon wave vector. We hence find

$$\hbar\omega_k = \frac{\hbar^2}{2m^*}\left[\boldsymbol{p}_e^2 - \boldsymbol{p}_h^2\right] = \frac{\hbar^2}{2m^*}\left[(\boldsymbol{p}_h+\boldsymbol{k})^2 - \boldsymbol{p}_h^2\right] = \frac{\hbar^2}{2m^*}\left[\boldsymbol{k}^2 + 2\boldsymbol{k}\cdot\boldsymbol{p}_h\right] \tag{2.63}$$

As $-kp_h \leq \boldsymbol{k} \cdot \boldsymbol{p}_h \leq kp_h$, and $p_h < k_F$, we get

$$\frac{\hbar^2}{2m^*} k \left[k - 2k_F\right] \leq \hbar\omega_k \leq \frac{\hbar^2}{2m^*} k \left[k + 2k_F\right] \tag{2.64}$$

for the single pair excitation regime. The phrase is used to distinguish from a regime, in which multiple pairs can be excited, see, e.g., [32]. When expressed in terms of Fermi energy and wave vector, the long-wavelength boundary of the single pair excitation regime is at $\frac{E}{E_F} = \frac{k}{k_F}(\frac{k}{k_F} + 2)$.

Natural oscillations are undamped outside the single pair excitation region, because they do cannot fulfill energy and momentum conservation for the decay into an electron-hole pair. At higher temperatures, the Fermi-sea is smeared out, so that the decay of a plasmon into an electron-hole pair is always possible (if unlikely), and the natural oscillations are always Landau-damped (if only by a small amount).

Imaginary part of the zero temperature polarizability At zero temperature, the Fermi-Dirac distribution function Eq. (2.23) becomes

$$f^0_{\boldsymbol{P}} = \begin{cases} 1 & |\boldsymbol{P}| < 1 \\ \frac{1}{2} & |\boldsymbol{P}| = 1 \\ 1 & |\boldsymbol{P}| > 1 \end{cases} \tag{2.65}$$

with the wave vector $\boldsymbol{P} = \boldsymbol{p}/k_F$. Consequently, the quantity Eq. (2.45) is

$$F_P^2 = \begin{cases} 2\sqrt{1 - P^2} & |P| < 1 \\ 0 & |P| \geq 1 \end{cases} \tag{2.66}$$

in the 2d case and

$$F_P^3 = \begin{cases} \pi\left(1 - P^2\right) & |P| < 1 \\ 0 & |P| \geq 1 \end{cases} \tag{2.67}$$

in the 3d case. Using the notation

$$D_\pm = \begin{cases} 1 & |z \pm u| < 1 \\ 0 & |z \pm u| \geq 1 \end{cases} \tag{2.68}$$

introduced by Stern [46], we can write the imaginary part of the polarizability as

$$\mathfrak{Im}\left\{\alpha^d_{k,\omega}\right\} = \frac{A^d}{4z} \begin{cases} D_-\sqrt{1 - (u - z)^2} - D_+\sqrt{1 - (u + z)^2} & d = 2 \\ \frac{\pi}{2}\left\{D_-\left[1 - (u - z)^2\right] - D_+\left[1 - (u + z)^2\right]\right\} & d = 3 \end{cases} \tag{2.69}$$

This expression contains the claim we made above, that the imaginary part of the dielectric function is only nonzero in the single pair excitation region. To make this point clearer, we define the matrix

$$Sgn = \begin{pmatrix} \mathrm{sgn}(1+z-u) & \mathrm{sgn}(-1+z-u) \\ \mathrm{sgn}(1-z-u) & \mathrm{sgn}(-1-z-u) \end{pmatrix}, \tag{2.70}$$

which can have 9 different values for $\pm 1 \pm z - u \neq 0$.

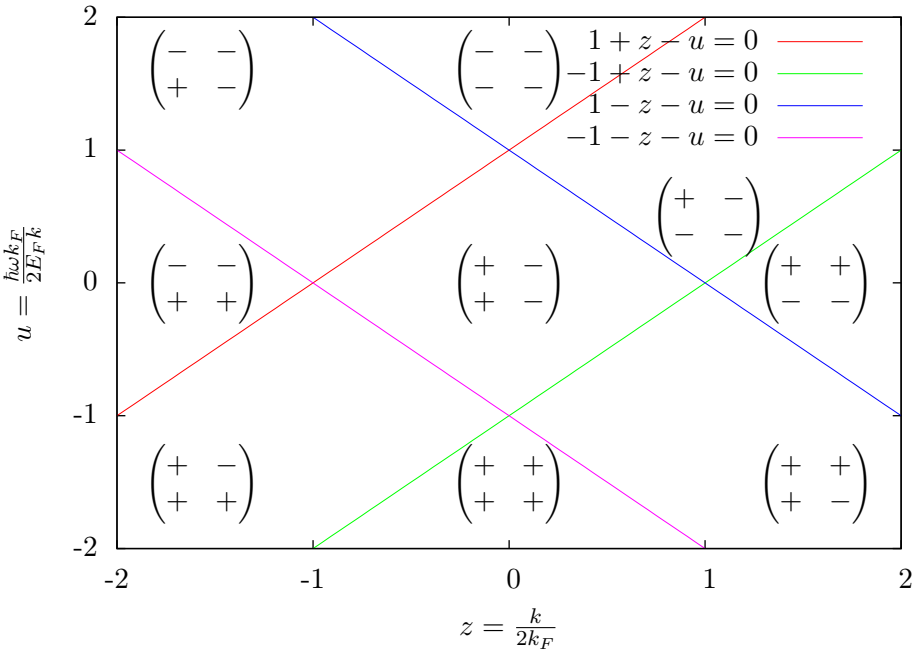

Figure 2.4: The nine different values of the matrix Eq. (2.70) in a plan spanned by the quantities z and u. The lines $\pm 1 \pm z - u = 0$ where sign changes in one of the elements in the matrix Eq. (2.70) occurs are also included.

These values are plotted as a function of z and u in Fig. 2.4. If the signs in the upper row of the sign matrix are equal, $D_- = 0$. If the signs in the lower row of the sign matrix are equal, $D_+ = 0$. If both of these conditions apply, $D_\pm = 0$, and hence $\mathfrak{Im}\left\{\alpha^d_{k,\omega}\right\} = 0$. That means the dielectric function is entirely real in those regions.

If the signs in the upper row of the sign matrix are not equal, $D_- = 1$. If the signs in the lower row of the sign matrix are not equal, $D_+ = 1$. If one of these conditions applies, $\mathfrak{Im}\left\{\alpha^d_{k,\omega}\right\}$ is nonzero, and the dielectric function is complex-valued.

Fig. 2.5 is similar to Fig. 2.4, but it shows the sign matrix Eq. (2.70) for wave vectors $k > 0$ and frequencies $\omega > 0$. We see that the borders of the region where $\mathfrak{Im}\left\{\alpha^d_{k,\omega}\right\} \neq 0$, are the parabolas $u = z \pm 1$, or $\hbar\omega/E_F = k/k_F\,(k/k_F \pm 2)$, i.e., the borders of the single pair excitation region Eq. (2.64).

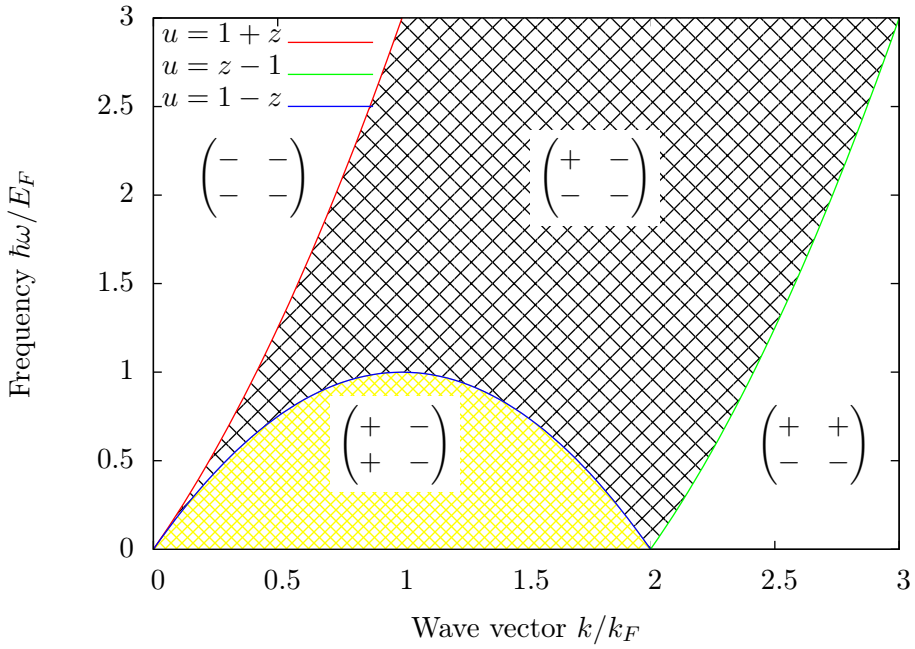

Figure 2.5: Values of the sign matrix defined in Eq. (2.70) in the part of the wave vector–frequency plane where the wave vector $k > 0$ and the frequency $\omega > 0$. The $T = 0$ dielectric function in 2d and 3d only has imaginary contributions in the shaded areas, and is real elsewhere for $k > 0$ and $\omega > 0$.

Real part of the zero temperature polarizability The real part of the zero temperature polarizability in 2d is [46]

$$\mathfrak{Re}\left\{\alpha_{k,\omega}^{d=2}\right\} = \frac{A^{d=2}}{4z}\left[2z - D_{-}\mathrm{sgn}(z-u)\sqrt{1-(u-z)^2} - D_{+}\mathrm{sgn}(z+u)\sqrt{1-(u+z)^2}\right]. \tag{2.71}$$

and in 3d is [41]

$$\mathfrak{Re}\left\{\alpha_{k,\omega}^{d=3}\right\} = \frac{A^{d=3}}{8z}\left\{4z + \ln\frac{|1+z-u|}{|1-z+u|}\left[1-(u-z)^2\right] - \ln\frac{|1-z-u|}{|1+z+u|}\left[1-(u+z)^2\right]\right\} \quad \text{for } 1 \pm z \pm u \neq 0. \tag{2.72}$$

This means the real part of the Lindhard dielectric function is

$$\mathfrak{Re}\left\{\alpha_{k,\omega}^{d=3}\right\} = \varepsilon^{\infty} + \frac{\nu_k^{d=3} A^{d=3}}{8z}\left\{4z + \ln\frac{|1+z-u|}{|1-z+u|}\left[1-(u-z)^2\right] - \ln\frac{|1-z-u|}{|1+z+u|}\left[1-(u+z)^2\right]\right\} \quad \text{for } 1 \pm z \pm u \neq 0. \tag{2.73}$$

See [73] for a step by step derivation. $\mathfrak{Re}\left\{\alpha_{k,\omega}^{d=3}\right\}$ has singularities at the arguments of the logarithms, see Fig. 2.5 and Fig. 2.4.

2.2.3 $\mathfrak{Im}\left\{\frac{-1}{\varepsilon_{\boldsymbol{k},\omega}}\right\}$ and the f-sum rule

As mentioned in chapter 1 the imaginary part of the inverse dielectric function is a crucial quantitiy in this thesis. In this section, we discuss some features of the imaginary part of the inverse carrier dielectric function.

2.2.3.1 $\mathfrak{Im}\left\{\frac{-1}{\varepsilon_{k,\omega}}\right\}$

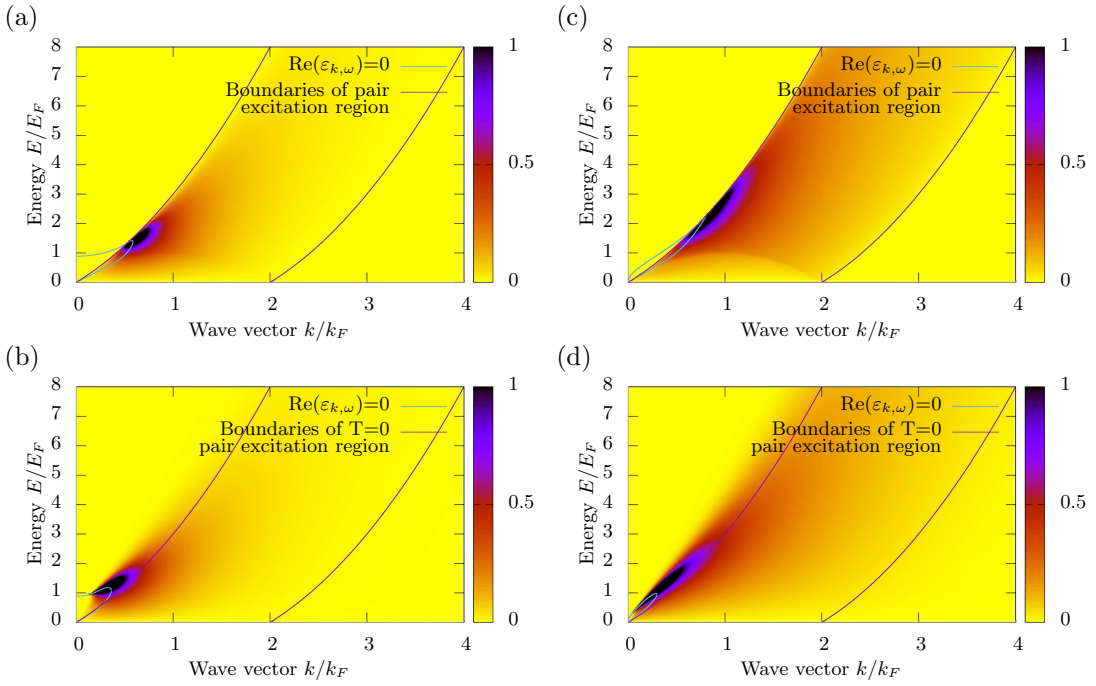

Figure 2.6: $\mathfrak{Im}\left\{\frac{-\varepsilon^{\infty}}{\varepsilon_{k,\omega}}\right\}$ as a function of wave vector and energy $E = \hbar\omega$. The left column, (a) and (b) show the three-dimensional dielectric function for electrons in GaAs. The right column, (c) and (d) show the two-dimensional dielectric function for electrons in the $z = 0$ plane in GaAs. In first row, (a) and (c), the temperature is $T = 0$. In second row, (b) and (d), the temperature is $T = 300K$. In the three-dimensional case, the electron density $n = 5 \times 10^{17} cm^{-3}$. In the two-dimensional case, the electron sheet density n_S has been chosen so that the Fermi-wave vector is the same as in the three-dimensional case: $n_S = \frac{1}{2\pi}(3\pi^2 n)^{\frac{2}{3}} \approx 9.6 \times 10^{11} cm^{-2}$. All subplots have the zeros of the real part of the dielectric function and the boundaries of the $T = 0$ pair excitation region marked Eq. (2.64).

In this section, we discuss some properties of the imaginary part of the inverse dielectric function. The quantity

$$\mathfrak{Im}\left\{\frac{-1}{\varepsilon_{k,\omega}}\right\} = \frac{\mathfrak{Im}\left\{\varepsilon_{k,\omega}\right\}}{\mathfrak{Im}\left\{\varepsilon_{k,\omega}\right\}^2 + \mathfrak{Re}\left\{\varepsilon_{k,\omega}\right\}^2} \tag{2.74}$$

is a measure of the strength of the collective excitations described by the dielectric

function depending on their wave vector and frequency, e.g.[63].

This is particularly evident for excitations where $\mathfrak{Im}\{\varepsilon_{k,\omega}\}$ is zero, or very small. As $\mathfrak{Im}\left\{\frac{-1}{\varepsilon_{k,\omega}}\right\}$ is proportional to the Poisson representation of the delta function, Eq. (2.52),

$$\mathfrak{Im}\left\{\frac{-1}{\varepsilon^{tot}_{k,\omega}}\right\} \longrightarrow \pi\delta\left\{\left|\mathfrak{Re}\left\{\varepsilon_{k,\omega}\right\}\right|\right\} = \pi\sum_i \frac{\delta\left\{\omega-\omega^i_k\right\}}{\left|\frac{\partial}{\partial\omega}\mathfrak{Re}\left\{\varepsilon_{k,\omega}\right\}\right|} \qquad \text{for } \mathfrak{Im}\{\varepsilon\}\to 0, \tag{2.75}$$

where ω^i_k are the zeros of the dielectric function. When $\mathfrak{Im}\{\varepsilon_{k,\omega}\}$ vanishes, $\mathfrak{Im}\left\{\frac{-1}{\varepsilon_{k,\omega}}\right\}$ is proportional to a delta function. This behavior is the signature of an undamped collective excitation. In the case of carrier dielectric function, this excitation is an undamped plasma excitation. We can observe this in Fig. 2.6(a) and (c), which show Eq. (2.74) in the three- and two-dimensional case, respectively. $\mathfrak{Im}\{\varepsilon_{k,\omega}\}=0$ outside the single pair excitation region Eq. (2.64). Consequently, outside the single pair excitation region, $\mathfrak{Im}\left\{\frac{-1}{\varepsilon_{k,\omega}}\right\}$ is a delta-peak at the zeros of $\mathfrak{Re}\{\varepsilon_{k,\omega}\}$. As delta-peaks are invisible in our color plot, we have marked the line with $\mathfrak{Re}\{\varepsilon_{k,\omega}\}=0$ in Fig. 2.6.

Inside the excitation region, there is a broad peak, which is associated with the decay of the collective excitations into quasi-electron and quasi-hole pairs, as discussed in paragraph 2.2.2.2.1. Hence, the plasma excitation is damped inside the single pair excitation region. Note that the line where $\mathfrak{Re}\{\varepsilon_{k,\omega}\}=0$ extends into the single pair excitation region, but there is no delta peak, because $\mathfrak{Im}\{\varepsilon_{k,\omega}\}>0$ inside that region.

For nonzero temperatures, the boundary between damped and undamped plasma excitations is blurry. As in the classical limit (cf. appendix A), all plasma excitations are damped. However, the magnitude of the damping depends strongly on the wave vector and frequency. As can be seen in Fig. 2.6(b) and (d), $\mathfrak{Im}\left\{\frac{-1}{\varepsilon_{k,\omega}}\right\}$ has a sharp peak for small wave vectors, and broadens strongly for higher wave vectors.

In the long-wavelength limit, the imaginary part of the dielectric function vanishes for all temperatures, and $\mathfrak{Im}\left\{\frac{-1}{\varepsilon_{k,\omega}}\right\}$ is a delta-peak at ω_P, the plasma frequency. In the 3d case, the plasma frequency Eq. (2.17) is independent of wave vector k. In the 2d case, the plasma frequency is proportional to k for small wave vectors k.

2.2.3.2 The f-sum rule

Sum rules [63, 32] make statements about integrals of the imaginary part of the inverse dielectric function times a power of frequency over frequency The derivation of the so-called f-sum rule can be seen in [63], for example. As the f-sum rule is exact, we can use it to test if our numerical evaluations of $\mathfrak{Im}\left\{\frac{-1}{\varepsilon_{k,\omega}}\right\}$, and especially the real part of the dielectric function, are correct. For carriers in a vacuum, i.e., $\varepsilon^{\infty}=1$, the

f-sum rule can be written as [74]

$$\int_0^\infty \mathrm{d}\omega\, \omega \mathfrak{Im}\left\{\frac{-1}{\varepsilon_{k,\omega}}\right\} = \frac{\pi \nu_k^d n^d k^2}{2m} \tag{2.76}$$

with $d = 2$ for two dimensions and $d = 3$ for three dimensions. For carriers in a medium, this has to be changed to

$$\int_0^\infty \mathrm{d}\omega\, \omega \mathfrak{Im}\left\{-\frac{\varepsilon^\infty}{\varepsilon_{k,\omega}}\right\} = \frac{\pi \nu_k^d n^d k^2}{2m^* \varepsilon^\infty} \tag{2.77}$$

In 3d, this is

$$\int_0^\infty \mathrm{d}\omega\, \omega \mathfrak{Im}\left\{-\frac{\varepsilon^\infty}{\varepsilon_{k,\omega}}\right\} = \frac{\pi}{2}\omega_P^2 \tag{2.78}$$

i.e., the integral over $\omega \mathfrak{Im}\left\{\frac{-1}{\varepsilon_{k,\omega}}\right\}$ is proportional to the square of the plasma frequency Eq. (2.17).

Eq. (2.78) also holds in 2d, when we take into account that the two-dimensional plasma frequency depends linearly on the wave vector k:

$$\left(\omega_P^{d=2}\right)_k = \frac{2\pi n^{d=2} e^2}{m^* \varepsilon^\infty} k \tag{2.79}$$

Zero temperature dielectric functions in two and three dimensions In the case of the zero temperature dielectric functions, there are two distinct contributions to the sum-rule integral:
The first is from the undamped part of the dielectric function, $\frac{\hbar\omega}{E_F} < \frac{k}{k_F}\left(\frac{k}{k_F} + 2\right)$, where the imaginary part of the dielectric function is identically zero. With Eq. (2.75), the delta-contribution to the f-sum rule integral is

$$\int \mathrm{d}\omega\, \omega \mathfrak{Im}\left\{-\frac{\varepsilon^\infty}{\varepsilon_{k,\omega}}\right\} = \frac{\pi (\omega_P)_k}{\left|\frac{\partial}{\partial\omega}\mathfrak{Re}\left\{\varepsilon_{k,(\omega_P)_k}\right\}\right|} \text{ for all k with } \frac{\hbar\omega}{E_F} < \frac{k}{k_F}\left(\frac{k}{k_F} + 2\right). \tag{2.80}$$

The second contribution to the sum rule integral is from the damped part of the dielectric function. The damping broadens the peak, making

$$\int\limits_{\frac{\hbar\omega}{E_F} > \frac{k}{k_F}\left(\frac{k}{k_F}+2\right)} \mathrm{d}\omega\, \omega \mathfrak{Im}\left\{-\frac{\varepsilon^\infty}{\varepsilon_{k,\omega}}\right\} \tag{2.81}$$

numerically integrable. Figure 2.7 shows how the two contributions add up to the result predicted by the f-sum rule in 2d.

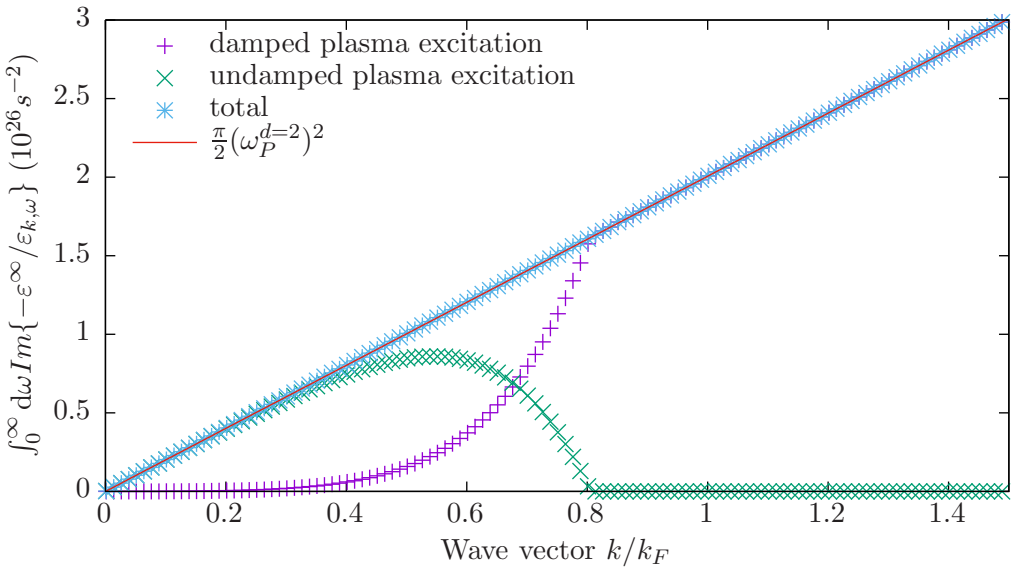

Figure 2.7: f-sum rule integral $\int_0^\infty \mathrm{d}\omega\, \omega \mathfrak{Im}\left\{-\frac{\varepsilon^\infty}{\varepsilon_{k,\omega}}\right\}$ for the $T = 0$ dielectric function of electrons in a two-dimensional plane in GaAs as a function of wave vector. The sheet density is $n_S = 9.6 \times 10^{11} cm^{-2}$, as in Fig. 2.6c. We give the contributions from inside and outside the single pair excitation region, i.e., for the damped and the undamped plasma excitation separately.

Nonzero temperature dielectric function For the nonzero temperature case of the RPA dielectric function, we calculate the sum rule integral entirely numerically. In the wave vector - frequency region without sharp peaks in the energy loss function $\propto \mathfrak{Im}\{1/\varepsilon\}$ this is not problematic, but for small wave vectors or low temperatures, there are almost delta-shaped peaks. Approximating them as actual delta-peaks positioned at the zeros of the real part of the dielectric function can be the easiest way to integrate them.

2.3 Total carrier and lattice dielectric functions in bulk semiconductors

In a polar semiconductor, we have to take into account the polarization due to the motion of the ions, and the electrons in the valence and the conduction bands. This yields the total displacement field

$$\boldsymbol{D}^{tot}_{k,\omega} = \boldsymbol{E}_\omega + 4\pi \left(\boldsymbol{P}^{\text{e-valence}}_\omega + \boldsymbol{P}^{c}_{k,\omega} + \boldsymbol{P}^{ph}_\omega \right) = \varepsilon^{tot}_{k,\omega} \boldsymbol{E}_\omega \tag{2.82}$$

with the polarization $\boldsymbol{P}^{ph}$ due to the polar phonons, $\boldsymbol{P}^{e-valence}$ due to valence electrons. and $\boldsymbol{P}^{c}$ due to free carriers, which might be electrons or holes. The

Table 2.4: Important energies in GaAs for the electron concentration $n = 5 \times 10^{17} cm^{-3}$

	$\hbar\omega_{LO}$	$\hbar\omega_{TO}$	$\hbar\omega_P$	$\hbar\omega_+$	$\hbar\omega_-$	E_F
Energy (meV)	36.14	33.25	30.45	39.84	25.41	34.29
Energy/E_F	1.05	0.97	0.88	1.16	0.74	1
Phonon content (%)				70.12	29.88	

corresponding total dielectric function is

$$\begin{aligned} \varepsilon_\omega^{tot} &= 1 + \chi_\omega^{\text{e-valence}} + \chi_{k,\omega}^{c} + \chi_\omega^{ph} \\ &= 1 + (\varepsilon^\infty - 1) + \left(\varepsilon_{k,\omega}^{c} - \varepsilon^\infty\right) + \left(\varepsilon_\omega^{ph} - \varepsilon^\infty\right) = \varepsilon_\omega^{ph} + \varepsilon_{k,\omega}^{c} - \varepsilon^\infty \end{aligned} \tag{2.83}$$

Note that the carrier and phonon susceptibilities are $\chi^{c/ph} = \varepsilon_\omega^{c/ph} - \varepsilon^\infty$, because both the phonon and the carrier dielectric function above include the contribution from the valence electrons. This is not always the case in the literature. In discussion of the carrier dielectric functions [41, 59] , especially for the carrier dielectric function of a single parabolic band, it is natural not to include the response of the valence electrons, because they are not part of the model. In discussion of the lattice dielectric function, the valence electron response is often included. It is thus important to be aware of the convention when combining dielectric functions.

2.3.1 Total dielectric function for a polar semiconductor in the long-wavelength limit

We discuss the $k \to 0$ limit of the total dielectric function in bulk semiconductors first.

$$\varepsilon_{k=0,\omega}^{tot} = \varepsilon^\infty \left(\frac{\omega_{LO}^2 - \omega^2 - i\omega\gamma}{\omega_{TO}^2 - \omega^2 - i\omega\gamma} - \frac{\omega_P^2}{\omega^2} \right). \tag{2.84}$$

See Fig. 2.8 for an example of the long wavelength dielectric functions in a polar semiconductor.

Coupled modes in the long-wavelength and low damping limit In many polar semiconductors, the damping rate γ is small compared to ω_{TO} and ω_{LO}, see [3, Tab. 6.5]. In room temperature GaAs, e.g., $\gamma = 0.007\omega_{TO}$. Hence, it is often assumed that the ionic motion is entirely undamped. In this case,

$$\varepsilon_{\omega,\gamma=0}^{tot} = \varepsilon^\infty \left(\frac{\omega_{LO}^2 - \omega^2}{\omega_{TO}^2 - \omega^2} - \frac{\omega_P^2}{\omega^2} \right), \tag{2.85}$$

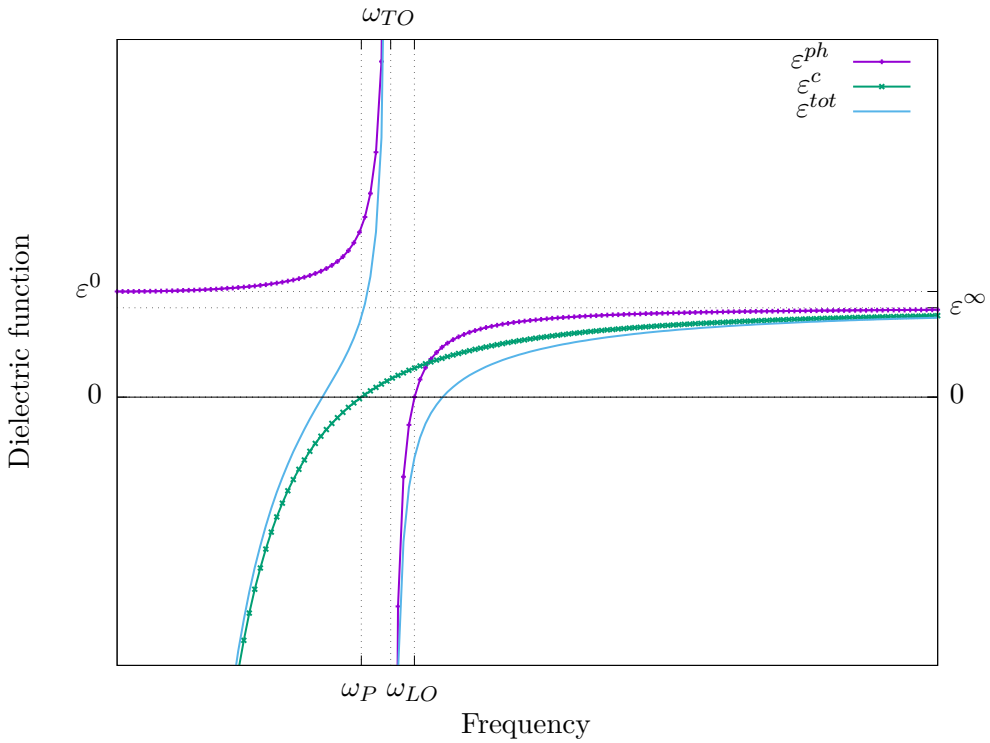

Figure 2.8: Long wavelength dielectric functions in GaAs for an electron concentration of $n = 4 \times 10^{17} cm^{-3}$ in the absence of damping, as a function of frequency. The solid blue line is the total dielectric function Eq. (2.84), the purple line with dots is the lattice dielectric function Eq. (2.11) with $\gamma = 0$, and the green line with crosses is the carrier dielectric function Eq. (2.18). Also marked are the high and low frequency limits of the dielectric function ε^∞ and ε^0, and the LO-, TO- and plasma frequencies, ω_{LO}, ω_{TO} and ω_P.

the natural oscillation frequencies $\omega_\pm$, the zeros of $\varepsilon^{tot}_{\omega,\gamma=0}$, obey the bi-quadratic equation

$$\omega_\pm^4 - \omega_\pm^2 \left(\omega_{LO}^2 + \omega_P^2\right) + \omega_P^2 \omega_{TO}^2 = 0 \tag{2.86}$$

$$\text{or} \quad \omega_\pm^2 = \frac{1}{2}\left(\omega_{LO}^2 + \omega_P^2\right) \pm \frac{1}{2}\sqrt{\left(\omega_{LO}^2 + \omega_P^2\right)^2 - 4\omega_P^2 \omega_{TO}^2} \tag{2.87}$$

We will call these oscillation frequencies coupled collective mode frequencies, because they are hybridized plasmon-phonon excitations. Fig. 3.3 shows them in GaAs for a range of conduction band electronic density and hence a range of plasma frequencies. We can see that when the plasma frequency is much smaller than the optical phonon frequency, the coupled collective mode frequencies almost coincide with the plasma and the LO-phonon frequency. When the plasma frequency is much larger than the optical phonon frequencies, the coupled collective mode frequencies are almost identical to the TO phonon frequency and the plasma frequency. Only when the plasma frequency and the optical phonon frequencies are of the same order of magnitude do the coupled collective mode frequencies differ significantly from ω_P,

ω_{LO} or ω_{TO}. We will call the parameter range in which this happens the strong coupling regime. To quantify this, we introduce the strong coupling density n_C, with

$$n_C = \frac{\omega_{LO}^2 m^* \varepsilon^\infty}{4\pi e^2}. \tag{2.88}$$

In GaAs, the strong coupling regime is roughly $10^{17} cm^{-3} \leq n \leq 10^{18} cm^{-3}$, with $n_C = 7.04 \times 10^{17} cm^{-3}$.

2.3.2 Total dielectric function of a polar semiconductor in the RPA

For the total dielectric function in the RPA in three dimensions, we use Eq. (2.83) with the ionic dielectric function ε_ω^{ph} Eq. (2.11), discussed in section 2.1, which is independent of wave vector altogether. In general, we use a temperature dependent RPA carrier dielectric function for $\varepsilon_{k,\omega}^c$ as discussed in great detail in section 2.2. Its real part is described by Eq. (2.61) and its imaginary part by Eq. (2.59). To emphasize the differences between the dielectric functions, we also discuss the zero temperature total dielectric function in the RPA, where the carrier dielectric function is the Lindhard dielectric function discussed in subsubsection 2.2.2.2. Its imaginary part is described by Eq. (2.69), and the real part by Eq. (2.73).

In subsubsection 2.2.3.1, we established that the imaginary part of the inverse dielectric function Eq. (2.74) can be used as a measure for the strength of the collective excitation. In this section, we investigate the imaginary part of the inverse total dielectric function in the RPA, $\mathfrak{Im}\{\frac{-1}{\varepsilon^{tot}}\}_{k,\omega}$ depends on temperature and the anharmonic damping rate. We can identify three different effects:

Firstly, the delta-peaks in the plots for $T = 0$ start to blur abruptly as soon as they move into the single pair excitation regime. This can be seen in the plots of the imaginary part of the inverse dielectric function for $T = 0$ (Fig. 2.9a-c). Fig. 2.9a shows $\mathfrak{Im}\left\{-\frac{\varepsilon^\infty}{\varepsilon^c}\right\}$, and Fig. 2.9b, shows $\mathfrak{Im}\left\{-\frac{\varepsilon^\infty}{\varepsilon^{tot}}\right\}$, where the electronic dielectric function is the $T = 0$ RPA dielectric function, and the lattice dielectric function is the undamped ($\gamma \to 0$) limit of Eq. (2.11). This shows that the excitation of quasi-electron-hole pairs is captured by the RPA dielectric function, as expected.

Secondly, the damping rate in the lattice dielectric function broadens the LO-phonon peak from a delta-peak to a Lorentzian, and also has an effect on the width of the coupled peaks before they reach the single pair excitation regime, see Fig. 2.9(b) and (e).

Thirdly, the temperature dependence in the electronic part of the dielectric function again broadens both coupled peaks. Moreover, it causes the boundaries of the single pair excitation limit to blur. For an example, compare Fig. 2.9a-c with Fig. 2.9d-f, which show $\mathfrak{Im}\left\{-\frac{\varepsilon^\infty}{\varepsilon^{tot}}\right\}$ for $T > 0$. This blurring occurs, because of the thermal

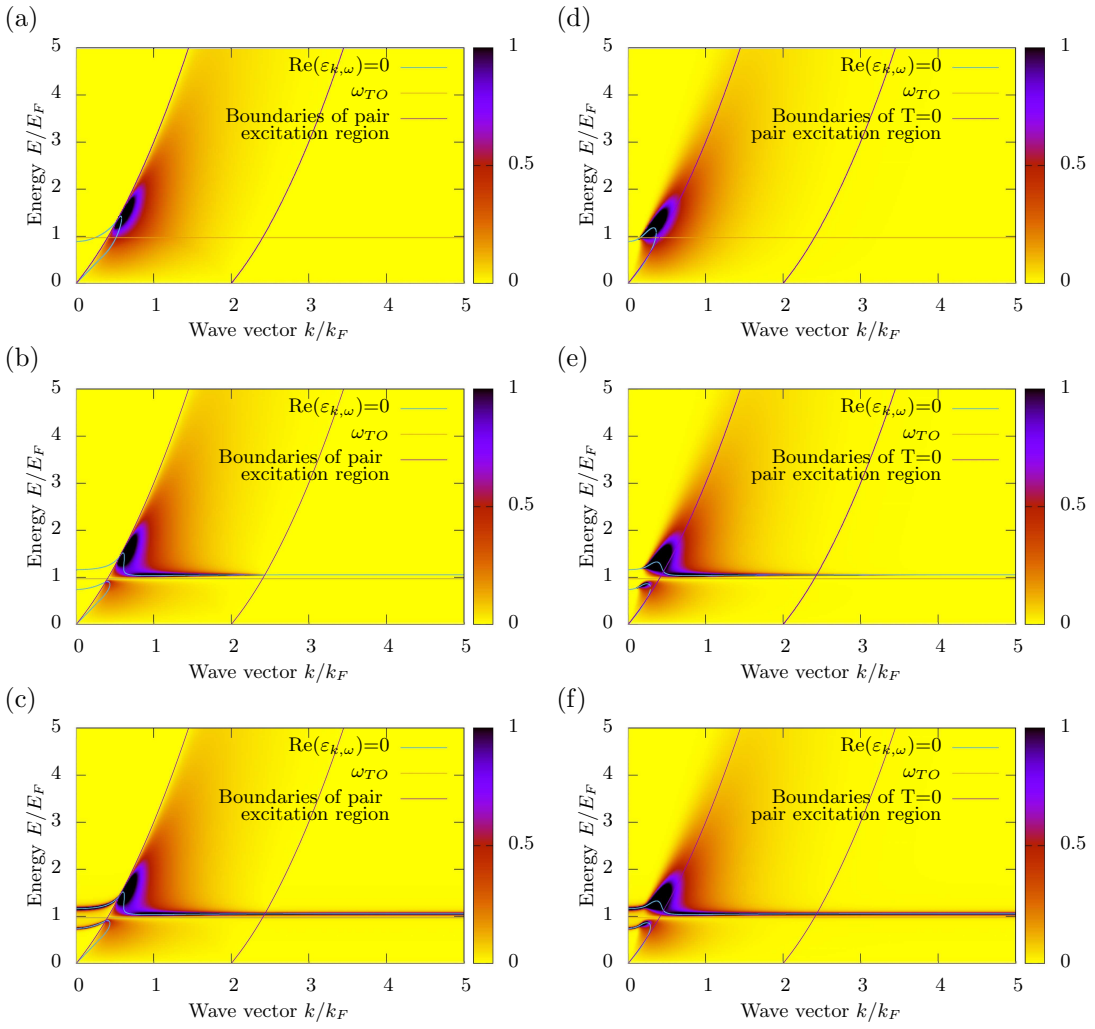

Figure 2.9: Imaginary part of the inverse dielectric function $\mathfrak{Im}\{-\frac{\varepsilon^{\infty}}{\varepsilon_{k,\omega}}\}$ in GaAs with $n = 5 \times 10^{17} cm^{-3}$ at T=0 (a-c) and T=300K(d-f) as a function of wave vector k and energy $E = \hbar\omega$. The dielectric function in each of the subplots is the electron dielectric function in (a) and (d), the total dielectric function with an anharmonic optical phonon damping rate $\gamma = 0$ (b) and (e), and the total dielectric function with an anharmonic optical phonon damping rate $\gamma = 0.007\omega_{TO}$ (c) and (f). As the delta peak at the zeros of $\mathfrak{Re}\left\{\varepsilon^{tot}_{k,\omega}\right\}$ is infinitely sharp at zero temperature, it does not show in the color plot. To make up for this, lines with $\mathfrak{Re}\left\{\varepsilon^{tot}_{k,\omega}\right\} = 0$ are also marked.

excitation of quasi-electrons and quasi-holes from the Fermi sea. In the classical limit, this contribution to the damping of the modes is referred to as Landau damping[2].

In the long wavelength limit $k = 0$, we can make out the two peaks in $\mathfrak{Im}\left\{-\frac{\varepsilon^{\infty}}{\varepsilon^{tot}_{k=0,\omega}}\right\}$ at $\omega = \omega_{\pm}$ discussed in subsection 2.3.1, independent of temperature, see Fig. 2.9(b),(c),(e) and (f) at $k = 0$.

Chapter 3

Carrier scattering by coupled polar phonon and plasmon modes

In this chapter, we review how carrier–coupled phonon-plasmon collective mode scattering is calculated. We start with the description of the energy relaxation rate as given by Kim et al. [36]. We are not interested in energy relaxation as such, but in the carrier-coupled mode scattering matrix element squared (we will refer to it a "scattering rate" for the sake of brevity from here on) as described by Fermi's golden rule [75], because this quantity will be used throughout this thesis. This scattering rate is determined by the imaginary part of the inverse total dielectric function. We examine the scattering rate more closely for carrier scattering with damped and undamped LO-phonons, and see that our approach of describing the scattering in terms of continuous modes with the damping expressed through the imaginary part of the dielectric function is equivalent to a description with discrete modes, where the damping is accounted for explicitly as the imaginary part of the mode frequency which enters into the expression for energy conservation in Fermi's golden rule. We show explicitly that carrier–plasmon scattering can be expressed equivalently as carrier–carrier scattering.

In section 3.2, we extend a calculation by Maslov [45] to polar heterostructures with anisotropic dielectric functions to be able to describe the scattering between carriers and interface polar optical modes in terms of the imaginary part of the inverse of an effective dielectric function of a polar semiconductor heterostructure involving the anisotropic material MoS_2.

In section 3.3, we discuss why momentum relaxation due to carrier–coupled mode scattering is more difficult to capture than energy relaxation, and analyse one approximate treatment of momentum relaxation.

3.1 Carrier-coupled plasmon-phonon mode scattering: energy relaxation

Kim et al. [36] give the energy relaxation time τ_p^E for a carrier scattering with a coupled plasmon-phonon mode. For our case, where the carrier wave functions are described by plane waves, and we only have one band present, this is

$$\frac{1}{\tau_p^E} = \int_{-\infty}^{\infty} \mathrm{d}\hbar\omega \int_{\boldsymbol{k}} f_{\boldsymbol{p}}^0 \left(1 - f_{\boldsymbol{p}-\boldsymbol{k}}^0\right) \left(1 + N_{\boldsymbol{\omega}}^0\right) \delta\left(E_{\boldsymbol{p}-\boldsymbol{k}} - E_{\boldsymbol{p}} + \hbar\omega\right) W_{k,\omega}^0 \tag{3.1}$$

in our notation.[1] We use the notation

$$\int_{\boldsymbol{k}} = \frac{1}{(2\pi)^d} \int \mathrm{d}^d \boldsymbol{k} \tag{3.2}$$

for wave vector integrals in d dimensional semiconductors. Here, the superscript "E" stands for energy, to distinguish the energy relaxation time τ^E from the momentum relaxation time τ, which will be discussed later. N_ω^0 is the Bose-Einstein distribution function

$$N_\omega^0 = \frac{1}{e^{\hbar\omega\beta} - 1}, \tag{3.3}$$

where $\beta = \frac{1}{k_B T}$, the inverse of the thermal energy, was introduced in subsection 2.2.2, as was the Fermi-Dirac distribution $f_{\boldsymbol{p}}^0$ for carriers of wave vector $\boldsymbol{p}$. The quantity

$$W_{k,\omega}^0 = \frac{2\nu_k}{\hbar} \mathfrak{Im} \left\{ -\frac{1}{\varepsilon_{k,\omega}^{tot}} \right\} \tag{3.4}$$

gives the probability of a carrier being scattered by a coupled plasmon–LO-phonon mode, given that the mode is occupied, per unit time and reciprocal space volume. We will use the expression carrier-coupled mode scattering rate for Eq. (3.4). Note that we use a convention, where ω can be negative [49]. Consequently, the energy relaxation rate Eq. (3.1) contains a contribution from the emission of a coupled mode ($\omega > 0$) and a contribution from the absorption of a coupled mode ($\omega < 0$).

The scattering rate formally becomes negative for $\omega < 0$, because $W_{\boldsymbol{k},-\omega}^0 = -W_{\boldsymbol{k},\omega}^0$, yet the product $W_{\boldsymbol{k},-\omega}^0 \left(N_{\boldsymbol{k},-\omega}^0 + 1\right) = W_{\boldsymbol{k},\omega}^0 N_{\boldsymbol{k},\omega}^0$ is always positive, because $N_{\boldsymbol{k},-\omega}^0 + 1 = -N_{\boldsymbol{k},\omega}^0$. We use this convention for the sake of brevity. However, it is important to keep in mind that both the emission and absorption contributions matter. (Compare [44], which stresses this issue in a correction to [43].)

Kim et al. [36] discuss this result in the cases where the total dielectric function ε^{tot} is made up of the Lindhard dielectric function for the electrons and an undamped lattice dielectric function of the type Eq. (2.11). We will apply it to the total RPA dielectric

[1] We think Kim et al. [36] are missing a factor 2 in their equation 12, which we corrected.

function Eq. (2.83) discussed in subsection 2.3.2, where the carrier dielectric function is temperature dependent and the lattice dielectric function is damped.

The expression Eq. (3.4) can be derived by evaluating the probability for a scattering event with Fermi's Golden rule [75] (or, equivalently, in the Born approximation), in terms of the dynamic form factor [38]. With the dissipation-fluctuation theorem [76, 77, 78], the scattering probability can be cast in terms of the dielectric function and distribution function of the collective excitation. This derivation has been given on a fairly abstract level [47], or with more detail [36]. We will roughly sketch out the derivation, but then motivate it extensively by discussing the scattering rates for the more familiar limiting cases of carrier–carrier scattering and carrier–LO-phonon scattering.

Derivation In the Born approximation, the probability $P_{\boldsymbol{k},\omega}$ per unit time that a carrier transfers energy to collective excitations with wave vector $\boldsymbol{k}$ and frequency ω through inelastic scattering, can be expressed through the dynamical form factor $S_{\boldsymbol{k},\omega}$ of the system,

$$P_{\boldsymbol{k},\omega} = \frac{2\pi}{\hbar}\nu_k^2 S_{\boldsymbol{k},\omega} \tag{3.5}$$

see [32, chapter 2.6],[47]. The ν_k were introduced in Eq. (2.35). If the system is in equilibrium, the dynamical form factor can in turn be expressed through the imaginary part of the density-density response function $\tilde{\chi}$

$$\mathfrak{Im}\left\{\tilde{\chi}_{\boldsymbol{k},\omega}\right\} = -\pi\left(1 - e^{-\beta\omega}\right) S_{\boldsymbol{k},\omega} \text{ or } S_{\boldsymbol{k},\omega} = -\frac{1}{\pi}\left(N_\omega^0 + 1\right)\mathfrak{Im}\tilde{\chi}_{\boldsymbol{k},\omega} \tag{3.6}$$

through the fluctuation-dissipation theorem[32, 77, 76]. The density-density response function is related, but not identical to the susceptibility discussed in chapter 2. Using [32, chapter 4]

$$\frac{1}{\varepsilon_{\boldsymbol{k},\omega}} = 1 + \nu_k\tilde{\chi}_{\boldsymbol{k},\omega} \tag{3.7}$$

yields an expression for the dynamical form factor in terms of the imaginary part of the inverse dielectric function

$$S_{\boldsymbol{k},\omega} = \frac{1}{\pi\nu_k}\mathfrak{Im}\left(\frac{-1}{\varepsilon_{\boldsymbol{k},\omega}}\right)\left(N_\omega^0 + 1\right). \tag{3.8}$$

The zero temperature limit (with $N_\omega^0 = 0$, and the T=0 or Lindhard dielectric function [41]) of this expression is more commonly cited (cf. [79, 63, 22]). With Eq. (3.5), we find

$$P_{\boldsymbol{k},\omega} = \frac{2\nu_k}{\hbar}\mathfrak{Im}\left(\frac{-1}{\varepsilon_{\boldsymbol{k},\omega}}\right)\left(N_\omega^0 + 1\right). \tag{3.9}$$

Similarly, the probability per unit time that a carrier absorbs energy from a collective excitation is

$$P_{-\boldsymbol{k},-\omega} = \frac{2\nu_k}{\hbar}\mathfrak{Im}\left\{\frac{-1}{\varepsilon_{\boldsymbol{k},\omega}}\right\} N_\omega^0. \tag{3.10}$$

In our discussion, it is useful to isolate the occupation factor from the probability, and writing

$$P_{\boldsymbol{k},\omega} = W_{\boldsymbol{k},\omega}^0\left(N_\omega^0 + 1\right) \tag{3.11}$$

leads to Eq. (3.4).

3.1.1 Carrier–carrier scattering

In this section, we show the connection between carrier–carrier scattering, and carrier–plasmon scattering. We follow the presentation in [22] and [32], but we give expressions which also hold for nonzero temperatures.

According to Eq. (3.1), the energy relaxation time for an electron due to the interaction with a plasmon is

$$\frac{1}{\tau_p^E} = \int\limits_{\hbar\omega}\int\limits_{\boldsymbol{k}} \frac{2\nu_k}{\hbar}\frac{\mathfrak{Im}\left\{\varepsilon_{k,\omega}^c\right\}}{|\varepsilon_{k,\omega}^c|^2} f_{\boldsymbol{p}}^0\left(1 - f_{\boldsymbol{p}-\boldsymbol{k}}^0\right)\left(1 + N_{\boldsymbol{\omega}}^0\right)\delta\left(E_{\boldsymbol{p}-\boldsymbol{k}} - E_{\boldsymbol{p}} + \hbar\omega\right) \tag{3.12}$$

Here, we have substituted the carrier-plasmon equilibrium scattering rate Eq. (3.4)

$$W_{k,\omega}^0 = \frac{2\nu_k}{\hbar}\mathfrak{Im}\left\{\frac{-1}{\varepsilon_{k,\omega}}\right\} = \frac{2\nu_k}{\hbar}\frac{\mathfrak{Im}\left\{\varepsilon_{k,\omega}^c\right\}}{|\varepsilon_{k,\omega}^c|^2} \tag{3.13}$$

with the carrier dielectric function $\varepsilon_{k,\omega}^c$. Using the definition Eq. (2.41) of the imaginary part of the dielectric function, Eq. (3.12) becomes

$$\begin{aligned}\frac{1}{\tau_p^E} = \int\limits_{\hbar\omega}\iint\limits_{\boldsymbol{k}\,\boldsymbol{q}} \frac{4\pi\nu_k^2}{\hbar|\varepsilon_{\boldsymbol{k},\omega}^c|^2}\delta\left(E_{\boldsymbol{p}-\boldsymbol{k}} - E_{\boldsymbol{p}} + \hbar\omega\right)\delta\left(E_{\boldsymbol{q}+\boldsymbol{k}} - E_{\boldsymbol{q}} - \hbar\omega\right)\\ \times f_{\boldsymbol{p}}^0\left(1 - f_{\boldsymbol{p}-\boldsymbol{k}}^0\right)\left(f_{\boldsymbol{q}}^0 - f_{\boldsymbol{q}+\boldsymbol{k}}^0\right)\left(N_\omega^0 + 1\right)\end{aligned} \tag{3.14}$$

Using the equation of detailed balance Eq. (C.3b) discussed in appendix C.1, we can eliminate the plasmon distribution N_ω^0 for carrier distribution functions. Moreover, we can carry out the integral over ω, thus eliminating the plasmon frequency from the equation. The resulting energy relaxation rate only contains carrier quantities.

$$\frac{1}{\tau_p^E} = \iint\limits_{\boldsymbol{k}\,\boldsymbol{q}} \frac{4\pi\nu_k^2}{\hbar\left|\varepsilon_{\boldsymbol{k},\left(E_{\boldsymbol{p}} - E_{\boldsymbol{p}-\boldsymbol{k}}\right)/\hbar}^c\right|^2}\delta\left(E_{\boldsymbol{p}-\boldsymbol{k}} - E_{\boldsymbol{p}} - E_{\boldsymbol{q}+\boldsymbol{k}} - E_{\boldsymbol{q}}\right) f_{\boldsymbol{p}}^0\left(1 - f_{\boldsymbol{p}-\boldsymbol{k}}^0\right) f_{\boldsymbol{q}}^0\left(1 - f_{\boldsymbol{q}+\boldsymbol{k}}^0\right) \tag{3.15}$$

To highlight that this describes an interaction of two carriers with the initial

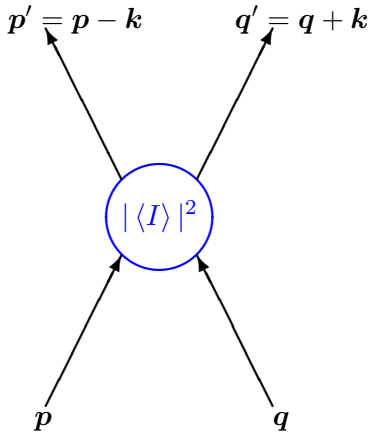

Figure 3.1: Schematic explaining wave vector transfer between carriers in carrier carrier scattering. The blue circle stands for the carrier–carrier interaction with a matrix element $< I >$.

momentum $\boldsymbol{p}$ and $\boldsymbol{q}$, and final momentum $\boldsymbol{p}' = \boldsymbol{p} - \boldsymbol{k}$ and $\boldsymbol{q}' = \boldsymbol{q} + \boldsymbol{k}$ for all possible sets of $\boldsymbol{k}$ and $\boldsymbol{q}$, we express Eq. (3.15) as

$$\frac{1}{\tau_p^E} = \int_{\boldsymbol{p}'} \iint_{\boldsymbol{q}'\,\boldsymbol{q}} \frac{4\pi\nu_k^2}{\hbar \left|\varepsilon^c_{\boldsymbol{k},(E_{\boldsymbol{p}}-E_{\boldsymbol{p}'})/\hbar}\right|^2} f^0_{\boldsymbol{p}} \left(1 - f^0_{\boldsymbol{p}'}\right) f^0_{\boldsymbol{q}} \left(1 - f^0_{\boldsymbol{q}'}\right) \times \delta\left(\boldsymbol{p}' + \boldsymbol{q}' - \boldsymbol{p} - \boldsymbol{q}\right) \delta\left(E_{\boldsymbol{p}'} - E_{\boldsymbol{p}} - E_{\boldsymbol{q}'} - E_{\boldsymbol{q}}\right) \tag{3.16}$$

This is also a proof that Eq. (3.1) with Eq. (3.4) describes the energy relaxation time for a carrier interaction with a carrier gas. Note that the carrier–carrier scattering is mediated by the screened Coulomb interaction, ν_k/ε^c, rather than the bare Coulomb interaction ν_k.

The energy relaxation time discussed here is related to the lifetime of a quasi-particle in the RPA electron gas, which was first expressed by Quinn and Ferrell [80]. We show how this expression is evaluated explicitly in appendix C.2.1.

3.1.2 Carrier–longitudinal optical–phonon scattering

According to Eq. (3.1), the energy relaxation time for an electron due to the interaction with an longitudinal optical phonon is

$$\frac{1}{\tau_p^E} = \int_{\hbar\omega} \int_{\boldsymbol{k}} \frac{2\nu_k}{\hbar} \frac{\mathfrak{Im}\left\{\varepsilon^{ph}_\omega\right\}}{|\varepsilon^{ph}_\omega|^2} f^0_{\boldsymbol{p}} \left(1 - f^0_{\boldsymbol{p}-\boldsymbol{k}}\right) \left(1 + N^0_{\boldsymbol{\omega}}\right) \delta\left(E_{\boldsymbol{p}-\boldsymbol{k}} - E_{\boldsymbol{p}} + \hbar\omega\right) \tag{3.17}$$

Here, we have substituted the carrier-plasmon equilibrium scattering rate Eq. (3.4)

$$W^0_{k,\omega} = \frac{2\nu_k}{\hbar}\mathfrak{Im}\left\{\frac{-1}{\varepsilon^{ph}_\omega}\right\} = \frac{2\nu_k}{\hbar}\frac{\mathfrak{Im}\left\{\varepsilon^{ph}_\omega\right\}}{|\varepsilon^{ph}_\omega|^2}. \tag{3.18}$$

With the lattice dielectric function $\varepsilon^{ph}_{k,\omega}$, Eq. (2.11), this can be written explicitly as

$$W^0_{k,\omega} = \frac{2\nu_k}{\hbar}\frac{\omega^2_{LO}-\omega^2_{TO}}{\varepsilon^\infty}\frac{\omega\gamma}{\left(\omega^2_{LO}-\omega^2\right)^2+\omega^2\gamma^2}. \tag{3.19}$$

3.1.2.1 Carrier–longitudinal optical–phonon scattering without damping

If the anharmonic damping rate γ is vanishingly small, the scattering rate becomes a delta-function

$$\begin{aligned} W^{0,\gamma=0}_{k,\omega} =& \mathrm{sgn}(\omega)\frac{2\pi\nu_k}{\hbar}\frac{\omega^2_{LO}-\omega^2_{TO}}{\varepsilon^\infty}\delta\left(\omega^2_{LO}-\omega^2\right) \\ =& \frac{2\pi\nu_k}{\hbar}\frac{\omega^2_{LO}-\omega^2_{TO}}{2\omega_{LO}\varepsilon^\infty}\left[\delta\left(\omega_{LO}-\omega\right)-\delta\left(\omega_{LO}+\omega\right)\right]. \end{aligned} \tag{3.20}$$

Here, we have used Eq. (2.52), the Poisson representation of the Dirac delta function. Introducing the unscreened Fröhlich scattering strength

$$F^u_k = \nu_k\frac{\omega_{LO}}{2}\left(\frac{1}{\varepsilon^\infty}-\frac{1}{\varepsilon^0}\right). \tag{3.21}$$

the energy relaxation time can be expressed as

$$W^{0,\gamma=0}_{k,\omega} = \frac{2\pi}{\hbar}F^u_k\left[\delta(\omega_{LO}-\omega)-\delta(\omega_{LO}+\omega)\right] \tag{3.22}$$

Consequently, the energy relaxation rate [33] is $\frac{1}{\tau^E_p} = \frac{1}{\tau^+_p}+\frac{1}{\tau^-_p}$ with

$$\frac{1}{\tau^\pm_p} = \frac{2\pi}{\hbar}\left(N^0_{\boldsymbol{\omega}_{LO}}+\frac{1\pm1}{2}\right)\int_{\boldsymbol{k}}F^u_k\delta\left(\frac{E_{\boldsymbol{p}-\boldsymbol{k}}-E_{\boldsymbol{p}}}{\hbar}\pm\omega_{LO}\right)f^0_{\boldsymbol{p}}\left(1-f^0_{\boldsymbol{p}-\boldsymbol{k}}\right), \tag{3.23}$$

compare the expressions by Ehrenreich [33] and Kim et al. [36] derived from the Fröhlich Hamiltonian [81].

3.1.2.2 Carrier–longitudinal optical–phonon scattering with damping

For nonzero anharmonic damping γ, the frequencies where $\varepsilon^{ph}_{k,\omega'} = 0$ are

$$\omega' = \pm\sqrt{\omega^2_{LO}-\frac{\gamma^2}{4}}-i\frac{\gamma}{2} \quad \text{with } \omega_{LO} > \frac{\gamma}{2} \tag{3.24}$$

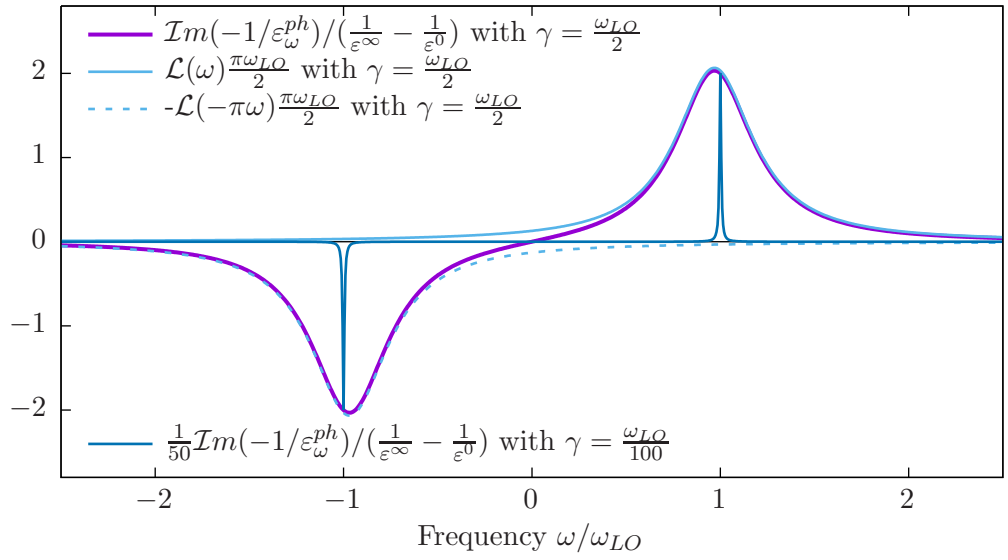

Figure 3.2: Scaled imaginary part of the inverse dielectric function $\mathfrak{Im}\{-\frac{1}{\varepsilon_\omega^{ph}}\}/(\frac{1}{\varepsilon^\infty}-\frac{1}{\varepsilon^0})$ from Eq. (3.26), and the scaled Lorentzians that make it up, for a very large damping rate $\gamma=\frac{\omega_{LO}}{2}$ as a function of frequency ω. The frequency-axis is scaled by the LO-phonon frequency ω_{LO}. The imaginary part of the inverse dielectric function $\frac{1}{50}\mathfrak{Im}\{-\frac{1}{\varepsilon_\omega^{ph}}\}/(\frac{1}{\varepsilon^\infty}-\frac{1}{\varepsilon^0})$ is also plotted against frequency for $\gamma=\frac{\omega_{LO}}{100}$ – note the scaling factor 50.

and we can write

$$\mathfrak{Im}\left\{-\frac{1}{\varepsilon_\omega^{ph}}\right\}=\frac{\omega_{LO}^2-\omega_{TO}^2}{\varepsilon^\infty}\frac{1}{2\sqrt{\omega_{LO}^2-(\frac{\gamma}{2})^2}}\left[\frac{\frac{\gamma}{2}}{\left(\omega-\sqrt{\omega_{LO}^2-(\frac{\gamma}{2})^2}\right)^2+(\frac{\gamma}{2})^2}-\frac{\frac{\gamma}{2}}{\left(\omega+\sqrt{\omega_{LO}^2-(\frac{\gamma}{2})^2}\right)^2+(\frac{\gamma}{2})^2}\right] \tag{3.25}$$

or

$$\mathfrak{Im}\left\{-\frac{1}{\varepsilon_\omega^{ph}}\right\}=\left(\frac{1}{\varepsilon^\infty}-\frac{1}{\varepsilon^0}\right)\ \omega_{LO}\ \frac{\pi}{2}\left[\mathfrak{L}(\omega)-\mathfrak{L}(-\omega)\right] \tag{3.26}$$

with the scaled Lorentzian $\mathfrak{L}(\omega)$ defined as

$$\mathfrak{L}(\omega)=\frac{1}{\pi}\frac{\omega_{LO}}{\sqrt{\omega_{LO}^2-(\frac{\gamma}{2})^2}}\frac{\frac{\gamma}{2}}{\left(\omega-\sqrt{\omega_{LO}^2-(\frac{\gamma}{2})^2}\right)^2+(\frac{\gamma}{2})^2} \tag{3.27}$$

Fig. 3.2 shows how the antisymmetric function $\mathfrak{Im}\{-\frac{1}{\varepsilon_\omega^{ph}}\}$ is made up of the two Lorentzians Eq. (3.27) at positive and negative frequency. With Eq. (3.26), we can write Eq. (3.18) as

$$W_{k,\omega}^0=\frac{2\pi}{\hbar}F_k^u\left[\mathfrak{L}(\omega)-\mathfrak{L}(-\omega)\right] \tag{3.28}$$

in complete correspondence to Eq. (3.22). Comparing the scattering rates for undamped phonons Eq. (3.28) with the one for damped phonons Eq. (3.22), we see that delta function at $\omega = \pm\omega_{LO}$ in the undamped case is replaced by a Lorentzian at $\omega = \pm\sqrt{\omega_{LO}^2 - \frac{\gamma^2}{4}}$ of with $\frac{\gamma}{2}$. These two are of course the same in the limit $\gamma \to 0$.

We can now write the energy relaxation time as

$$\frac{1}{\tau_p^{\pm}} = \frac{2\pi}{\hbar} \int_{\boldsymbol{k}} F_k^u f_{\boldsymbol{p}}^0 \left(1 - f_{\boldsymbol{p}-\boldsymbol{k}}^0\right) \left(N^0_{\left|\frac{E_{\boldsymbol{p}-\boldsymbol{k}} - E_{\boldsymbol{p}}}{\hbar}\right|} + \frac{1 \pm 1}{2} \right) \mathfrak{L}\left(\pm \frac{1}{\hbar} \left(E_{\boldsymbol{p}} - E_{\boldsymbol{p}-\boldsymbol{k}} \right) \right) \tag{3.29}$$

which means that the energy-conserving delta function in Eq. (3.23) has been replaced by a scaled Lorentzian in Fermi's Golden rule. This can be interpreted as energy conservation being smeared out, because the energy of an excitation is only defined exactly when the lifetime is infinitely long (cf, e.g. [26]).

In the cases where we are concerned, the damping rates are much smaller than the excitation frequencies, a typical value being $\frac{\gamma}{\omega_{TO}} \approx 0.01$, compare Tab. 2.2.

Eq. (3.29) and Eq. (3.17) with the scattering rate Eq. (3.19) are equivalent.

Eq. (3.29) expresses the energy relaxation in terms of the single, damped mode described by Eq. (3.24). The scattering strength F_k^u is always the same, but energy conservation is smeared out.

Eq. (3.17) involves an integral over a all possible frequencies ω. The scattering rate Eq. (3.18), which depends on the real frequency ω, is proportional to $\mathfrak{Im}\left\{\frac{-1}{\varepsilon_\omega^{ph}}\right\}$, which is a measure for the strength of damped LO-phonon excitation at each frequency. Energy conservation is explicitly enforced at each frequency.

In the long wavelength limit, and with only a single mode present, these two approaches are equally useful. In general however, where both the frequency and the damping rate of an excitation depend on wave vector, and where several modes might be important, energy-conservation would not be smeared out by a simple Lorentzian, but by a complicated function $D^i_{k,\omega}$:

$$W^0_{\boldsymbol{k},\omega} = \frac{2\pi}{\hbar} \sum_i F^i_{\boldsymbol{k}} [D^i_{\boldsymbol{k},\omega} - D^i_{\boldsymbol{k},-\omega}] \tag{3.30}$$

We adopt the approach, where the damping is accounted for in the scattering rate, rather than in the energy conservation, for the rest of this thesis.

An example for a more complicated scenario is Eq. (3.12), where the energy relaxation of the carrier is due to a single plasma excitation which is damped through Landau damping. In the energy relaxation due to carrier–coupled phonon-plasmon mode scattering Eq. (3.1), the damping of the plasmon mode is caused by Landau damping, and the damping of the phonon mode is due to anharmonic damping. This

reflects in the scattering rate Eq. (3.4), where the finite width of the peaks in $W^0_{k,\omega}$, cannot, in general, be attributed to either Landau or anharmonic damping, but only to a mixture of the two. (Compare the discussion of plot of $\mathfrak{Im}\{\frac{1}{\varepsilon_{k,\omega}}\}$ in Fig. 2.9 in subsection 2.3.2.)

3.1.3 Common approximate treatments of carrier–coupled phonon-plasmon mode scattering

We now briefly discuss a few common limiting cases of Eq. (3.4), which can be expressed in terms of discrete scattering strengths, because the collective excitations are undamped (cf. subsubsection 2.2.3.1). As our approach contains all the relevant information about the system in the dielectric function, this means making the appropriate approximations for the dielectric function. These approximations often are that the imaginary part of the dielectric function vanishes in a certain region. As the scattering rate $W^0_{\boldsymbol{k},\omega}$ from Eq. (3.4) has the form of the Poisson representation of the delta function for small $\mathfrak{Im}\left\{\varepsilon^{tot}\right\}$, we see that when the imaginary part of the dielectric function vanishes, $W^0_{\boldsymbol{k},\omega}$ becomes a delta function at the zeros of the real part of the dielectric function,

$$\frac{1}{\pi}\mathfrak{Im}\left\{\frac{-1}{\varepsilon^{tot}_{\boldsymbol{k},\omega}}\right\} \longrightarrow \delta\left(\left|\mathfrak{Re}\left\{\varepsilon^{tot}_{\boldsymbol{k},\omega}\right\}\right|\right) = \sum_i \frac{\delta\left(\omega-\omega^i_{\boldsymbol{k}}\right)}{\left|\frac{\partial}{\partial\omega}\mathfrak{Re}\left\{\varepsilon^{tot}_{\boldsymbol{k},\omega}\right\}\right|} \quad \text{for } \mathfrak{Im}\{\varepsilon^{tot}\}\to 0, \tag{3.31}$$

where $\omega^i_{\boldsymbol{k}}$ are the zeros of the total dielectric function. Consequently, the treatment of the problem is now in terms of discrete modes rather than a continuous spectrum, and it will be convenient to describe the scattering in terms of the scattering strength F^i of each mode i than in terms of the continuous scattering rate $W^0_{k,\omega}$,

$$W^0_{k,\omega} = \sum_{i=+,-} \frac{2\pi}{\hbar} F^i_k \left[\delta(\omega-\omega_i)-\delta(\omega+\omega_i)\right] \tag{3.32}$$

with the scattering strengths

$$F^i_k = \frac{\nu_k}{\left|\frac{\partial}{\partial\omega}\mathfrak{Re}\left(\varepsilon^{tot}_{\boldsymbol{k},\omega}\right)\right|_{\omega=\omega^i_k}}. \tag{3.33}$$

This reproduces the unscreened Fröhlich scattering strength F^u_k in Eq. (3.21) if we set $\varepsilon^{tot}_{k,\omega} = \varepsilon^{ph}_\omega$ with ε^{ph}_ω from Eq. (2.11) with $\gamma = 0$.

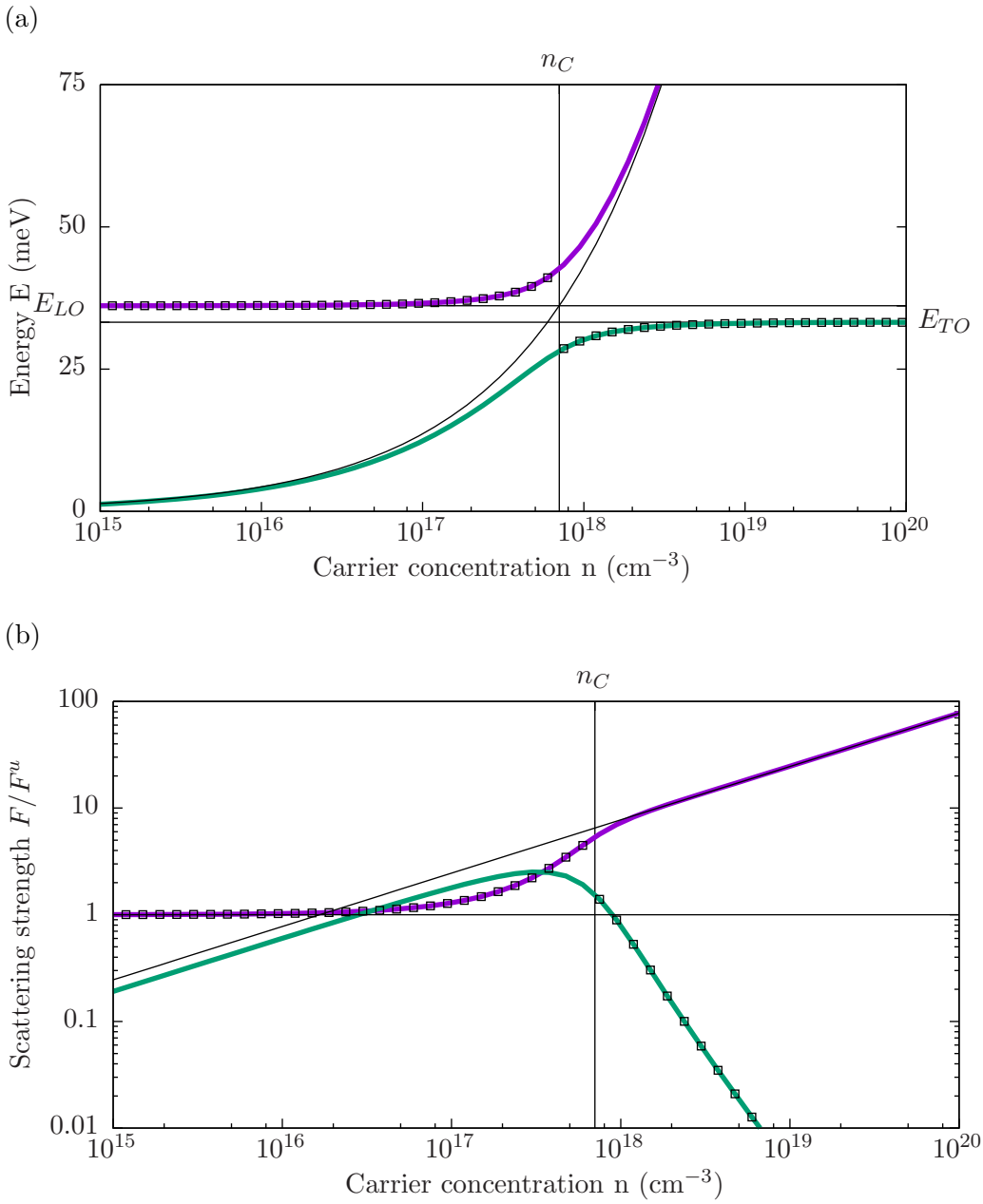

Figure 3.3: (a) Coupled mode energies $\hbar\omega_\pm$ from Eq. (2.87) in n-type GaAs in the long wavelength limit (thick lines) as a function of carrier concentration n in three dimensions. Additional horizontal grid lines mark the LO- and TO-phonon energy. The thin line indicates the plasmon energy $\hbar\omega_P(n)$ in the long wavelength limit . (b) Carrier scattering strength $F^\pm$, Eq. (3.34) of the coupled modes (thick lines), the plasma mode F^p Eq. (3.35)(thin), as a function of the carrier concentration n in three dimension. All scattering strengths are divided by the LO-phonon scattering strength F^u. Both plots have a vertical grid line marking the critical density n_C where $\omega_P = \omega_{LO}$. The more phonon-like of the two coupled modes is marked with open squares.

3.1.3.1 Carrier–coupled phonon-plasmon mode scattering in the long-wavelength limit

In subsection 2.3.1, we described how the coupling of the long wavelength plasmon and LO-phonon excitation gives rise to the two coupled natural oscillation frequencies $\omega_\pm$ in Eq. (2.87). The scattering strength for each coupled mode follows from Eq. (3.33) with the long wavelength and undamped limit of the total dielectric function, Eq. (2.85),

$$F^\pm = \nu_k \frac{\omega_\pm}{2\varepsilon^\infty} \frac{\omega_\pm^2 - \omega_{TO}^2}{\omega_\pm^2 - \omega_\mp^2}. \tag{3.34}$$

(Compare Kim et al. [36]'s screened Fröhlich scattering strengths $F_s^s(\omega_\pm)$ in their Eq. 33.) The last fraction in Eq. (3.34) is always positive. For comparison with carrier-plasmon scattering, we introduce the plasmon scattering strength

$$F^p = \nu_k \frac{\omega_P}{2\varepsilon^\infty}. \tag{3.35}$$

These quantities are useful for comparisons between expression in terms of a continuous mode frequency and a discrete mode number. We show these different scattering strengths for a range of carrier concentrations in n-type GaAs in Fig. 3.3b.

Equivalent expressions for the long-wavelength scattering strength Eq. (3.34) have been derived by Ridley [26] and Fischetti et al. [1]. We will demonstrate this equivalence explicitly in appendix B.

3.1.3.2 Carrier–longitudinal optical phonon scattering with Thomas-Fermi screening

This section discusses Thomas-Fermi-screening of LO-phonon modes, which holds for high carrier densities and nonzero wave vectors. In cases where $\omega_P \gg \omega_{LO}$, the carrier dielectric function is often approximated by the Thomas-Fermi limit

$$\varepsilon_k^c = \varepsilon^\infty + \frac{k_{TF}^2}{k^2}, \tag{3.36}$$

where k_{TF} is the Thomas-Fermi wave vector, e.g. [24]. Whenever we take this to hold in a medium, where $\varepsilon^\infty \neq 1$, a little caution is necessary. The term $\frac{k_{TF}^2}{k^2}$ is the Thomas-Fermi limit of the susceptibility of the free carriers, so k_{TF} does not depend on ε^∞. It can be useful to write the Thomas-Fermi limit of the dielectric function in terms of a scaled Thomas-Fermi wave vector $k_{TF}^* = \frac{k_{TF}}{\sqrt{\varepsilon^\infty}}$

$$\varepsilon_k^c = \varepsilon^\infty \left[1 + \left(\frac{k_{TF}^*}{k}\right)^2\right] \tag{3.37}$$

The scaled Thomas-Fermi wave vector, $k^*_{TF} = \sqrt{\frac{4}{\pi k_F a^*_0}} k_F$ can be expressed through the effective Bohr radius a^*_0 from Eq. (2.20), with $a^*_0 \propto \varepsilon^\infty$.

Assuming that the lattice dielectric function is undamped, $\gamma = 0$, this yields zeros of the total dielectric function at the frequency [36]

$$\omega_k^{TF} = \sqrt{\frac{\omega_{TO}^2 + \left(\frac{k}{k^*_{TF}}\right)^2 \omega_{LO}^2}{1 + \left(\frac{k}{k^*_{TF}}\right)^2}} \tag{3.38}$$

with the scattering strength [33, 36]

$$F_k^{TF} = \frac{\nu_k}{2\varepsilon^\infty \omega_k^{TF}} \frac{[(\omega_k^{TF})^2 - \omega_{TO}^2]^2}{\omega_{LO}^2 - \omega_{TO}^2}. \tag{3.39}$$

In this approximation, the frequency of the single relevant mode goes from ω_{TO} at $k = 0$ to ω_{LO} at $k \to \infty$, while the scattering strength goes from zero to the LO-phonon value Eq. (3.21). Note that it is the scaled Thomas-Fermi wave vector k^*_{TF}, and not the Fermi wave vector k_{TF} itself which determines the length scale on which ω_k^{TF} moves from ω_{TO} to ω_{LO}. (ω_k^{TF} and F_k^{TF} are shown in Fig. 5.1c and Fig. 5.3 in the context of chapter 5.)

3.2 Screened interface phonon scattering

In this section, we show that the expression Eq. (3.4) also holds for two-dimensional semiconductor heterostructures, as long as we find the appropriate dielectric functions for these composite structures. Specifically, we show that this holds when the carriers are confined to a single interface, i.e., we consider them as truly two-dimensional.

Maslov [45] did this to describe the Coulomb drag between a 2d electron gas (2DEG) in interaction with a 3d electron gas. His approach has been applied to Coulomb drag in various heterostructures, e.g. [82, 60], and also to remote phonon scattering, the interaction of a 2DEG with the surrounding optical phonons[83]. We will refer to this as screened interface phonon scattering.

Following Maslov [45], we use the fluctuation-dissipation theorem to describe interface scattering with the scattering rate

$$W^0_{\boldsymbol{k},\omega} \propto \int \mathrm{d}z_1 \int \mathrm{d}z_2 \psi_n^2(z_1)\psi_n^2(z_2) \mathfrak{Im}\left\{\varphi_{\boldsymbol{k},\omega}(z_1, z_2)\right\} \tag{3.40}$$

where the z-axis is perpendicular to the interface and $\boldsymbol{k}$ is the wave vector component parallel to the interface and ω the frequency of the relevant excitation. $\varphi_{\boldsymbol{k},\omega}(z_1, z_2)$ is the electrostatic potential at point z_1 introduced by a point charge at z_2. $\psi_n(z)$ is the

transverse wave function of the carriers in the n^{th} subband.

If we take the interface to be infinitely thin and situated at $z = 0$, $\psi_n(z) \propto \delta(z)^2$, so that

$$W^0_{\boldsymbol{k},\omega} \propto \mathfrak{Im}\left\{\varphi_{\boldsymbol{k},\omega}(z_1 = 0, z_2 = 0)\right\} \tag{3.41}$$

and we only have to determine the electrostatic potential $\varphi_{\boldsymbol{k},\omega}(0,0)$ at $z_1 = 0$ due to a point charge at $z_2 = 0$. We will drop the argument $z_2 = 0$ on φ in the subsequent discussion.

3.2.1 Solution of the Poisson equation in a heterostructure of anisotropic dielectrics

As Maslov [45] discusses a case with isotropic dielectrics, we show the solution to the Poisson equation for a heterostructure of anisotropic, dispersive media, and a sheet charge density in an interface at $z = 0$. We need a solution of the Poisson equation which captures anisotropy, because we want to treat materials with anisotropic dielectric constants such as hexagonal boron nitride (BN) or MoS_2, cf. chapter 6.

The potential $\varphi(\boldsymbol{r}, t)$ fulfills the Maxwell equation, [6, 31]

$$\nabla \boldsymbol{D}(\boldsymbol{r}, t) = 4\pi\rho(\boldsymbol{r}, t) \text{ or } \sum_i \partial^i D^i(\boldsymbol{r}, t) = 4\pi\rho(\boldsymbol{r}, t) \tag{3.42}$$

where the sum runs over the Cartesian axes. The dielectric displacement $\boldsymbol{D}$ has the Fourier components

$$D^i_{\boldsymbol{k},\omega} = \sum_j \varepsilon^{ij}_\omega E^j_{\boldsymbol{k},\omega} \tag{3.43}$$

with the dielectric tensor ε^{ij}_ω, which we assume to be independent of wave vector k. The electric field $\boldsymbol{E}$ has the components

$$E^j(\boldsymbol{r}, t) = -\partial^j \varphi(\boldsymbol{r}, t). \tag{3.44}$$

In the absence of external charge ρ, and for a constant or sufficiently slowly varying dielectric tensor, the Laplace equation

$$\sum_{i,j} \varepsilon^{ij}(t)\partial^i\partial^j\varphi(\boldsymbol{r}, t) = 0 \tag{3.45}$$

holds. If we assume that the interface is aligned with one of the principal axes in the crystal, $\varepsilon^{ij} = \delta^{ij}\varepsilon^{ii}$ becomes diagonal. We also assume that the two principal axes parallel to the interface have the same dielectric constant, $\varepsilon^{xx} = \varepsilon^{yy}$. If $\varphi_{\boldsymbol{k},\omega}(z)$ is the Fourier transform of $\varphi(\boldsymbol{r}, t)$ in the x and y coordinates, and in time, the Laplace

[2] $\delta(z)$ is the Dirac delta function.

equation becomes

$$\left(\frac{\partial^2}{\partial z^2} - \frac{\varepsilon^{xx}}{\varepsilon^{zz}}|\boldsymbol{k}|^2\right)\varphi_{\boldsymbol{k},\omega}(z) = 0. \tag{3.46}$$

We can introduce the scaled wave vector K

$$K_{k,\omega} = k\sqrt{\frac{\varepsilon_\omega^{xx}}{\varepsilon_\omega^{zz}}} \tag{3.47}$$

in order to write the anisotropic Laplace equation the same way as the isotropic one. We plugged in explicitly that the dielectric functions are independent of wave vector, which makes $\boldsymbol{K} \parallel \boldsymbol{k}$.

$$\left(\frac{\partial^2}{\partial z^2} - K^2\right)\varphi_{k,\omega}(z) = 0 \tag{3.48}$$

In general, all dielectric functions, and hence K, are complex. We choose the root in Eq. (3.47), to lie in the right half plane, $\mathfrak{Re}\{K\} > 0$. Hence, we know that the term $\propto e^{-Kz}$ in the solution to the differential equation of second order Eq. (3.48)

$$\varphi_{k,\omega}(z) = \alpha e^{-Kz} + \beta e^{Kz} \tag{3.49}$$

corresponds to an exponentially decreasing oscillatory term, whereas the term $\propto e^{Kz}$ corresponds to an exponentially growing one. Eq. (3.49) requires two boundary conditions to determine the complex coefficients α and β. For convenience, we introduce the quantity,[31]

$$\varepsilon'_\omega \equiv \varepsilon_\omega^{zz}\sqrt{\frac{\varepsilon_\omega^{xx}}{\varepsilon_\omega^{zz}}}, \tag{3.50}$$

an effective scalar dielectric function. Again, we take the root in the right half-plane.

Boundary conditions

In a system with a series of homogeneous dielectrics changing along the z-axis, between interfaces $z = z_n$ (Fig. 3.4), there are three kinds of boundary conditions: [6, 31]

1. The potential on the edges of the relevant domain needs to be known.

$$\varphi_{k,\omega}(z_a) = \varphi_a \qquad\qquad \varphi_{k,\omega}(z_b) = \varphi_b \tag{3.51}$$

   We use the requirement $\lim_{z\to\pm\infty}\varphi_{k,\omega}(z) = 0$ that the potential vanishes far away from the interface.

2. The potential has to be continuous at the interfaces.

$$\lim_{\delta\to 0}\varphi_{k,\omega}(z_n - \delta) = \lim_{\delta\to 0}\varphi_{k,\omega}(z_n + \delta) \tag{3.52}$$

3. The component of the dielectric displacement D^z perpendicular to the interface on either side of the interface has to differ by the surface charge $\sigma_{k,\omega}$: This follows from Gauss's law in its integral form :

$$\lim_{\delta\to 0} D^z_{k,\omega}(z_n+\delta) - \lim_{\delta\to 0} D^z_{k,\omega}(z_n-\delta) = 4\pi\sigma_{k,\omega} \tag{3.53}$$

With the dielectric displacement D^z defined as

$$D^z_{k,\omega} = \varepsilon^{zz} E^z_{k,\omega} = -\varepsilon^{zz}_{\omega} \frac{\partial}{\partial z}\varphi_{k,\omega}(z), \tag{3.54}$$

this can be written as

$$\varepsilon^{zz}_{n+1} \lim_{\delta\to 0} \frac{\partial}{\partial z}\varphi_{k,\omega}(z_n+\delta) - \varepsilon^{zz}_{n} \lim_{\delta\to 0} \frac{\partial}{\partial z}\varphi_{k,\omega}(z_n-\delta) = -4\pi\sigma_{k,\omega} \tag{3.55}$$

Where ε_n is the dielectric to left of the interface at z_n and ε_{n+1} the dielectric to the right of the interface at z_n. Both these dielectric functions can depend on frequency.

For a system with n interfaces, and n + 1 different layers, this will yield 2n +2 equations for the 2(n+1) variables α_n and β_n. For heterostructures with a large number of interfaces, it is convenient to apply a transfer matrix model [84], which solves the this system of equations step by step. In this thesis, we only treat systems with up to two interfaces (cf. Fig. 3.4b), and it is still tractable to solve the six equations for six variables by hand.

3.2.2 Effective scalar dielectric function $\varepsilon^{\text{interface}}$ for the heterostructure

Imagine a 2d test sheet charge density at z=0, which is constant as a function of wave vector and frequency, $\sigma_{k,\omega} = \sigma$, surrounded by a uniform medium with the dielectric function ε_ω. This gives rise to a potential

$$\varphi^{\text{uniform}}_{k,\omega}(z=0) = \frac{2\pi\sigma}{k\varepsilon^{\text{uniform}}_{\omega}} \tag{3.56}$$

at z=0. We define an effective dielectric constant $\varepsilon^{interface}_{k,\omega}$ due to a test charge density σ at $z = 0$ in the composite system as

$$\varepsilon^{\text{interface}}_{k,\omega} \equiv \frac{2\pi\sigma}{k\varphi^{\text{interface}}_{k,\omega}(z=0)} \tag{3.57}$$

so that Eq. (3.56) for the uniform background holds for the the case with the interface. With Eq. (3.57), we can express the scattering rate in terms of the

imaginary part of the inverse dielectric function

$$W^0_{k,\omega} = \frac{2\nu_k}{\hbar}\mathfrak{Im}\left\{\frac{-1}{\varepsilon^{\text{interface}}_{k,\omega}}\right\}. \tag{3.58}$$

Effective dielectric function for a infinitely thin interface between two different dielectrics

For the example in Fig. 3.4a, an interface between two different dielectrics, we get

- $\alpha_1 = 0$, $\beta_2 = 0$ due to the boundary condition Eq. (3.51) at $z = \pm\infty$
- $\beta_1 = \alpha_2 = \varphi(0)$ due to the boundary condition Eq. (3.53) at $z = 0$
- Eq. (3.55) at $z = 0$ lets us fix the last variable,

$$\varphi(0) = \frac{4\pi\sigma}{K_1\varepsilon_1^{zz} + K_2\varepsilon_2^{zz}} = \frac{4\pi\sigma}{k\left(\varepsilon'_1 + \varepsilon'_2\right)}.$$

This yields

$$\varepsilon^{\text{interface 1a}} = \frac{1}{2}\left(\varepsilon'_1 + \varepsilon'_2\right) \tag{3.59}$$

We can retrieve Hess and Vogl's[51] case of remote polar phonon modes at the interface between a non-polar semiconductor and an oxide if we set $\varepsilon'_1 = \varepsilon^{\infty}_S$ and $\varepsilon'_2 = \varepsilon_{ox}$ to Eq. (2.11) with $\gamma = 0$.

Effective dielectric function for a thin layer with dielectric ε_L between two different dielectrics

For the example in Fig. 3.4b, a thin layer with dielectric ε'_L between two different dielectrics, the same procedure yields

$$\varepsilon^{\text{interface 1b}} = \varepsilon'_L\frac{B - A}{(1 + A)(1 + B)} \tag{3.60}$$
$$\text{with } A = \frac{\varepsilon'_L - \varepsilon'_1}{\varepsilon'_L + \varepsilon'_1}e^{-K_L a}, \qquad B = \frac{\varepsilon'_L + \varepsilon'_2}{\varepsilon'_L - \varepsilon'_2}e^{K_L a}.$$

In the examples, we indexed the effective dielectric functions ε', Eq. (3.50) and the scaled wave vector K, Eq. (3.47) with the indices 1 and 2 for the left and right side of the interface and with an "L" for layer in the case where there is a small interface layer of thickness a (See Fig. 3.4b).

The static limit of Eq. (3.60) is shown as a function of layer thickness in Fig. 3.4c. It is equal to Eq. (3.59) for zero wave vector k, and goes towards the low-frequency dielectric function of the layer material, ε'^0_L as $k \to \infty$.

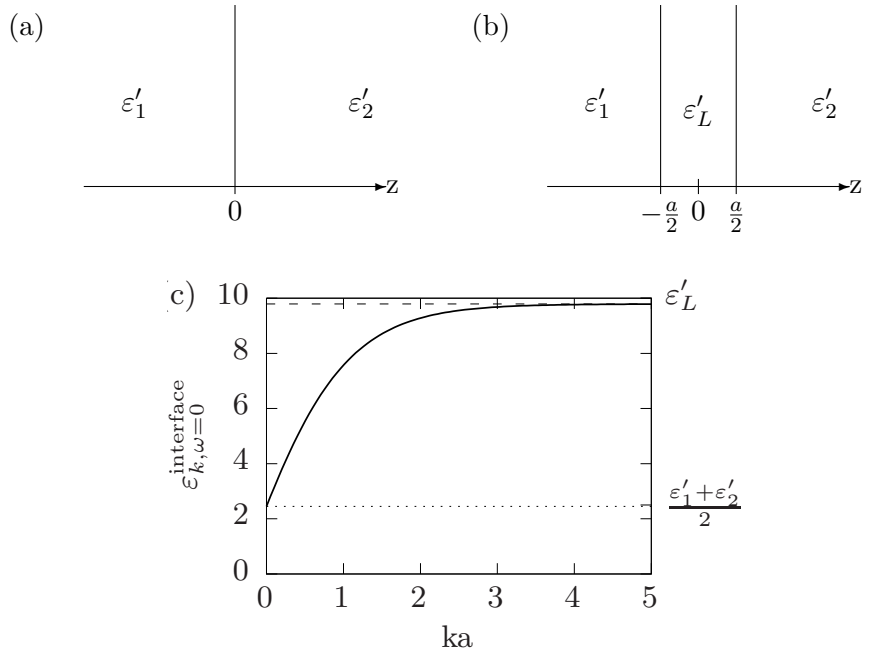

Figure 3.4: Interface layer with the dielectric function ε_L' between two dielectrics with the dielectric functions ε_1' and ε_2' on the left and right, respectively. (a) Assuming the interface is infinitely thin. (b) The interface has a finite thickness a. (c) Static interface dielectric $\varepsilon_{k,\omega=0}^{\text{interface}}$, Eq. (3.60), as a function of wave vector k and layer thickness a. The example is for a structure as shown in subplot b, at $\omega = 0$, where material 1 is SiO_2, the layer consists of MoS_2 of a thickness a=6.145Å, and the "material" 2 is vacuum. ε_L', ε_1' and ε_2' are all evaluated at $\omega = 0$.

3.2.3 Dielectric response of carriers – screening of polar interface modes

As we assume that all free carriers are localized in the plane at $z = 0$, we can use purely two-dimensional expressions for the dielectric response of the carrier gas.

We derived the expression Eq. (2.33),

$$\varepsilon_{\boldsymbol{k},\omega}^{c} = \varepsilon^{\infty} + \chi_{\boldsymbol{k},\omega}^{d=2} \tag{3.61}$$

for the dielectric function of a two-dimensional electron gas surrounded by a -homogeneous- dielectric medium [46] in section 2.2. Here $\chi_{\boldsymbol{k},\omega}^{d=2}$ is the susceptibility of the two-dimensional electron gas in the RPA, and ε^{∞} is the high frequency dielectric constant of the background medium. Following Maslov [45] we use Eq. (3.61) replacing the dielectric constant for the homogeneous surrounding medium with the dielectric function of our composite structure, $\varepsilon^{\text{interface}}$. This yields the total dielectric function (phonon and plasmon response) of the composite structure

$$\varepsilon_{\boldsymbol{k},\omega}^{tot} = \varepsilon_{\boldsymbol{k},\omega}^{\text{interface}} + \chi_{\boldsymbol{k},\omega}^{d=2} = \varepsilon_{\boldsymbol{k},\omega}^{\text{interface}} + \varepsilon_{\boldsymbol{k},\omega}^{c,d=2} - \varepsilon^{\infty} \tag{3.62}$$

This expression is formally identical to the expression for the total dielectric function in section 2.3, Eq. (2.83), with $\varepsilon^{\text{interface}}$, the dielectric response of a polar composite structure replacing ε^{ph}, the dielectric function of a polar bulk material. Hence, the expression Eq. (3.4) discussed for bulk materials in section 3.1 can be applied to composite structures:

$$W^0_{k,\omega} = \frac{2\nu_k}{\hbar}\mathfrak{Im}\left\{\frac{-1}{\varepsilon^{\text{tot}}_{k,\omega}}\right\} = \frac{2\nu_k}{\hbar}\mathfrak{Im}\left\{\frac{-1}{\varepsilon^{\text{interface}}_{k,\omega} + \chi^{d=2}_{\boldsymbol{k},\omega}}\right\} \tag{3.63}$$

As various materials are involved in composite structures, the calculations become more complex than those for bulk materials. Even when neglecting the dielectric response of the carriers, the multiple optical modes from different constituents of the composite structures will couple. To avoid confusion with the coupled collective phonon-plasmon modes in the simpler bulk case, we will call these coupled optical modes unscreened interface modes. When we take the carrier response into account, we obtain screened interface modes. In general, we treat this screening dynamically. As static screening is a common approximation, we also consider this limit.

3.2.4 Screened interface polar phonon scattering in pseudo-2d vs truly 2d heterostructures

In this thesis, we only treat carrier scattering with interface polar phonons in strictly two-dimensional systems. Explicitly, this means that the carriers are confined to exactly one plane in three-dimensional space. This criterion goes beyond what is often used to specify as a two-dimensional electron gas (2DEG) in semiconductor physics [85, 58], where a step-like density of states is essentially the criterion for two-dimensionality. We will call this type of two-dimensionality "pseudo-2d", whereas we call the carriers "truly-2d", if they are confined to a single plane.

The truly 2d carriers will have delta-functions as wave functions in the direction of the confinement, whereas the pseudo-2d carriers will extend into the confinement direction, and have finite transverse wave functions in this direction (which is perpendicular, or transverse to the direction of transport). We illustrate this for an n-type MOSFET:

Transverse wave function in an n-MOSFET If we consider an n-MOSFET in inversion, the substrate is p-doped. Hence, with no gate voltage applied, electrons would be minority carriers in the substrate. However, applying a gate voltage causes the bands to bend - eventually strong enough to cause inversion. An n-conducting region, the channel, will emerge at the oxide-semiconductor interface, see, e.g.,[58].

In order to determine the band banding, a Poisson equation must be solved, where

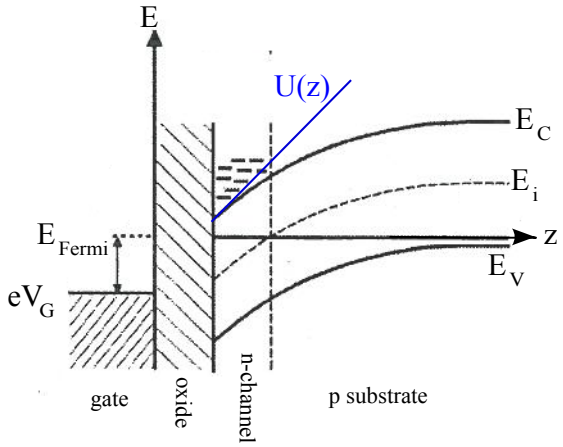

Figure 3.5: Schematic sketch of the band bending at a semiconductor-oxide interface in a MOSFET in the z-direction, the direction of confinement, cf. [85, 58] . A triangular well approximation to the potential (blue line) is also included.

the charge that determines the potential depends on the potential. The charge distribution follows from the transverse wave functions, which are the solution of a Schrödinger equation with the potential determining the Hamiltonian. This inter-dependency means that the Poisson and Schrödinger equations have to be solved self-consistently. In practice, the potential is often approximated, for example as a triangular well like in Fig. 3.5.

The confinement in the z-direction gives rise to so-called subbands. The solution to the Schrödinger equation in the transverse direction z has discrete eigenvalues E_n, so that the energy of a pseudo-2d carrier is

$$E_{p_x,p_y,n} = E_n + \frac{\hbar^2(p_x^2 + p_y^2)}{2m^*} \tag{3.64}$$

This energy dependence has to be taken into account in the calculation of the dielectric function and the mobility. The presence of subbands also means that not only intra-subband scattering, but also inter-subband scattering needs to be taken into account. Moreover, the extension of the wave function also affects the scattering rate Eq. (3.63), as mentioned at the beginning of section 3.2. Furthermore, if the confinement region is sizable, the interaction of the pseudo-2d carriers with confined polar optical modes cannot be neglected [86], see the section on LO-phonon scattering in appendix E.2.

None of these complications apply for truly-2d carriers. Therefore, we approximate the carriers in MoS_2-monolayers as truly-2d.

Historically, most treatments of interface phonon scattering or "remote phonon scattering" has been for pseudo-2d structures, mainly MOSFETS. [51, 1, 87, 88, 83] Only recently has remote phonon scattering in MOSFETs with truly-2d channels –such as graphene– been treated [89, 90, 91].

Originally, Hess and Vogl [51] applied remote phonon scattering to the silicon–silicon oxide interface in a MOSFET. As mentioned briefly in subsection 3.2.2, this can be described as a limiting case of Eq. (3.59). We will discuss here how Hess and Vogl's expressions follow from our expression in subsection 3.2.2 explicitly, but the procedure is the same for obtaining the long-wavelength, zero-damping limits for the descriptions of remote phonon scattering in MOSFETs, e.g. [1, 92].

The interface dielectric function for Hess and Vogl's Si-SiO_2-interface is

$$\varepsilon_\omega^{HV} = \frac{1}{2}\left[\varepsilon_{Si}^\infty + \varepsilon^\infty + \omega_{TO}^2 \frac{\varepsilon^0 - \varepsilon^\infty}{\omega_{TO}^2 - \omega^2}\right], \tag{3.65}$$

where the quantities $\varepsilon^\infty, \varepsilon^0, \omega_{TO}$ all refer to the SiO_2. This means the natural oscillation frequency is at

$$\omega_{HV} = \omega_{TO}\sqrt{\frac{\varepsilon_{Si}^\infty + \varepsilon^0}{\varepsilon^\infty + \varepsilon^\infty}} \tag{3.66}$$

The scattering strength F_k^{HV} follows from Eq. (3.33) as

$$F_k^{HV} = \frac{\nu_k}{4}\omega_{HV}\frac{\varepsilon^0 - \varepsilon^\infty}{(\varepsilon_{Si}^\infty + \varepsilon^0)(\varepsilon_{Si}^\infty + \varepsilon^\infty)} = \frac{\nu_k}{4}\omega_{HV}\left[\frac{1}{\varepsilon_{Si}^\infty + \varepsilon^0} - \frac{1}{\varepsilon_{Si}^\infty + \varepsilon^\infty}\right], \tag{3.67}$$

compare [51, Eq. 2b]. Note the formal similarity between the difference of the two inverse dielectric function in the Hess and Vogl scattering strength Eq. (3.67) and the Fröhlich scattering strength Eq. (3.21).[3]

3.3 Approximate treatment of momentum relaxation for carrier–phonon-plasmon scattering

Naively, one could expect to be able to treat the momentum relaxation due to a carrier scattering with a coupled plasmon-phonon mode similar to energy relaxation, so that the momentum relaxation rate would be described by

$$\frac{1}{\tau_p} = \int_{-\infty}^{\infty} \mathrm{d}\hbar\omega \int_{\boldsymbol{k}} \frac{f_{\boldsymbol{p}}^0}{f_{\boldsymbol{p}-\boldsymbol{k}}^0}\left(1 + N_{\boldsymbol{\omega}}^0\right)\delta\left(E_{\boldsymbol{p}-\boldsymbol{k}} - E_{\boldsymbol{p}} + \hbar\omega\right) W_{k,\omega}^0 \left(1 - \cos\theta_{\boldsymbol{p},\boldsymbol{p}-\boldsymbol{k}}\right) \tag{3.68}$$

for quasi-elastic scattering processes[4] with the scattering rate Eq. (3.4). $\theta_{\boldsymbol{p},\boldsymbol{p}-\boldsymbol{k}}$ is the angle between the vectors $\boldsymbol{p}$ and $\boldsymbol{p}-\boldsymbol{k}$.

This assumption has two main problems: Firstly, carrier-coupled mode scattering will

[3] Compare also the expression for the scattering strength of the coupled modes in Fischetti et al. notation, appendix B.

[4] This is a textbook expression, e.g.,[3]. We will obtain Eq. (3.68) as a limiting case from our discussion in chapter 4.

in general be inelastic. Secondly, momentum relaxation in carrier–carrier scattering and carrier–LO-phonon scattering are vastly different, but Eq. (3.4) treats the momentum relaxation through carrier–carrier scattering in them same way as it does carrier–LO-phonon scattering. We will discuss this point in great detail in chapter 4. Here, we only try to give some intuitive understanding for the problem. In carrier–LO-phonon scattering carrier momentum is relaxed (colloquially: lost), because it is transferred to the LO-phonons, which, in turn, transfer it to other phonons through anharmonic decay.

In carrier–carrier scattering no momentum is lost, because momentum is only transferred between carriers and plasmons. The plasmons do not have an anharmonic decay mechanism like the LO-phonons, and any damping of the plasmons is Landau-damping, i.e, decay into an quasi-electron and quasi-hole pair, and this decay mechanism transfers the momentum back to the carrier distribution. The momentum relaxation rate must thus fulfill $\frac{1}{\tau_p} = 0$, but it is quite clear that Eq. (3.68) will in general be nonzero.

Coupled phonon-plasmon modes can decay through both of these scattering mechanisms. Hence, the momentum relaxation of carriers through these coupled modes cannot be described by either the carrier–carrier scattering limit or the carrier–LO-phonon scattering limit. The formalism we develop in this thesis to treat carrier–coupled mode scattering is presented in chapter 4.

3.3.1 Approximate treatment of carrier-coupled mode scattering by Fischetti et al. [1]

Here, we review the approximate treatment of carrier–coupled mode scattering by Fischetti et al. [1]. Their approximation is based on the zero temperature dielectric function, where the regions in the wave vector–energy plane in which the plasmons are damped (single pair excitation region or SPER) and undamped, are strictly divided, cf. subsubsection 2.2.2.2. Hence, when the plasmon is undamped, on the long-wavelength side of the SPER, the coupled modes only have anharmonic decay available as a decay mechanism. This makes the momentum relaxation mechanism the same as for carrier-LO-phonon scattering only. In a quasi-elastic approximation, the momentum relaxation rate would indeed obey Eq. (3.68).

When the plasmon is damped, inside the SPER, the plasmons are neglected entirely, and the momentum relaxation rate, in the quasi-elastic approximation, is described by Eq. (3.68) with the carrier–LO-phonon scattering rate $W_\omega^{0,ph}$ Eq. (3.22). This can be interpreted as treating the plasmons and the LO-phonons separately, and adding the carrier–carrier momentum relaxation rate and the carrier–LO-phonon momentum relaxation rate – the carrier–carrier relaxation rate being zero.

3.3.2 Approximate treatment of Landau damping at zero temperature by Fischetti et al. [1]

Fischetti et al. [1] additionally approximate the boundaries of the SPER and the plasmon dispersion. This is because they applied this treatment to MOSFET structures with a poly-silicon gate, so that they have a gate plasmon and a substrate plasmon, and therefore a gate-SPER and a substrate SPER. Their approximate treatment of "Landau damping at $T = 0$"[5] simplifies the computation of the momentum relaxation time. In our case, where only one SPER is present, this additional approximation is not strictly necessary, but we still present it, because it has merit in yielding the simplest possible expressions for the momentum relaxation time due to carrier–coupled mode scattering. We will investigate its validity carefully later on in this work, see chapter 5.

In their approximation of Landau damping, Fischetti et al. [1] treat the plasma modes as damped out entirely as soon as they hit the single pair excitation regime in the degenerate limit, see Fig. 3.6a. Figure 3.6a sketches the situation with only the plasma mode present: The plasmon has constant frequency and is undamped on the long-wavelength side of the single pair excitation limit, and damped out entirely on the short-wavelength side of it.

Applied to the case of coupled carrier–LO-phonon modes in bulk semiconductors, Fischetti et al. [1]'s method only uses the coupled modes for wave vectors shorter than the wave vector where the plasmon-like mode enters the single pair excitation regime. The plasmon-like mode, with the frequency ω_c at $k = 0$, is defined by

$$\omega_c = \begin{cases} \omega_+ & S_+ \leq S_- \\ \omega_- & S_- < S_+ \end{cases}. \tag{3.69}$$

To determine which of the two modes $\omega_\pm$ is more plasmon-like or phonon-like, Fischetti et al. use Varga's "phonon content" [30, 36] $S_\pm$, which is discussed in section B.1. In the case of only two coupled modes in the 3d case, the plasmon like mode is the lower mode if $n < n_C$ and the upper mode if $n > n_c$. (See Fig. 3.3). This makes the wave vector where ω_c enters the single pair excitation region

$$k_c = k_F \left(\sqrt{\frac{\hbar\omega_c}{E_F} + 1} - 1 \right). \tag{3.70}$$

For $k > k_c$, only the LO-phonon mode is considered. This means that the plasmon-like mode disappears when it reaches the single pair excitation regime. The

[5] This approach is called an approximate treatment of "Landau damping" by the authors of [1]. The reader should not be confused by the fact that Landau damping [2] is indeed the classical limit of the process that is described here in its "extreme quantum limit" [1]. This is explained in great detail in Appendix A.

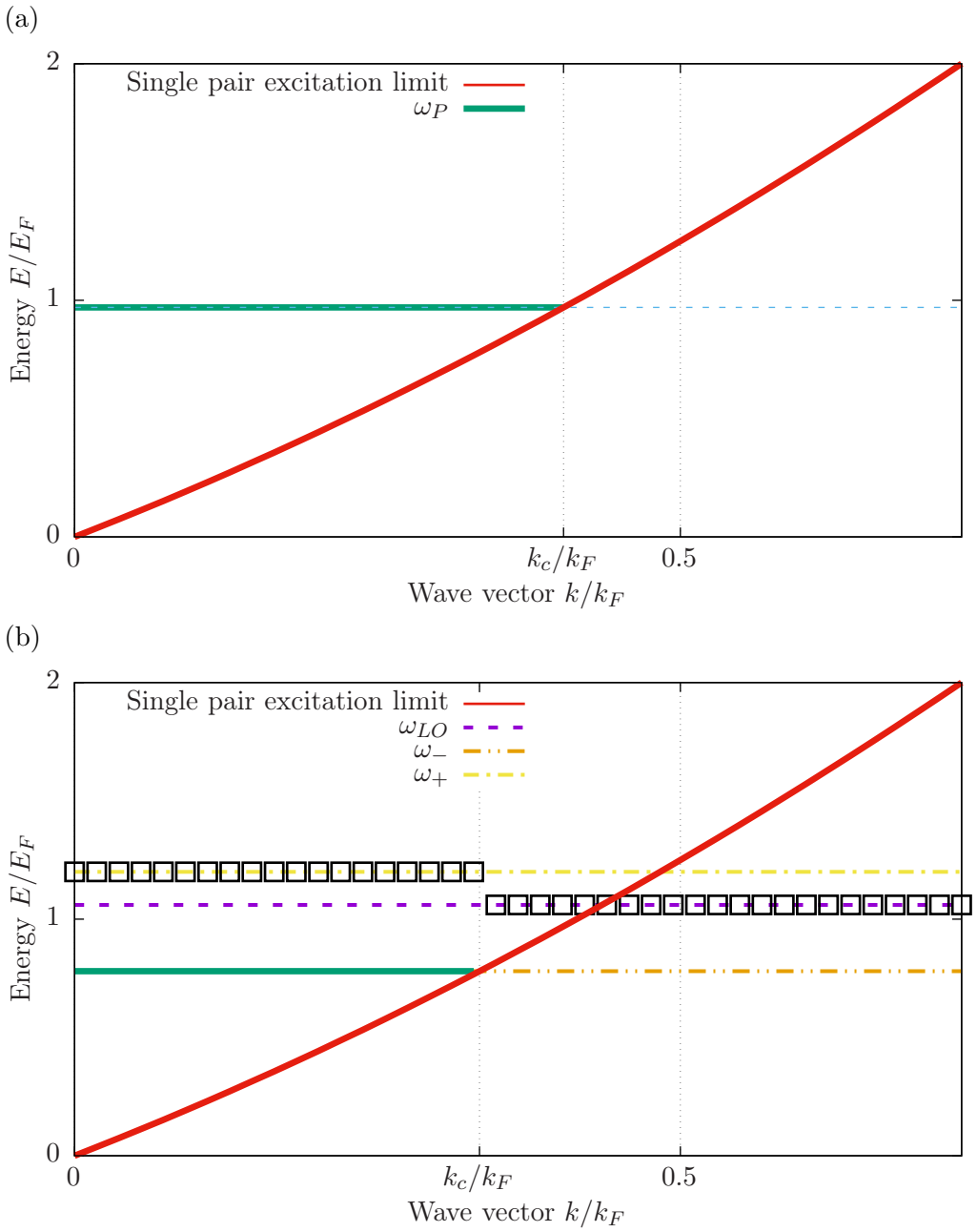

Figure 3.6: Model dispersion in GaAs for $n = 5 \times 10^{17} cm^{-3}$ as suggested by Fischetti et al. [1]. (a) Plasma frequency as a function of wave vector: A constant frequency plasma excitation is Landau-damped out as soon as it would have to cross the border into the single pair excitation limit. (b) Coupled plasmon-LO-phonon mode frequency as a function of wave vector: The plasmon like mode, Eq. (3.60)(thick solid line) is damped out as soon as it enters the single pair excitation region, at $k = k_c$, Eq. (3.70). The phonon like mode (open squares) jumps from ω_+ to ω_{LO} at $k = k_c$.

frequency of the phonon-like mode jumps from $\omega_\pm$ to ω_{LO} at $k = k_c$ (Fig. 5.2). The scattering strengths for the Fischetti approximation $F^\pm_{Fischetti}$ consequently jump from the long-wavelength expression Eq. (3.34) to the Fröhlich expression Eq. (3.21) at $k = k_c$.

$$F^\pm_{k,Fischetti} = \begin{cases} F^\pm & k \leq k_c \\ F^u & k > k_c \text{ and } \omega_\pm \neq \omega_c \\ 0 & \text{elsewhere} \end{cases} \tag{3.71}$$

The scattering strengths $F^\pm_{k,Fischetti}$ will then be substituted in the scattering rate Eq. (3.32), and finally into Eq. (3.68). The approximate dispersion of the coupled modes is plotted for GaAs at $n = 5 \times 10^{17} cm^{-3}$ in Fig. 3.6b. The parameters used are in table 2.4.

Approximate treatment of Landau damping at zero temperature by Fischetti et al. [1] in more complex structures

The approximation due to Fischetti et al. [1] discussed in subsection 3.3.1 can be applied directly to more complicated structures, say the two-dimensional semiconductors described in section 3.2, or bulk semiconductors with several optical phonon modes. However, the additional approximate treatment of $T = 0$ Landau damping from subsection 3.3.2 will not be applicable, because there will generally be more than two coupled modes, and the phonon content of these modes will not be defined any more.

In this thesis, we will only discuss Fischetti et al.'s approximate momentum relaxation for bulk GaAs, see section 5.2.1.

Chapter 4

Coupled carrier–collective mode Boltzmann equations

This chapter is the main part of this thesis. Here, we develop our model for the momentum relaxation due carrier–coupled collective mode scattering in polar semiconductors. The treatment here is formulated to apply to bulk polar semiconductors and polar semiconductor heterostructures equally. The only difference is that the corrsponding two- or three-dimensional scattering rates, dielctric functions and integrals need to be substituted. Morover, even though the examples which will be discussed in latter chapters of this thesis are all semiconductors with spherical parabolic bands, we formulate the equations in this chapter for semiconductors with parabolic bands which do not necessarily have to be spherical. We do this to stress the point that pure carrier–carrier scattering in semiconductors within parabolic bands does not contribute to the momentum relaxation rate.

We present coupled linearized Boltzmann equations, for the carriers and for the collective modes. The crucial terms in the Boltzmann equation are due to the non-equilbrium contribution to the distribution function of the collective modes, caused by their interaction with equilibrium carriers on the one hand ("drag term") and due to anharmonic decay on the other hand. In the limiting case of carrier–plasmon scattering, there is no anharmonic decay, so that the momentum transfer between the plasmon and carriers compensates each other. The "plasmon drag" is just such that the total transferred momentum equals zero. In the limiting case of carrier–LO-phonon scattering, the anharmonic decay dominates so strongly that the LO-phonon distribution function can be considered pinned at the equilibrium value. This means that the phonon drag term vanishes, and thus the total transferred momentum is nonvanishing. In the general case of carrier–coupled mode scattering, the coupled-mode drag term will vary between these two extremes, depending of wave vector and frequency.

Describing the momentum relaxation accurately involves iterating the coupled Boltzmann equations to self-consistency. We also discuss the relaxation time solution (RTA) to the coupled Boltzmann equations.

The coupled Boltzmann equations for carriers and phonons can be found in many textbooks. We follow the description by Peierls [49, chapter 6], using the notation in [22, chapter 5].[1] However, we apply Peierl's phonon Boltzmann equation to all collective modes of the coupled phonon-plasmon system.

Our model incorporates three distinct effects: Firstly, the carriers and the collective excitations interact with each other. Secondly, the carriers are accelerated by an external electric field. Thirdly, the collective excitations can decay. The decay will be different for phonons, plasmons and coupled phonon-plasmon excitations.

We find the mobility of the carriers by solving the coupled Boltzmann equations self-consistently for both the distribution function $f_{\boldsymbol{p}}$ of a carrier of wave vector $\boldsymbol{p}$ and the distribution function $N_{\boldsymbol{k},\omega}$ of a collective mode of wave vector $\boldsymbol{k}$ and frequency ω. We do this in the weak field approximation.

4.1 Linearized Boltzmann equations for the weak field limit

The issue in solving the coupled Boltzmann equations is that both the distribution functions $N_{\boldsymbol{k},\omega}$ and $f_{\boldsymbol{p}}$ and the scattering rate $W_{\boldsymbol{k},\omega}$ are unknown. All we have are their equilibrium values. In the case where the field is small enough to drive the system only slightly out of equilibrium, we can linearize the Boltzmann equations around the equilibrium expressions. This gives us equations featuring the familiar equilibrium values $N^0_{\boldsymbol{k},\omega}$, $f^0_{\boldsymbol{p}}$ and $W^0_{\boldsymbol{k},\omega}$, which we subsequently solve for the small deviations g and G of the distributions from their equilibrium values. All first order terms will be denoted by the superscript 1, and all equilibrium, or zeroth order terms by the superscript 0.

We use Peierls's notation [49] for the linearized distribution functions:

$$f^1_{\boldsymbol{p}} = \quad f^0_{E_{\boldsymbol{p}}} - g_{\boldsymbol{p}} \frac{\partial f^0_{E_{\boldsymbol{p}}}}{\partial E_{\boldsymbol{p}}} \quad = f^0_{E_{\boldsymbol{p}}} + f^0_{E_{\boldsymbol{p}}} \left(1 - f^0_{E_{\boldsymbol{p}}}\right) \beta g_{\boldsymbol{p}} \tag{4.1}$$

and

$$N^1_{\boldsymbol{k},\sigma} = N^0_{\omega^\sigma_{\boldsymbol{k}}} - G_{\boldsymbol{k},\omega^\sigma_{\boldsymbol{k}}} \frac{\partial N^0_{\omega^\sigma_{\boldsymbol{k}}}}{\partial \hbar \omega^\sigma_{\boldsymbol{k}}} \qquad = N^0_{\omega^\sigma_{\boldsymbol{k}}} + N^0_{\omega^\sigma_{\boldsymbol{k}}} \left(1 + N^0_{\omega^\sigma_{\boldsymbol{k}}}\right) \beta G_{\boldsymbol{k},\omega^\sigma_{\boldsymbol{k}}}, \tag{4.2}$$

where we assume that $\beta G_{\boldsymbol{k},\omega^\sigma_{\boldsymbol{k}}} \ll N^0_{\omega^\sigma_{\boldsymbol{k}}}$ and $\beta g_{\boldsymbol{p}} \ll f^0_{E_{\boldsymbol{p}}}$. $\hbar\omega^\sigma_{\boldsymbol{k}}$ is the energy of a mode

[1] The description in [22] is more pedagogical, whereas the one in [49] has fewer typographical errors.

$(\boldsymbol{k}, \sigma)$, $E_{\boldsymbol{p}}$ is the kinetic energy of a carrier with wave vector $\boldsymbol{p}$, and $\beta = \frac{1}{k_B T}$ is the inverse of the temperature T times the Boltzmann constant k_B. N^0_ω is the equilibrium distribution function of the collective mode, the Bose-Einstein distribution function first introduced in Eq. (3.3). f^0_E is the equilibrium distribution function of the carriers, the Fermi-Dirac distribution function, first introduced in Eq. (2.23)

4.2 Collective mode Boltzmann equation

The stationary Boltzmann equation for the collective excitations requires that the change of the distribution $N_{\boldsymbol{k},\sigma}$ due to collisions with carriers is balanced by the decay due to anharmonic coupling.

$$\left(\frac{\partial N_{\boldsymbol{k},\sigma}}{\partial t}\right)_{\text{coll}} + \left(\frac{\partial N_{\boldsymbol{k},\sigma}}{\partial t}\right)_{\text{decay}} = 0 \tag{4.3}$$

The collective mode index is $|\sigma| \in \{1, \dots \Sigma\}$, where Σ is the number of discrete modes.

We assume that the rate of decay of the collective mode $(\boldsymbol{k}, \sigma)$ due to anharmonic processes is proportional to the deviation $\Delta N_{\boldsymbol{k},\sigma}$ of the distribution function from its equilibrium value. We will allow the constant of proportionality, the relaxation time $\tau_{\boldsymbol{k},\sigma}$ to depend on $(\boldsymbol{k}, \sigma)$. We will specify its exact form of $\tau_{\boldsymbol{k},\sigma}$ in subsection 4.2.2.

$$\left(\frac{\partial N_{\boldsymbol{k},\sigma}}{\partial t}\right)_{\text{decay}} = -\frac{\Delta N_{\boldsymbol{k},\sigma}}{\tau_{\boldsymbol{k},\sigma}} \tag{4.4}$$

We make this relaxation time approximation for the collective modes to account for their anharmonic decay in a simple model. [2] As we will discuss shortly, we will express this relaxation time in terms of dielectric functions, which, in turn, accounts for anharmonic damping phenomenologically. This collective mode RTA must not be mistaken with the RTA for the carriers. While we always employ the RTA for the anharmonic decay rate of collective modes throughout this thesis, we do not, in general, make use of the RTA for the carriers.

To first order, the deviation of the distribution function of the collective excitation from its equilibrium value is $\Delta N_{\boldsymbol{k},\sigma} = N^0_{\boldsymbol{k},\sigma}\left(1 + N^0_{\boldsymbol{k},\sigma}\right)\beta G_{\boldsymbol{k},\omega^\sigma_{\boldsymbol{k}}}$, so that

$$\left(\frac{\partial N_{\boldsymbol{k},\sigma}}{\partial t}\right)^1_{\text{decay}} = -\frac{N^0_{\boldsymbol{k},\sigma}\left(1 + N^0_{\boldsymbol{k},\sigma}\right)\beta G_{\boldsymbol{k},\omega^\sigma_{\boldsymbol{k}}}}{\tau_{\boldsymbol{k},\sigma}}. \tag{4.5}$$

As we discuss in appendix C.1, the collisional integral for the collective mode σ to

[2] The alternative would be to account for the interaction of these collective modes with different collective modes (cf. three-phonon processes in thermal transport) explicitly and to formulate another Boltzmann equation for these other collective modes. This would lead too far afield for this thesis.

first order is

$$\left(\frac{\partial N_{\boldsymbol{k},\sigma}}{\partial t}\right)^{1}_{\text{coll}} = 2\int_{\boldsymbol{p}} 2\pi F^{\sigma}_{\boldsymbol{k}}\delta(E_{\boldsymbol{p}+\boldsymbol{k}} - E_{\boldsymbol{p}} - \hbar\omega^{\sigma}_{\boldsymbol{k}})\left(f^{0}_{E_{\boldsymbol{p}}} - f^{0}_{E_{\boldsymbol{p}+\boldsymbol{k}}}\right)\beta N^{0}_{\boldsymbol{k},\sigma}\left(N^{0}_{\boldsymbol{k},\sigma}+1\right) \times \left(g_{\boldsymbol{p}+\boldsymbol{k}} - g_{\boldsymbol{p}} - G_{\boldsymbol{k},\omega^{\sigma}_{\boldsymbol{k}}}\right). \quad (4.6)$$

(See, e.g., Peierls [49],[22]). The factor 2 accounts for the spin degeneracy. The symbol $\int_{\boldsymbol{p}}$ signifies a d-dimensional integration over all carrier states $\boldsymbol{p}$. We show how this is parametrized in practice for two and three dimensional semiconductors in appendix C.3. The scattering strength F^{σ}_{k} of a discrete mode with index σ and wave vector $\boldsymbol{k}$ has been discussed in chapter 3. We also assume that $F^{\sigma}_{\boldsymbol{k}}$ only depends on the transferred wave vector $\boldsymbol{k}$, and not on the initial and final wave vectors $\boldsymbol{p}$ and $\boldsymbol{p}+\boldsymbol{k}$. The validity of this assumption will be discussed in chapter 5.

4.2.1 Solution to collective mode Boltzmann equation

We now solve the collective mode Boltzmann equation Eq. (4.3) in its linearized form for the non-equilibrium distribution $G_{\boldsymbol{k},\omega^{\sigma}_{\boldsymbol{k}}}$,

$$G_{\boldsymbol{k},\omega^{\sigma}_{\boldsymbol{k}}} = \frac{4\pi F^{\sigma}_{\boldsymbol{k}}\int_{\boldsymbol{p}}\delta(E_{\boldsymbol{p}+\boldsymbol{k}} - E_{\boldsymbol{p}} - \hbar\omega^{\sigma}_{\boldsymbol{k}})(f^{0}_{E_{\boldsymbol{p}}} - f^{0}_{E_{\boldsymbol{p}+\boldsymbol{k}}})\,(g_{\boldsymbol{p}+\boldsymbol{k}} - g_{\boldsymbol{p}})}{\frac{1}{\tau_{\boldsymbol{k},\sigma}} + \frac{2F^{\sigma}_{\boldsymbol{k}}}{\nu_{k}}\mathfrak{Im}\left(\varepsilon^{c}_{\boldsymbol{k},\omega^{\sigma}_{\boldsymbol{k}}}\right)} \quad (4.7)$$

We simplified the second term in the denominator of Eq. (4.7) by using Eq. (2.41), the definition of the imaginary part of the carrier dielectric function $\mathfrak{Im}\left(\varepsilon^{c}_{\boldsymbol{k},\omega}\right)$ in the random phase approximation (RPA), cf. section 2.2, [22, chapter 3].

We interpret the second term in the denominator of $G_{\boldsymbol{k},\omega^{\sigma}_{\boldsymbol{k}}}$, Eq. (4.7),

$$\frac{1}{\tau^{coupled-c}_{\boldsymbol{k},\sigma}} = \frac{2F^{\sigma}_{\boldsymbol{k}}}{\nu_{k}}\mathfrak{Im}\left(\varepsilon^{c}_{\boldsymbol{k},\omega^{\sigma}_{\boldsymbol{k}}}\right) \quad (4.8)$$

as the inverse of the lifetime $\tau^{coupled-c}_{\boldsymbol{k},\sigma}$ of the coupled mode $(\boldsymbol{k},\sigma)$ due to interaction with the carriers (marked c in the superscript). This lifetime can be understood from the decay of the coupled modes into pairs of quasi-electrons and quasi-holes in the carrier gas in the conduction or valence band.

4.2.2 Anharmonic decay of the coupled modes

Let us now consider the first term in the denominator of $G_{\boldsymbol{k},\omega^{\sigma}_{\boldsymbol{k}}}$, Eq. (4.7), the inverse of the lifetime $\tau_{\boldsymbol{k},\sigma}$ of the coupled excitation due to anharmonic damping of the coupled modes. If we assume that the plasma excitations have no anharmonic decay

channel, the anharmonic decay of the coupled plasmon-phonon modes is solely due to the anharmonic decay of the phonons. We stress this by adding superscripts to this effect to τ: $\tau_{\boldsymbol{k},\sigma} = \tau^{coupled-ph}_{\boldsymbol{k},\sigma}$.

The imaginary part of the dielectric function is a measure for the dissipation rate of energy when an external electric field is applied to a dielectric. Eq. (4.8) shows explicitly that this holds for $\tau^{coupled-c}_{\boldsymbol{k},\sigma}$. We construct $\tau^{coupled-ph}_{\boldsymbol{k},\sigma}$, the lifetime of a coupled mode due to decay into phonons, such that it depends on the imaginary part of the dielectric function of the optical phonons, $\mathfrak{Im}\left(\varepsilon^{ph}_{\boldsymbol{k},\omega^\sigma_{\boldsymbol{k}}}\right)$, in the same way,

$$\frac{\tau^{coupled-ph}_{\boldsymbol{k},\sigma}}{\tau^{coupled-c}_{\boldsymbol{k},\sigma}} = \frac{\mathfrak{Im}\left(\varepsilon^{c}_{\boldsymbol{k},\omega^\sigma_{\boldsymbol{k}}}\right)}{\mathfrak{Im}\left(\varepsilon^{ph}_{\boldsymbol{k},\omega^\sigma_{\boldsymbol{k}}}\right)}, \tag{4.9}$$

This means that the contribution to the lifetime of a coupled mode due to decay into phonons obeys

$$\frac{1}{\tau^{coupled-ph}_{\boldsymbol{k},\sigma}} = \frac{2F^\sigma_{\boldsymbol{k}}}{\nu_k}\mathfrak{Im}\left(\varepsilon^{ph}_{\omega^\sigma_{\boldsymbol{k}}}\right). \tag{4.10}$$

The imaginary part of the phonon dielectric function, $\mathfrak{Im}\left(\varepsilon^{ph}_{\omega}\right)$ is shown for bulk GaAs in the long-wavelength limit in Figure 1.3.

In the limit where the collective modes are just LO-phonons, F^σ_k will be replaced by the Fröhlich scattering strength Eq. (3.21), and the lifetime of the LO-phonon mode can be written as $\frac{1}{\tau^{ph-ph}_{LO}} = \gamma\frac{\left(1-\frac{\varepsilon^\infty}{\varepsilon^0}\right)^2}{\left(1-\frac{\varepsilon^\infty}{\varepsilon^0}\right)^2+\frac{\gamma^2}{\omega^2_{LO}}}$. Typically $\frac{\gamma}{\omega_{LO}} \approx 0.01$, and $1-\frac{\varepsilon^\infty}{\varepsilon^0} \approx 0.1$, cf. Table 2.2, so that $\frac{1}{\tau^{ph-ph}_{LO}} \approx \gamma$, i.e., the lifetime of the LO-phonons due to anharmonic decay is roughly equal to the phenomenological damping rate parameter in Eq. (2.11).

The total lifetime of the coupled modes can be calculated from Eq. (4.10) and Eq. (4.8) and consequently equals

$$\frac{1}{\tau^{coupled}_{\boldsymbol{k},\sigma}} = \frac{2F^\sigma_{\boldsymbol{k}}}{\nu_k}\mathfrak{Im}\left(\varepsilon^{tot}_{\boldsymbol{k},\omega^\sigma_{\boldsymbol{k}}}\right), \tag{4.11}$$

where $\mathfrak{Im}\left(\varepsilon^{tot}_{\boldsymbol{k},\omega^\sigma_{\boldsymbol{k}}}\right)$ is the imaginary part of the total dielectric function. This finally gives us the expression for the "coupled mode drag term" G,

$$G_{\boldsymbol{k},\omega^\sigma_{\boldsymbol{k}}} = \frac{2\pi\nu_k}{\mathfrak{Im}\left(\varepsilon^{tot}_{\boldsymbol{k},\omega^\sigma_{\boldsymbol{k}}}\right)}\int_{\boldsymbol{p}}\delta\left(E_{\boldsymbol{p}+\boldsymbol{k}} - E_{\boldsymbol{p}} - \hbar\omega^\sigma_{\boldsymbol{k}}\right)\left(f^0_{E_{\boldsymbol{p}}} - f^0_{E_{\boldsymbol{p}+\boldsymbol{k}}}\right)\left(g_{\boldsymbol{p}+\boldsymbol{k}} - g_{\boldsymbol{p}}\right) \tag{4.12}$$

Note that the scattering strength F^σ_k cancels in G. This is the only term which depends explicitly on σ, and we will describe G through its dependence on frequency

directly from now on:

$$G_{\boldsymbol{k},\omega} = \frac{2\pi\nu_k}{\mathfrak{Im}\left(\varepsilon^{tot}_{\boldsymbol{k},\omega}\right)} \int_{\boldsymbol{p}} \delta\left(E_{\boldsymbol{p}+\boldsymbol{k}} - E_{\boldsymbol{p}} - \hbar\omega\right) \left(f^0_{E_{\boldsymbol{p}}} - f^0_{E_{\boldsymbol{p}+\boldsymbol{k}}}\right) \left(g_{\boldsymbol{p}+\boldsymbol{k}} - g_{\boldsymbol{p}}\right) \tag{4.13}$$

G is called the drag term, because the coupled modes are dragged out of equilibrium due their interaction with the carriers. This will be discussed more in subsection 4.4.3.

4.3 Carrier Boltzmann equation

As we are interested in a stationary, homogeneous solution to the carrier Boltzmann equation, only the field term and the collision term are non-vanishing. Hence, the Boltzmann equation for the carriers states that the change of the distribution $f_{\boldsymbol{p}}$ of carriers of wave vector $\boldsymbol{p}$ due to the electric field is balanced by its change due to collisions with collective excitations.

$$\left(\frac{\partial f_{\boldsymbol{p}}}{\partial t}\right)_{\text{field}} = \left(\frac{\partial f_{\boldsymbol{p}}}{\partial t}\right)_{\text{coll}} \tag{4.14}$$

The field term

$$\left(\frac{\partial f_{\boldsymbol{p}}}{\partial t}\right)_{\text{field}} = \frac{\partial f}{\partial \boldsymbol{p}} \cdot \frac{\mathrm{d}\boldsymbol{p}}{\mathrm{d}t} \tag{4.15}$$

can be expressed in terms of the force $e\boldsymbol{E}$ caused by the external electric field $\boldsymbol{E}$ [93, appendix E]. As the external force driving the distribution function out of equilibrium is already of first order, the field term can only be of first order if the gradient of the carrier distribution function is of zeroth order. Hence, to first order the field term is

$$\left(\frac{\partial f_{\boldsymbol{p}}}{\partial \boldsymbol{p}} \cdot \frac{e\boldsymbol{E}}{\hbar}\right)^1 = \frac{\partial f^0_{E_{\boldsymbol{p}}}}{\partial \boldsymbol{p}} \cdot \frac{e\boldsymbol{E}}{\hbar} = -\beta f^0_E \left(1 - f^0_E\right) \boldsymbol{v}_{\boldsymbol{p}} \cdot e\boldsymbol{E} \tag{4.16}$$

where $\boldsymbol{v}_{\boldsymbol{p}} = \frac{1}{\hbar}\frac{\partial E_{\boldsymbol{p}}}{\partial \boldsymbol{p}}$ is the group velocity.

Peierls's carrier collision term in the Boltzmann equation [49] is

$$\left(\frac{\partial f_{\boldsymbol{p}}}{\partial t}\right)^1_{\text{coll}} = 2\pi \int_{\boldsymbol{k}} \sum_{\sigma} F^{\sigma}_{\boldsymbol{k}}\, \delta\left(E_{\boldsymbol{p}+\boldsymbol{k}} - E_{\boldsymbol{p}} - \hbar\omega^{\sigma}_{\boldsymbol{k}}\right) f^0_{E_{\boldsymbol{p}+\boldsymbol{k}}} \left(1 - f^0_{E_{\boldsymbol{p}}}\right) \beta \left(N^0_{\boldsymbol{k},\sigma} + 1\right) \times \left(g_{\boldsymbol{p}+\boldsymbol{k}} - g_{\boldsymbol{p}} - G_{\boldsymbol{k},\omega^{\sigma}_{\boldsymbol{k}}}\right) \tag{4.17}$$

to first order in our notation. We demonstrate this in detail in appendix C.1. Note that the integrand on the r.h.s. of Eq. (4.17) is identical to the integrand on the r.h.s. of Eq. (4.6) for the rate of change of the collective mode distribution function. We use Peierl's short convention [49], where negative values of σ mean a negative transferred energy $\hbar\omega_{\boldsymbol{k},-|\sigma|} = -\hbar|\omega_{\boldsymbol{k},|\sigma|}|$.

4.3.1 Broadening and continuous modes

As we take damping of the modes into account, the modes will, in general, be broadened. This means that energy-conservation is smeared out as discussed in section 3.1. We can take this into account by including the function $D^{\sigma}_{\boldsymbol{k},\omega}$ and an integral over wave vector.

$$\left(\frac{\partial f_{\boldsymbol{p}}}{\partial t}\right)^{1}_{\text{coll}} = \frac{2\pi}{\hbar}\iint\limits_{\boldsymbol{k}\ \hbar\omega}\sum_{\sigma} F^{\sigma}_{\boldsymbol{k}} D^{\sigma}_{\boldsymbol{k},\omega}\delta\left(E_{\boldsymbol{p}+\boldsymbol{k}} - E_{\boldsymbol{p}} - \hbar\omega\right) f^{0}_{E_{\boldsymbol{p}+\boldsymbol{k}}}\left(1 - f^{0}_{E_{\boldsymbol{p}}}\right)\beta\left(N^{0}_{\boldsymbol{k},\sigma} + 1\right) \times \left(g_{\boldsymbol{p}+\boldsymbol{k}} - g_{\boldsymbol{p}} - G_{\boldsymbol{k},\omega^{\sigma}_{\boldsymbol{k}}}\right) \quad (4.18)$$

In this sense, $D^{\sigma}_{\boldsymbol{k},\omega}$ is the density of states of the collective excitation of wave vector k. Employing Eq. (3.30), we can write the collision term as

$$\left(\frac{\partial f_{\boldsymbol{p}}}{\partial t}\right)^{1}_{\text{coll}} = \iint\limits_{\boldsymbol{k}\ \hbar\omega} W^{0}_{\boldsymbol{k},\omega}\delta\left(E_{\boldsymbol{p}+\boldsymbol{k}} - E_{\boldsymbol{p}} - \hbar\omega\right) f^{0}_{E_{\boldsymbol{p}+\boldsymbol{k}}}\left(1 - f^{0}_{E_{\boldsymbol{p}}}\right)\beta\left(N^{0}_{\omega} + 1\right) \times \left(g_{\boldsymbol{p}+\boldsymbol{k}} - g_{\boldsymbol{p}} - G_{\boldsymbol{k},\omega}\right) \quad (4.19)$$

This gives the scattering rate due to collisions in the usual form, except that the summation over discrete modes at each wave vector $\boldsymbol{k}$ is replaced by an integral over mode energy $\hbar\omega$.

Our non-equilibrium Boltzmann equations do not contain a non-equilibrium scattering-rate term, because if it was combined with the first order distribution functions, the whole term would be second order, and if it was combined with the equilibrium distribution function, they fulfill an equation of detailed balance and the collision term would cancel.

4.4 Solution of coupled Boltzmann equations

We can now solve the coupled carrier Boltzmann equation and collective mode Boltzmann equation in first order for the non-equilibrium distribution functions g and G. With the first order field term Eq. (4.16) and collision term Eq. (4.19) we get the first order Boltzmann equation for the carriers

$$-\boldsymbol{v}_{\boldsymbol{p}}\cdot e\boldsymbol{E} = \iint\limits_{\boldsymbol{k}\ \hbar\omega} W^{0}_{\boldsymbol{k},\omega}\delta\left(E_{\boldsymbol{p}+\boldsymbol{k}} - E_{\boldsymbol{p}} - \hbar\omega\right)\frac{f^{0}_{E_{\boldsymbol{p}+\boldsymbol{k}}}}{f^{0}_{E_{\boldsymbol{p}}}}\left(N^{0}_{\omega} + 1\right)\left(g_{\boldsymbol{p}+\boldsymbol{k}} - g_{\boldsymbol{p}} - G_{\boldsymbol{k},\omega}\right) \quad (4.20)$$

where $G_{\boldsymbol{k},\omega}$ is determined from Eq. (4.13), which is also a function of the non-equilibrium carrier distribution functions g. Note that Eq. (4.20) is not defined for all $\boldsymbol{p}$ as the temperature goes to zero and the Fermi-Dirac distribution in the

denominator becomes zero for $E_{\boldsymbol{p}} > E_F$. Consequently, for $E_{\boldsymbol{p}} > E_F$, $\frac{f^0_{E_{\boldsymbol{p}+\boldsymbol{k}}}}{f^0_{E_{\boldsymbol{p}}}}\left(N^0_\omega + 1\right)$ has to be replaced with $\frac{1-f^0_{E_{\boldsymbol{p}+\boldsymbol{k}}}}{1-f^0_{E_{\boldsymbol{p}}}} N^0_\omega$ which holds because the equilibrium distribution functions fulfill the equations of detailed balance Eq. (C.3).

4.4.1 Iterative solution

We find the solution of the coupled Boltzmann equations by solving Eq. (4.20) for g and iterating the resulting equation to self-consistency:

$$\frac{\boldsymbol{v}_{\boldsymbol{p}} \cdot e\boldsymbol{E}}{g^{n+1}_{\boldsymbol{p}}} = \iint\limits_{\boldsymbol{k}\ \hbar\omega} W^0_{\boldsymbol{k},\omega} \delta\left(E_{\boldsymbol{p}+\boldsymbol{k}} - E_{\boldsymbol{p}} - \hbar\omega\right) \frac{f^0_{E_{\boldsymbol{p}+\boldsymbol{k}}}}{f^0_{E_{\boldsymbol{p}}}} \left(N^0_\omega + 1\right) \left(1 - \frac{g^n_{\boldsymbol{p}+\boldsymbol{k}}}{g^n_{\boldsymbol{p}}} + \frac{G^n_{\boldsymbol{k},\omega}}{g^n_{\boldsymbol{p}}}\right) \tag{4.21}$$

Here, the n in g^n stands for the n^{th} step in the iteration process. G^n means that G was calculated with $g = g^n$ in Eq. (4.13). As the g and G depend on the magnitude of the applied field, one usually introduces "lifetimes"

$$\tau_{\boldsymbol{p}} = \frac{g_{\boldsymbol{p}}}{\boldsymbol{v}_{\boldsymbol{p}} \cdot e\boldsymbol{E}}, \tag{4.22}$$

which only depends on the direction of the field. We also define a corresponding lifetime

$$T_{\boldsymbol{k},\omega} = \frac{G_{\boldsymbol{k},\omega}}{\boldsymbol{v}_{\boldsymbol{k}} \cdot e\boldsymbol{E}} \tag{4.23}$$

for the non-equilibrium collective mode. The remaining equation can be expressed as a function of $\tau_{\boldsymbol{p}}$ only, and can be solved iteratively for the latter:

$$\begin{aligned}
&\frac{1}{\tau^{n+1}_{\boldsymbol{p}}} \\
&= \iint\limits_{\boldsymbol{k}\ \hbar\omega} W^0_{\boldsymbol{k},\omega} \delta\left(E_{\boldsymbol{p}+\boldsymbol{k}} - E_{\boldsymbol{p}} - \hbar\omega\right) \frac{f^0_{E_{\boldsymbol{p}+\boldsymbol{k}}}}{f^0_{E_{\boldsymbol{p}}}} \left(N^0_\omega + 1\right) \left[1 - \frac{\tau^n_{\boldsymbol{p}+\boldsymbol{k}}}{\tau^n_{\boldsymbol{p}}} \frac{\boldsymbol{v}_{\boldsymbol{p}+\boldsymbol{k}} \cdot \boldsymbol{E}}{\boldsymbol{v}_{\boldsymbol{p}} \cdot \boldsymbol{E}} + \frac{T_{\boldsymbol{k},\omega}(\tau^n_{\boldsymbol{p}}) \boldsymbol{v}_{\boldsymbol{k}} \cdot \boldsymbol{E}}{\tau^n_{\boldsymbol{p}}\ \boldsymbol{v}_{\boldsymbol{p}} \cdot \boldsymbol{E}}\right]
\end{aligned} \tag{4.24}$$

The self-consistent momentum relaxation time, $\tau_{\boldsymbol{p}} = \lim\limits_{n\to\infty} \tau^n_{\boldsymbol{p}}$ fulfills the equation

$$\frac{1}{\tau_{\boldsymbol{p}}} = \iint\limits_{\boldsymbol{k}\ \hbar\omega} W^0_{\boldsymbol{k},\omega} \delta\left(E_{\boldsymbol{p}+\boldsymbol{k}} - E_{\boldsymbol{p}} - \hbar\omega\right) \frac{f^0_{E_{\boldsymbol{p}+\boldsymbol{k}}}}{f^0_{E_{\boldsymbol{p}}}} \left(N^0_\omega + 1\right) \left[1 - \frac{\tau_{\boldsymbol{p}+\boldsymbol{k}}}{\tau_{\boldsymbol{p}}} \frac{\boldsymbol{v}_{\boldsymbol{p}+\boldsymbol{k}} \cdot \boldsymbol{E}}{\boldsymbol{v}_{\boldsymbol{p}} \cdot \boldsymbol{E}} + \frac{T_{\boldsymbol{k},\omega}(\tau_{\boldsymbol{p}}) \boldsymbol{v}_{\boldsymbol{k}} \cdot \boldsymbol{E}}{\tau_{\boldsymbol{p}}\ \boldsymbol{v}_{\boldsymbol{p}} \cdot \boldsymbol{E}}\right] \tag{4.25}$$

with

$$T_{\boldsymbol{k},\omega} = \frac{2\pi\nu_k}{\mathfrak{Im}\left(\varepsilon^{tot}_{\boldsymbol{k},\omega}\right)} \int\limits_{\boldsymbol{q}} \delta\left(E_{\boldsymbol{q}+\boldsymbol{k}} - E_{\boldsymbol{q}} - \hbar\omega\right) \left(f^0_{E_{\boldsymbol{q}}} - f^0_{E_{\boldsymbol{q}+\boldsymbol{k}}}\right) \frac{\left[\tau_{\boldsymbol{q}+\boldsymbol{k}} \boldsymbol{v}_{\boldsymbol{q}+\boldsymbol{k}} - \tau_{\boldsymbol{q}} \boldsymbol{v}_{\boldsymbol{q}}\right] \cdot \boldsymbol{E}}{\boldsymbol{v}_{\boldsymbol{p}} \cdot \boldsymbol{E}}. \tag{4.26}$$

In chapter 5 and chapter 6, we will evaluate the equation for semiconductors with spherical parabolic conduction bands. This lets us simplify the expression for τ_p significantly. For details on the evaluation of these and all following integrals for spherical parabolic bands, refer to appendix C.3 and C.4.

4.4.2 Initial step and the relaxation time approximation

The iteration processes converges the faster the better the initial step is. We use an approximate solution to the coupled Boltzmann equation as an initial "guess".

For this, we assume a parabolic band structure

$$E_{\boldsymbol{p}} = \frac{\hbar^2}{2} \boldsymbol{p} \cdot \mathbf{M}^{-1} \cdot \boldsymbol{p} \tag{4.27}$$

where $\mathbf{M}$ is the constant effective mass tensor. This means that the group velocity is

$$\boldsymbol{v}_{\boldsymbol{p}} = \hbar \boldsymbol{p} \cdot \mathbf{M}^{-1} \tag{4.28}$$

Let us furthermore set $\tau^0_{\boldsymbol{p}} = \tau^0$, a constant, for the initial step to the coupled mode solution Eq. (4.13). As this means that $g^0_{\boldsymbol{p}+\boldsymbol{k}} - g^0_{\boldsymbol{p}} = g^0_{\boldsymbol{k}}$, we find

$$G^0_{\boldsymbol{k},\omega} = g^0_{\boldsymbol{k}} \frac{\mathfrak{Im}\left(\varepsilon^c_{\boldsymbol{k},\omega}\right)}{\mathfrak{Im}\left(\varepsilon^{tot}_{\boldsymbol{k},\omega}\right)} \quad \text{or} \quad T^0_{\boldsymbol{k},\omega} = \tau^0 \frac{\mathfrak{Im}\left(\varepsilon^c_{\boldsymbol{k},\omega}\right)}{\mathfrak{Im}\left(\varepsilon^{tot}_{\boldsymbol{k},\omega}\right)}. \tag{4.29}$$

The superscripts "0" on τ, g, G and T mark the initial step $n = 0$ in the iteration process. Substituting Eq. (4.29) into Eq. (4.24) yields

$$\frac{1}{\tau^1_{\boldsymbol{p}}} = \iint_{\boldsymbol{k}\ \hbar\omega} W^0_{\boldsymbol{k},\omega} \frac{\mathfrak{Im}\left(\varepsilon^{ph}_{\boldsymbol{k},\omega}\right)}{\mathfrak{Im}\left(\varepsilon^{tot}_{\boldsymbol{k},\omega}\right)} \delta\left(E_{\boldsymbol{p}+\boldsymbol{k}} - E_{\boldsymbol{p}} - \hbar\omega\right) \frac{f^0_{E_{\boldsymbol{p}+\boldsymbol{k}}}}{f^0_{E_{\boldsymbol{p}}}} \left(N^0_\omega + 1\right) \left[1 - \frac{(\boldsymbol{p}+\boldsymbol{k}) \cdot \mathbf{M}^{-1} \cdot \boldsymbol{E}}{\boldsymbol{p} \cdot \mathbf{M}^{-1} \cdot \boldsymbol{E}}\right] \tag{4.30}$$

for the first step in the iteration. This expression takes the form of the relaxation time approximation, and $\tau^1_{\boldsymbol{p}}$ can be referred to as the relaxation time solution to the coupled Boltzmann equation. It is important to understand that our fully self-consistent solution to Eq. (4.24) goes beyond the relaxation time approximation. The non-relaxation time $\tau_{\boldsymbol{p}}$ from Eq. (4.22) are sometimes called "effective momentum relaxation times" [26] to stress this point. We will demonstrate the difference between the fully self-consistent effective momentum relaxation time and the momentum relaxation time in section 5.3 and in section 6.4.

Quasi-elastic approximation It is clear that the square bracket in Eq. (4.30) can become negative for certain $\boldsymbol{p}$, $\boldsymbol{k}$ and ω. If these negative values have enough weight, $\tau^1_{\boldsymbol{p}}$ itself can become negative, which is non-physical. If one makes the approximation of quasi-elastic scattering $|\boldsymbol{p}+\boldsymbol{k}| \approx p$ in the square bracket in Eq. (4.30), however little this might be justified physically, this problem is circumvented, see appendix C.3.

$$\frac{1}{\tau^1_{\boldsymbol{p}}} = \iint\limits_{\boldsymbol{k}\ \hbar\omega} W^0_{\boldsymbol{k},\omega} \frac{\mathfrak{Im}\left(\varepsilon^{ph}_{\boldsymbol{k},\omega}\right)}{\mathfrak{Im}\left(\varepsilon^{tot}_{\boldsymbol{k},\omega}\right)} \delta\left(E_{\boldsymbol{p}+\boldsymbol{k}} - E_{\boldsymbol{p}} - \hbar\omega\right) \frac{f^0_{E_{\boldsymbol{p}+\boldsymbol{k}}}}{f^0_{E_{\boldsymbol{p}}}} \left(N^0_\omega + 1\right) \left[1 - \frac{\frac{\boldsymbol{k}+\boldsymbol{p}}{|\boldsymbol{k}+\boldsymbol{p}|} \cdot \mathbf{M}^{-1} \cdot \boldsymbol{E}}{\frac{\boldsymbol{p}}{p} \cdot \mathbf{M}^{-1} \cdot \boldsymbol{E}}\right] \tag{4.31}$$

In all calculations of the relaxation time $\tau^1_{\boldsymbol{p}}$ in the results of chapter 5 and chapter 6, we use the quasi-elastic approximation Eq. (4.31).

4.4.3 Phonon dissipation weight factor

The scattering rate $W^0_{\boldsymbol{k},\omega}$ in Eq. (4.30) and Eq. (4.31) is multiplied by the scalar factor

$$C_{\boldsymbol{k},\omega} = \frac{\mathfrak{Im}\left(\varepsilon^{ph}_{\boldsymbol{k},\omega}\right)}{\mathfrak{Im}\left(\varepsilon^{tot}_{\boldsymbol{k},\omega}\right)}, \tag{4.32}$$

which we will call the phonon dissipation weight factor. In a non-polar material, carrier–coupled mode scattering reduces to carrier–plasmon scattering. This solution has $C_{\boldsymbol{k},\omega} \equiv 0$, giving an infinite relaxation time. We discuss this limit in detail in subsubsection 4.4.4.1. In an undoped semiconductor with low intrinsic carrier concentration, Landau damping is weak compared to the anharmonic decay rate of the optical phonon, the drag term G vanishes, and only the carrier–LO-phonon scattering need be considered. This solution has $C_{\boldsymbol{k},\omega} \equiv 1$, reducing Eq. (4.30) to the usual expression for the relaxation time for carrier–phonon scattering (Discussed in subsubsection 4.4.4.3).

We call $C_{\boldsymbol{k},\omega}$ the phonon dissipation weight factor, because it equals one when the coupled excitations decay infinitely fast, as in the usual approximate treatment of carrier–phonon scattering [94] and zero when the coupled excitations are infinitely long-lived, as in the approximate treatment of carrier–carrier scattering [25]. In general, the intermediate decay rate of the coupled excitations at given wave vectors and frequencies will result in

$$0 \leq C_{\boldsymbol{k},\omega} \leq 1. \tag{4.33}$$

This mapping of the decay mechanism onto a scale between 0 and 1 makes the phonon dissipation factor $C_{\boldsymbol{k},\omega}$ useful for developing an intuition for the character of the coupled modes. Moreover, $C_{\boldsymbol{k},\omega}$ can be evaluated analytically within the temperature dependent RPA.

We also define an effective scattering rate

$$W^{0,eff}_{\boldsymbol{k},\omega} = C_{\boldsymbol{k},\omega} W^{0}_{\boldsymbol{k},\omega}, \tag{4.34}$$

which will be illustrated in section 5.1. Through the phonon dissipation weight factor, the effective scattering rate reflects not only how strongly a coupled mode scatters carriers, but also how long-lived it is. Therefore, it is a better measure of momentum relaxation than the scattering rate alone.

4.4.4 Solution of the coupled Boltzmann equation in limiting cases

As our approach treats LO-phonons and plasmons on an equal footing, it contains carrier–carrier scattering and carrier–LO-phonon scattering as limiting cases. In this section, we discuss these limiting cases in some detail.

4.4.4.1 Infinite mobility in the absence of anharmonic decay

In the absence of an external field, and if the collective excitations are infinitely long-lived, any set of g and G satisfying

$$g_{\boldsymbol{p}+\boldsymbol{k}} - g_{\boldsymbol{p}} - G_{\boldsymbol{k},\omega} = 0 \tag{4.35}$$

are a solution to the coupled system of Boltzmann equations Eq. (4.20) and Eq. (4.12).

Peierls discusses different sets of g and G which fulfill the above in [49]. With constant relaxation times Eq. (4.22) and Eq. (4.23)

$$\tau_{\boldsymbol{p}+\boldsymbol{k}} \equiv \tau_{\boldsymbol{p}} \equiv T_{\boldsymbol{k},\omega} \equiv \tau, \tag{4.36}$$

Eq. (4.35) becomes

$$\boldsymbol{v}_{\boldsymbol{p}+\boldsymbol{k}} - \boldsymbol{v}_{\boldsymbol{p}} - \boldsymbol{v}_{\boldsymbol{k}} = 0 \tag{4.37}$$

for any field direction. If the band structure is parabolic Eq. (4.27) the group velocity Eq. (4.28) fulfills Eq. (4.37). The reason Eq. (4.35) is fulfilled for a parabolic bandstructure is the conservation of quasi-momentum. In particular, it is important that no Umklapp processes occur, i.e., no momentum is transferred to the lattice:

$$\boldsymbol{p}' = \boldsymbol{p} + \boldsymbol{k} \tag{4.38}$$

If all wave vectors need to be small compared to the dimensions of the Brillouin zone, the absence of Umklapp processes is a reasonable assumption.

This solution allows an electric current to flow without an applied external field, which means infinite carrier mobility. Equivalently, one can see that the momentum relaxation time has to be infinite directly by substituting the phonon dissipation weight factor $C_{\boldsymbol{k},\omega} \equiv 0$ into Eq. (4.30).

This shows that in materials with a parabolic band structure, any relaxation time solution to the coupled first order Boltzmann equation yields infinite mobility as long as the collective excitations are infinitely long-lived.

Drag term The solution to Eq. (4.35) requires that

$$G_{\boldsymbol{k}} = g_{\boldsymbol{k}} = e\tau \boldsymbol{v}_{\boldsymbol{k}} \cdot \boldsymbol{E}, \tag{4.39}$$

that is, the collective excitations are dragged out of equilibrium by their interaction with the carriers. When the collective excitations are phonons, this term is known to contribute to the lattice thermal conductivity [25], and the Seebeck coefficient [50] , and is referred to as "phonon drag". We will discuss the drag term in more detail in the following section.

4.4.4.2 Carrier-carrier scattering vs carrier–plasmon scattering

When the collective modes are infinitely long-lived, i.e, $\tau_{\boldsymbol{k},\omega} \to \infty$, G (Eq. (4.3)) is determined by carrier quantities alone:

$$G_{\boldsymbol{k},\omega} = \frac{\int\limits_{\boldsymbol{p}} \delta\left(E_{\boldsymbol{p}+\boldsymbol{k}} - E_{\boldsymbol{p}} - \hbar\omega\right)\left(f^0_{E_{\boldsymbol{p}}} - f^0_{E_{\boldsymbol{p}+\boldsymbol{k}}}\right)\left(g_{\boldsymbol{p}+\boldsymbol{k}} - g_{\boldsymbol{p}}\right)}{\int\limits_{\boldsymbol{p}} \delta\left(E_{\boldsymbol{p}+\boldsymbol{k}} - E_{\boldsymbol{p}} - \hbar\omega\right)\left(f^0_{E_{\boldsymbol{p}}} - f^0_{E_{\boldsymbol{p}+\boldsymbol{k}}}\right)} \tag{4.40}$$

and we see that $G_{\boldsymbol{k},\omega} = g_{\boldsymbol{k}}$ if $g_{\boldsymbol{p}+\boldsymbol{k}} - g_{\boldsymbol{p}} = g_{\boldsymbol{k}}$, i.e., in a parabolic band without Umklapp processes, as discussed above. See Eq. (4.39).

Substituting G into the carrier–plasmon collision term to first order, Eq. (4.19) yields the first order carrier–carrier collision term (see [49, chapter 6.5], [48, appendix]). We demonstrate this explicitly in appendix C.2. This shows that our description of carrier–plasmon scattering with two coupled Boltzmann equations, one for the carriers and one for the bosonic plasmons, and the description with one Boltzmann equation for carrier–carrier scattering [49, chapter 6.5] are equivalent.

4.4.4.3 Carrier–phonon scattering

Carrier–phonon scattering is the other limit of our approach. Here, it is commonly and often implicitly assumed that $G = 0$, i.e., that the phonon distribution is the

Bose-Einstein distribution function. The physics behind this is that the phonons are taken to equilibrate, through phonon–phonon interaction, on a faster time-scale than through carrier–phonon interactions.

We will illustrate this in the relaxation time approximation with parabolic bands. Eq. (4.29) states the momentum relaxation time for the phonons, T is much smaller than the momentum relaxation time for the carriers τ,

$$T^0_{\boldsymbol{k},\omega} = \tau^0 \frac{\mathfrak{Im}\left(\varepsilon^c_{\boldsymbol{k},\omega}\right)}{\mathfrak{Im}\left(\varepsilon^{tot}_{\boldsymbol{k},\omega}\right)} \ll \tau^0 \quad \text{or} \quad G_{\boldsymbol{k},\omega} \ll g_{\boldsymbol{k}} \tag{4.41}$$

if $\mathfrak{Im}\left(\varepsilon^c_{\boldsymbol{k},\omega}\right) \ll \mathfrak{Im}\left(\varepsilon^{ph}_{\boldsymbol{k},\omega}\right)$ As we have assumed that $\frac{\mathfrak{Im}\left(\varepsilon^c_{\boldsymbol{k},\omega}\right)}{\mathfrak{Im}\left(\varepsilon^{ph}_{\boldsymbol{k},\omega}\right)}$ determines the ratio of the lifetime of phonon modes due to anharmonic decay compared to decay into electron-hole pairs, Eq. (4.9), this is the same as saying the phonon modes equilibrate too fast due to interaction with other phonons to contribute to phonon drag.

The momentum relaxation time solution for carrier–phonon scattering, in the quasi-elastic limit, and in parabolic bands, becomes

$$\frac{1}{\tau^1_{\boldsymbol{p}}} = \iint_{\boldsymbol{k}\ \hbar\omega} W^0_\omega \delta\left(E_{\boldsymbol{p}+\boldsymbol{k}} - E_{\boldsymbol{p}} - \hbar\omega\right) \frac{f^0_{E_{\boldsymbol{p}+\boldsymbol{k}}}}{f^0_{E_{\boldsymbol{p}}}} \left(N^0_\omega + 1\right) \left[1 - \frac{\frac{\boldsymbol{k}+\boldsymbol{p}}{|\boldsymbol{k}+\boldsymbol{p}|} \cdot \mathbf{M}^{-1} \cdot \boldsymbol{E}}{\frac{\boldsymbol{p}}{p} \cdot \mathbf{M}^{-1} \cdot \boldsymbol{E}}\right] \tag{4.42}$$

We give this expression explicitly, because it is often used for the electron-phonon momentum relaxation time, often with the additional assumption of spherical bands. The scattering rate for carrier–LO-phonon scattering Eq. (3.22) has been discussed already in section 3.1.

For the fully self-consistent carrier–phonon effective momentum relaxation rate, Eq. (4.41) means setting $G_{\boldsymbol{k},\omega} \equiv 0$ in Eq. (4.20) or $T_{\boldsymbol{k},\omega} \equiv 0$ in Eq. (4.24), yielding the expression used in the literature.[94, 95, 96]

$$\frac{1}{\tau^{n+1}_{\boldsymbol{p}}} = \iint_{\boldsymbol{k}\ \hbar\omega} W^0_{\boldsymbol{k},\omega} \delta\left(E_{\boldsymbol{p}+\boldsymbol{k}} - E_{\boldsymbol{p}} - \hbar\omega\right) \frac{f^0_{E_{\boldsymbol{p}+\boldsymbol{k}}}}{f^0_{E_{\boldsymbol{p}}}} \left(N^0_\omega + 1\right) \left[1 - \frac{\tau^n_{\boldsymbol{p}+\boldsymbol{k}}}{\tau^n_{\boldsymbol{p}}} \frac{\boldsymbol{v}_{\boldsymbol{p}+\boldsymbol{k}} \cdot \boldsymbol{E}}{\boldsymbol{v}_{\boldsymbol{p}} \cdot \boldsymbol{E}}\right] \tag{4.43}$$

We will discuss the differences between the effective momentum relaxation rate for carrier–LO-phonon scattering and that for carrier–coupled mode scattering in chapter 5 and chapter 6.

Chapter 5

Coupled collective mode scattering in bulk polar semiconductors

The formalism developed in chapter 4 is applicable to polar semiconductors in general. The level of approximation manifests itself in the expressions used for the dielectric functions. In principle, one could use expressions for the carrier and lattice dielectric functions extracted from electron and phonon band structure calculations. In practice, we expect our assumptions to work best, and to be most consistent with each other, for screened electron–LO-phonon scattering in semiconductors with a parabolic conduction band: We consider n-type semiconductors, because conduction bands are usually better described with parabolic approximations than valence bands [3]. We take the doping concentrations to be low enough that higher bands are not significantly occupied and that the conduction band can be described as parabolic. Consequently, we can use model carrier dielectric functions for parabolic bands [41, 59]. Moreover, the wave vectors at the bottom of the conduction band relevant for intra-valley scattering will be small on the scale of the Brillouin zone, so that the assumption that the scattering rate only depends on the transferred wave vector and not the initial or final wave vector should be good. This also justifies the use of the long wavelength limit of the lattice dielectric function. All these approximations are common for the calculations of electron–LO-phonon scattering in bulk semiconductors, see, e.g., [94]. Our phenomenological account of the lifetime of the coupled plasmon–LO-phonon modes is new, but nontheless consistent with previous treatments of electron–LO-phonon scattering and electron-electron scattering in the appropriate limits (See appendix 5.2 and [47, 48, 97, 94]).

In section 5.1 we illustrate coupled collective mode scattering in GaAs with the help of carrier-coupled mode scattering rates. In section 5.2, we connect back to important

limiting cases of coupled collective mode scattering, which were discussed in Appendix B. In section 5.3, we discuss the effect of carrier collective mode scattering on the effective momentum relaxation times and carrier mobilities in GaAs. In section 5.4, we explore how the screened LO-phonon limited mobility depends on material parameters, by calculating mobilities for a selection of polar semiconductors.

5.1 Scattering rate, effective scattering rate and the phonon dissipation weight factor

5.1.1 Phonon dissipation weight

The phonon dissipation weight factor Eq. (4.32) (See Fig. 5.1(b) at zero and (e) at room temperature) introduced in subsection 4.4.3, which provides a measure of the decay mechanism of the coupled modes, can be evaluated analytically with the carrier dielectric function discussed in section 2.2 and the lattice dielectric function Eq. (2.11). Using the analytic expression Eq. (2.59), we find the phonon dissipation weight factor

$$C_{K,\Omega} = \left\{ 1+ \frac{2\left[\left(\Omega_{TO}^2-\Omega^2\right)^2+\Omega^2\Gamma^2\right]}{E_F\beta k_F a_0^*\left(\Omega_{LO}^2-\Omega_{TO}^2\right)\Gamma\Omega K^3}\ln\left[\frac{1+e^{\beta\tilde{\mu}-.5E_F\beta(\Omega/K-K)^2}}{1+e^{\beta\tilde{\mu}-.5E_F\beta(\Omega/K+K)^2}}\right]\right\}^{-1} \quad (5.1)$$

where the capital letters all stand for dimensionless quantities, defined by the same lower case letter scaled by the Fermi wave vector or energy, cf. Eq. (2.43). $a_0^* = \frac{\varepsilon^\infty \hbar^2}{m^* e^2}$ is the effective Bohr radius with the effective mass m^*. Note that the phonon dissipation factor only makes sense when the damping of the optical phonons is finite, i.e., $\Gamma > 0$.

In the zero temperature limit, $\mathfrak{Im}(\varepsilon^c)$ vanishes outside the single-pair excitation region (See the discussion in section 2.2). Consequently, $C_{k,\omega}^{T=0} = 1$ everywhere except the single pair excitation region, see Fig. 5.1b. As the imaginary part of the carrier dielectric function is antisymmetric in K, $C_{K,\Omega} \to 1$ as $K \to 0$, see Fig. 5.1(b) and (e). This ensures that our effective scattering rate (Fig. 5.1c and f), and the scattering rate (Fig. 5.1a and d) have the same long-wavelength behavior.

5.1.2 Effective scattering rate

The effective scattering rate Eq. (4.34) governs the momentum relaxation time τ_p^1 from Eq. (4.30). As plotted in Fig. 5.1c for $T = 0$ and (f) for $T = 300K$, the effective scattering rate is the product of the scattering rate (Fig. 5.1a) and the phonon dissipation weight factor (Fig. 5.1b). Consequently, the phonon dissipation weight factor, which is small throughout the single pair excitation regime (except for

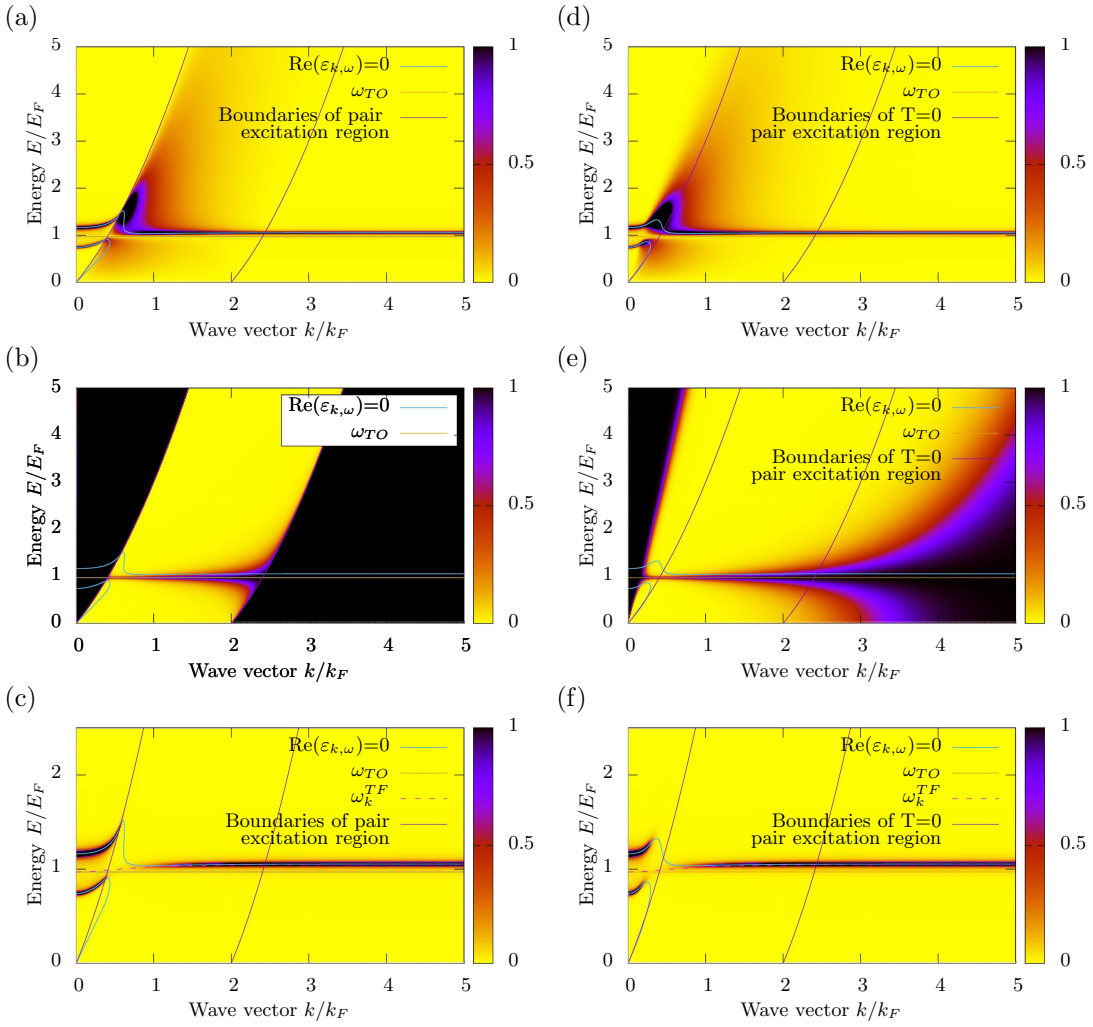

Figure 5.1: (a) and (d) $\mathfrak{Im}\left(-\frac{\varepsilon^{\infty}}{\varepsilon^{tot}_{k,\omega}}\right) \propto W^0_{k,\omega}/\nu_k$, the scattering rate Eq. (3.4), (b) and (e) phonon dissipation weight factor $C_{k,\omega}$, Eq. (4.32), and (c) and (f) $C_{k,\omega}\mathfrak{Im}\left(-\frac{\varepsilon^{\infty}}{\varepsilon^{tot}_{k,\omega}}\right) \propto W^{0,eff}_{k,\omega}/\nu_k$ effective scattering rate Eq. (4.34) as a function of wave vector k and energy $E = \hbar\omega$, for GaAs at $n = 5 \times 10^{17} cm^{-3}$. The temperature is $T = 0K$ (a-c) and $T = 300K$ (d-f)

frequencies close to ω_{TO}) suppresses the large, dispersive features seen in the single pair excitation region in Fig. 5.1(a) and (d). As we can see in Fig. 2.9(a) and (d), this blurred feature is characteristic of electron-plasmon scattering. We can ascribe it to Landau damping in the classical picture [2], or to the excitation of single pairs of quasi-electrons and holes in the Fermi sea in the quantum mechanical picture [32, 63] (See appendix A). Crucially for our purpose, these features characterize scattering of the carriers amongst themselves, which does not contribute to momentum relaxation.

Consequently, the effective scattering rate is only, if at all, significant close to the zeros of the real part of the dielectric function (Fig. 5.1(c) and (f)).

5.2 Treatment of carrier–coupled mode scattering in limiting cases

5.2.1 Recovery of descriptions in the literature as limiting cases of our approach

In this section, we show that the method presented in chapter 4 contains previous descriptions of the long-wavelength-limit of carrier–coupled mode scattering [26, 36, 30] as its long-wavelength limit. We also demonstrate how the approximate treatment of Landau damping by Fischetti et al. [1] compares to our approach, which has Landau damping built in. We discuss these limits in the three-dimensional case of bulk polar semiconductors, rather than the 2d case (interface or remote phonon scattering) because its comparative simplicity gives a clearer view of the basic physics involved.

Long wavelength limit As mentioned in subsection 5.1.1, the phonon dissipation weight factor goes to 1 in the long-wavelength limit, so that the scattering rate and the effective scattering rate show the same long-wavelength behavior. Consequently, we only have the behavior of the scattering rate as $k \to 0$ left to consider. If the lattice dielectric function is undamped, the scattering rate follows Eq. (3.32) and can be described through a discrete set of F_k^i. We discuss these scattering strengths F_k^i Eq. (3.34) in the long wavelength limit for carrier LO-phonon scattering and carrier-coupled mode scattering in Appendix B. They can be derived in several different ways, and we show, that they lead to equivalent expressions to Eq. (3.33).

Static screening Carrier scattering with coupled plasmon-LO-phonon modes is sometimes described as statically screened LO-phonon scattering, especially when the carrier concentration is high. The assumption behind static screening is that for high carrier concentrations, optical phonon frequencies are very small compared to the plasma frequencies $\omega_{LO} \ll \omega_P$. Consequently, the carrier dielectric function might as well be approximated by its zero frequency value on a scale determined by the optical phonon frequencies.

We obtain the static screening limit from our expressions by setting $\omega = 0$ in the carrier dielectric function $\varepsilon^c_{k,\omega=0}$. Obviously, we have to retain the frequency dependence in the lattice dielectric function. As the static, i.e. $\omega = 0$ carrier dielectric function is real (cf. section 2.2), the phonon dissipation weight factor equals one, and we have the same scenario as in the long wavelength limit, insofar as the effective scattering rate and the scattering rate are identical.

In the case where the lattice dielectric function is undamped, we can describe static

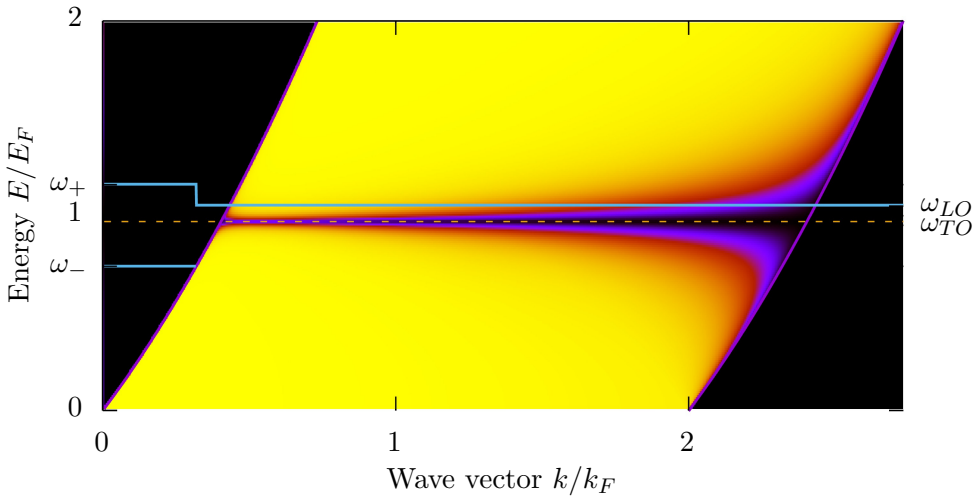

Figure 5.2: Phonon dissipation factor $C_{k,\omega}$, Eq. (4.32), for GaAs at $T = 0$, $n = 5 \times 10^{17} cm^{-3}$ as a function of wave vector k and energy $E = \hbar\omega$. The legend for the color plot is the same as in Fig. 5.1. Also shown are the coupled modes in the approximation by Fischetti et al. [1], subsection 3.3.1.

screening by a discrete scattering strength, Eq. (3.32). We give the scattering strength F_k^{TF}, Eq. (3.39), for static screening in the Thomas-Fermi limit in subsubsection 3.1.3.2.

Fischetti et al. approximate treatment of Landau damping The long wavelength approximation discussed above gives simple convenient expressions, but it neglects the dispersion and the damping of the modes. The latter issue is addressed by Fischetti et al. [1]. Their approximation was developed for two-dimensional structures, but it can be applied to three-dimensional cases. They approximately treat the plasma modes as damped out entirely as soon as they enter the single pair excitation regime in the degenerate limit. We discussed this in detail in subsection 3.3.1.

In Fig. 5.2, we plot the coupled modes in this approximation for GaAs with an electron density of $n = 5 \times 10^{17} cm^{-3}$, together with the phonon dissipation factor at zero temperature, $C_{k,\omega}^{T=0}$. $C_{k,\omega}$=1 on the long-wavelength side of the single-pair excitation limit, indicating that there, the carrier-coupled mode scattering is fully dissipative, just as for electron-phonon scattering. Fischetti's approximation incorporates this, only the cutoff for the single-pair excitation regime is chosen somewhat more simply. Hence, it is the only approximation discussed which reflects the importance of the lifetime of the coupled modes for the scattering rate, although indirectly. Fischetti's approximation, however, does not capture the situation inside the single pair excitation region accurately. We will discuss this in more detail in the

following section.

5.2.2 Discretization of continuous effective scattering rate

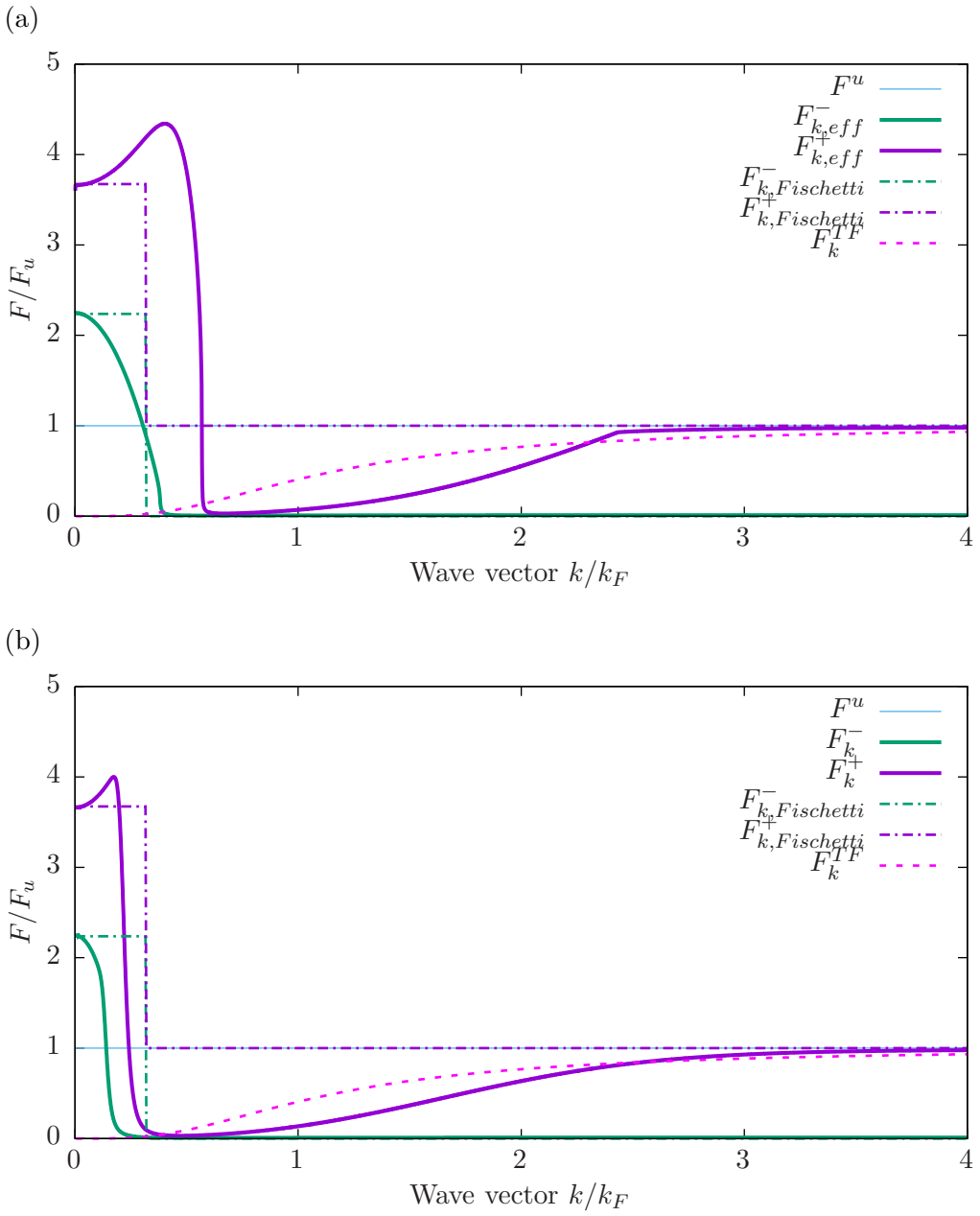

Figure 5.3: Discretized scattering strengths Eq. (5.2) and scattering strengths from subsection 3.3.1 for $n = 5 \times 10^{17} cm^{-3}$ as a function of wave vector k, (a) at zero temperature and (b) at room temperature. All scattering strengths are plotted as multiples of the carrier-LO-phonon scattering strength F^u, Eq. (3.21).

In order to compare the limiting cases from appendix B with the relaxation time approximation to the full solution from subsection 4.4.2 on the level of the scattering

strengths, we define the discretized effective scattering strength

$$F_k^{\pm} = \frac{\hbar}{2\pi} \int_{\omega_k^{\pm}-\Delta\omega}^{\omega_k^{\pm}+\Delta\omega} \mathrm{d}\omega' \, W_{\boldsymbol{k},\omega}^{0,eff} \tag{5.2}$$

with $W_{\boldsymbol{k},\omega}^{0,eff}$ from Eq. (4.34). The exact width $\Delta\omega$ of the integration interval is not crucially important, as the effective scattering rate has two well-defined peaks –see Fig. 5.1(c) and (f) – but it must be large enough to capture each peak. Fig. 5.3 shows the discretized scattering strengths calculated in this manner. Also shown are F^u Eq. (3.21), F_k^{TF} Eq. (3.39) , and $F_{k,Fischetti}^{\pm}$ Eq. (3.71).

$F_{Fischetti}^{+}$ is equal to F^u throughout the single pair excitation regime, while F_k^{+} is very small at the low k side of the single pair excitation region and only grows towards F^u as it leaves the single pair excitation region again. The Thomas-Fermi scattering strength F_k^{TF}, however, shows good qualitative agreement with the $F^{\pm}$ in the single particle excitation regime.

An approximation similar to Fischetti et al. [1], but with the scattering strength inside the single pair excitation region described by F_k^{TF} Eq. (3.39) rather than F^u Eq. (3.21), would improve the qualitative behavior while retaining much of the simplicity of the approximation. The resulting scattering strengths would be defined as

$$F_{k,Fischetti}^{\pm} = \begin{cases} F^{\pm} & k \leq k_c \\ F_k^{TF} & k > k_c \text{ and } \omega_{\pm} \neq \omega_c \\ 0 & \text{else} \, , \end{cases} \tag{5.3}$$

similar to Eq. (3.71).

5.3 Carrier momentum relaxation and mobility in bulk GaAs

In this section, we calculate the effective momentum relaxation time and mobility due to carrier-collective mode scattering in bulk GaAs. All relevant parameters are in Tab. 2.1. We compare these results for unscreened and statically screened carrier–LO-phonon scattering. We also investigate what difference it makes to use the relaxation time approximation (RTA) or the fully self-consitent solution to the coupled Boltzmann equations. We conclude this section with a calculation of the total carrier mobility in GaAs, which can be used for a comparison with experiment.

5.3.1 Notation

In chapter 4, we derived the effective momentum relaxation time Eq. (4.25) from a self-consistent solution to the coupled Boltzmann equations for the carriers and coupled modes. In appendix C.3, we give the explicit expression for the effective momentum relaxation time Eq. (C.42) for carrier–coupled collective mode scattering, in materials with a spherical, parabolic conduction band.

- We call the τ_p satisfying Eq. (4.25) with the scattering rate Eq. (3.4) the dynamically screened effective momentum relaxation time. This calculation is our best description of carrier–coupled mode scattering, and we will judge all other approximate treatments of carrier–coupled mode scattering on its accordance with this one.
- To stress the importance of the drag term on the momentum relaxation time, we calculate the momentum relaxation time without the drag term, i.e., $T_{\boldsymbol{k},\omega} = 0$ in Eq. (4.25). This will be tagged “dynamical screening no drag”.
- As discussed in subsubsection 4.4.4.3, carrier–LO-phonon scattering yields an effective momentum relaxation time Eq. (4.43) without a drag term. The difference to dynamical screening without drag is that here, we use the electron-LO-phonon scattering rate $W^0_{\boldsymbol{k},\omega}$, Eq. (3.22) We tag this with the term “unscreened” in the figures below.

On top of the self-consistent effective momentum relaxation times discussed above, we also calculate actual relaxation times. All these will receive the tag "RTA".

- The dynamically screening momentum relaxation time is calculated from Eq. (4.31) with the scattering rate Eq. (3.4)
- The unscreened momentum relaxation time "unscreened RTA" is calculated from Eq. (4.42), with the scattering rate Eq. (3.22)
- We also calculate the momentum relaxation time for carrier–LO-phonon scattering, when screening is taken into account in the Thomas-Fermi model. Therefore we plug the scattering rate Eq. (3.32) with the Thomas-Fermi scattering strength Eq. (3.39) into equation Eq. (4.42). This is tagged “Thomas-Fermi RTA”.
- We calculate the momentum relaxation time for the Fischetti et al. approximation discussed in subsection 3.3.1 and section 5.2.1. Here, we plug the scattering rate Eq. (3.32) with the scattering strength Eq. (3.71) into equation Eq. (4.42). This is tagged “Fischetti RTA”.
- Finally, we calculate the momentum relaxation time for the mixture between the Fischetti et al. approximation and Thomas-Fermi screening which we

defined in section 5.2. Here, we plug the scattering rate Eq. (3.32) with the scattering strength Eq. (5.3) into equation Eq. (4.42). We will tag this "Fischetti-Thomas-Fermi RTA".

For the explicit evaluation of these relaxation times in a spherical, parabolic conduction band, see Eq. (C.44) in appendix C.3.

We calculate the carrier drift mobility, the proportionality factor between the applied external field and the velocity component in field direction using

$$\mu = \frac{e}{m^*} \frac{\int_0^\infty \mathrm{d}p\, p^3 \left(\frac{\partial}{\partial p} f_p^0\right) \tau_p}{\int_0^\infty \mathrm{d}p\, p^3 \left(\frac{\partial}{\partial p} f_p^0\right)}, \tag{5.4}$$

which holds if all the carriers are in a spherical parabolic conduction band, e.g., [98].

Here f^0 is the Fermi-Dirac distribution function. We do not assume that f^0 is a Boltzmann distribution, as is often done [3, 26]. We give a derivation of Eq. (5.4) in appendix C.5, including its corresponding expression in the Maxwell-Boltzmann limit. We obtain mobilities in the different approximations discussed above by substituting the corresponding momentum relaxation times into Eq. (5.4).

The derivative of the Fermi-Dirac distribution function is shown in the momentum relaxation time plots Fig. 5.4 and Fig. 5.5, to give an idea in what energy range τ contributes most to mobility.

5.3.2 Iteration of momentum relaxation time to self-consistency

It is evident that Eq. (4.25) in general cannot be solved analytically for τ_p, because it involves both τ_p and integrals over τ at different wave vectors. As mentioned in chapter 4, we therefore find a solution iteratively. Specifically, we write Eq. (4.25) as

$$\frac{1}{\tau_{\boldsymbol{p}}} = R^1_{\boldsymbol{p}} - R^2_{\boldsymbol{p}}\{\tau\}/\tau_{\boldsymbol{p}} + R^3_{\boldsymbol{p}}\{\tau\}/\tau_{\boldsymbol{p}} \tag{5.5}$$

where $R^1_{\boldsymbol{p}}$, $R^2_{\boldsymbol{p}}\{\tau\}$ and $R^3_{\boldsymbol{p}}\{\tau\}$ are the first, second and third terms in Eq. (4.25) multiplied by $\tau_{\boldsymbol{p}}$. The curly braces indicate that $R^2_{\boldsymbol{p}}\{\tau\}$ and $R^3_{\boldsymbol{p}}\{\tau\}$ are functionals of $\tau_{\boldsymbol{p}}$.

In principle, the iteration of Eq. (4.25) to self-consistency can be carried out as indicated in Eq. (4.24), i.e.,

$$\frac{1}{\tau^{n+1}_{\boldsymbol{p}}} = R^1_{\boldsymbol{p}} - R^2_{\boldsymbol{p}}\{\tau^n\}/\tau^n_{\boldsymbol{p}} + R^3_{\boldsymbol{p}}\{\tau^n\}/\tau^n_{\boldsymbol{p}} \tag{5.6}$$

However, we have found that the iteration procedure Eq. (5.6) is not very numerically

stable for the examples discussed in this thesis. Fortunately, we have found that rewriting Eq. (5.5) as

$$\tau_{\boldsymbol{p}} = \frac{1}{R^1_{\boldsymbol{p}}} \left(1 + R^2_{\boldsymbol{p}}\{\tau\} - R^3_{\boldsymbol{p}}\{\tau\}\right) \tag{5.7}$$

yields an iteration procedure

$$\tau^{n+1}_{\boldsymbol{p}} = \frac{1}{R^1_{\boldsymbol{p}}} \left(1 + R^2_{\boldsymbol{p}}\{\tau^n\} - R^3_{\boldsymbol{p}}\{\tau^n\}\right), \tag{5.8}$$

which is very numerically stable even for undamped iteration. If $\tau^n_{\boldsymbol{p}} \to \tau_{\boldsymbol{p}}$, it will fulfill Eq. (4.25) – and the equivalent expressions Eq. (5.7) and Eq. (5.5) .

Fig. 5.4 shows how the momentum relaxation time changes as it is iterated towards self-consistency for dynamically screened LO-phonon scattering. The initial iteration τ^1 is the RTA and all subsequent ones are calculated from Eq. (5.8).

The examples are for GaAs with $n = 5 \times 10^{19} cm^{-3}$, $n = 5 \times 10^{17} cm^{-3}$ and $n = 5 \times 10^{15} cm^{-3}$ at $T = 300K$, corresponding to the highly degenerate limit, the concentration where the optical phonon frequencies are close to the plasma frequency, and the classical limit, respectively. We can see that for the first few steps in the iteration, there are notable differences between τ^n and τ^{n+1}, but these differences become smaller as the iteration converges. We also observe that the iteration process smooths the curve, and makes it flatter.

When comparing the iteration steps for different carrier concentrations, we have to keep in mind that the energy axis is scaled with the Fermi energy, which is different for each carrier concentration. Therefore $\frac{\partial}{\partial \boldsymbol{p}} f^0_{E_{\boldsymbol{p}}}$ is only significant close to the Fermi energy for $n = 5 \times 10^{19} cm^{-3}$, while it is broadened for lower carrier concentrations, and a larger energy range is important for mobility calculations. We mark the LO-phonon energy $\hbar\omega_{LO}$ in each of the plots for orientation. We see that for $n = 5 \times 10^{15} cm^{-3}$ and $n = 5 \times 10^{17} cm^{-3}$, the step at the LO-phonon energy is clearly visible in the initial iteration and flattens out for subsequent ones. This also occurs at $n = 5 \times 10^{19} cm^{-3}$, but is hardly visible, because $\hbar\omega_{LO} \ll E_F$.

The smoothing of the self-consistent momentum relaxation time does not happen throughout the energy range in the case of unscreened LO-phonon scattering, which is discussed in appendix C.3.2.1. Instead, the unscreened effective momentum relaxation times in Fig. 5.5, and Fig. C.4 show sharp steps at multiples of the LO-phonon energy for carrier energies small compared to the thermal energy [94].

We can gain operational understanding of the structure of the curve by considering how the carrier–LO-phonon momentum relaxation time Eq. (4.43) is iterated to self-consistency. This calculation can be carried out analytically, and the relevant expressions are given in appendix C.3.2.1. We find that the iteration relation links the momentum relaxation τ_E at one energy, and $\tau_{\sqrt{E+\hbar\omega_{LO}}}$, at the energy plus or minus

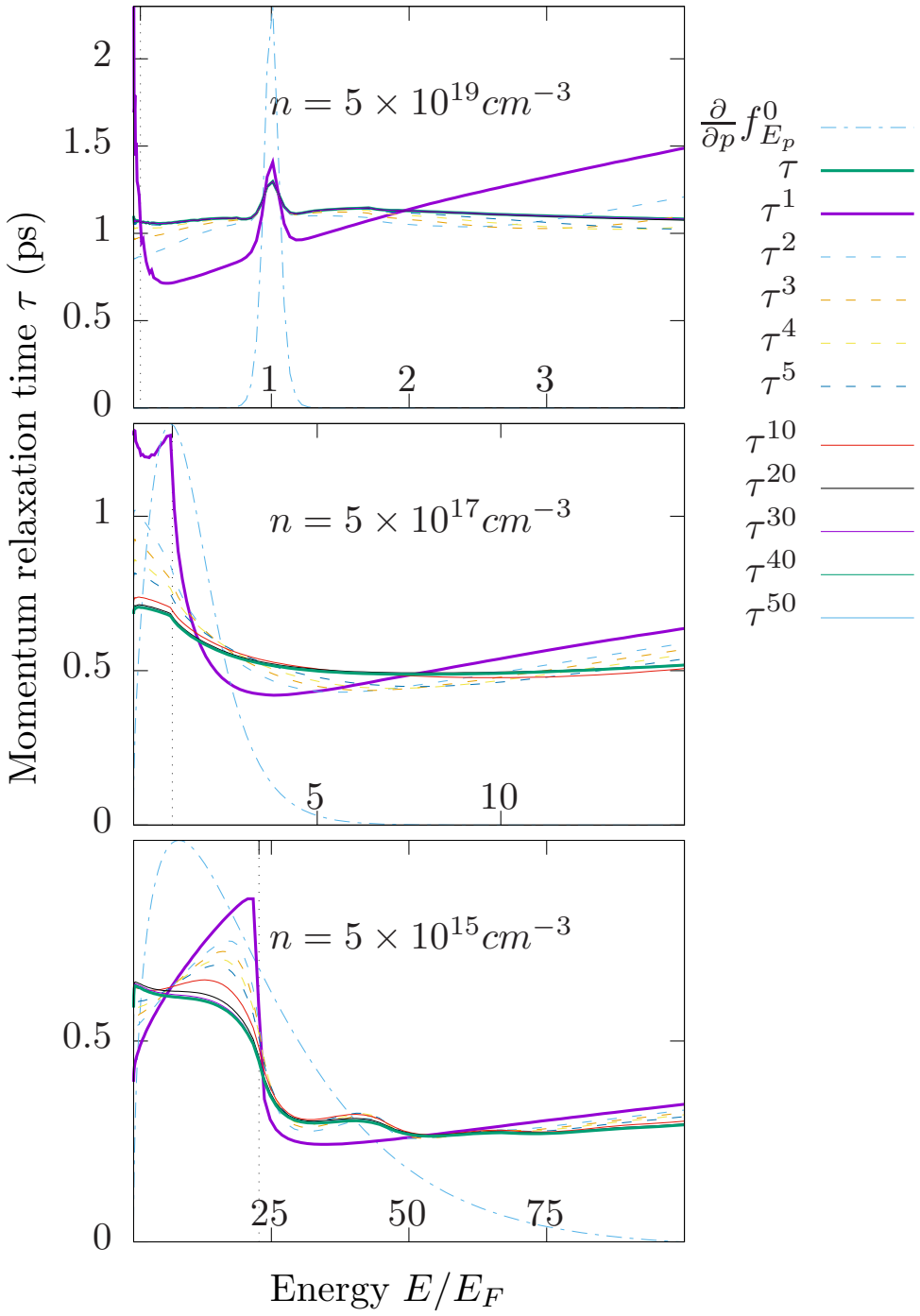

Figure 5.4: Momentum relaxation time τ^n, Eq. (5.8), at different steps n in the iteration process as a function of energy E, in GaAs at $T = 300K$ for $n = 5{\times}10^{19}, 10^{17}, 10^{15} cm^{-3}$. The initial and final curves of the iteration τ^1 and τ are thick lines. The first five iterations are the dashed lines. We only plot every tenth step after the τ^{10}. The derivative of the distribution function (dash-dotted, in arbitrary units) gives an indication how the momentum relaxation time contributes to mobility. The vertical dotted line marks $\hbar\omega_{LO}$.

the LO-phonon energy. The steps in the momentum relaxation time τ^1 in the first iteration occur when the carrier has enough energy to emit an LO-phonon, at $E = \hbar\omega_{LO}$. The next iteration, τ_E^2 is a weighted sum of the $\tau^1_{E\pm\hbar\omega_{LO}}$, and will consequently feature another step at $E = 2\hbar\omega_{LO}$, and so on. Hence, we see that the sharp peak structure critically depends on the constant frequency of the LO-phonon, which only couples energies which are $\hbar\omega_{LO}$ apart in the iteration process.

As the coupled mode frequencies do depend on wave vector, τ_E^{n+1} depends on τ_E^n in a more complicated way than when we are concerned with LO-phonon scattering alone. Roughly speaking, the less the coupled mode dispersion resembles an LO-phonon, the more will the LO-phonon-like steps be washed out.

5.3.3 Comparison of momentum relaxation times in different approximations

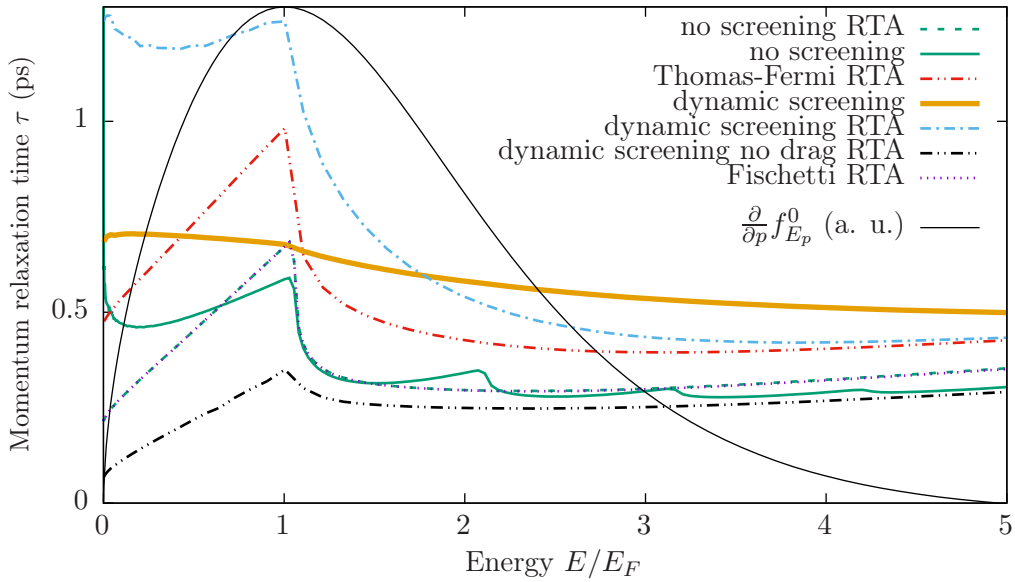

Figure 5.5: Momentum relaxation times τ for carrier–coupled mode scattering in different approximations for GaAs at $n = 5 \times 10^{17} cm^{-3}$ at $T = 300K$, as a function of the carrier energy. The lines marked "RTA" are relaxation times Eq. (4.31), the others are effective momentum relaxation times, solutions to Eq. (4.25). Details on the calculations are given in subsection 5.3.1. The derivative of the Fermi-Dirac distribution function with respect to wave vector is shown in arbitrary units.

In this section, we compare the effective momentum relaxation time for dynamically screened LO-phonon scattering to those calculated in other approximations. We plot the derivative of the Fermi-Dirac distribution function in Fig. 5.5. For the energies for which it is large, the momentum relaxation time contributes significantly to mobility Eq. (5.4). Thus, this curve marks the energy ranges which interest us most.

We can associate the kinks in the momentum relaxation lines with scattering

processes which are allowed as soon as the carrier has enough energy. As we can see in Tab. 2.4, the dip in all the effective momentum relaxation times at $E = 1.05E_F$ is due to the ability of the carrier to emit an LO-phonon.

We see that the curve for dynamic screening does not show sharp kinks at multiples of the LO-phonon frequency, as all the other curves do. We explained in subsection 5.3.2 that this is due to the fact that coupled LO-phonon–plasmon modes have dispersion, while we assumed that uncoupled LO-phonons have a constant frequency for all wave vectors. The difference between the dynamic screening curve and its RTA version are striking. It suggests that the RTA underestimates scattering for low energies and overestimates it for high carrier energies. However, as carrier mobilities are proportional to energy averages of the momentum relaxation time (specifically Eq. (5.4)), the difference between the RTA and the fully self-consistent mobilities will not be as striking.

The Thomas-Fermi RTA curve lies quite close to the one for dynamic screening, but the unscreened RTA curve underestimate the momentum relaxation time drastically. Moreover, the momentum relaxation times in the unscreened and Fischetti et al. approximation are virtually identical at this carrier concentration.

At this point, it is illustrative to reexamine Fig. 5.3(b), which shows the scattering strengths corresponding to the Fischetti RTA, the unscreened RTA and the Thomas-Fermi-RTA curves for $n = 5 \times 10^{17} cm^{-3}$ at room temperature.

The momentum relaxation times shown in Fig. 5.5 are characteristic of the scattering strengths in Fig. 5.3(b) for wave vectors $k > k_c$ (Eq. (3.70)): For $k > k_c$, the Fischetti scattering strength $F^+_{k,Fischetti}$ (Eq. (3.71)), is equal to the unscreened scattering strength F^u (Eq. (3.21)). Moreover, the Thomas-Fermi scattering strength Eq. (3.39) is similar to F^+_k. The behavior of the scattering strengths for $k < k_c$ cannot be important for the momentum relaxation time, otherwise, the momentum relaxation times would show different trends.

When we compare the dynamic screening RTA curves with and without drag, it helps to look back to Fig. 5.1(d) and (f), which show the scattering rate Eq. (3.4) and effective scattering rate Eq. (4.34), respectively. As explained in subsection 5.3.1, dynamic screening in the RTA without drag is calculated from an integral over the scattering rate, whereas dynamic screening in the RTA is calculated from the same integral, except that the scattering rate is replaced by the effective scattering rate. Hence, as the scattering rate is much larger than the effective scattering rate, the dynamic screening momentum relaxation time with drag is much smaller than the dynamic screening momentum relaxation time without drag.

To investigate if these observations about the different approximations of screened carrier–LO-phonon scattering carry over to other parameter ranges, we next consider

carrier mobility.

5.3.4 Comparison of carrier mobilities in different approximations

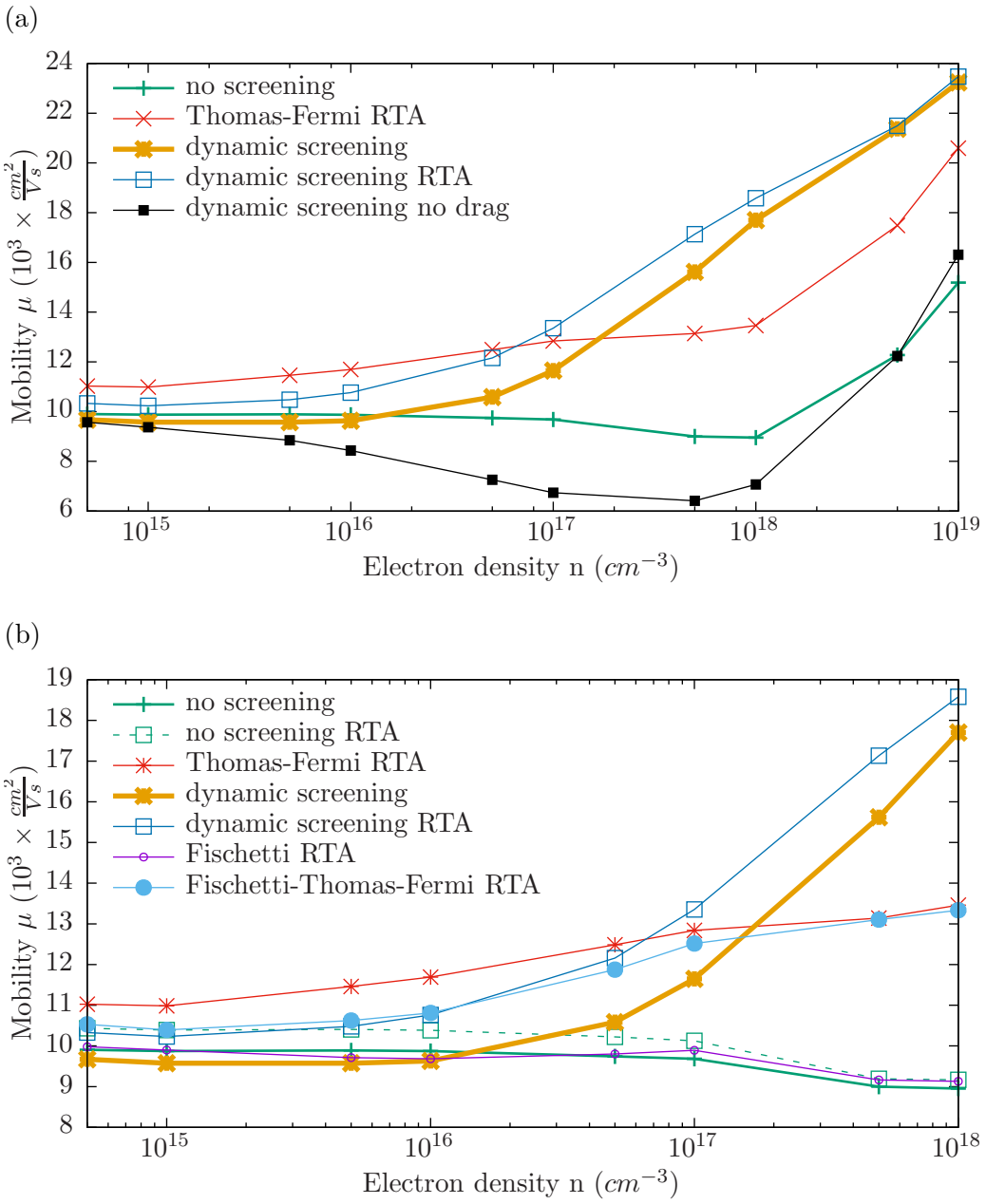

Figure 5.6: Dependence of carrier-collective mode scattering limited mobility μ on the electron density n, at room temperature, in different approximations. How the mobilities are calculated in detail is described in subsection 5.3.1. Different curves are plotted to highlight (a) the accuracy of the RTA for dynamic screening, signatures of anti-screening (b) the Fischetti et al. approximation discussed in section 5.2.1 and subsection 3.3.1.

In Fig. 5.6, we plot mobilities from the momentum relaxation times which we showed

for $n = 5 \times 10^{17} cm^{-3}$ in Fig. 5.5, over a range of electron densities. Mobility curves calculated in different approximations are named in the same way as the (effective) momentum relaxation times they are calculated from – see subsection 5.3.1.

Fig. 5.6(a) shows that the dynamical screening curve with and without the RTA show the same qualitative behavior throughout the electron density range. The curve for dynamical screening without drag underestimates the mobility significantly compared to the curve with drag. This is exactly what we expect, because when we neglect the drag term, we treat the momentum relaxation of carriers due to coupled modes exactly like momentum relaxation of carriers due to phonon modes. The magnitude of the discrepancy is a measure for the importance of the drag term. For low carrier concentrations around $n = 10^{15} cm^{-3}$, this discrepancy is small, but for intermediate and high carrier concentration, it is large, such that, for $n = 10^{18} cm^{-3}$, the dynamically screened mobility with drag is almost three times as high as the one without drag. As the calculation of the dynamically screened mobilities without drag differs from the calculation of the unscreened mobilities only in the scattering rate –see subsection 5.3.1– and as the scattering rate is larger in the presence of carriers than in their absence, it is no wonder that the mobilities of dynamic screening without drag are typically smaller than the unscreened mobilities. The usual effect of screening, i.e., of taking carriers into account, is to increase the mobility. When taking carriers into account leads to lower mobilities, we speak of anti-screening [26].

The dynamically screened mobility is slightly smaller than the unscreened mobility up to about $n < 2 \times 10^{16} cm^{-3}$ (anti-screening regime), and becomes up to around twice as large as the unscreened mobility for higher carrier concentrations (screening regime). Roughly speaking, the anti-screening regime is dominated by an increased scattering rate compared to the case without carriers, and in the screening regime, this effect is overcompensated due to the drag term.

Thomas-Fermi screening yields higher mobilities than dynamical screening at carrier concentrations up to around $n < 2 \times 10^{17} cm^{-3}$, and lower mobilities for higher carrier concentrations. The agreement between Thomas-Fermi screening and dynamic screening is generally poorer than between dynamical screening with and without the RTA. Nonetheless, Thomas-Fermi screening captures the general carrier density-mobility behavior much better than dynamic screening without drag or the unscreened case.

We plot the mobility calculated according to the approximation by Fischetti et al. [1] in Fig. 5.6b, which shows a section of Fig. 5.6a. This mobility curve differs very little from the unscreened mobility curve. This makes it a poor approximation to the dynamically screened mobility for intermediate and high carrier concentrations. At low carrier concentrations, the agreement between the Fischetti et al. and the dynamically screened mobility are good. In fact, the Fischetti curve captures

anti-screening to a certain extent: We can see that when we compare it to the curve for the unscreened mobility in the RTA. The Fischetti curve is about the same as the unscreened mobility curve without the RTA, but significantly lower than the unscreened mobility curve with the RTA. As the Fischetti curve itself is calculated in the RTA, this is the signature of anti-screening.

In section 5.2 above, we suggested combining the Thomas-Fermi with the Fischetti et al. approximation to a model which hopefully had the advantages of both. We plot the resulting mobility curve in Fig. 5.6(b). It behaves as the Thomas-Fermi curve for intermediate and high carrier concentrations. For low carrier concentrations, it lies between the Fischetti and the Thomas-Fermi curve and is quite similar to the curve for dynamic screening in the RTA.

The differences between the RTA and the fully self-consistent mobilities are only large when the drag term is taken into account. Therefore, the RTA version of the dynamic screening without drag curve was excluded from the plots. The RTA curve for the unscreened mobility only differs slightly from the fully self-consistent one. We included this curve in Fig. 5.6(b), so that we can disentangle the effects of anti-screening on mobility from the effects of self-consistency on mobility.

5.3.5 Total carrier mobility in bulk GaAs

The mobility in n-GaAs is dominated by polar scattering in the high temperature limit and by charged impurity scattering in the low temperature limit [94]. Other scattering mechanisms, like neutral impurity, piezoelectric or deformation potential scattering usually contribute less [94, 35], and we include only carrier LO and LA phonon scattering and charged impurity scattering in the present discussion. Appendix E.1 gives computational details on the two latter scattering mechanisms.

5.3.5.1 Calculation of total mobility

There are three conceivable methods to calculate the total mobility:

1. Substitute the momentum relaxation times τ_i for each scattering mechanism i in Eq. (5.4). This yields individual mobilities μ_i, and the total mobility is calculated from Matthiessen's rule [25, chapter 7][99].

$$\mu_{tot,1}^{-1} = \sum_i \frac{1}{\mu_i} \tag{5.9}$$

2. Iterate the polar contribution τ_{polar} (i.e., coupled mode scattering in one of the approximations discussed in subsection 5.3.1) to self-consistency according to

Eq. (5.8). Calculate the total momentum relaxation time τ_{tot} from the self-consistent τ_{polar}, τ_{LA} and τ_{CI}.

$$\tau_{p,tot}^{-1} = \sum_i \tau_{p,i}^{-1}, \tag{5.10}$$

Calculate the total mobility $\mu_{tot,2}$ from substituting $\tau_{p,tot}$ in Eq. (5.4). This procedure is usually adopted when one is mainly interested in polar scattering mechanisms, e.g. [94].

3. In general, an expression of the structure Eq. (5.5) must hold for the total momentum relaxation time, not just for its polar contribution. Rode [100] used this approach, listing the "avoidance of Matthiessen's rule" as an advantage. Obviously, the coefficients R^i have to be different to include the additional scattering mechanisms. The present case is quite simple, because the additional scattering mechanisms, charged impurity and acoustic phonon scattering, are well described by elastic scattering (appendix E.1), so that for charged impurity (CI) and acoustic phonon (LA) scattering, Eq. (5.5) becomes

$$\frac{1}{\tau_{\boldsymbol{p},CI}} = R^1_{\boldsymbol{p},CI} \qquad \text{and} \qquad \frac{1}{\tau_{\boldsymbol{p},LA}} = R^1_{\boldsymbol{p},LA}. \tag{5.11}$$

The total momentum relaxation time due to charged impurity, acoustic and polar phonon scattering consequently is

$$\begin{aligned}\frac{1}{\tau_{\boldsymbol{p},tot}} =& R^1_{\boldsymbol{p},CI} + R^1_{\boldsymbol{p},LA} + R^1_{\boldsymbol{p},polar} - R^2_{\boldsymbol{p},polar}\{\tau_{tot}\}/\tau_{\boldsymbol{p},tot} + R^3_{\boldsymbol{p},polar}\{\tau_{tot}\}/\tau_{\boldsymbol{p},tot} \\ =& \frac{1}{\tau_{\boldsymbol{p},CI}} + \frac{1}{\tau_{\boldsymbol{p},LA}} + R^1_{\boldsymbol{p},polar} - R^2_{\boldsymbol{p},polar}\{\tau_{tot}\}/\tau_{\boldsymbol{p},tot} + R^3_{\boldsymbol{p},polar}\{\tau_{tot}\}/\tau_{\boldsymbol{p},tot}\end{aligned} \tag{5.12}$$

This allows us to iterate $\tau_{\boldsymbol{p},tot}$ to self-consistency using

$$\tau^{n+1}_{\boldsymbol{p},tot} = \frac{1}{R^1_{\boldsymbol{p},polar} + \frac{1}{\tau_{\boldsymbol{p},CI}} + \frac{1}{\tau_{\boldsymbol{p},LA}}} \left(1 + R^2_{\boldsymbol{p},polar}\{\tau^n_{tot}\} - R^3_{\boldsymbol{p},polar}\{\tau^n_{tot}\}\right). \tag{5.13}$$

We can then calculate the total mobility $\mu_{tot,3}$ from substituting $\tau_{p,tot} = \lim_{n\to\infty} \tau^n_{p,tot}$ in Eq. (5.4). This approach has been used by Sanborn [48], for example, and should yield the most accurate total mobilities.

5.3.5.2 Electron density dependence of the electronic mobility

Fig. 5.7a shows that at room temperature, LO-phonon scattering is the most important scattering mechanism for low carrier densities up to around $n \approx 10^{17} cm^{-3}$, and charged impurity scattering is the most important scattering mechanism at

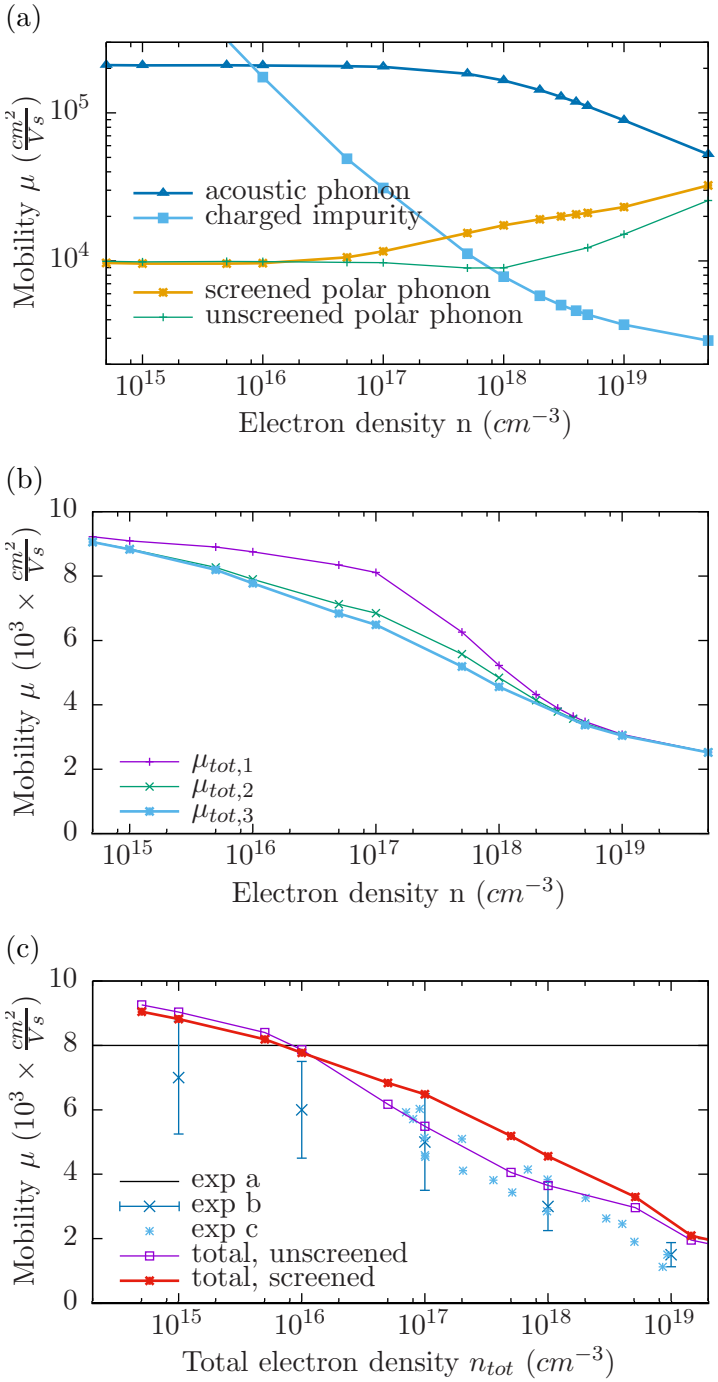

Figure 5.7: Electron density dependence of the mobility in GaAs at $T = 300K$. In (a) and (b) the mobility is plotted against the electron density in the Γ valley, in (c), mobility is plotted against the total electron density in all valleys (See appendix C.5.4). (a) Mobility limited through carrier scattering with charged impurity scattering μ_{CI}, LA phonon scattering, and screened and unscreened LO-phonon scattering. (b) The three different methods of calculating the total mobility from charged impurity scattering, LA phonon scattering and screened LO-phonon scattering is marked "total, screened" – see subsubsection 5.3.5.1. (c) Exp a is the total mobility for low carrier concentration [94]. Exp b is from [101] and c from [102]. The total mobility from charged impurity scattering, LA phonon scattering and screened LO-phonon scattering is marked "total, screened". The total mobility from charged impurity scattering, LA phonon scattering and unscreened LO-phonon scattering is marked "total, unscreened".

carrier densities higher than around $n \approx 10^{18} cm^{-3}$. The difference between the screened and the unscreened LO-phonon limited mobility is not large in the electron density region where LO-phonon scattering is dominant. Acoustic phonon scattering is significantly less important than LO-phonon scattering and charged impurity scattering for all carrier densities at room temperature.

The three methods to obtain the total mobility from charged impurity, acoustic phonon and screened polar phonon scattering are compared in Fig. 5.7b. We find that methods 1 through 3 yield successively smaller mobilities. However, the difference between method 2 and 3 is quite small for all considered electron densities. The difference between methods 1 and methods 2 and 3 does not exceed 30%, and is very small for low carrier concentrations and high carrier concentrations. That the precise method of calculating the total mobility is not too important in parameter regions where it is dominated by a single scattering mechanism should not be surprising.

In Fig. 5.7c, the total mobility was calculated with the third method, and the notation $\mu_{screened}$ is the total mobility where the polar contribution was screened LO-phonon scattering, whereas $\mu_{screened}$ is the total mobility where the polar contribution was pure LO-phonon scattering.

The population of the L-valley and X-valleys becomes significant at higher carrier concentrations, so that the total carrier concentration is not identical to the carrier concentration n in the lowest conduction band. We treat this approximately in appendix C.5.4. Note that the horizontal axis in Fig. 5.7c marks the total carrier concentration n_{tot}, and not the carrier concentration n in the Γ valley, like Fig. 5.7(a) and (b).

The total mobilities with screened and unscreened carrier LO-phonon scattering $\mu_{screened}$ and $\mu_{unscreened}$ are plotted against some experimental values. As charged impurity scattering dominates in the "strong coupling regime" around $n = 5 \times 10^{17} cm^{-3}$, where screened and unscreened polar phonon scattering differ most (Fig. 5.7a), the screening effect is not very striking. Polar phonon scattering is the dominant scattering for small carrier concentrations, so that Fig. 5.7c reveals anti-screening ($\mu_{screened} < \mu_{unscreened}$), which is hardly perceptible in Fig. 5.6.

Comparison with experiment In Fig. 5.7c, we show our calculated total mobilities compared to experiment for room temperature GaAs against the total electron density n_{tot} in the occupied conduction bands (See appendix C.5.4 for an account of the occupation of the relative occupation of these bands and its effect on mobility).

Our calculated total screened mobility is higher than the experimental values (a[101], b[102]) for all electron concentrations. Our calculation of the total unscreened

mobility agrees somewhat better with experimental values for intermediate carrier concentrations of about $10^{16}cm^{-3} \leq n \leq 10^{18}cm^{-3}$.

Piezoelectric scattering is not thought to be important for the mobility in room temperature GaAs [100, 35], and therefore our neglect of piezoelectric scattering cannot explain the deviations between our calculations and experiment. The same holds for neutral impurity scattering [35].

A more elaborate account of charged impurity scattering [98, 102] might improve agreement with experiment at intermediate and high carrier concentrations, but is unlikely to be significant at lower carrier concentrations.

We have assumed that the deformation potential is 6eV (See Tab. 2.1 [3]), but values of 7eV have also been used, e.g., [35, 100]. This would lead to a reduction in the mobility due to acoustic phonon scattering by $(6/7)^2 \approx 27\%$ (See appendix E.1 for how we calculate acoustic phonon scattering). For $n = 5 \times 10^{14}cm^{-3}$, this decreased the total mobility calculated in the Matthiessen method (Method 1 in subsubsection 5.3.5.1) by only 1.6%. Consequently, this alone cannot explain our deviation from experiment either.

We attribute the deviation of our calculations from experiment largely to our neglect of non-parabolicity of the lowest conduction band, the Γ band. Rode [100] calculated the mobility due acoustic phonon scattering, piezoelectric scattering and unscreened polar phonon scattering and found an effect of several percent for undoped (i.e., low electron density) GaAs at room temperature[100, Fig. 3]. The effects of non-parabolicity would certainly not be smaller for room temperature GaAs at higher carrier concentrations than at lower carrier concentrations. We do not carry out calculations with non-parabolic bands in this thesis, but such calculations are possible within the framework developed in chapter 4, and we will discuss them in our outlook section 7.2.

5.3.5.3 Temperature dependence of the carrier mobility

For Fig. 5.8, we calculated mobilities over a range of temperatures for a carrier density of $n = 5 \times 10^{17}cm^{-3}$. At this electron concentration, the room temperature mobilities for screened and unscreened polar phonon scattering differed strongly. We now investigate how these two mobilities behave as a function of temperature. We assume that the GaAs parameters in Tab. 2.1 do not depend on temperature.

Temperature is an easy variable to change experimentally, and therefore the dependence of mobility on temperature is often used to characterize and distinguish different scattering mechanisms, e.g. [35]. Doubly logarithmic plots of mobility against temperature are useful, as power laws $\mu \propto T^{\alpha}$, with real numbers α will be straight lines in such plots. We show the mobility due to screened and unscreened

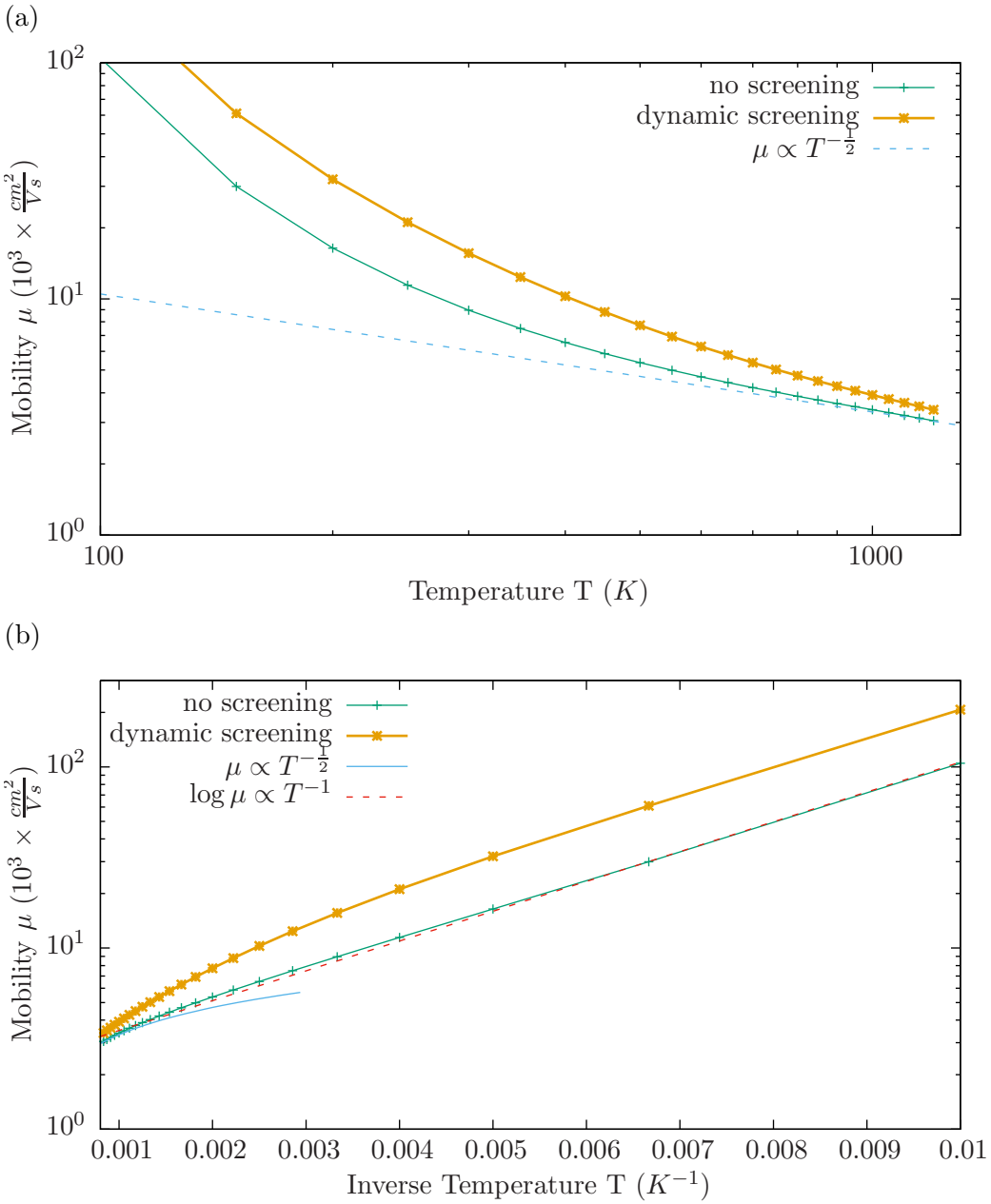

Figure 5.8: Mobility due to screened and unscreened polar phonon scattering in GaAs at the carrier concentration $n = 5 \times 10^{17} cm^{-3}$ for a range of temperatures. (a) The mobility is plotted against temperature. Both axis are logarithmic. (b) The mobility is plotted on a log scale against inverse temperature.

polar phonon scattering in GaAs at the carrier concentration $n = 5 \times 10^{17} cm^{-3}$ in the doubly logarithmic Fig. 5.8(a). We fit a power law line $\mu \propto T^{-\frac{1}{2}}$ to the unscreened mobility curve for high temperatures. This is the high temperature behavior for LO-phonon scattering, where it can be described as quasi-elastic, cf. Eq. (C.53) [26]. Yet, the polar phonon limited mobility does not have a power law dependence on temperature throughout the plotted temperature range.

In Fig. 5.8(b), we plot the screened and unscreened polar phonon mobilities in GaAs at the carrier concentration $n = 5 \times 10^{17} cm^{-3}$ against the inverse temperature. A fit shows that the unscreened polar phonon mobility roughly behaves as $\log \mu \propto T^{-1}$ through a large temperature range, as long as the temperatures are not too high.

Unfortunately for the purpose of distinguishing experimentally between screened and unscreened polar phonon scattering, the temperature signatures of both curves are very similar.

Fig. 5.9(a) shows the temperature dependence of the electron mobility due to charged impurity and acoustic phonon scattering (See section E.1), and screened and unscreened polar phonon scattering in GaAs at the carrier concentration $n = 5 \times 10^{17} cm^{-3}$. With growing temperature, coupled mode scattering increases and charged impurity scattering decreases. Therefore, carrier-coupled mode scattering becomes the dominant scattering mechanism at higher temperature. While charged impurity scattering dominates at low temperatures, coupled-collective excitation scattering is the most important scattering mechanism at high temperatures, starting from $T \approx 400K$.

The difference between the "total screened" and the "total unscreened" mobility curve are vanishingly small at $T < 50K$. At higher temperatures, the difference between the curves is intelligible: As shown in Fig. 5.9, the ratio $\mu_{tot,screened}/\mu_{tot,unscreened}$ is 1.28 at most, the room temperature value.

We did not find $T - \mu$ curves in the experimental literature for $n = 5 \times 10^{17} cm^{-3}$ in particular. However, we included the value of $\mu = 3500 \frac{cm^2}{Vs}$ at room temperature from the collection of experimental values in Sze and Irvin [101], with the 25% deviation they report.

We also calculated the Seebeck coefficient in room temperature GaAs, but found it to be very insensitive to the effects of screening, cf. appendix D.

5.4 Magnitude of effect in different polar materials

Whether explicit treatment of coupled collective mode scattering is important in a material depends on two factors. Firstly, coupled collective mode scattering has to

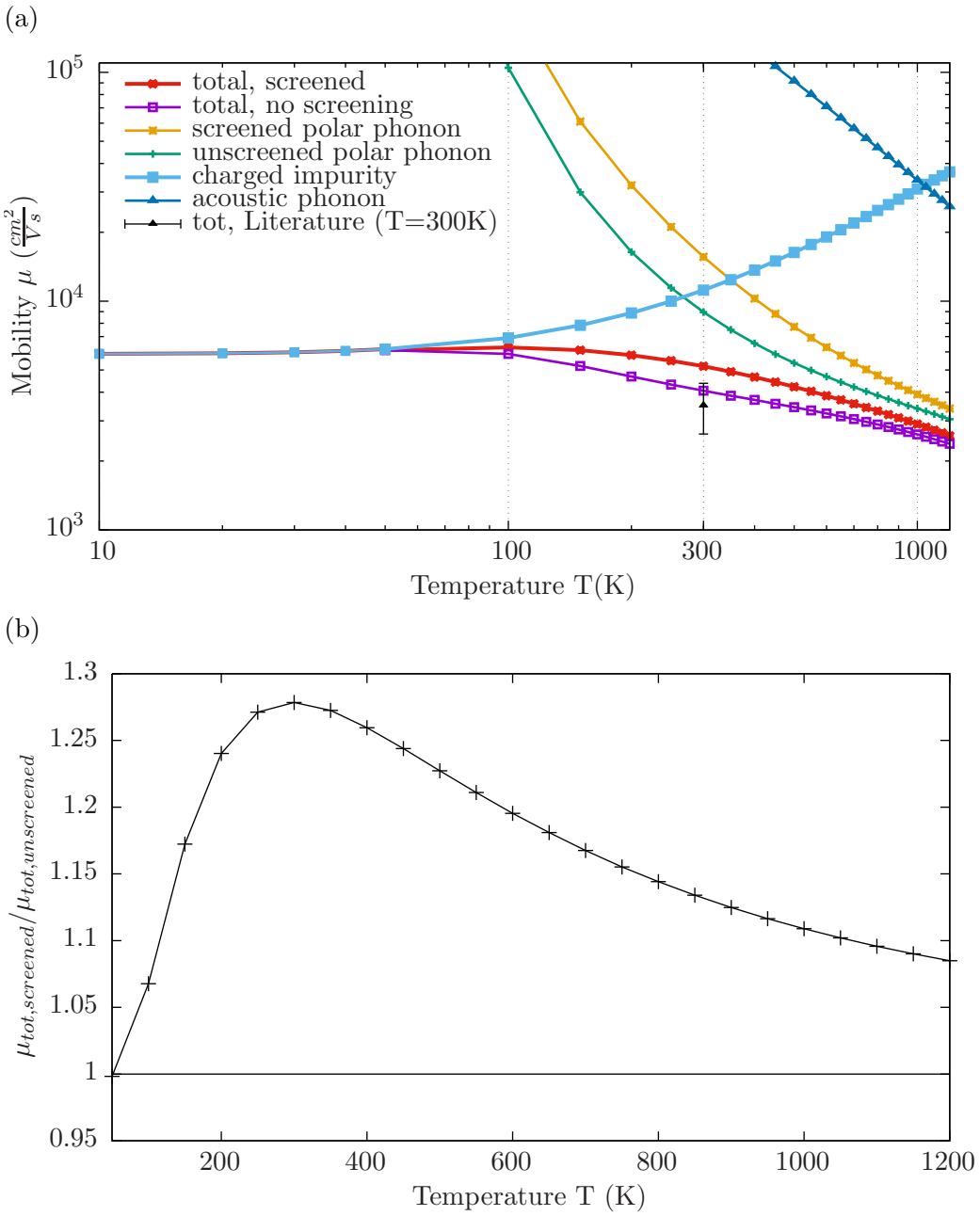

Figure 5.9: (a) Temperature dependence of total mobility due to charged impurity, acoustic phonon and screened or unscreened polar phonon scattering in GaAs with an electron concentration kept constant at $n = 5 \times 10^{17} cm^{-3}$. The total mobility curves are calculated with method 3 from subsubsection 5.3.5.1. The line marked μ_{tot}^{Lit} is the total measured mobility at $T = 300K$ from [101]. (b) Ratio of the two mobility curves marked "total, screened" and "total, no screening" in subplot(a) as a function of temperature.

differ significantly from LO-phonon scattering for a certain density. Secondly, polar scattering mechanisms have to be an important scattering mechanism at that density. This depends on the other relevant scattering mechanisms in the material.

In this section, we address the first factor for some polar semiconductors similar to GaAs. We also describe them with a single spherical parabolic conduction band, and compare the mobility limited by coupled collective mode scattering ("μ_{screened}") to the mobility due to LO-phonon scattering ("$\mu_{\text{unscreened}}$") . Appendix C.3 describes the evaluation of the momentum relaxation time in detail. The mobilities are calculated from Eq. (5.4). The parameters used for these calculations are given in Tab. 2.2, and the ratio of the screened to the unscreened LO-phonon mobility $\frac{\mu_{\text{screened}}}{\mu_{\text{unscreened}}}$ is plotted for some n-type materials at room temperature in Fig. 5.10a.

In the long-wavelength limit, the coupling between LO-phonons and plasmons is strongest when the plasma frequency and the LO-phonon frequency are similar (See Fig. 3.3 in appendix 5.2), or $n \approx n_C$, with the strong coupling density n_C from Eq. (2.88). We see that $\frac{\mu_{\text{screened}}}{\mu_{\text{unscreened}}}$ is slightly smaller than one for low carrier densities ("anti-screening"), and larger than one ("screening") for high carrier densities across all materials. The ratio $\frac{\mu_{\text{screened}}}{\mu_{\text{unscreened}}}$ has a broad peak around $n = n_C$, and decreases towards one again for larger n.

The curve for InP, which has very similar m^*, 14% lower ε^∞ and higher optical phonon frequencies than GaAs, is very similar to the GaAs curve. InAs, which has a much smaller m^* than GaAs or InP, similar ε^∞ to GaAs and smaller optical phonon frequencies, has smaller maximal $\frac{\mu_{\text{screened}}}{\mu_{\text{unscreened}}}$. InSb, which is even lighter, and has higher ε^∞, has even lower $\frac{\mu_{\text{screened}}}{\mu_{\text{unscreened}}}$. PbTe has the smallest maximal $\frac{\mu_{\text{screened}}}{\mu_{\text{unscreened}}}$ of all considered materials. It has quite a low effective mass, and the highest ε^∞ of all considered materials. Moreover, its optical phonon frequencies are very small, with ω_{TO} only a fraction of ω_{LO}.

We see much larger $\frac{\mu_{\text{screened}}}{\mu_{\text{unscreened}}}$ in ZnSe, which has roughly twice the GaAs effective mass and half its ε^∞, and whose optical phonon frequencies are similar to InAs. ZnS, which has even higher m^* and lower ε^∞ than ZnSe, shows the largest $\frac{\mu_{\text{screened}}}{\mu_{\text{unscreened}}}$ of the investigated materials.

To investigate how $\frac{\mu_{\text{screened}}}{\mu_{\text{unscreened}}}$ depends on the parameters, we consider hypothetical materials which have:

- ZnSe parameters, but a GaAs effective mass
- ZnSe parameters, but a GaAs ε^∞
- ZnSe parameters, but GaAs ε^∞ and m^*

When we change ε^∞, we leave ω_{LO} and ω_{TO} constant, but adjust ε^0 to satisfy the Lyddane-Sachs-Teller relation.

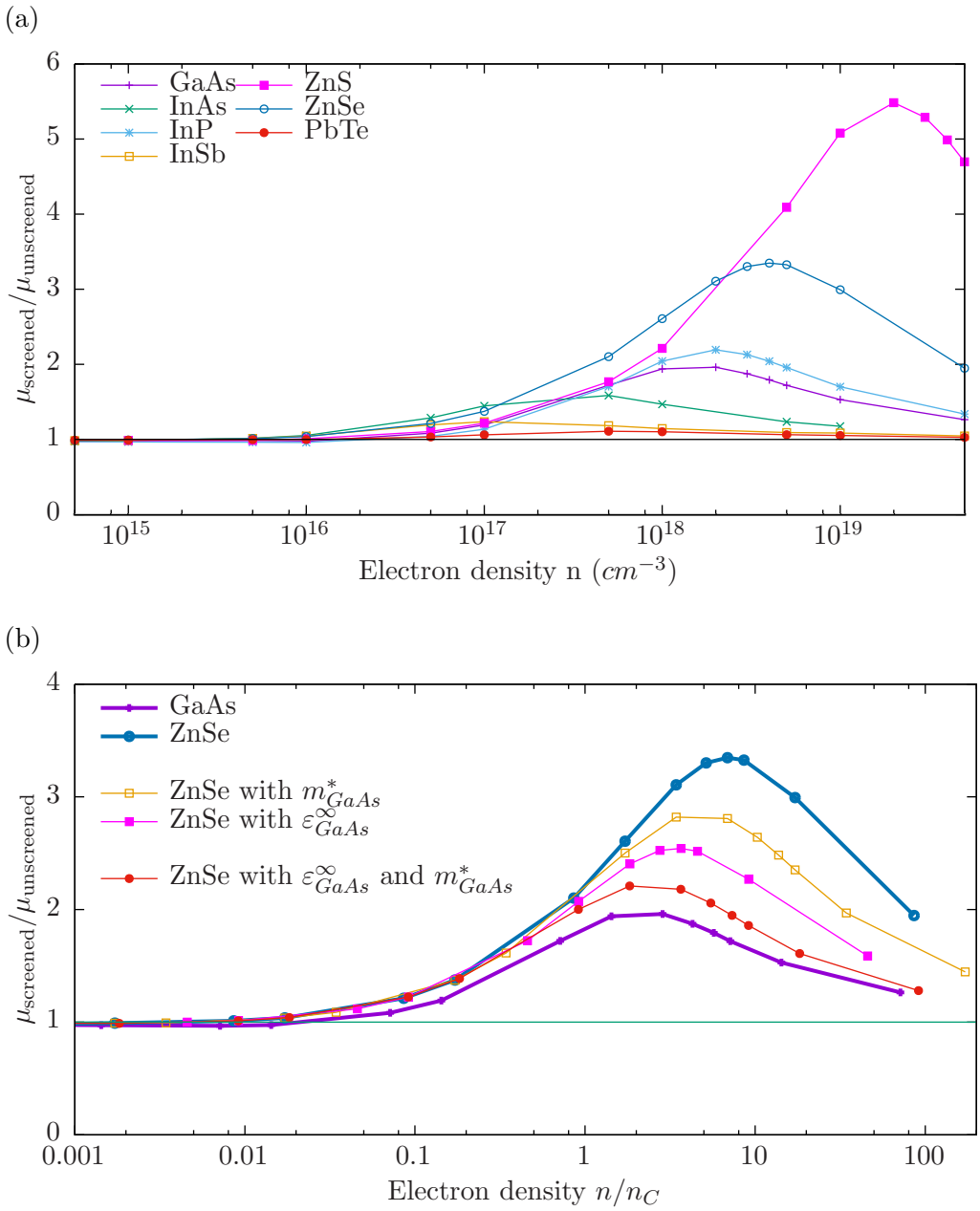

Figure 5.10: Fraction $\frac{\mu_{\text{screened}}}{\mu_{\text{unscreened}}}$ at $T = 300K$ (a) for n-type GaAs, InAs, InP, InSb, ZnSe, PbTe and ZnS depending on electron density. (b) for n-type GaAs, ZnSe, and hypothetical materials with mixed GaAs and ZnSe parameters, depending on electron density normalized by their respective characteristic density n_C.

Fig. 5.10b shows that $\frac{\mu_{\text{screened}}}{\mu_{\text{unscreened}}}$ grows with increasing m^* and falls with increasing ε^∞. Changing the ZnSe effective mass and ε^∞ to their GaAs value results in a $\frac{\mu_{\text{screened}}}{\mu_{\text{unscreened}}}$ which is very similar to the GaAs curve.

Extrapolating from the comparison between GaAs and ZnSe, and the trend observed in Fig. 5.10a, we expect the relative difference between screened and unscreened LO-phonon mobility to be largest in materials with large effective mass and low high frequency dielectric constant. We explain this as follows: The Thomas-Fermi wave vector k_{TF} is proportional to the effective mass, and the static free carrier susceptibility proportional to k_{TF} for small k. That means that the free carrier susceptibility will be the more important compared to the valence band susceptibility ε^∞ if the latter is small, or if m^* is large. In materials which are very strongly polar, like PbTe, ε^0 is much larger than ε^∞, and the free carrier susceptibility plays an even smaller role.

Chapter 6

Screened interface phonon scattering in polar MoS_2 heterostructures

We calculate the carrier mobility due to interface phonon-plasmon scattering for MoS_2-sandwiches, that is, for a single layer of MoS_2 between dielectric 1 on the one side and dielectric 2 on the other side (Fig. 3.4b). We first calculate the effective momentum relaxation time from Eq. (4.24). We discuss how this expression is calculated in detail in appendix C.4, yielding Eq. (C.61) for the fully self-consistent effective momentum relaxation time. We discuss the treatment of screening in detail in section 6.3. In the second step, we then calculate the carrier mobilities from the momentum relaxation times using Eq. (C.106).

In order to assess the mobility which could be achieved in a device which is not dominated by charged impurity scattering, we include acoustic deformation potential scattering, piezoelectric scattering and optical deformation potential scattering in the calculation of the total mobility, using the parameters calculated by Kaasbjerg et al. [57, 5]. In appendix E, we describe how to calculate the momentum relaxation times due to acoustic and optical deformation potential scattering and piezoelectric scattering [57, 5, 54]. Like Kaasbjerg et al. [57], but unlike Ma and Jena [54], we do not think longitudinal optical phonon scattering in the layer of MoS_2 itself contributes significantly to the scattering. See appendix E for details.

We then calculate a "total" momentum relaxation time τ_{tot} due to these scattering processes, and screened interface phonon scattering from

$$\tau_{tot} = \frac{1}{\sum_i \frac{1}{\tau_i}} \tag{6.1}$$

where the sum is over the different scattering processes above. We put quotes around

total here, because in realistic structures, the mobility is often dominated by charged impurity scattering caused by a large number of defects [56, 55], which we do not include here. The corresponding "total" mobility μ_{tot} due to acoustic and optical deformation potential scattering, piezoelectric scattering and screened interface phonon scattering is calculated by substituting τ_{tot} in Eq. (C.106).

6.1 Modeling of channel material: MoS_2

Hexagonal molybdenite in its bulk form has been long known and characterized (see Fig. 1.2, or Ref [7] for its crystal structure). Bulk MoS_2(2H) consists of weakly bonded layers with a gap between layers that is similar to the layer thickness. All layers are identical, but they are offset to each other, so that a primitive unit cell has to contain atoms from two layers [7]. The individual layers are not completely planar, because the sulfur atoms, which are strongly chemically bonded to each molybdenum atom, are offset in the direction of the c-axis, cf. [7], Fig. 1.2. The microscopic details

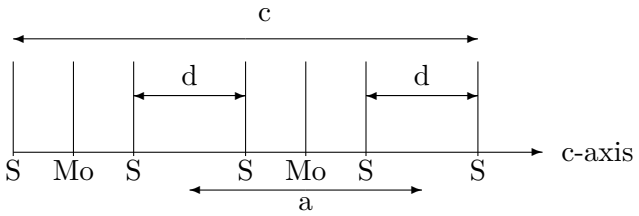

Figure 6.1: Projection of the MoS_2(2H) primitive unit cell onto the c-axis, to scale. Lines perpendicular to the c-axis mark the planes in which the marked atoms sit. The length of the unit cell is c=12.29Å, the inter-atomic distance is d=2.96Å. [7] The size of a unit cell of a monolayer a=c/2=6.145Å.

of the crystal structure are not necessary for our transport calculations, and, as far as electrostatics are concerned, we treat monolayer MoS_2 as a slab of bulk MoS_2 of width a=c/2=6.145Å, cf. Fig. 6.1. While this is quite crude a description of the atomic structure of MoS_2, it offers the chance to investigate the effects of dynamic screening in these 2d structures.

We treat the electrons in the MoS_2 conduction band minima as truly two-dimensional (cf. subsection 3.2.4), that is, we take their wave functions to be delta functions at z=0 in Fig. 3.4b, in the middle of the monolayer. Monolayer MoS_2 has two equivalent conduction band minima at the K points (cf. Fig. 1.4). Kaasbjerg et al.[57, Fig. 2] fit a parabola to the K-point minimum with good agreement, and comment that the closest conduction band valley lies about 200meV higher, so that low field transport is well described by effective mass theory. The effective masses in the longitudinal and transverse directions are almost identical [52, 57]. We will use $m^* = 0.35m_e$, which Cheiwchanchamnangij and Lambrecht [52] determined with a self-consistent

GW-method rather then the value of $m^* = 0.48m_e$ which Kaasbjerg et al. [57] obtained with density functional theory and the local density approximation.

6.2 Influence of surrounding dielectrics

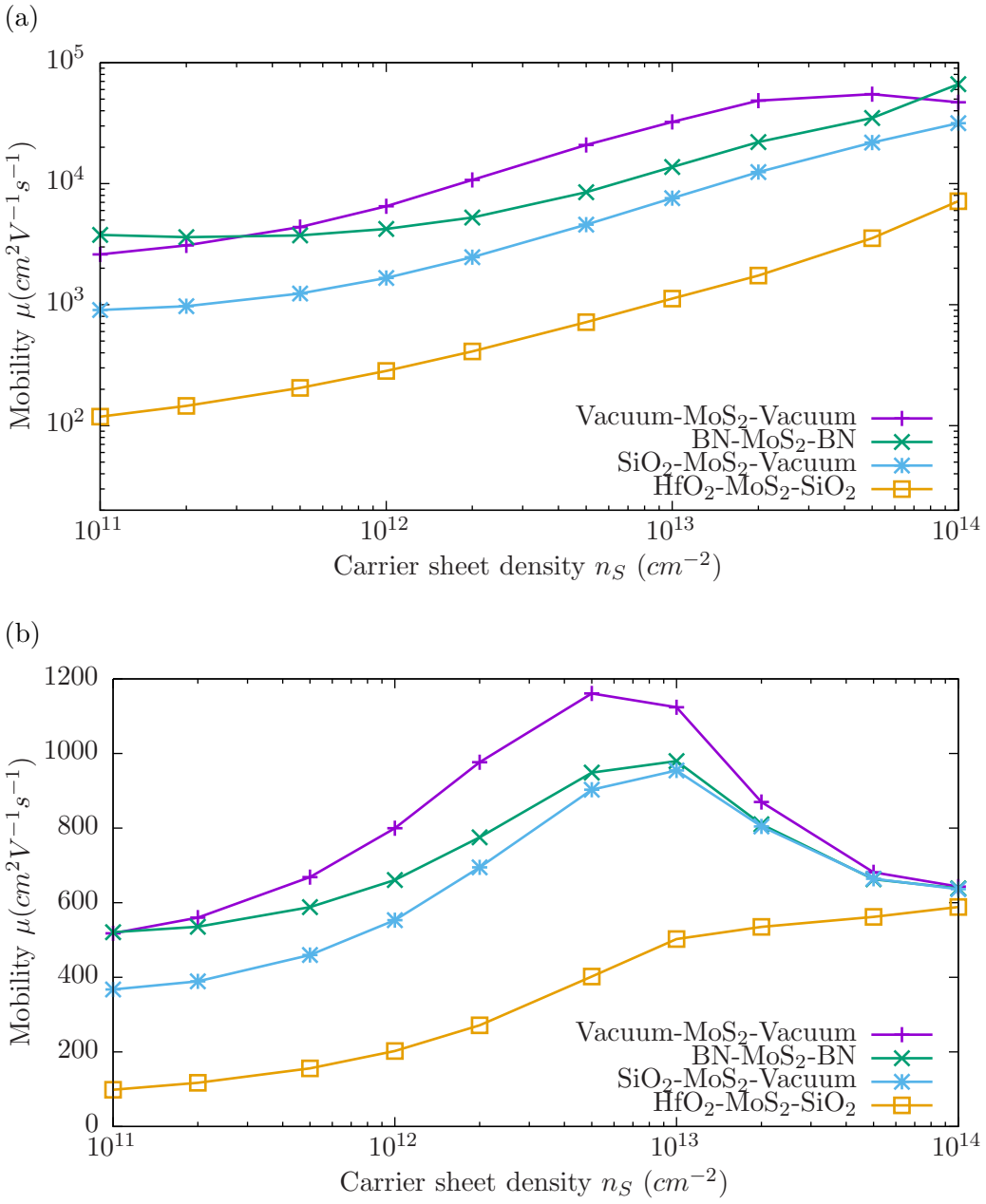

Figure 6.2: (a) Mobility limited by dynamically screened interface phonon scattering (b) Total mobility due to dynamically screened interface phonon scattering, deformation potential and piezoelectric scattering (appendix E) in different structures, at T=300K, as a function of carrier sheet density n_S.

We calculate both μ, the dynamically screened interface phonon scattering, and μ_{tot}

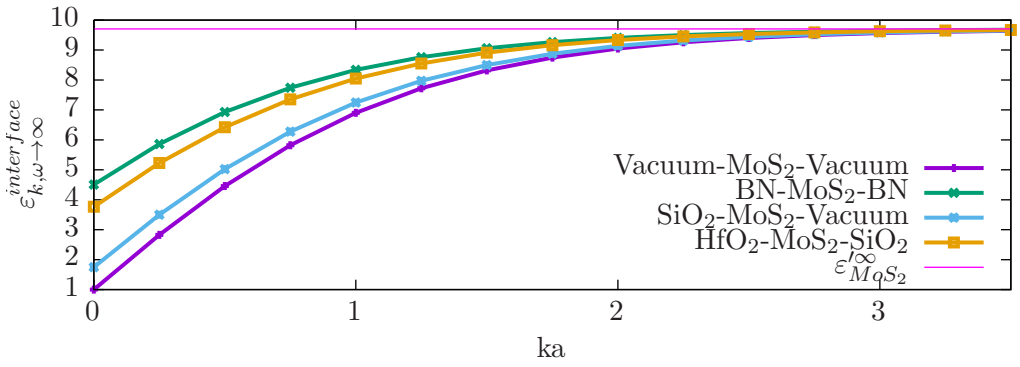

Figure 6.3: High frequency interface dielectric function $\varepsilon^{\text{interface}}_{k,\omega\to\infty}$ as a function of the wave vector times the interface layer thickness a. (See Eq. (3.60)) for different structures discussed in chapter 6. The lines are marked with the materials which make up the heterostructure described in Fig. 3.4(b), in the order "left dielectric"-"interface layer material"-"right dielectric". In this plot, the interface layer is always MoS_2, with a thickness of a=6.145Å, as discussed in section 6.1.

for MoS_2 surrounded by different dielectrics. A free-standing MoS_2-monolayer, a layer of MoS_2 between layers of hexagonal boron nitride BN, a layer of MoS_2 on SiO_2, and a MoS_2-monolayer between SiO_2 and HfO_2. This is shown in Fig. 6.2(a) and (b).

Hexagonal boron nitride (BN) is mildly anisotropic with $\varepsilon'^{\infty} = 4.5$ and $\varepsilon'^{0} = 6$, compared to the strongly anisotropic but barely polar MoS_2 with $\varepsilon'^{\infty} = 9.71$ and $\varepsilon'^{0} = 9.79$. SiO_2 and HfO_2 are isotropic oxides. SiO_2 has $\varepsilon^{\infty} = 2.5$ and $\varepsilon^{0} = 3.9$, HfO_2, with $\varepsilon^{\infty} = 5.03$ and $\varepsilon^{0} = 22.0$ is very strongly polar. Details of the dielectric functions are in Tab. 2.3, and the high-frequency interface dielectric function for each of the four sandwiches are plotted in Fig. 6.3.

The structures SiO_2-MoS_2-vacuum and SiO_2-MoS_2-HfO_2 were investigated experimentally in [17], the freestanding MoS_2 case is useful as a reference and relevant for studies of the intrinsic, phonon-limited mobility of MoS_2 such as [57, 5]. The BN-MoS_2-BN structure is interesting because hexagonal BN has a layered structure similar to MoS_2 and its optical phonon frequencies are very high.

Fig. 6.2 shows that the most strongly polar sandwich, SiO_2-MoS_2-HfO_2, has the lowest room temperature mobility. HfO_2 also has the lowest TO-phonon energy $\hbar\omega_{TO} = 12.4$meV of the considered dielectrics.

The SiO_2-MoS_2-vacuum structure has the next lowest mobility, which is still roughly a factor of 10 larger than that of the SiO_2-MoS_2-HfO_2 structure throughout all carrier concentrations. This is because SiO_2 is much less polar than HfO_2 and its lowest TO-phonon energy $\hbar\omega_{TO} = 55.6$meV is much higher, even larger than the thermal energy of 25meV.

As the lowest TO-phonon energy in BN is around four times the thermal energy, the mobility of the BN-MoS_2-BN structure is higher still, and very similar to mobility of

the free-standing MoS_2.

Fig. 6.5(c) and (f) show the effect of the different surrounding dielectrics on the effective scattering rate Eq. (4.34). We can see the hybridized plasmon-phonon modes at long wavelengths, and the flat LO-phonon-like modes at larger wave vectors. The low energy HfO_2-like mode and the high energy SiO_2-like mode are clearly distinguishable in Fig. 6.5f, unlike the remaining modes around 50meV. We can qualitatively understand that the scattering will decrease if we remove the HfO_2-type resonances from the effective matrix element in Fig. 6.5f, essentially yielding the SiO_2-MoS_2-vacuum $W^{0,eff}_{k,\omega}$ in Fig. 6.5c.

6.3 Treatment of screening

In this section, we compare carrier mobilities and momentum relaxation times, where the screening of interface polar phonon scattering is treated in different approximations:

1. The tag "dynamic screening" means fully self-consistent τ_p and $T_{k,\omega}$ from Eq. (C.61) and Eq. (C.76). The scattering rate in τ_p is calculated from Eq. (3.63)
2. The tag "dynamic screening no drag" means fully self-consistent τ_p from Eq. (C.61), but the drag term $T_{k,\omega}$ Eq. (C.76) is set to zero. The scattering rate in τ_p is calculated from Eq. (3.63)
3. The tag "no screening" applies to calculations where the drag term is equally zero (See discussion in subsection 4.4.3), but the scattering rate in τ_p is calculated from Eq. (3.58), i.e., free carriers have no effect on the scattering rate.
4. The tag "dynamic screening RTA" refers to dynamic screening in the relaxation time approximation. The relaxation time is calculated in a quasi-elastic approximation according to Eq. (4.31). The explicit expression is Eq. (C.63) in appendix C.4. The scattering rate in τ_p is calculated from Eq. (3.63)
5. The tag "static screening" also refers to a RTA solution. To obtain the static limit of the relaxation time, we have to replace the scattering rate Eq. (3.63) with its static limit $W^0_{k,\omega=0}$ and set the phonon dissipation weight factor Eq. (4.32) to its static limit $C_{k,\omega=0} = 1$ in the momentum relaxation time Eq. (C.63) in appendix C.4.

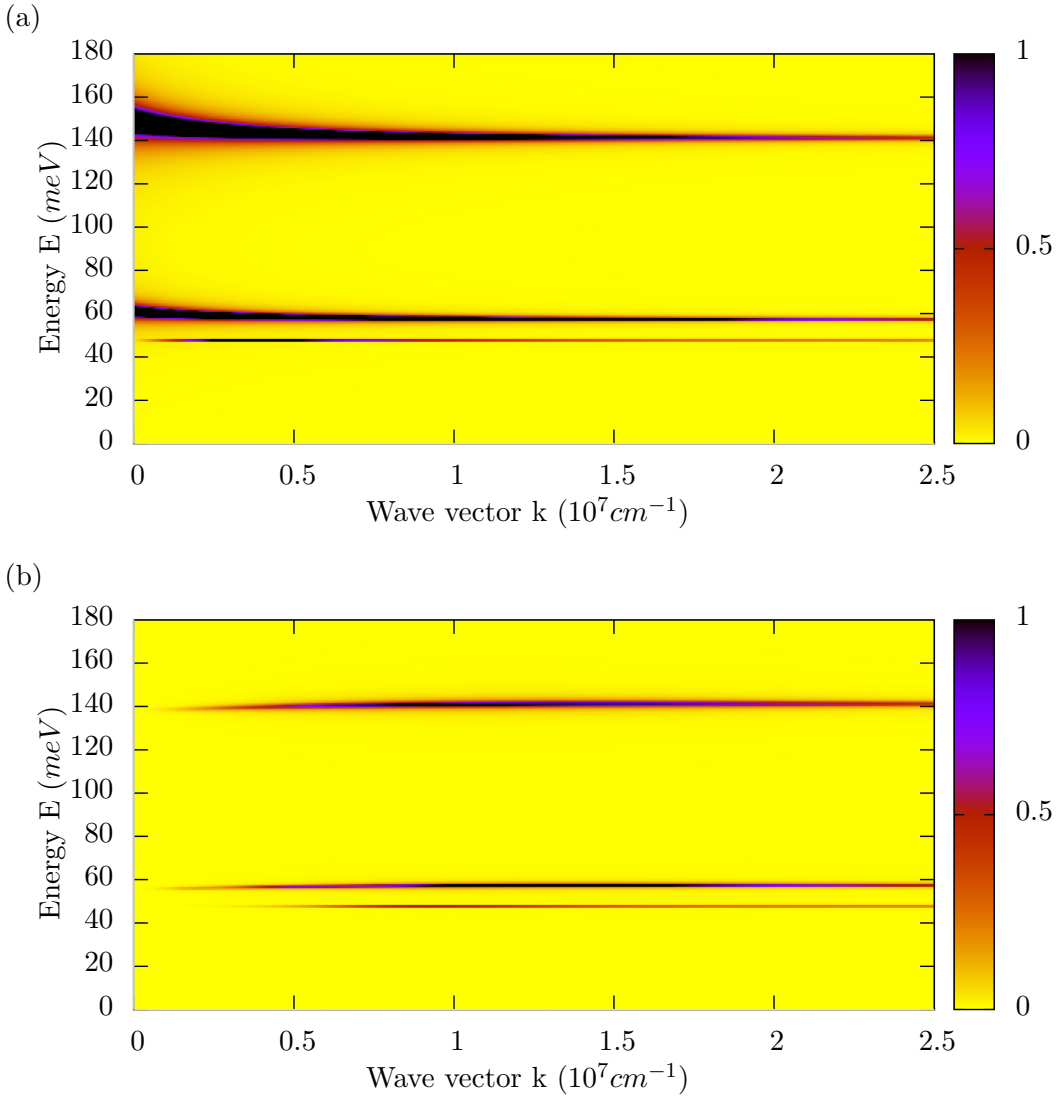

Figure 6.4: $\mathfrak{Im}\left(\frac{-\varepsilon^{\infty}}{\varepsilon^{c}+\varepsilon^{interface}-\varepsilon^{\infty}}\right) \propto W^0_{k,\omega}/\nu_k$ Eq. (3.63) in the SiO_2-MoS_2-vacuum structure at T=300K, $n = 2\times10^{12} cm^{-2}$, as a function of wave vector k and energy $E = \hbar\omega$, with different treatments of screening: (a) no screening $\varepsilon^c = 0$ (b) static screening $\varepsilon^c = \varepsilon^c_{k,\omega=0}$

6.3.1 Neglecting screening

If one neglects electronic screening altogether, the scattering matrix rate will look like Fig. 6.4a, where no hybridization effects occur. Qualitatively, and across all systems considered, one can say that for medium and high carrier concentrations, this will overestimate the scattering. We can also see this in plots of the momentum relaxation rate (Fig. 6.9) or the mobility (Fig. 6.6).

6.3.2 Dynamic screening neglecting phonon drag

Let us illustrate the point we made in chapter 4 that not only the change of the scattering rate on introduction of free carriers is important, but also the lifetime of the coupled modes the carriers scatter with. Therefore we compare the scattering rate for the SiO_2-MoS_2-Vacuum device (Fig. 6.5a), with the corresponding effective scattering element (Fig. 6.5c), and the scattering rate for the HfO_2-MoS_2-SiO_2 device (Fig. 6.5d), with the corresponding effective scattering element (Fig. 6.5f). The respective phonon dissipation factors (Fig. 6.5b and e), capturing the lifetime of the coupled modes reduces the scattering strength of the striking plasmon-like peaks in Fig. 6.5(a) and (d) to the peaks of Fig. 6.5(c) and (f). Qualitatively speaking, we can infer from a comparison of these plots that a neglect of the phonon dissipation factor would dramatically overestimate the scattering.

On the level of the Boltzmann equation, neglecting the finite lifetime of the coupled modes means neglecting the phonon drag term $G_{\boldsymbol{k},\Omega}$ (chapter 4). For a quantitative analysis, we calculate the fully self-consistent, dynamically screened effective momentum relaxation rate neglecting the phonon drag term. Kasiyan and Russu [37] carried out an approximate version of such a calculation. The resulting mobility for the SiO_2-MoS_2-Vacuum structure is plotted in Fig. 6.6a. As expected, the mobility is much lower than for dynamic screening including phonon drag.

Dynamic screening without phonon drag typically (but not always, see HfO_2-MoS_2-SiO_2-sandwich in Fig. 6.6b) yields so-called anti-screening, the effect that scattering is increased, not reduced by the introduction of free carriers.

6.3.3 Dynamic screening including phonon drag

Anti-screening in fact exists, but dynamic screening without phonon-drag overestimates it unless the relevant carrier concentrations are close to the intrinsic carrier concentration.

For low carrier concentrations, longer wavelength hybridized modes contribute more to the scattering of carriers. As we can see in Fig. 6.5, the coupling of the plasmon and phonon modes gives rise to dispersive coupled modes at long wavelengths. The lowest frequencies of these coupled modes are smaller than the lowest optical mode frequencies. If these modes significantly contribute to scattering of carriers, anti-screening can occur. Heuristically speaking, at long wavelengths, the electronic response is slower than the phonon response, so the electrons cannot screen the optical phonon interaction. To the contrary, as these modes have a phonon dissipation factor close to one, they contribute significantly to momentum relaxation.

We can see how anti-screening is captured in the SiO_2-MoS_2-Vacuum structure in

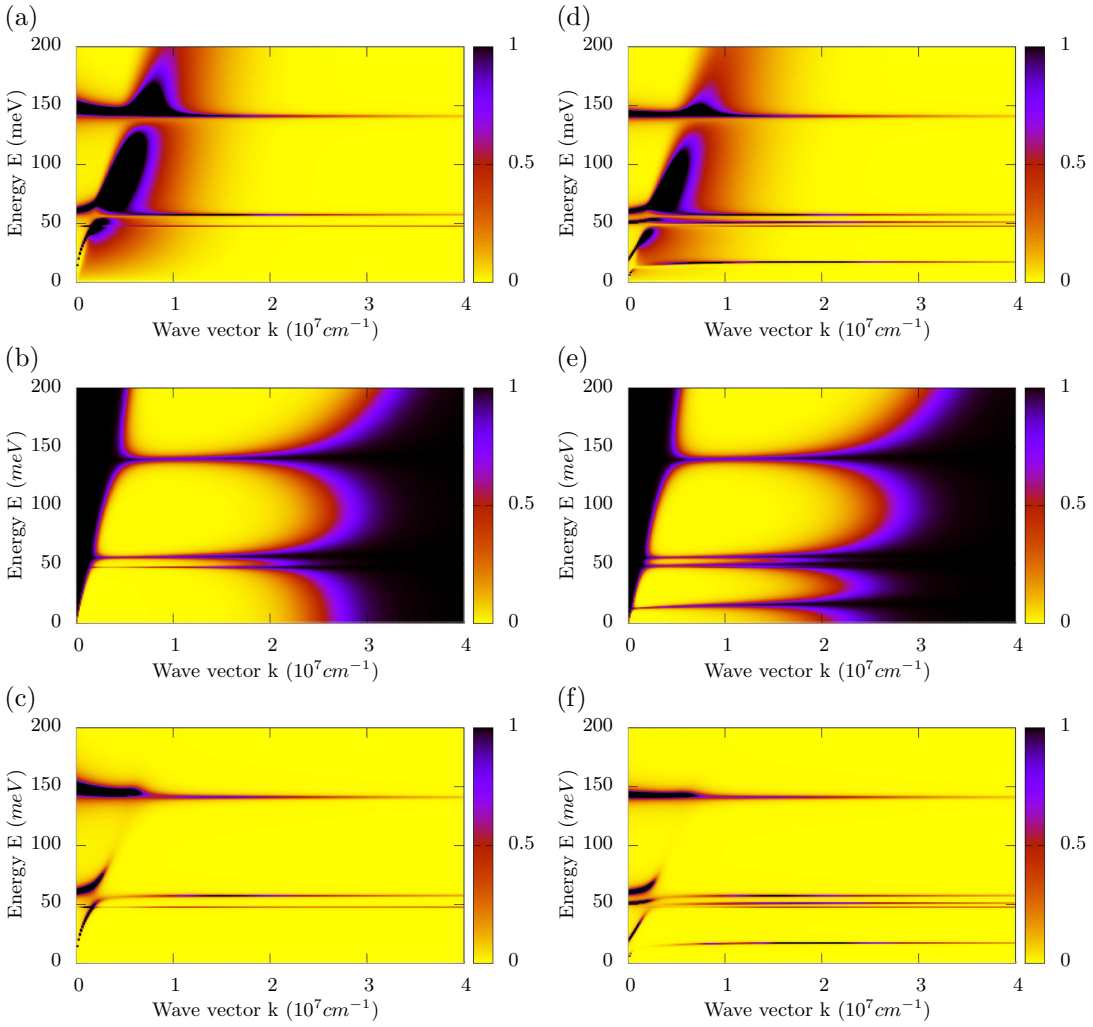

Figure 6.5: (a) and (d): $\mathfrak{Im}\left(-\frac{\varepsilon^{\infty}}{\varepsilon^{tot}_{k,\omega}}\right) \propto W^0_{k,\omega}/\nu_k$, Eq. (3.63) as a function of wave vector k and energy $E = \hbar\omega$ for screened interface phonon scattering in the (a) HfO_2-MoS_2-SiO_2 structure (d) SiO_2-MoS_2-Vacuum structure. (b) and (e): Phonon dissipation weight factor Eq. (4.32) as a function of wave vector k and energy $E = \hbar\omega$ (b) HfO_2-MoS_2-SiO_2 structure (e) SiO_2-MoS_2-Vacuum structure. (c) and (f): Eq. (4.32) $\frac{\mathfrak{Im}\left(\varepsilon^{\text{interface}}\right)}{|\varepsilon^{tot}|^2} \propto W^{0,eff}_{k,\omega}/\nu_k$, Eq. (4.34) as a function of wave vector k and energy $E = \hbar\omega$ as a function of wave vector k and energy $E = \hbar\omega$ for screened interface phonon scattering in the (b) HfO_2-MoS_2-SiO_2 structure (e) SiO_2-MoS_2-Vacuum structure. All plots are for T=300K and $n_S = 2 \times 10^{12} cm^{-2}$.

Fig. 6.6a when we compare the mobility calculated without screening with the mobility calculated with dynamic screening. Fig. 6.7a shows the ratio $\frac{\mu_{\text{dynamic}}}{\mu_{\text{no screening}}}$ between those mobilities directly. Anti-screening is visible for all the structures except the HfO_2-MoS_2-SiO_2 sandwich, whose lowest TO energy is only roughly half the carrier energy at room temperature. This is because the plasmon-like modes which are still lower in energy, and which would have to contribute for anti-screening to

happen, are low in intensity (See Fig. 6.5d and f). See also Fig. 6.6b for more detail on the mobility of the HfO_2-MoS_2-SiO_2 sandwich.

(a)

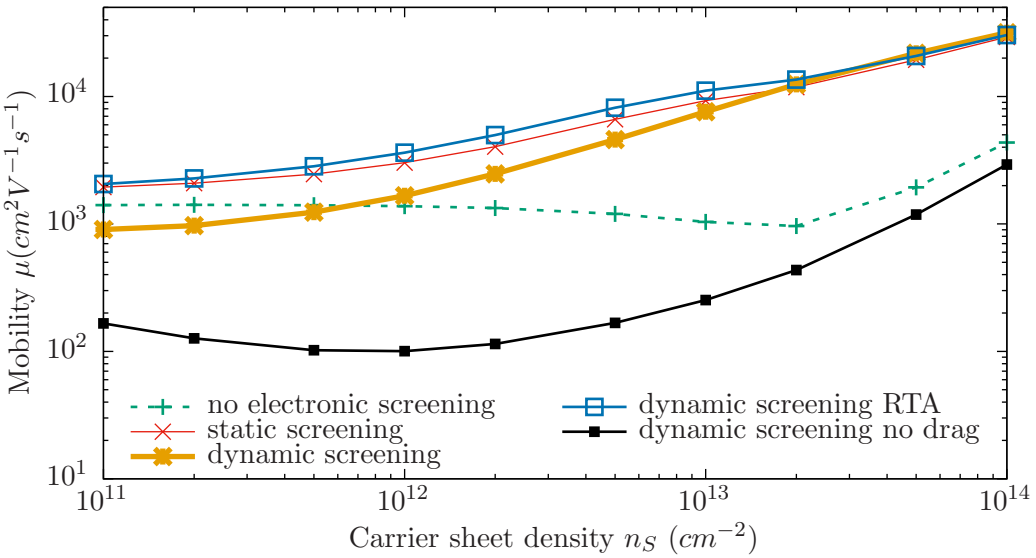

(b)

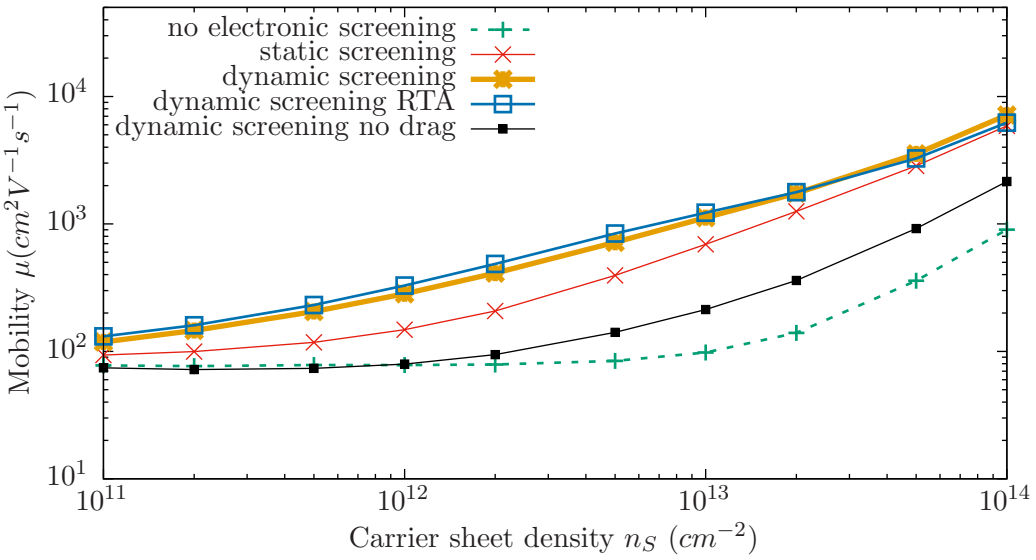

Figure 6.6: Room temperature mobility limited by interface phonon-plasmon scattering in the (a) SiO_2-MoS_2-vacuum (b) HfO_2-MoS_2-SiO_2 structure as a function of carrier sheet density n_S. section 6.3 explains how the mobilities tagged "no screening", "dynamic screening", "dynamic screening RTA", "dynamic screening no drag" and "static screening" are calculated.

6.3.4 Static screening

By treating screening statically, the hybridization effects for small wave vectors are neglected and the scattering rate at the long wavelength limit is generally decreased. (See the statically screened scattering rate in Fig. 6.4b). It is therefore clear that static screening can never describe the anti-screening effect at low carrier concentration. Fig. 6.7b, showing the ratio $\frac{\mu_{\text{static}}}{\mu_{\text{unscreened}}}$ demonstrates this.

At high carrier concentrations, static screening is often a good approximation, because here, the strongly coupled modes lie at very long wavelengths and hence do not contribute much to momentum relaxation. For intermediate carrier concentrations, the effects on the mobility are generally more subtle.

To quantify the mistake one would make by treating screening statically, we plot the ratio $\frac{\mu_{\text{dynamic}}}{\mu_{\text{static}}}$ of the mobility with dynamic and static screening in Fig. 6.8. The error is smaller when one takes all other scattering mechanisms into account, especially for the sandwiches where the interface-phonon-plasmon limited mobility is quite high. (Compare Fig. 6.8a and b.) Even so, statically screening the interface-phonon-plasmon scattering overestimates the total mobility in the SiO_2-MoS_2-Vacuum sandwich by up to 15%, and underestimates the total mobility in the HfO_2-MoS_2-SiO_2 sandwich by up to 75%.

6.3.5 Effect of screening between different sandwiches

In section 5.4, we established that the ratio of the screened to the unscreened mobility increased with an increased effective mass of the carriers, and a decrease of the high frequency dielectric constant. In our X-MoS_2-Y sandwiches, the effective mass is always the same, but their interface dielectric differs. Fig. 6.3 shows the high frequency limit of the interface dielectric functions of the investigated sandwiches. We see that the rough relation "The higher $\varepsilon^{\text{interface}}_{k,\omega\to\infty}$, the lower $\mu_{\text{screened}}/\mu_{\text{unscreened}}$", also holds for the height of the peaks in Fig. 6.7a and b. While static screening (Fig. 6.7b) gets the order of the peaks right, it underestimates their magnitude somewhat.

In the bulk case, $\mu_{\text{screened}}/\mu_{\text{unscreened}} \lesssim 6$ (Fig. 5.10a in section 5.4) compared to that for the X-MoS_2-Y sandwiches $\mu_{\text{screened}}/\mu_{\text{unscreened}} \lesssim 16$ (Fig. 6.7), even though the effective masses of ZnS, which has the largest such ratio of the considered bulk materials, and MoS_2 are almost identical, and the $\varepsilon^{\text{interface}}_{k\approx 1/a,\omega\to\infty}$ around $ka \approx 1$ and $\varepsilon^{\infty}_{ZnS}$ are similar. This difference is due to the difference of the dielectric response of a three-dimensional compared to a two-dimensional electron gas.

In section 5.4 we introduced a critical carrier density where the optical phonon frequency and the plasma frequency are roughly equal, and observed that density was roughly where the peak in $\mu_{\text{screened}}/\mu_{\text{unscreened}}$ lay. For the interface phonon case, such

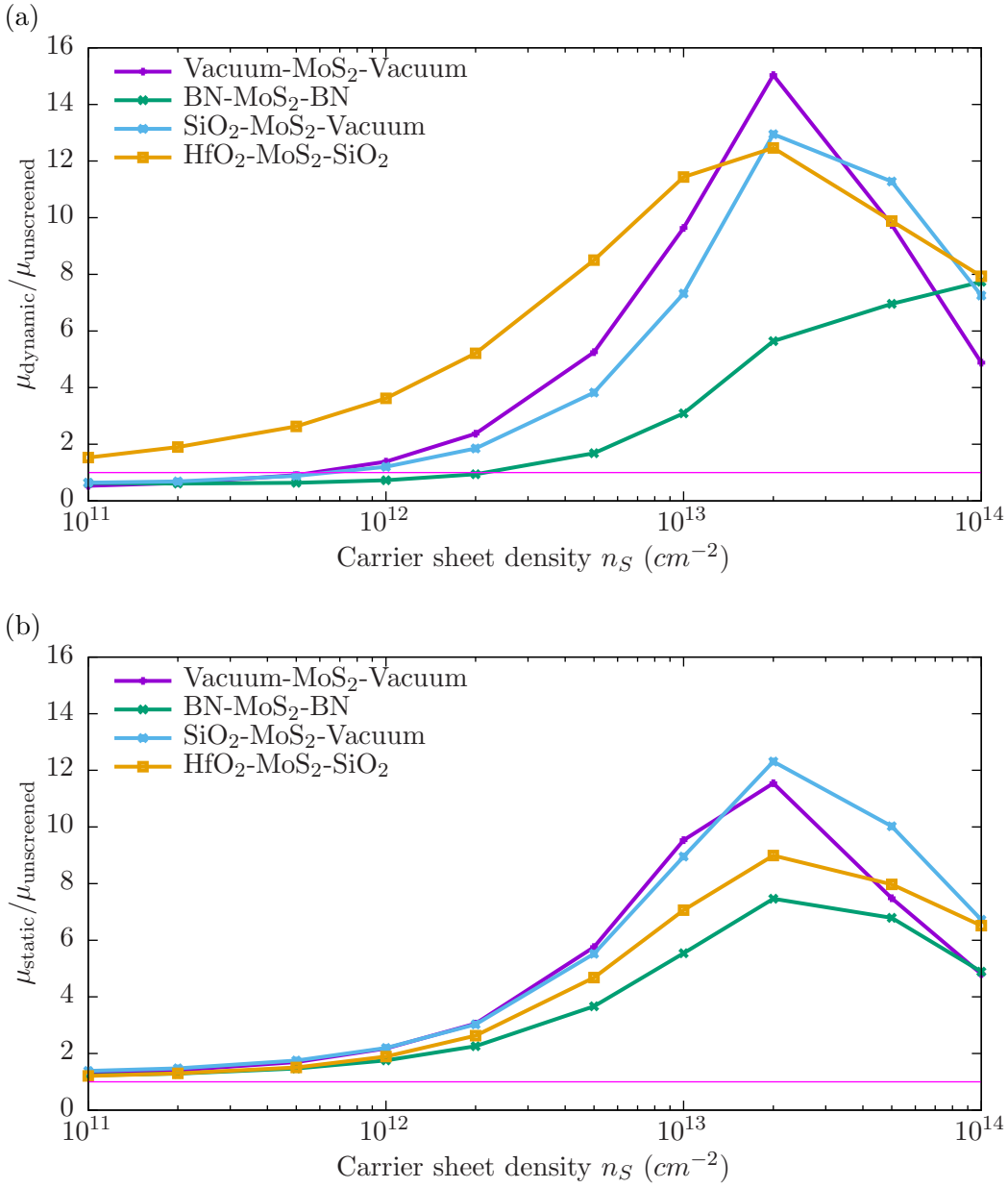

Figure 6.7: Ratio between the screened and unscreened interface phonon scattering limited mobilities in different structures at room temperature as a function of carrier sheet density n_S: (a) Ratio of the dynamically screened to the unscreened mobility $\mu_{\text{dynamic}}/\mu_{\text{unscreened}}$. (b) Ratio of the statically screened to the unscreened mobility $\mu_{\text{static}}/\mu_{\text{unscreened}}$. Section 6.3 explains how the evaluation of the mobilities with "no screening", "dynamic screening" and "static screening" differ.

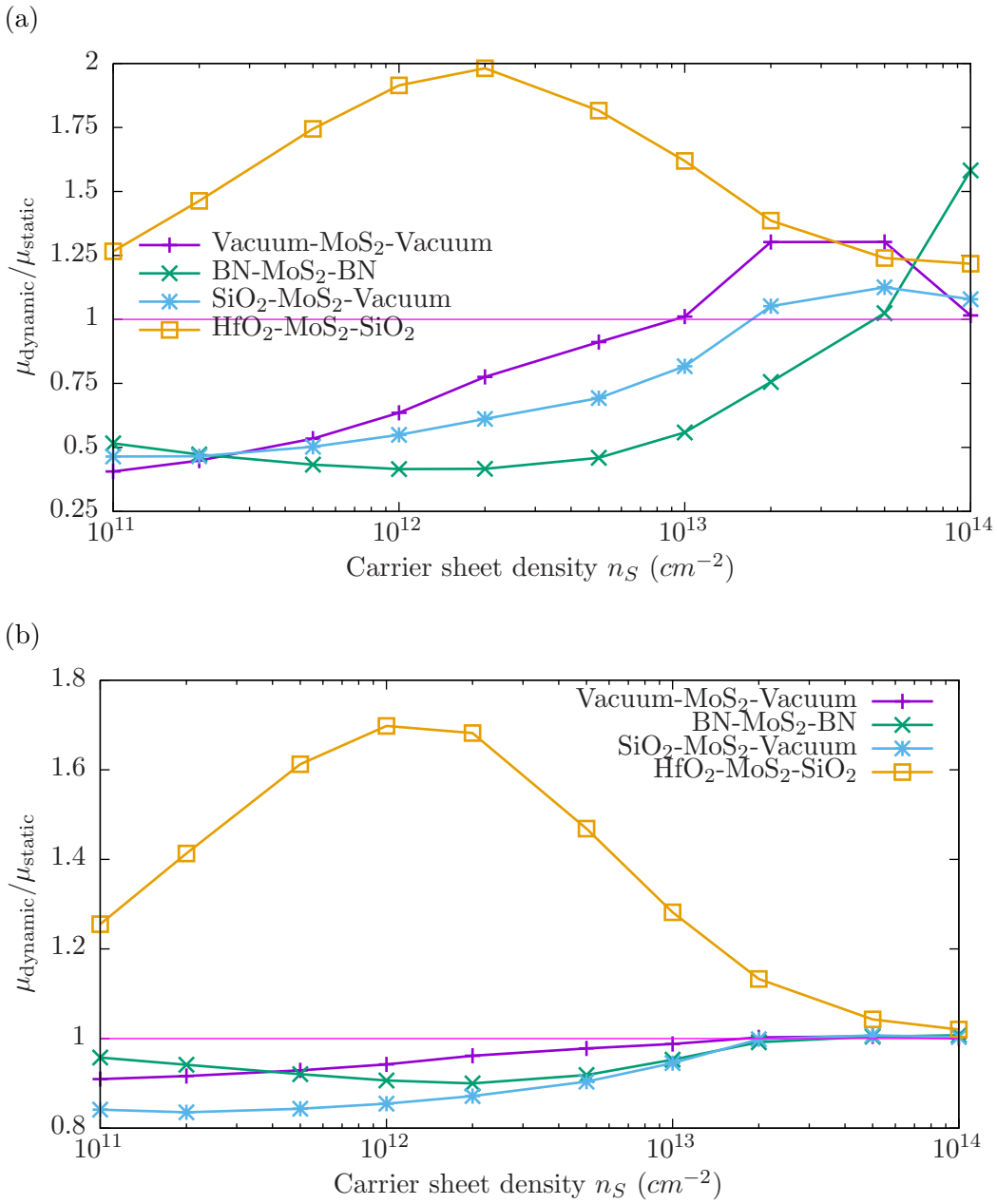

Figure 6.8: Ratio of dynamically to statically screened carrier mobility $\mu_{\text{dynamic}}/\mu_{\text{static}}$ in different structures at room temperature as a function of carrier sheet density n_S: (a) Interface phonon scattering limited mobility (b) Total mobility (also including deformation potential and piezoelectric scattering, see appendix E).

a critical carrier density would be more difficult to define, firstly, because there are more optical phonon modes present, and secondly, because the plasma frequency has a linear, not constant, dispersion in the long wavelength limit. However, we can still see how the peaks in $\mu_{\text{dynamic}}/\mu_{\text{unscreened}}$ in Fig. 6.7a are ordered along the sheet density axes roughly according to the position to their optical phonon frequencies: The HfO_2-MoS_2-SiO_2 sandwich has the lowest TO-phonon frequency and it peaks at the lowest sheet density. The BN-MoS_2-BN sandwich has very high TO-phonon

frequencies apart from the TO-frequencies of the weakly polar MoS_2 which all sandwiches share.

Note that these shifts are absent in the $\mu_{\text{static}}/\mu_{\text{unscreened}}$ in Fig. 6.7b, as static screening is by construction blind to dynamic effects such as the dispersion of the plasma excitations.

6.4 Relaxation time approximation compared to self-consistent solution of the Boltzmann equation

We observed that for the calculations without screening and with static screening, the relaxation time approximation (RTA) is fairly close to the self-consistent solution for all investigated structures. [1] This also holds for the calculations with dynamic screening without the phonon drag term.

However, in general, it does not hold for the calculations with dynamic screening including the drag term. The agreement between the RTA and the fully self-consistent solution is good for the mobility calculations in HfO_2-MoS_2-SiO_2 (Fig. 6.6b), but not for the other investigated structures.

In particular, the RTA does not capture anti-screening, as can be seen in Fig. 6.6a. Explicitly this means, the hybridized modes in $W^{0,eff}_{k,\omega}$ in Fig. 6.5(c) and (f) do not contribute significantly to scattering in the RTA. However, they do contribute critically in the fully self-consistent solution. One can see that in Fig. 6.9, where the fully self-consistent effective momentum relaxation rate (marked "dynamic screening") is larger than its RTA correspondent (marked "dynamic screening RTA") for energies smaller than 60 meV where hybridization occurs, and smaller for energies over 60 meV, where hybridization is less important. The fully self-consistent effective momentum relaxation rate shows none of the steps associated with a certain onset of the emission of optical phonons, seen very strongly in the unscreened curve, and to a lesser extend in the static screening and dynamic screening in RTA curve. This flatness is another indication that the coupling to plasmons, which are dispersive and hence produce less featured momentum relaxation rates, are more important in the fully self-consistent effective momentum relaxation time than in the RTA.

The iteration to self-consistency is a process to find the right balance between the case where all the coupled modes relax momentum (no drag term), and the case where all plasma effects are neglected (no screening case). The RTA is only a rough guess.

Keeping in mind that the effective scattering rate $W^{0,eff}_{k,\omega}$ from Eq. (4.34) only strictly

[1] In all plots, we show the no electronic screening case in the self-consistent solution, but static screening case in the RTA, because the previous study by Ma and Jena [54] used static screening and the RTA.

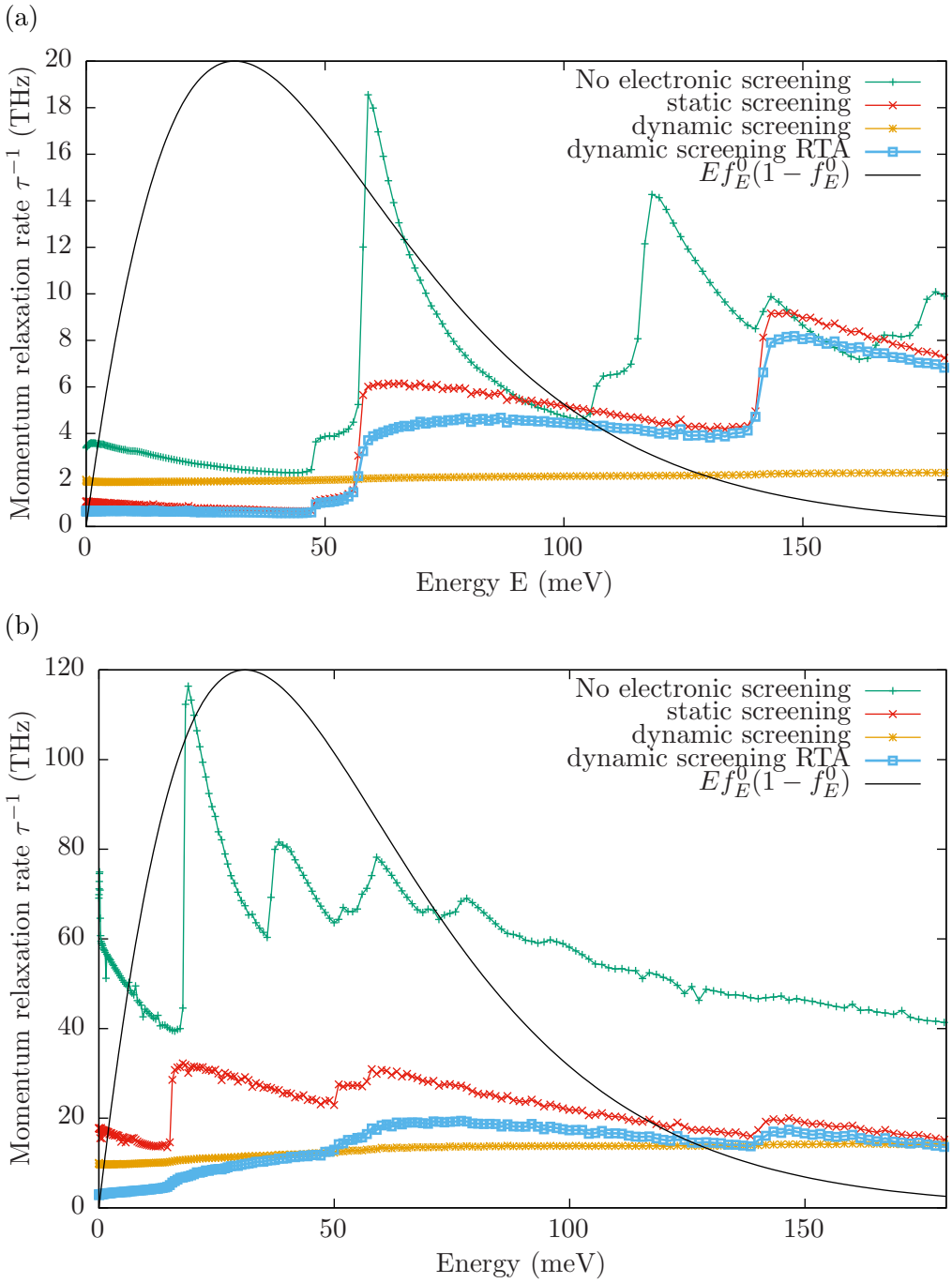

Figure 6.9: Momentum relaxation rate calculated with different treatments of screening, as a function of electron energy E, for a (a) SiO_2-MoS_2-vacuum device. (b) HfO_2-MoS_2-SiO_2 device at T=300K, $n = 2 \times 10^{12} cm^{-2}$. section 6.3 explains how the momentum relaxation rates $\frac{1}{\tau}$ tagged "no screening", "dynamic screening", "dynamic screening RTA", "dynamic screening no drag" and "static screening" are calculated.

has meaning within the RTA, it still conveys some intuition for the qualitative effects of dynamic screening. However, our calculations show that, in general, the RTA is no viable shortcut, and it is necessary to find the fully self-consistent effective momentum relaxation time to capture dynamically screened interface-phonon scattering correctly.

6.5 Present work compared to previous studies

Simulations of the carrier mobility in MoS_2 have mainly been of one of the following two types: The first kind treat freestanding single layers of MoS_2 from first principles, e.g. [57, 5, 103]. Such calculations aim to predict the "intrinsic" carrier mobility, due to scattering with the monolayer MoS_2-phonons. The second kind focuses on other scattering mechanisms, which limit the mobility in realistic devices, taking into account impurities, and the type and dimensions of the surrounding dielectrics [56, 55, 54]. The methodology there tends to rely on effective mass theory and macroscopic electrostatics, though the parameters might be obtained from electron [57, 52] and phonon [18, 19] band structure calculations. Free carrier screening, present due to the impurity doping of non-ideal samples of MoS_2 or due to gating in FETs, falls into the second type of treatment.

Kaasbjerg et al. [57, 5] calculated the intrinsic mobility in a free-standing layer of MoS_2. They performed first principles electronic structure calculations to obtain the relevant scattering matrix elements in the low carrier concentration limit. However, rather than accounting for the free-carriers effects explicitly in another ab-initio calculation, they take screening into account ad hoc by dividing their $n \to 0$ matrix elements by appropriate model dielectric functions [5].

Ma and Jena [54] published a study of the mobility of different structures consisting of MoS_2 surrounded by different dielectrics, using model dielectric functions to statically screen the matrix elements calculated by Kaasbjerg et al. [5]. While lacking the detail of a microscopic dielectric function, these numerically cheap model dielectric functions can capture the electrostatic effects of placing a monolayer of MoS_2 between a large number of permutations of different dielectrics.

This work uses Kaasbjerg et al.'s "screening by hand" approach for composite structures, as Ma and Jena [54] have. Its methodology is very similar to Ma and Jena's in that it also applies single particle transport and macroscopic electrostatics to MoS_2-heterostructures. However, it uses the formalism established in chapter 4 and section 3.2 to focus particularly on the screening of the interface phonon scattering effect, which is important in polar MoS_2-heterostructures.

Comparison of present work with calculations from Ma and Jena [54] In this section, we compare some of our results with some results from the literature. Out of the studies discussed above, [57, 5, 103] give calculation of the carrier mobility as a function of the sheet carrier density, but only for MoS_2 suspended in a vacuum, and neglecting screening. We therefore compare our results with some presented by Ma and Jena [54]. In their Fig. 7(b), they present calculations of a mobility due to statically screened interface phonon scattering, charged impurity scattering, acoustic and optical deformation potential scattering and LO-phonon scattering, as a function of carrier sheet density at room temperature. The impurity concentration is fixed at $N_I = 10^{11} cm^{-2}$. This mobility is plotted against some of our own calculations for a HfO_2-MoS_2-SiO_2 structure in Fig. 6.10. We choose the HfO_2-MoS_2-SiO_2 structure, because its mobility is dominated by screened polar interface phonon scattering, the scattering mechanism we are particularly interested in in this thesis. We include other scattering mechanisms (acoustic and optical deformation potential scattering and piezoelectric scattering, as discussed in appendix E), but they have barely any influence on the total mobility. The effect of neglecting charged impurity scattering, which we have not included, should also be negligible for $N_I = 10^{11} cm^{-2}$. We can see this from Ma and Jena's [54, Fig. 7a] calculations for $n_S = 10^{13} cm^{-2}$ and $N_I = 10^{9} cm^{-2}$, which we included in Fig. 6.10 as a diamond. It lies on the line for the mobilities with a $N_I = 10^{13} cm^{-2}$ impurity concentrations for the HfO_2-MoS_2-SiO_2 structure.

Fig. 6.10 compares calculations of the total room temperature mobility in a HfO_2-MoS_2-SiO_2 structure as a function of carrier sheet density by Ma and Jena [54] to ours. Ma and Jena's treatment of screened interface polar phonon scattering differ from ours in several important points. In order to disentangle the effects of these differences on the mobility from each other, we go step by step: We start with the calculation which we believe to best describe screened polar interface phonon scattering in the HfO_2-MoS_2-SiO_2 structure. We then change our treatment to agree with that by Ma and Jena [54], eliminating one difference at a time. Each change will be discussed first, and then retained for all subsequent calculations. Incidentally, each of these changes reduces the mobility by a certain amount, until we finally reproduce Ma and Jena's mobilities quite accurately, which are around an order of magnitude lower than our "dynamic screening" results from Fig. 6.10.

1. Dynamic screening: Our best description of interface polar phonon scattering involves dynamic screening as discussed in section 6.3. This curve was first presented in Fig. 6.2(b), and is marked "dynamic screening" in Fig. 6.10.

2. Static screening and the RTA: Ma and Jena [54] employ static screening and the relaxation time approximation. We include our calculation of with static screening and the RTA in Fig. 6.10 marked "Static screening RTA". As shown in

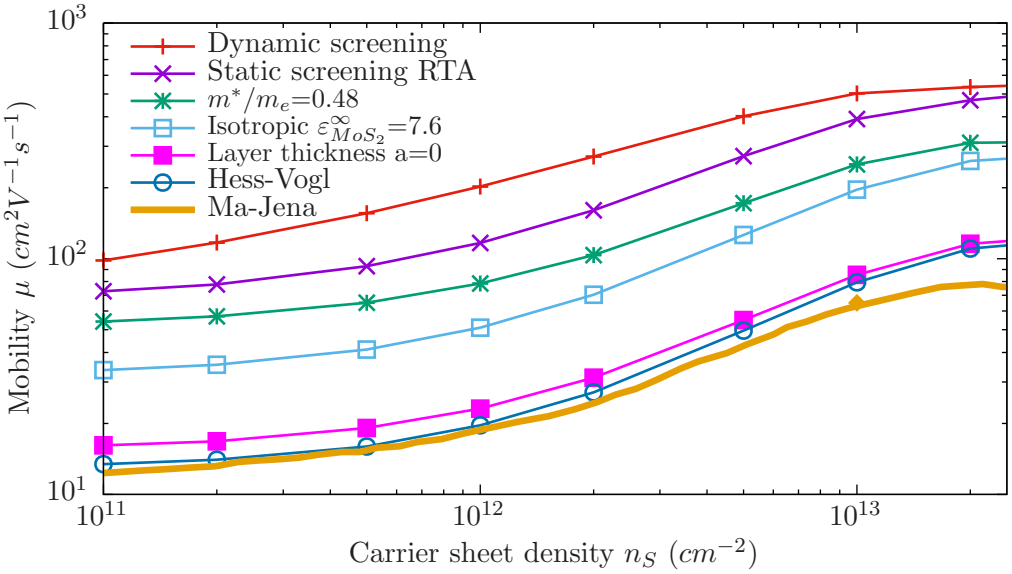

Figure 6.10: Room temperature mobility in a HfO_2-MoS_2-SiO_2 structure as a function of carrier sheet density. The thick orange solid line is from a calculation by Ma and Jena [54]. All other curves are from our calculations. The top red line with the crosses marked "dynamic screening" is our best description of the mobility in the HfO_2-MoS_2-SiO_2 structure, and was first presented in Fig. 6.2(b). Each successive curve is marked with the additional assumption that has been made to calculate it, as explained in section 6.5.

Fig. 6.8b, using static rather than dynamic screening decreases the mobility by up to 43%. All calculations described below also employ static screening and the RTA.

3. MoS_2 effective mass: Ma and Jena use the LDA effective mass of $m^* = 0.48m_e$ [57]. We used a GW effective mass of $m^* = 0.35m_e$ [52], because GW band structures compare more favorably with experiment than those calculated in the LDA (cf. [104] and references therein). From here on, we will use the LDA value of $m^* = 0.48m_e$, like Ma and Jena. This causes the mobility to decrease by about 25% to 35% throughout all carrier densities.

4. Isotropic dielectric constant of MoS_2: Ma and Jena use an isotropic dielectric constant of MoS_2 of 7.6.[2] We use a formalism (subsection 3.2.2) which accounts for the anisotropic dielectric functions of MoS_2. Our effective scalar high frequency constant for MoS_2 $\varepsilon'^{\infty}_{MoS_2} = 9.7$, see Tab. 2.3 and Eq. (3.50). Taking Ma and Jena's isotropic dielectric constant decreases the mobility by between 38% at low carrier sheet density and 20% at high carrier concentration.

5. Interface layer thickness: Ma and Jena use an expression for the polar interface phonon scattering limited mobility which only holds if the MoS_2-interface layer

[2] They do not specify if this is supposed to be ε^{∞} or ε^0, but as the LO-TO splitting in MoS_2 is very small [18, 19], this does not matter much.

is infinitely thin, $a = 0$. We account for a finite layer thickness a=6.145Å, see subsection 3.2.2. Fig. 6.11 shows how, according to our continuum model, the unscreened polar interface scattering limited mobility would vary if it was possible to change the thickness of a monolayer of MoS_2 at will. The inset demonstrates that the mobility would change drastically if one could vary the layer thickness by several orders of magnitude. The main figure shows that changes of the layer thickness by a fraction of an Å around our value of a=6.145Å, a realistic guess for the uncertainty of a, has much smaller effects on the mobility. Still, setting $a = 0$, as Ma and Jena do, reduces the mobility by more than a factor of two for all the considered n_S.

6. Hess and Vogl treatment: Ma and Jena treat the HfO_2-MoS_2-SiO_2 structure with Hess and Vogl's expression for interface polar phonon scattering (discussed in subsection 3.2.2, Eq. (3.67)). Here, this means "switching off" the polar phonons in SiO_2 by fixing the silica dielectric function at its high frequency limit, ignoring the electrostatics of the MoS_2-layer, and only considering the lowest frequency polar phonon in HfO_2. This reduces the mobility further to give very good agreement with Ma and Jena's calculation.

Implementing all these changes gives excellent agreement between our mobility calculations and those by Ma and Jena [54] at low carrier sheet densities. Ma and Jena's slightly lower mobilities at high carrier sheet densities could be due to an inconsistency of their treatment of electrostatics in screening: While they neglect the MoS_2 thickness in their treatment of unscreened interface polar phonon scattering, they take it into account in their generic treatment of screening of all scattering processes. Another possible cause for the slight discrepancy are differences in the treatment of other scattering mechanisms (appendix E). We checked that our different treatment of the electronic wave functions in the transverse directions (Ma and Jena have particle in a box wave functions, and we delta functions) amounts to less than a 3% difference in the mobility at any n_S.

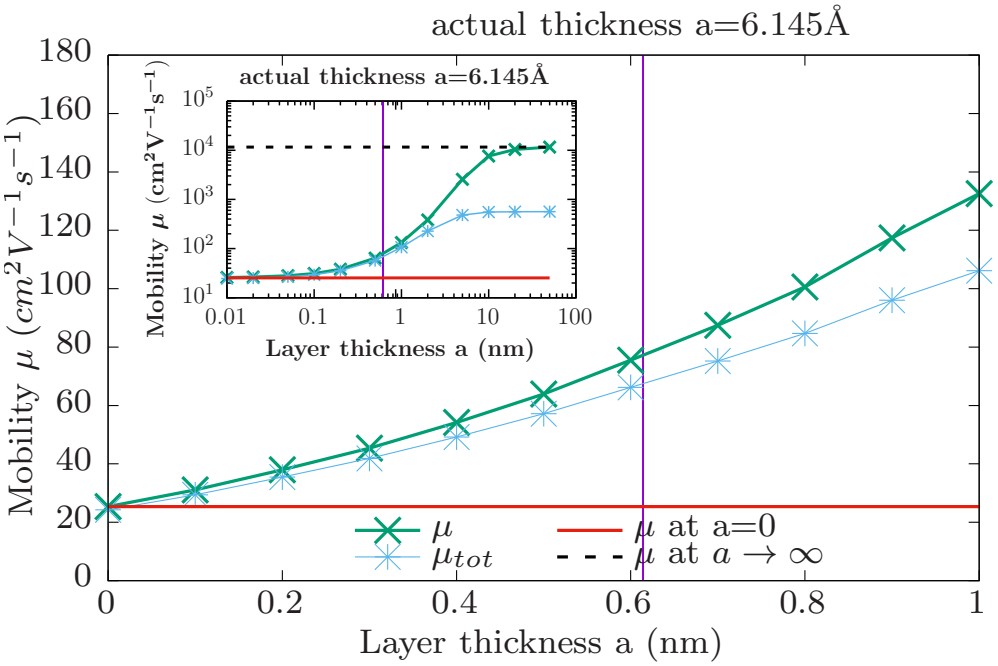

Figure 6.11: Dependence of the mobility μ due to unscreened polar interface phonon scattering and the total mobility μ_{tot} on the thickness a of the interface layer in structures of the type described in Fig. 3.4b. This plot is for a HfO_2-MoS_2-SiO_2 structure at room temperature and a carrier sheet density $n_S = 10^{11}cm^{-2}$. The main plot shows layer thicknesses around the actual thickness of MoS_2 of a=6.145Å, while the inset shows how the mobilities when a is varied over several orders of magnitude.

Chapter 7

Conclusions and Outlook

7.1 Conclusions

The aim of this thesis was to develop a formalism which describes momentum relaxation due to carriers scattered by coupled longitudinal-optical phonons and plasmons. This seems difficult, because the mechanisms for momentum relaxation due to carrier–LO-phonon modes and carrier–carrier scattering are very different, and previous authors have struggled with treating momentum relaxation due to carrier scattering with coupled plasmon-LO-phonon modes in terms of one of those two mechanisms, or a mixture of the two [37, 1, 47, 48]. We overcame these struggles by modeling the momentum relaxation mechanism due to carrier–collective mode scattering, and recognizing that these two different momentum relaxation mechanisms mentioned above mark two limiting cases of the momentum relaxation mechanism of coupled LO-phonon–plasmon excitations.

To understand this, we needed to focus on the effect of the non-equilibrium collective excitations in the coupled Boltzmann equations for collective longitudinal excitations and carriers. The crucial term in the collective mode Boltzmann equation is known as the "phonon drag" term in the context of thermal conductivity [25], where phonons obtain momentum from interaction with carriers, or are, colloquially speaking, "dragged along". We improved on previous models [47, 48, 1, 37] by including the anharmonic lifetime of the coupled collective excitations in the Boltzmann equation for the collective excitation. This quantity affects the drag term, and consequently the momentum relaxation rate:
If carriers transfer momentum into a collective mode with an anharmonic lifetime which is much longer than the carrier-collective mode relaxation time, the collective mode will likely not decay before it can transfer the momentum back to the carriers. Conversely, if carriers transfer momentum into a collective mode with an anharmonic lifetime which is much shorter than the carrier-collective mode relaxation time, it will

likely decay almost immediately, and the carrier momentum will be lost. Conventionally, carrier–plasmon scattering has been treated in the infinite lifetime limit, and carrier–LO-phonon scattering in the zero lifetime limit. Our approach naturally unites these two limits by assigning a finite lifetime to each of the coupled collective modes.

Solving the two coupled Boltzmann equations for the carriers and the collective modes self-consistently requires a certain numerical effort in the most general cases, and it is not always immediately obvious why the resulting momentum relaxation times and mobilities behave the way they do. We carefully analyzed these calculations in order to establish an intuitive understanding for momentum relaxation due to carrier–collective mode scattering. Studying the relaxation time approximation (RTA) limit to our self-consistent solution to the coupled Boltzmann equations proved particularly enlightening in that regard. Our formulas for the RTA momentum relaxation time are as simple to use as the equations for energy relaxation by Kim et al. [36]. More importantly, our solution naturally introduced the phonon dissipation weight factor, the ratio between the imaginary part of the dielectric function of the phonons alone and the imaginary part of the total dielectric function. This quantity lets us assess how phonon-like or plasmon-like the coupled excitations behave at a certain frequency and wave vector when it comes to degradation of an electric current. We used map plots of the phonon dissipation weight factor in a wave vector–frequency plane alongside map plots of the scattering rate to help develop an intuition for momentum relaxation. Map plots of the scattering rate can help to illustrate energy relaxation by showing at which wave vector and frequency the collective excitations scatters carriers the most strongly. Map plots of the phonon dissipation weight factor assign a number between zero and one to the collective mode corresponding to their decay mechanism – with one meaning LO-phonon-like decay and zero meaning plasmon-like decay. Combining the scattering rate and the phonon dissipation factor yields our "effective scattering rate". Map plots of the effective scattering rate hence shows peaks at wave vectors and frequencies where the collective excitations contribute most strongly to momentum relaxation.

When we applied our approach to dynamically screened electron–LO-phonon scattering in bulk polar semiconductors, we observed that the mobility limited by coupled collective mode scattering is most increased compared to mobility limited by pure LO-phonon scattering at a density where the plasma frequency is similar to the optical phonon frequencies. Calculations for a variety of direct gap polar semiconductors assuming a single, spherical conduction band indicate that this increase is strongest for materials with large effective mass and small high-frequency dielectric constant.

We also investigated the effect of the treatment of screening and the RTA on

momentum relaxation in bulk polar semiconductors, by comparing our fully self-consistent, dynamically screened results to such obtained in other methods. These methods included the RTA limit of our own approach, and the Thomas-Fermi screening with the RTA, which gave good qualitative agreement with our mobility calculations in room temperature GaAs for a range of carrier densities.

Finally, we applied our approach to screened polar interface phonon scattering in structures where a monolayer of molybdenite lies between different polar dielectrics. We found that the difference between screened interface phonon scattering (i.e., coupled collective mode scattering) and unscreened interface phonon scattering is strongest for heterostructures with a small high frequency interface dielectric function, which is an insight that carries over from the bulk case. Our fully self-consistent dynamically screened interface phonon scattering calculation can capture anti-screening at low carrier concentration, unlike previous calculations of interface phonon scattering, which used static screening and the RTA. [54] Using static screening leads to an overestimation of the total mobility by up to 15% at low electron concentrations around $n_S = 10^{11} cm^{-2}$ in devices with a molybdenite monolayer on silica, due to the neglect of anti-screening. In devices with a monolayer of molybdenite between hafnia and silica, static screening can underestimate the mobility by up to 75% at intermediate carrier concentrations around $n_S = 10^{12} cm^{-2}$. At high carrier concentrations, the agreement between static and dynamic screening is good.

We also demonstrated that taking the thickness of the MoS_2 layer into account as far as electrostatics are concerned is important for the mobility. It changes the mobility of a structure with a monolayer of MoS_2 between hafnia and silica by more than a factor of two for all considered carrier sheet densities.

Given these findings, we recommend carrying out a fully self-consistent dynamically screened LO-phonon or interface phonon scattering calculation including phonon drag if the LO-phonon or interface phonon scattering contributes significantly to the total mobilities, and the relevant carrier concentrations are in an intermediate regime.

7.2 Outlook

Below are some thoughts on the accuracy of the formalism developed in this thesis and its applicability beyond the examples discussed in it, in no particular order.

- Our best calculations for the total mobility in n-type GaAs at room temperature yield larger mobilities than experiment throughout the considered carrier concentrations. We would need to include non-parabolicity in our calculations in order to compare our GaAs calculations with experiment in any meaningful way. The large effect we would expect non-parabolicity to have in

p-type semiconductors is a major reason why we chose n-type semiconductors for the calculations in this thesis.

The effects of non-parabolicity on the occupation of the bands is quite easy to capture within the Kane [105] model, cf. [100, 106], but the effects of non-parabolicity on the momentum relaxation time itself would require more significant changes. Rode [100] included non-parabolicity effects in the fully-self-consistent solution to the carrier-Boltzmann equation. This should give an indication of what is required to take non-parabolicity into account in the coupled carrier and collective mode Boltzmann equations.

- The calculations in bulk polar semiconductors were carried out assuming one perfectly parabolic, spherical conduction band. Neglecting inter-valley scattering, this could be generalized to materials with several spherical parabolic bands, and we applied this generalization to transport in monolayer MoS_2, which has two equivalent conduction band valleys.

  An extension of our approach to materials with parabolic and elliptical bands would be conceptionally straightforward, if computationally cumbersome. We formulated our treatment of momentum relaxation due to carrier-collective mode scattering such that it also applies to carriers in parabolic, but non-spherical bands, cf. chapter 4. However, such a treatment would require the carrier dielectric functions to be recalculated for elliptical bands, and the explicit evaluation of the Boltzmann integrals (cf. appendix C.3 and appendix C.4) would differ.

  It is possible that a simple re-scaling of the ellipsoidal bands to spherical bands as discussed by Herring and Vogt [107] would yield expressions similar to the ones for the spherical bands. However, as this approach should not in general yield isotropic carrier dielectric functions (cf., e.g., [108]), the resulting expressions for the momentum relaxation time would be more complicated than the spherical ones.

- Our formalism relies heavily on the RPA, and cannot capture mechanisms beyond the RPA, such as the excitation of multiple pairs rather than just single pairs [32]. There have been attempts to improve on the RPA, e.g., by introducing correction factors into the dielectric function [109, 110, 63]. Such corrections could probably be incorporated into our method, but given that even descriptions in terms of simpler dielectric functions (like the Thomas-Fermi-limit) can yield reasonable results, the benefits might not justify the additional effort.

- Our derivation of the effective scalar dielectric function in section 3.2, which we use to describe the polar semiconductor heterostructures can only be used with

phonon dielectric functions which do not depend on wave vector in the present form. This has to do with local field effects and ties in with the question whether our continuum model gives an accurate description of the electrostatics of such a small-scale structure. It would be interesting to see dielectric functions for the composite structures discussed here calculated from first principles, taking into account the detailed atomistic structure of the heterostructure, and how mobilities calculated within our method with this dielectric function would differ from the ones calculated with the continuum model.

- There are indications in this work that the minutia of the dielectric function influences the carrier mobility due to screened interface phonon scattering, which we have not explored in this thesis. Plotting the ratio of the screened to the unscreened mobility for a much denser carrier concentration grid than in Fig. 6.7 reveals that the peak in Fig. 6.7 really consists of multiple peaks of smaller width, which are associated with different optical phonon modes in the dielectric function of the composite structure. This demonstrates a sensitivity of the carrier mobility to the dielectric function which relates back to the point raised above about the possibility of calculating the dielectric function from first principles.
- We already briefly discussed in subsection 3.2.4 what the extension from truly-2d to what we called "pseudo-2d" systems would entail. This is mainly an increase in bookkeeping, as we now substitute Eq. (3.64), the carrier energy which now depends on the subband energies E_n into the equations for the carrier dielectric functions in section 2.2 and in all the Boltzmann equations in chapter 4. The transverse wave functions in pseudo-2d materials would enter through the scattering rate, and affect the screening. On the level of technical complexity, a MOSFET with multiple layers of MoS_2 as a channel material, which is an interesting system to study on its own merit, would be an intermediate step towards pseudo-2d systems.

Appendix A

Landau damping for three-dimensional classical plasmas

In this appendix, we give a derivation of the carrier dielectric function in the classical limit, as derived by Landau [2]. We then calculate the complex-valued, wave vector dependent plasma frequency from zeros of this dielectric function. The imaginary part of the plasma frequency can be seen as the damping rate of the plasma oscillation. This damping mechanism is now called "Landau damping", after Landau's 1946 paper [2].

A.1 Landau's article [2]

Landau damping is now textbook material, e.g. [111, 112]. We will largely follow the presentation and notation of the material in Landau's original article [2]. This means that there will be some differences to the notation in the rest of the thesis. For example, in the classical context, we describe a particle's energy in terms of its velocity rather than its wave vector, $E = \frac{1}{2}mv^2$. This differences in notation should not be problematic, because this appendix is a stand-alone part of this thesis.

Let us consider a slightly disturbed plasma. The perturbation $f_1(\boldsymbol{r}, \boldsymbol{v}, t)$ is small compared to the equilibrium distribution function $f_0(\boldsymbol{v})$. The Vlasov equation [113]

$$\frac{\partial f}{\partial t} + \boldsymbol{v} \cdot \frac{\partial f}{\partial \boldsymbol{r}} + \frac{\boldsymbol{F}}{m} \cdot \frac{\partial f}{\partial \boldsymbol{v}} = 0 \tag{A.1}$$

holds for the total distribution function to first order

$$f(\boldsymbol{r}, \boldsymbol{v}, t) = f_0(\boldsymbol{v}) + f_1(\boldsymbol{r}, \boldsymbol{v}, t), \tag{A.2}$$

and can be written as

$$\frac{\partial f_1}{\partial t} + \boldsymbol{v} \cdot \frac{\partial f_1}{\partial \boldsymbol{r}} + \frac{\boldsymbol{F}}{m} \cdot \left(\frac{\partial f_0}{\partial \boldsymbol{v}} + \frac{\partial f_1}{\partial \boldsymbol{v}} \right) = 0. \tag{A.3}$$

Hence, the Vlasov equation is equivalent to a Boltzmann equation without collision terms, cf. chapter 4.

We assume a homogeneous ion distribution. In solid state physics this is often called a jellium model, e.g. [24]. The equilibrium electronic charge $e \int \mathrm{d}\boldsymbol{v}\, f_0(\boldsymbol{v})$ cancels out the background ionic charge $|e|NZ$, so that the plasma is neutral in the absence of perturbations.

In general $\boldsymbol{F}$ includes both external fields, and the self-consistent fields of electrons and ions in the plasma. In our case $\boldsymbol{F} = e\boldsymbol{E}$ is only the self-consistent field due to a small perturbation of the electrons. Gauss's law, e.g., [6]

$$\nabla \cdot \boldsymbol{E}(\boldsymbol{r}, t) = 4\pi\rho(\boldsymbol{r}, t) = 4\pi e \int \mathrm{d}\boldsymbol{v}\, f_1(\boldsymbol{r}, \boldsymbol{v}, t) \tag{A.4}$$

provides the connection between f_1 and $\boldsymbol{E}$, and tells us that $\boldsymbol{E}$ is also a perturbation of the order of f_1. That means that the last term in the Vlasov equation (A.3) is of second order in the perturbation, so that the linearized Vlasov equation reads

$$\frac{\partial f_1}{\partial t} + \boldsymbol{v} \cdot \frac{\partial f_1}{\partial \boldsymbol{r}} + \frac{e\boldsymbol{E}}{m} \cdot \frac{\partial f_0}{\partial \boldsymbol{v}} = 0. \tag{A.5}$$

The scenario described has been called a "Vlasov-Poisson" model, for example in the review article [70]; this becomes more obvious if one uses the electrostatic potential φ such that

$$\boldsymbol{E} = -\nabla\varphi \tag{A.6}$$

in equation (A.5) and (A.4).

Vlasov solved Eq. (A.5) only after Fourier-transforming them. [113] Only Landau solved the linearized Vlasov equation as an initial value problem, found damped vibrations, and gloated that "most of [Vlasov's previous undamped] results turn out to be incorrect" [2].

Initial value problem

This discussion follows Landau's original paper[2] quite closely. Some additional explanations are taken from [114],[111] and [112]. Landau considered how a small perturbation that was turned on at $t = 0$ evolves. To that end he took the Fourier

transform in position of the Vlasov-Poisson-equations

$$\frac{\partial f_{1,\boldsymbol{k}}}{\partial t} + i\boldsymbol{v}\cdot\boldsymbol{k} f_{1,\boldsymbol{k}} - \frac{e\nabla\varphi_{\boldsymbol{k}}}{m}\cdot\frac{\partial f_0}{\partial \boldsymbol{v}} = 0 \tag{A.7}$$

$$k^2\varphi_{\boldsymbol{k}} = 4\pi e\int \mathrm{d}\boldsymbol{v}\, f_{1,\boldsymbol{k}}(\boldsymbol{v}) \tag{A.8}$$

and the Laplace transform

$$g_p = \int_0^\infty \mathrm{d}t\, e^{-pt} g(t) \quad p\in\mathbb{C}, \tag{A.9}$$

in time. Here, we use Landau's notation, where p is a complex frequency, whose real part corresponds to the damping rate, and whose imaginary part corresponds to the frequency:

$$p = -i\omega + \gamma \tag{A.10}$$

The Laplace transform, as a one-sided transform, is well suited for initial value problems, and the Laplace transform of a derivative

$$\int_0^\infty \mathrm{d}t\, e^{-pt}\frac{dg(t)}{dt} = pg_p - g(0) \tag{A.11}$$

features the value of the function g at the time $t = 0$.

In order to make the following equations more reader-friendly, we drop the index $\boldsymbol{k}$, and we set $\boldsymbol{k} = k\boldsymbol{e}_z$ without loss of generality. The Laplace-transformed Vlasov-Poisson equations read

$$(p + ikv_z)f_{1,p} - ik\frac{e}{m}\varphi_p\frac{\partial f_0}{\partial v_z} = f_{1,t=0} \tag{A.12}$$

$$k^2\varphi_p = 4\pi e\int \mathrm{d}\boldsymbol{v}\, f_{1,p}(\boldsymbol{v}). \tag{A.13}$$

The first equation can be solved for $f_{1,p}$, and substituted into the second equation. This yields

$$\varphi_p = \frac{4\pi e}{k^2}\frac{\int \mathrm{d}\boldsymbol{v}\,\frac{f_{1,t=0}(\boldsymbol{v})}{p+ikv_z}}{1-\frac{4\pi i e^2}{km}\int d\boldsymbol{v}\frac{\partial f_0(\boldsymbol{v})\partial v_z}{p+ikv_z}}. \tag{A.14}$$

To illustrate that the problem is essentially longitudinal, the integrations along the v_x and v_y can already be carried out. Defining

$$F_0(v_z) = \int_0^\infty \mathrm{d}v_x \int_0^\infty \mathrm{d}v_y\, f_0(\boldsymbol{v}) \tag{A.15}$$

$$F_{1,t=0}(v_z) = \int_0^\infty \mathrm{d}v_x \int_0^\infty \mathrm{d}v_y\, f_1(t=0,\boldsymbol{v}) \tag{A.16}$$

the previous expression for φ_p becomes

$$\varphi_p = \frac{4\pi e}{k^2} \frac{\int \mathrm{d}v_z \, \frac{F_{1,t=0}(v_z)}{p+ikv_z}}{1 - \frac{4\pi i e^2}{km} \int \mathrm{d}v_z \, \frac{\partial F_0(v_z)/\partial v_z}{p+ikv_z}}. \tag{A.17}$$

The denominator of this is

$$\varepsilon(k,p) = 1 - \frac{4\pi e^2}{mk^2} \int_{-\infty}^{\infty} \frac{\mathrm{d}v}{v - ip/k} \frac{\partial F_0(v)}{\partial v}, \tag{A.18}$$

the dielectric function of the plasma.

Finally, the time dependence of the potential can be determined using the inverse Laplace transform

$$\varphi(t) = \frac{1}{2\pi i} \int_{\sigma-i\infty}^{\sigma+i\infty} \mathrm{d}p \, \varphi_p e^{pt}, \quad \sigma > p_{max} \text{ and } \sigma > 0 \tag{A.19}$$

where the integration path is defined as a line parallel to the imaginary p-axis in the right half plane, which must lie to the right of all the poles p_n of φ_p to ensure convergence.

That means that the singular point in the integrands in the expressions for φ_p and ε_p above, $v = i\frac{p}{k}$ lies in the upper half plane, see Fig. A.2(a). As the velocity integration goes along the real axis, i.e., always below the singular point, the integrands in eq (A.17) will never be singular.

The potential $\varphi(t)$ can be expressed in a neat way if $\varphi_p e^{pt}$ is an analytic function to the left of the line σ except for isolated poles (meromorphic) [1] That means that we can use the residue theorem to express $\varphi(t)$ as

$$\varphi(t) = \sum_n \mathrm{Res}\left(\varphi_p e^{pt}, p_n\right), \tag{A.20}$$

while we have to show that the integral along the path that closes the contour vanishes, see Fig. A.1.

However, for φ_p to be meromorphic, we have to analytically continue the integrals of the form

$$\int_{-\infty}^{\infty} \mathrm{d}v \, \frac{g(v)}{v - ip/k} \tag{A.21}$$

in Eq. (A.17) into the left half plane, $\Re(p) <= \sigma$. That means that the pole in the integrand in Eq. (A.21), at $v = ipk$ can move into the lower half plane $\Im(v) <= 0$.

[1] For this appendix, an undergraduate level understanding of complex analysis is helpful, see, for example [115].

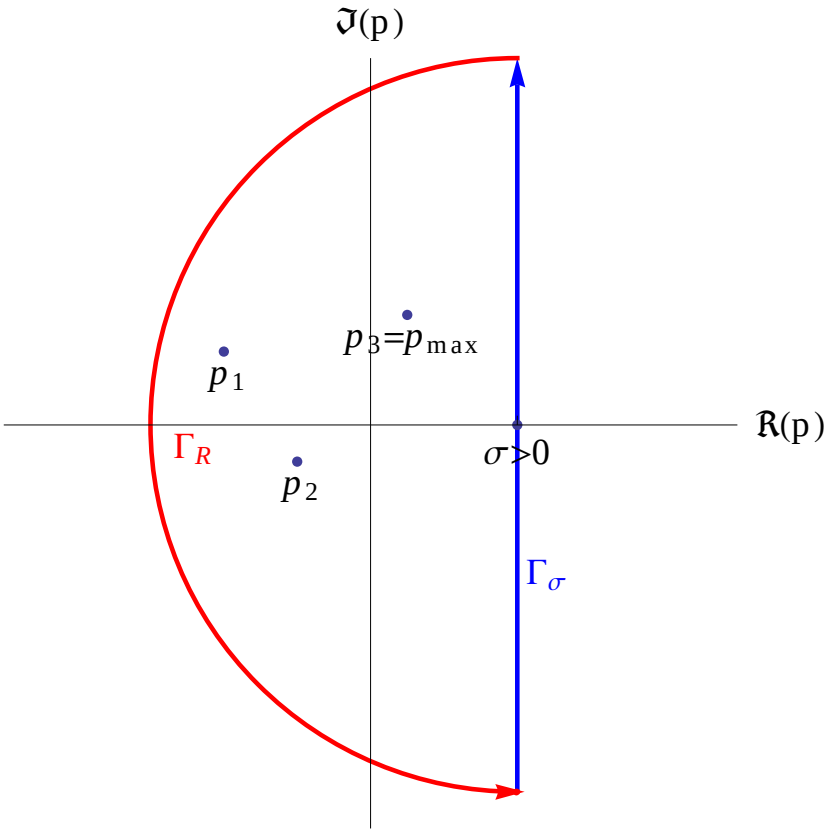

Figure A.1: Integration path in Eq. (A.19) goes along Γ_σ. For Eq. (A.20) to hold, the integral along Γ_R in the limit $R \to \infty$ needs to vanish.

That means that when you consider the integral as a function of ipk, it can have a discontinuity at the real axis, because the integration goes across the pole. Landau's approach to analytic continuation is to distort the integration path down from the real axis if necessary to avoid crossing the real axis, see Fig. A.2. We can use the Cauchy integral theorem to calculate the difference between the integration along the real axis and this "Landau-contour":
Consider an integration along the contour as in Fig. A.3, only with the contours closed at $\pm\infty$. If g(v) is an analytic function, the residue

$$\int_{\Gamma_L} \mathrm{d}v \, \frac{g(v)}{v - ip/k} - \int_{\Gamma_R} \mathrm{d}v \, \frac{g(v)}{v - ip/k} = 2\pi i \mathrm{Res}\left(\frac{g(v)}{v - ip/k}, ip/k\right) \tag{A.22}$$

gives the difference between the integral evaluated at a contour that runs below the singularity, and one that runs above it along the real axis, in the limit $\varepsilon \to 0$. If the pole is above the real axis, the two integrals are the same. If the pole lies exactly on the real axis, the difference is exactly half of 2π times the residue.

The figures A.4(a) and (b) compare a plot of the imaginary part of the analytically

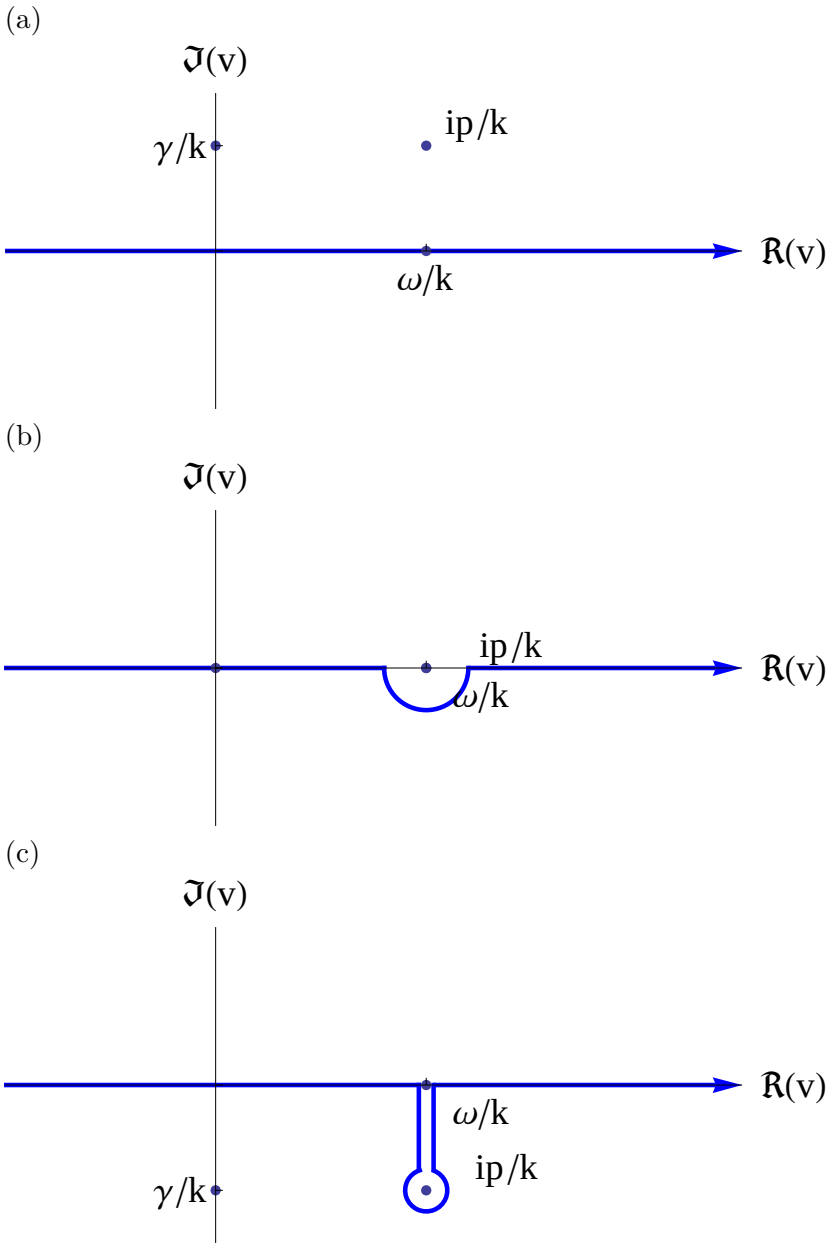

Figure A.2: Landau contour Γ_L for (a) γ>0, (b) $\gamma = 0$, (c) $\gamma < 0$ in the complex plane for the velocity v. $v = ip/k = \omega/k + i\gamma/k$ marks the singularity in the integrand of Eq. (A.18).

continued dielectric function

$$\varepsilon(k,p) = 1 - \frac{4\pi e^2}{mk^2} \int_{\Gamma_L} \frac{\mathrm{d}v}{v - ip/k} \frac{\partial F_0(v)}{\partial v} \tag{A.23}$$

to the one calculated along the real axis according to Eq. (A.18), for the Maxwell-Boltzmann distribution function Eq. (A.30).

Once we have the analytic expressions for both the integrals in the expression Eq. (A.17), we can see that the poles p_n that govern the time dependence of the

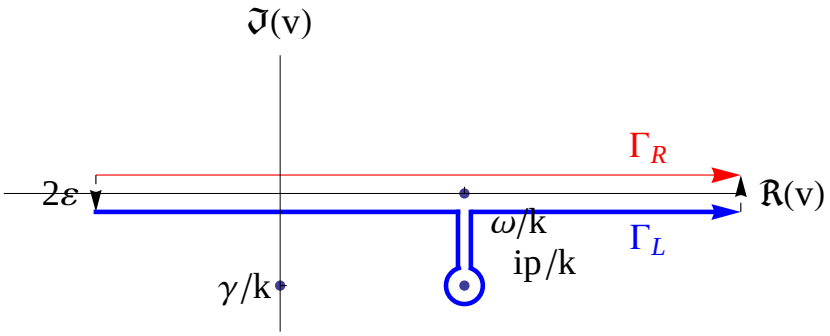

Figure A.3: Integration path above and below the pole, infinitesimally close to each other. If the contour is closed, the integral along this contour yields $2\pi i$ times the residue of the integrand at the pole.

potential $\varphi(t)$ are the zeros of the dielectric function Eq. (A.23). These zeros are in general complex and wave vector dependent. Per construction, these zeros can only be found after the analytical continuation of ε. As $\varphi(t)$ has an exponential time dependence, p_{max}, the p_k with the largest real part determines its long-time behaviour. If it is real, the plasma oscillations are undamped. If it lies in the left half plane, they are damped. A p_{max} in the right half plane corresponds to growing plasma oscillations, which, however, are not compatible with our assumption of small perturbations.

Longitudinal waves in a plasma

We have seen that the zeros of the dielectric function determine the oscillation and exponential growth or decay of the self-consistent potential - and hence the electric field in a plasma after a perturbation from equilibrium. Yet, we can also read

$$\varepsilon(k,p) = 0 \tag{A.24}$$

as the requirement for longitudinal waves in a plasma.

We see from Eq. (A.24) that the frequency of these "natural oscillations" in general depends on wave vector.

The solution $p(k)$ to Eq. (A.24) is complex . With the notation Eq. (A.10), we see that if $\gamma > 0$, the amplitude grows exponentially, if $\gamma < 0$ it is damped.

A.2 Classical dielectric function and Landau damping in three dimensions

The formalism above is valid for every equilibrium distribution function which is analytic as a function of the complex variable v_z as described above.

It is possible to simplify the expression for the dielectric function Eq. (A.23) further only using a few reasonable assumptions that will be discussed below.

We use an equilibrium distribution function f_0 which is normalized to the number of electrons per unit cube,[2]

$$n_0 = \int \mathrm{d}v\, f_0(\boldsymbol{v}). \tag{A.25}$$

Before substituting f_0 into Eq. (A.23), we have to integrate over v_x and v_y and differentiate with respect to v_z. It is convenient to do this in cylindrical coordinates - with $\rho = \sqrt{v_x^2 + v_y^2}$ and $z = v_z$:

$$\frac{dF_0(z)}{dz} = \frac{\partial}{\partial z} \int_0^{2\pi} \mathrm{d}\varphi \int_0^{\infty} \mathrm{d}\rho\, \rho f_0\left(\sqrt{\rho^2 + z^2}\right) = 2\pi \frac{\partial}{\partial z} \int_0^{\infty} \mathrm{d}\rho\, \rho f_0\left(\sqrt{\rho^2 + z^2}\right) \tag{A.26}$$

where we have used that $f_0(\boldsymbol{v}) = f_0(v)$. Now we can use a result from real analysis, namely that if $f_0(\sqrt{\rho^2 + z^2})$ is uniformly convergent, we can exchange the order of the differentiation and the integration in Eq. (A.26). [3] Hence, we can continue to equate

$$\begin{aligned} \frac{dF_0(z)}{dz} &= 2\pi \int_0^{\infty} \mathrm{d}\rho\, \rho \frac{\partial}{\partial z} f_0\left(\sqrt{\rho^2 + z^2}\right) \\ &= 2\pi z \int_0^{\infty} \mathrm{d}\rho\, \frac{\partial}{\partial \rho} f_0\left(\sqrt{\rho^2 + z^2}\right) \end{aligned} \tag{A.27}$$

having used $\frac{\partial f_0}{\partial z} = \frac{\partial f_0}{\partial v}\frac{\partial v}{\partial z} = \frac{\partial f_0}{\partial \rho}\frac{\partial v}{\partial z}\left(\frac{\partial v}{\partial \rho}\right)^{-1}$. Under the additional assumption that $\lim_{v\to\infty} f_0(v) = 0$, this provides us with the formula

$$\frac{dF_0(z)}{dz} = -2\pi z f_0\left(|z|\right). \tag{A.28}$$

Substituting the plasma frequency Eq. (2.17) and Eq. (A.28) in Eq. (A.23) yields

$$\varepsilon(k,p) = 1 + \frac{2\pi\omega_P^2}{n_0 k^2} \int_{\Gamma_L} \mathrm{d}z\, \frac{z f_0(|z|)}{z - ipk}, \tag{A.29}$$

into which we can substitute various equilibrium distribution functions $f_0(v)$.

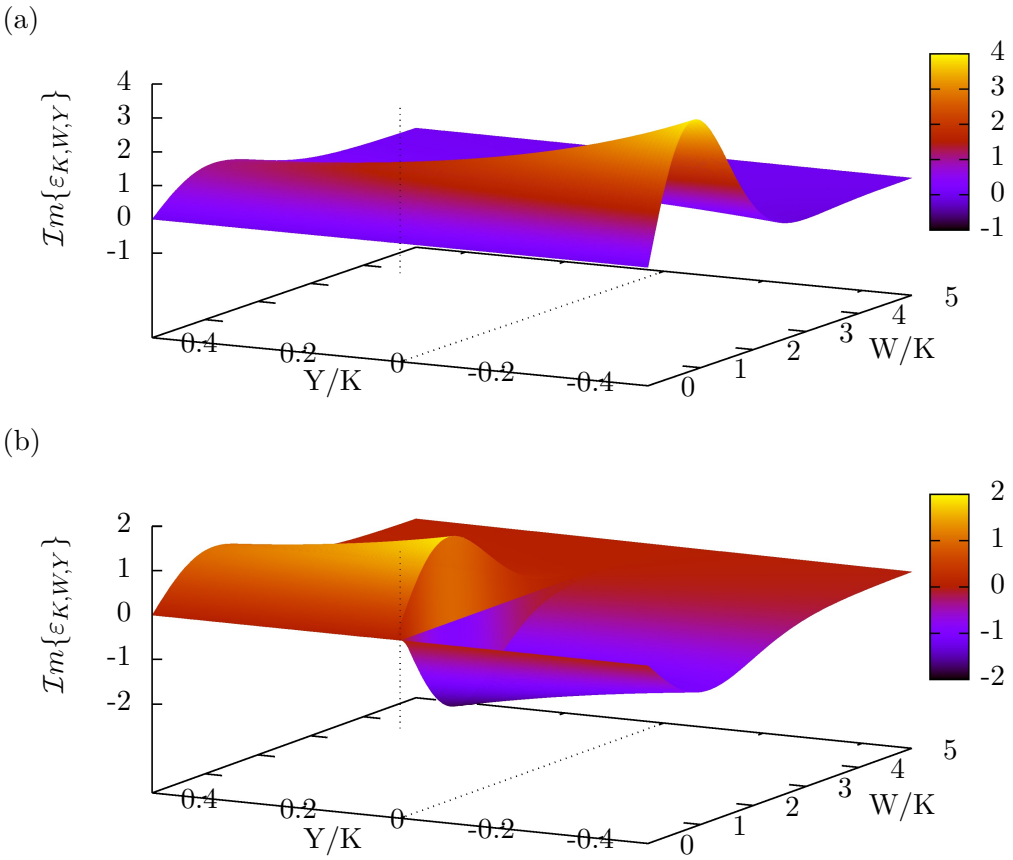

Figure A.4: Imaginary part of the dielectric function for the Maxwell-Boltzmann distribution function Eq. (A.30) as a function of W/K and Y/K, the real and imaginary part of the scaled complex frequency W, divided by the scaled wave vector K, evaluated (a) along the Landau contour (cf. Eq. (A.32) and Eq. (A.37)) , (b) along the real axis (cf. Eq. (A.33))

Maxwell - Boltzmann distribution function

In the following section, we will calculate the dielectric function Eq. (A.29), where $f_0(v)$ is the Maxwell-Boltzmann distribution function. That is the distribution function that Landau had in mind originally, and it is applicable for a large parameter space in classical plasma physics, where temperatures are usually high and electron densities small. We see that the Maxwell - Boltzmann distribution function

$$f_0(\boldsymbol{v}) = n_0 \left(\frac{m}{2\pi k_B T}\right)^{\frac{3}{2}} e^{-\frac{mv^2}{2k_B T}} \tag{A.30}$$

[2]This is different from the normalization in the rest of the thesis, in order to conform with Landau's notation.

[3]Physicists usually don't worry about uniform convergence of expressions like the Maxwell-Boltzmann distribution function, which are essentially Gaussians.

fulfills all the requirements to derive Eq. (A.29). It turns out that the dielectric function takes a compact form if we use the Debye length

$$\lambda_D = \sqrt{\frac{k_B T}{4\pi n_0 e^2}} \tag{A.31}$$

as a length scale, the dimensionless wave vector $K = k\lambda_D$ and the dimensionless frequency $W = \frac{ip}{\omega_p}$:

$$\varepsilon(K,W) = 1 + \frac{1}{\sqrt{2\pi}K^2} \int\limits_{\Gamma_L} \mathrm{d}u \, \frac{u e^{-\frac{u^2}{2}}}{u - \frac{W}{K}} \tag{A.32}$$

Next, we have to shift our focus to the integration path Γ_L, see Fig. A.2. As discussed above, integrating along the Landau contour Γ_L is a way of finding the analytic continuation of

$$\varepsilon(K,W) = 1 + \frac{1}{\sqrt{2\pi}K^2} \int\limits_{-\infty}^{\infty} \mathrm{d}u \, \frac{u e^{-\frac{u^2}{2}}}{u - \frac{W}{K}} \tag{A.33}$$

from the upper half plane $\mathfrak{Im}\frac{W}{K} > 0$ into the lower half plane $\mathfrak{Im}\frac{W}{K} < 0$. If one just evaluates Eq. (A.33) for all $\mathfrak{Im}\frac{W}{K}$, the resulting function will not be analytic at the real axis, see Fig. A.4(b).

We also described above how the contribution to the integral from the part of the Landau contour that passes below the pole $\mathfrak{Im}\frac{W}{K} < 0$ is

$$2\pi i \, \mathrm{Res}\left(u e^{-\frac{u^2}{2}}, \frac{W}{K}\right) = 2\pi i \frac{W}{K} e^{-\frac{1}{2}\frac{W^2}{K^2}} \tag{A.34}$$

Displaying the contribution to the dielectric function from the different parts of the Landau contour, the contribution from the integral along the real axes and the contribution from the residue yields

$$\varepsilon(K,W) = 1 + \frac{1}{\sqrt{2\pi}K^2} \left(\int\limits_{-\infty}^{\infty} \mathrm{d}u \, \frac{u e^{-\frac{u^2}{2}}}{u - \frac{W}{K}} + 2\pi i \frac{W}{K} e^{-\frac{1}{2}\frac{W^2}{K^2}} \right). \tag{A.35}$$

The integral in Eq. (A.35) can be transformed into an expression involving the imaginary error function [4] $\mathrm{erfi}(z) = \frac{2}{\sqrt{\pi}} \int\limits_0^{\infty} \mathrm{d}t \, e^{-t^2}$, which is well tabulated. Using

$$\int\limits_{-\infty}^{\infty} \mathrm{d}u \, \frac{u e^{-\frac{u^2}{2}}}{u - \frac{W}{K}} = \sqrt{2\pi} - \pi \frac{W}{K} \, e^{-\frac{1}{2}\frac{W^2}{K^2}} \left[i + \mathrm{erfi}\left(\frac{W}{\sqrt{2}K}\right) \right] \tag{A.36}$$

[4] A good account of a very similar calculation can be found in [112]- the main difference is that they use the Dawson function, which is closely related to the imaginary error function.

yields

$$\varepsilon(K,W) = 1 + \frac{1}{K^2}\left\{1 + \sqrt{\frac{\pi}{2}}\frac{W}{K}e^{-\frac{1}{2}\frac{W^2}{K^2}}\left[i - \operatorname{erfi}\left(\frac{W}{\sqrt{2}K}\right)\right]\right\} \text{ for } \mathfrak{Im}\frac{W}{K} < 0. \quad \text{(A.37)}$$

Its imaginary part is plotted in Fig. A.4(a). The two plots Fig. A.4(a) and (b) are identical in the upper half plane, but only if we use the Landau contour as integration path is there no discontinuity at the real axis. This serves as visual evidence for a correct analytical continuation.

Natural oscillation frequencies Landau gave approximations for the wave vector dependent plasma frequency $\omega(k)$ for small and large k, [2]. To the best of our knowledge, Eq. (A.37) cannot be solved for ω explicitly. Even Landau's approximate solution for large wave vectors K is only an implicit equation. There are some variations of those approximations in textbooks, e.g.,[111] for the small k approximation of γ, and [112] for a good treatment of approximations for ω for small and intermediate wave vectors, but we will constrain ourselves to Landau's ones. In

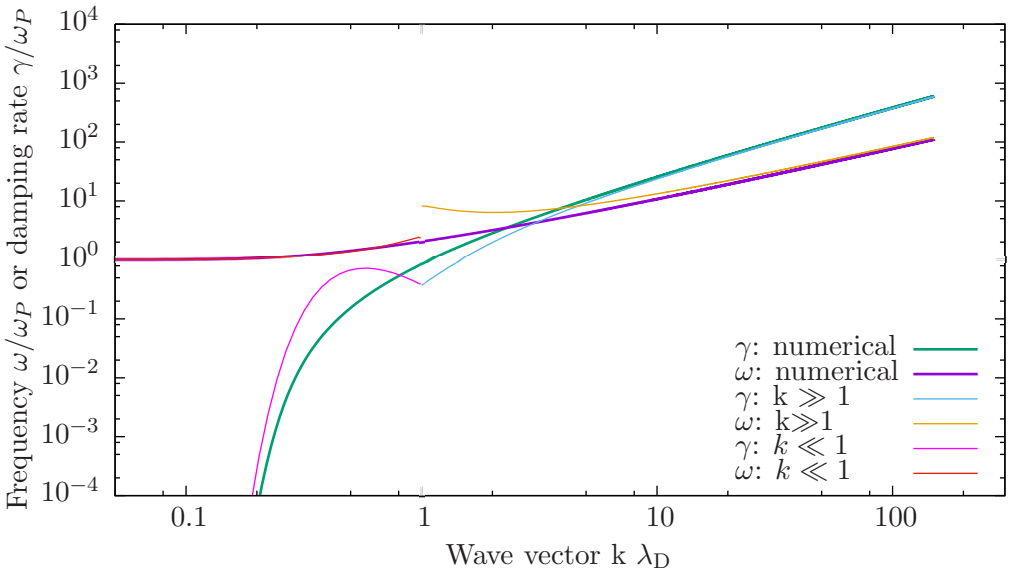

Figure A.5: Numerically calculated frequency $\omega(k)$ and damping rate $\gamma(k)$ of the plasma oscillations as a function of wave vector. Also shown are Landau's short and long - wavelength approximations Eq. (A.38) through Eq. (A.42) .

our notation they are

$$k\lambda_D \ll 1: \quad \omega(k) = \omega_p\left[1 + \frac{3}{2}(k\lambda_D)^2\right] \quad \text{(A.38)}$$

$$\gamma(k) = \omega_p\sqrt{\frac{\pi}{8}}(k\lambda_D)^{-3}\exp\left\{-\frac{1}{2(k\lambda_D)^2}\right\} \quad \text{(A.39)}$$

for small wave vectors and

$$k\lambda_D \gg 1: \quad \xi e^{\xi^2} 2 = \frac{(k\lambda_D)^2}{\sqrt{2\pi}} \tag{A.40}$$

$$\omega(k) = \frac{\pi}{\xi}(k\lambda_D) \tag{A.41}$$

$$\gamma(k) = \xi(k\lambda_D) \tag{A.42}$$

for large wave vectors. Figure A.5 shows those approximations, together with our numerical calculations.

Discussion of results We find that the plasma oscillations in a Maxwell-Boltzmann distributed plasma are always damped. The damping factor γ is very small for small wave vectors, comparable to the oscillation frequency ω at intermediate wave vectors $k\lambda_D \approx 1$. At large wave vectors, γ is even larger than ω. It is worth noting that both frequency and damping factor grow monotonously and continuously. Hence, it is difficult to specify a maximum wave vector or cutoff k_{max}, such that waves with $k > k_{max}$ can be said to be damped out entirely. It has been suggested [111] to set this cutoff at $\gamma(k_{max}) = \omega(k_{max})$, which means that the amplitude of the oscillation decreases to $\frac{1}{e}$ of its initial value after one oscillation. This definition is obviously somewhat arbitrary.

Experimental verification of collisionless damping Following Landau's predictions of collisionless damping, it was a matter of discussion whether it was a physical effect[111], and the experimental verification of Landau damping came only 20 years later [116, 117].

Appendix B

Approximate treatments of carrier–coupled phonon-plasmon mode scattering in three dimensions

This appendix deals with some of the concepts and expressions that have been used in the literature to capture carrier–coupled mode scattering, especially in the long-wavelength limit. Concepts such as the "phonon content" are not used in the formalism developed in the main part of this thesis, and only need to be introduced for the purpose of comparison with other descriptions in the literature.

The phonon content and the scattering strengths can be derived in different ways. The scattering strengths can be obtained naturally as the low-damping, long-wavelengths limits of the scattering rate Eq. (3.4), see subsection 3.1.3. To help readers who are looking to acquaint themselves with the literature, we show that the scattering strength Eq. (3.34) (used in [36]) is equivalent to expressions given used in [26], and [1].

The phonon content is not a quantity that arises within our description, but we also show how different expressions correspond with each other, because some of the descriptions of the scattering strengths [26] and [1] rely the concept of phonon content.

B.1 Phonon content in the long-wavelength, low-damping limit

Phonon content, roughly speaking, is a measure of how much the ions are moving when they are a part of a coupled phonon-plasmon oscillation. This is important in neutron scattering experiments, as neutrons only significantly interact with phonons, not with plasmons. In Fig. 3.3, we marked the coupled mode with the higher phonon content with open squares.

There are a number of different expressions for phonon-content used by Varga [30], Ridley [26], Kim et a. [36] and Fischetti et al. [1]. All apply to the case where the damping $\gamma = 0$. We will show explicitly that the last three expressions are entirely equivalent, and that the first only differs from the others by a simple factor.

Ridley form

Roughly following Ridley [26], we define the phonon content S of a coupled collective mode of frequency ω as the kinetic energy of the ions divided by the kinetic energy of both the ions and the electrons oscillating at frequency ω,

$$S_\omega = \frac{E_\omega^{kin,ion}}{E_\omega^{kin,ion} + E_\omega^{kin,e}}. \tag{B.1}$$

The kinetic energy of the ions can be expressed as

$$E_\omega^{kin,ion} = \frac{1}{2} N M \omega^2 |\boldsymbol{u}_\omega|^2 = \frac{|\boldsymbol{E}_\omega|^2}{2} \frac{NQ^2}{M} \frac{\omega^2}{\left(\omega^2 - \omega_{TO}^2\right)^2} = \varepsilon^\infty \frac{|\boldsymbol{E}_\omega|^2}{8\pi} \omega^2 \frac{\omega_{LO}^2 - \omega_{TO}^2}{\left(\omega^2 - \omega_{TO}^2\right)^2} \tag{B.2}$$

using the ionic displacement Eq. 2.2, and Eq. 2.9, cf. [30]. Similarly, we receive

$$E_\omega^{kin,e} = \frac{1}{2} N m^* \omega^2 |\boldsymbol{u}_\omega^e|^2 = \frac{|\boldsymbol{E}_\omega|^2}{2} \frac{Ne^2}{m^* \omega^2} = \varepsilon^\infty \frac{|\boldsymbol{E}_\omega|^2}{8\pi} \frac{\omega_P^2}{\omega^2} \tag{B.3}$$

as the kinetic energy of all the conduction band electrons, from using the electronic displacements $\boldsymbol{u}_\omega^e$ and Eq. 2.18.

This yields

$$S_\omega^R = \frac{1}{1 + \frac{E_\omega^{kin,e}}{E_\omega^{kin,ion}}} = \frac{1}{1 + \frac{\omega_P^2 \left(\omega^2 - \omega_{TO}^2\right)^2}{\omega^4 \left(\omega_{LO}^2 - \omega_{TO}^2\right)}}, \tag{B.4}$$

which is the form which appears in Ridley's textbook [26, page 334].

Varga form

Varga [30], Green's functions are used to find the phonon content

$$\left(S^V_{\omega,k}\right)^{-1} = \frac{\omega}{\omega_{LO}} + \frac{\left[1-(\omega/\omega_{TO})^2\right]^2}{2(\varepsilon^0-\varepsilon^\infty)}\frac{\omega^2_{TO}}{\omega_{LO}}\frac{\partial\varepsilon^e_{\omega,k}}{\partial\omega} \tag{B.5}$$

which is wave vector dependent in general. In the long wavelength limit, $\varepsilon^e_{\omega,k} = \varepsilon^\infty\left(1-\frac{\omega_P^2}{\omega^2}\right)$, so that

$$\begin{aligned}\left(S^V_\omega\right)^{-1} \equiv \left(S^V_{\omega,k=0}\right)^{-1} &= \frac{\omega}{\omega_{LO}}\left\{1+\frac{\omega_{LO}}{\omega}\frac{\left[1-(\omega/\omega_{TO})^2\right]^2}{(\varepsilon^0/\varepsilon^\infty-1)}\frac{\omega^2_{TO}}{\omega_{LO}}\frac{\omega_P^2}{\omega^3}\right\}\\ &= \frac{\omega}{\omega_{LO}}\left\{1+\frac{\left[1-(\omega/\omega_{TO})^2\right]^2}{(\omega_{LO}/\omega_{TO})^2-1}\frac{\omega^2_{TO}\omega_P^2}{\omega^4}\right\}\\ &= \frac{\omega}{\omega_{LO}}\left\{1+\frac{\left[\omega^2_{TO}-\omega^2\right]^2}{\omega^2_{LO}-\omega^2_{TO}}\frac{\omega_P^2}{\omega^4}\right\} = \frac{\omega}{\omega_{LO}}\left(S^R_\omega\right)^{-1}\end{aligned} \tag{B.6}$$

This means that the phrase "phonon content" is applied to quantities differing by ω_{LO}/ω by Varga and Ridley:

$$S^V_\omega = \frac{\omega_{LO}}{\omega}S^R_\omega \tag{B.7}$$

Varga also receives a sum rule

$$\sum_m \omega_m S^V_{\omega_m,k} = \omega_{LO} \text{ or } \sum_m S^R_{\omega_m} = 1 \tag{B.8}$$

i.e., the Ridley phonon content of the lower and the upper mode add up to one.

Kim et al. form

Guided by the expression Eq. (B.5), we write the kinetic energies as derivatives of the real part of the dielectric function with respect to frequency, and the phonon content becomes

$$S_\omega = \frac{\frac{\omega}{2}\frac{\partial}{\partial\omega}\mathfrak{Re}\left\{\varepsilon^{ion}_\omega\right\}}{\frac{\omega}{2}\frac{\partial}{\partial\omega}\mathfrak{Re}\left\{\varepsilon^{tot}_\omega\right\}}. \tag{B.9}$$

$$1-S_\omega = \frac{\frac{\omega}{2}\frac{\partial}{\partial\omega}\mathfrak{Re}\left\{\varepsilon^{e}_\omega\right\}}{\frac{\omega}{2}\frac{\partial}{\partial\omega}\mathfrak{Re}\left\{\varepsilon^{tot}_\omega\right\}} \tag{B.10}$$

is the corresponding plasmon content.

We use the form of the plasmon content involving derivatives to arrive at the expression of the phonon content used by Kim et al. [36]. The derivative of the real

part of the ionic dielectric function is

$$\frac{\partial}{\partial\omega}\mathfrak{Re}\left\{\varepsilon_\omega^{ion}\right\} = \varepsilon^\infty \frac{\partial}{\partial\omega}\frac{\omega_{TO}^2-\omega_{LO}^2}{\omega^2-\omega_{TO}^2} = 2\omega\varepsilon^\infty\frac{\omega_{LO}^2-\omega_{TO}^2}{(\omega^2-\omega_{TO}^2)^2}. \tag{B.11}$$

Writing the real part of the total dielectric function in terms of its poles and zeros,

$$\mathfrak{Re}\left\{\varepsilon_\omega^{tot}\right\} = \varepsilon^\infty\frac{(\omega^2-\omega_\pm^2)(\omega^2-\omega_\mp^2)}{\omega^2(\omega^2-\omega_{TO}^2)}, \tag{B.12}$$

yields

$$\frac{\partial}{\partial\omega}\mathfrak{Re}\left\{\varepsilon_\omega^{tot}\right\}\Big|_{\omega_\pm} = \frac{2\varepsilon^\infty}{\omega_\pm}\frac{\omega_\pm^2-\omega_\mp^2}{\omega_\pm^2-\omega_{TO}^2} \tag{B.13}$$

As the phonon content is only defined for $\omega_\pm$, it is not necessary to calculate the derivative everywhere. The plasmon content is

$$1-S_{\omega_\pm}^R = \frac{1}{\omega_\pm^2}\frac{\omega_P^2\omega_\pm^2-\omega_P^2\omega_{TO}^2}{\omega_\pm^2-\omega_\mp^2} \tag{B.14}$$

Using equation (2.87) the plasmon content

$$1-S_{\omega_\pm}^R = \frac{\omega_\pm^2-\omega_{LO}^2}{\omega_\pm^2-\omega_\mp^2} = \frac{\omega_P^2-\omega_\mp^2}{\omega_\pm^2-\omega_\mp^2} \tag{B.15}$$

can be written quite elegantly. The phonon content is then

$$S_{\omega_\pm}^R = \frac{\omega_{LO}^2-\omega_\mp^2}{\omega_\pm^2-\omega_\mp^2} = \frac{\omega_\pm^2-\omega_P^2}{\omega_\pm^2-\omega_\mp^2} \tag{B.16}$$

The last expression is the one used by Kim et al. [36] and Fischetti et al. [1].

B.2 Scattering strength in the long-wavelength limit

Having discussed the phonon content, we now focus on the expressions for the scattering strength Eq. (3.34) by different authors:

Kim et al.[36] give expressions for the energy relaxation rate, Ridley[26] gives a closely related so-called scattering rate, which is a modified energy relaxation rate Fischetti et al.[1] and O'Regan et al.[92] give expressions for the momentum relaxation rate. The comparison is made more complicated, because different systems of units are used. We have extracted the different scattering strengths used and converted them into Gaussion cgs units to facilitate comparison.

Kim et al. form

We call the scattering strength as presented in Eq. (3.34) the Kim et al. form, because this form follows straight from their expression for the scattering rate. We also took the phrase scattering strength from their paper [36] and based our notation for the Fröhlich- and coupled mode scattering strength on theirs. (They call the coupled mode scattering strength the screened Fröhlich scattering rate.) However, Kim et al.[36] actually only define the fraction $F^{\pm}/F^{u}$, so that proportionality factors are somewhat arbitrary. We take this into account in all our plots of scattering rates by scaling them with the Fröhlich scattering rate Eq. (3.21).

Ridley form

Ridley states in his book [26] that the formulation of carrier–coupled mode scattering in terms of the imaginary part of the inverse dielectric function as discussed in section 3.1 is equivalent to his derivation, which calculates how the polarization and the effective charges are modified through the presence of free carriers, in the long-wavelength limit. We will discuss the derivation using effective charges first, and then prove the equivalence.

Change in polarization and effective charge Let us first consider the response of the ions to an external electric field $\boldsymbol{E}$. From Eq. 2.3 and Eq. 2.9, we know that

$$\boldsymbol{P_\omega}^{ion} = -\boldsymbol{E}_\omega \frac{\varepsilon^\infty}{4\pi} \frac{\omega_{LO}^2 - \omega_{TO}^2}{\omega^2 - \omega_{TO}^2}, \tag{B.17}$$

when the damping rate γ is zero. Similarly to the phonon content Eq. B.1, we compare this to the polarization $\boldsymbol{P_\omega}^{coupled}$ due to both the ions and the conduction band electrons, which is just the polarization due to the coupled collective modes.

$$\boldsymbol{P_\omega}^{coupled} = \boldsymbol{P_\omega}^{ion} + \boldsymbol{P_\omega}^{e} = \boldsymbol{P_\omega}^{tot} - \boldsymbol{P_\omega}^{valence-e} = \frac{\boldsymbol{E}_\omega}{4\pi}\left[\varepsilon_\omega^{tot} - \varepsilon_\omega^\infty\right] = -\frac{\varepsilon^\infty \boldsymbol{E}_\omega}{4\pi} \tag{B.18}$$

In the last equality we have made explicit use of the fact that ε^{tot} vanishes for the coupled collective modes. This lets us express the ratio between the ionic polarization and the coupled mode polarization as

$$\frac{\boldsymbol{P_\omega}^{ion}}{\boldsymbol{P_\omega}^{coupled}} = \frac{\boldsymbol{P_\omega}^{ion}}{\boldsymbol{P_\omega}^{ion} + \boldsymbol{P_\omega}^{e}} = \frac{\omega_{LO}^2 - \omega_{TO}^2}{\omega^2 - \omega_{TO}^2} \tag{B.19}$$

Let us now re-express the coupled polarization analogously to the electronic and ionic polarization, Eq. 2.3 and Eq. 2.13

$$\boldsymbol{P_\omega}^{coupled} = NQ_\omega^{coupled}\boldsymbol{u}_\omega^{coupled} \tag{B.20}$$

where $Q_\omega^{coupled}$ is the effective charge of the coupled excitation. We will call $\boldsymbol{u}_\omega^{coupled}$ the effective displacement after Ridley [26, chapter 9.4]. We can obtain an expression for the effective displacement by assuming that the mass of the coupled ion-plasmon oscillators is the reduced mass of the ions, M. As the kinetic energy of the coupled excitations is

$$E_\omega^{kin,coupled} = E_\omega^{kin,ion} + E_\omega^{kin,e} = S_\omega^{-1} E_\omega^{kin,ion}, \tag{B.21}$$

the effective displacement then becomes

$$|\boldsymbol{u}_\omega^{coupled}|^2 S_\omega = |\boldsymbol{u}_\omega^{ion}|^2. \tag{B.22}$$

This enables us to express the effective displacement in terms of known quantities:

$$\left(Q_\omega^{coupled}\right)^2 = \frac{\left|\boldsymbol{P}_\omega^{coupled}\right|^2}{N\left|\boldsymbol{u}_\omega^{coupled}\right|^2} = \frac{\left|\boldsymbol{P}_\omega^{coupled}\right|^2}{\left|\boldsymbol{P}_\omega^{ion}\right|^2} \frac{|\boldsymbol{u}_\omega^{ion}|^2}{\left|\boldsymbol{u}_\omega^{coupled}\right|^2} Q^2 = \left(\frac{\omega^2 - \omega_{TO}^2}{\omega_{LO}^2 - \omega_{TO}^2}\right)^2 S_\omega Q^2 \tag{B.23}$$

The scattering strength for both carrier collective mode scattering proportional to the effective charge squared divided by the mode frequency. [26] This holds both for the LO-phonons and the coupled phonon-plasmon modes. Therefore, the scattering strength is

$$F_{Ridley}^{\pm} = \frac{\omega_{LO}}{\omega_\pm} \left(\frac{\omega_i^2 - \omega_{TO}^2}{\omega_{LO}^2 - \omega_{TO}^2}\right)^2 S_{\omega_i} F^u \tag{B.24}$$

where F^u refers to Fröhlich scattering strength Eq. (3.21). That Eq. (B.24) is equivalent to the coupled mode scattering strength in Kim et al's form, Eq. (3.34), can be proved by simple algebra:

$$\omega_{LO}\left(\frac{1}{\varepsilon^\infty} - \frac{1}{\varepsilon^0}\right) \frac{\omega_{LO}}{\omega_\pm} \left(\frac{\omega_\pm^2 - \omega_{TO}^2}{\omega_{LO}^2 - \omega_{TO}^2}\right)^2 \frac{\omega_\pm^2 - \omega_P^2}{\omega_\pm^2 - \omega_\mp^2} = \frac{\omega_\pm}{\varepsilon^\infty} \frac{\omega_\pm^2 - \omega_{TO}^2}{\omega_\pm^2 - \omega_\mp^2} \tag{B.25}$$

$$\Leftrightarrow \frac{1}{\omega_\pm}\left(\frac{\omega_\pm^2 - \omega_{TO}^2}{\omega_{LO}^2 - \omega_{TO}^2}\right)\left(\omega_\pm^2 - \omega_P^2\right) = \omega_\pm \tag{B.26}$$

The last line is a reformulation of the bi-quadratic equation 2.87 and hence true.

Fischetti et al. form

Fischetti et al.[1] remark that their description of carrier–coupled mode scattering are equivalent to those by Kim et al. and Ridley. In our notation, this means that the expressions for the scattering strengths are equivalent:

$$F_{Fischetti}^{\pm} = \frac{2\pi^2 e^2 \omega_\pm}{q^2}\left[\frac{1}{\varepsilon^\infty - \varepsilon^\infty \omega_P^2/\omega_\pm^2} - \frac{1}{\varepsilon^0 - \varepsilon^\infty \omega_P^2/\omega_\pm^2}\right]\frac{\omega_\pm^2 - \omega_P^2}{\omega_\pm^2 - \omega_\mp^2} = F_{Kim}^{\pm} = F_{Ridley}^{\pm} \tag{B.27}$$

Fischetti at al. [1] note that

> this agreement has been verified numerically here, although presumably more efforts could produce a more elegant algebraic proof

The said proof is lengthy, but straightforward, and not particularly elegant:

$$\begin{aligned}
\omega_\pm \left[\frac{1}{\varepsilon^\infty - \varepsilon^\infty\omega_P^2/\omega_\pm^2} - \frac{1}{\varepsilon^0 - \varepsilon^\infty\omega_P^2/\omega_\pm^2}\right]\frac{\omega_\pm^2-\omega_P^2}{\omega_\pm^2-\omega_\mp^2} &= \frac{\omega_\pm}{\varepsilon^\infty}\frac{\omega_\pm^2-\omega_{TO}^2}{\omega_\pm^2-\omega_\mp^2} \\
\Leftrightarrow \left[\frac{1}{1-\omega_P^2/\omega_\pm^2} - \frac{1}{\varepsilon^0/\varepsilon^\infty - \omega_P^2/\omega_\pm^2}\right]\left(\omega_\pm^2-\omega_P^2\right) &= \left(\omega_\pm^2-\omega_{TO}^2\right) \\
\Leftrightarrow \left[1 - \frac{1-\omega_P^2/\omega_\pm^2}{\omega_{LO}^2/\omega_{TO}^2 - \omega_P^2/\omega_\pm^2}\right]\frac{\omega_\pm^2-\omega_P^2}{1-\omega_P^2/\omega_\pm^2} &= \left(\omega_\pm^2-\omega_{TO}^2\right) \\
\Leftrightarrow \left[\frac{\omega_{LO}^2/\omega_{TO}^2 - 1}{\omega_{LO}^2/\omega_{TO}^2 - \omega_P^2/\omega_\pm^2}\right]\omega_\pm^2 &= \left(\omega_\pm^2-\omega_{TO}^2\right) \\
\Leftrightarrow \left[\frac{\omega_{LO}^2-\omega_{TO}^2}{\omega_{LO}^2\omega_\pm^2 - \omega_{TO}^2\omega_P^2}\right]\omega_\pm^4 &= \left(\omega_\pm^2-\omega_{TO}^2\right)
\end{aligned} \tag{B.28}$$

If we now use the bi-quadratic equation to re-express $\omega_{LO}^2\omega_\pm^2 - \omega_{TO}^2\omega_P^2$ as $\omega_\pm^2\left(\omega_\pm^2-\omega_P^2\right)$

$$\begin{aligned}
\Leftrightarrow \left[\frac{\omega_{LO}^2-\omega_{TO}^2}{\omega_{LO}^2\omega_\pm^2 - \omega_{TO}^2\omega_P^2}\right]\omega_\pm^4 &= \left(\omega_\pm^2-\omega_{TO}^2\right) \\
\Leftrightarrow \left[\frac{\omega_{LO}^2-\omega_{TO}^2}{\omega_\pm^2-\omega_P^2}\right]\omega_\pm^2 &= \left(\omega_\pm^2-\omega_{TO}^2\right)
\end{aligned} \tag{B.29}$$

The last line is again only a reformulation of the bi-quadratic equation 2.87, and hence true.

Appendix C

Explicit evaluation of important expressions

C.1 Linearization of the collisional integral

C.1.1 Collision term

Peierls's carrier collision term in the Boltzmann equation [49] is

$$\left(\frac{\partial f_{\boldsymbol{p}}}{\partial t}\right)_{\text{coll}} = \int_{\boldsymbol{k}} \sum_{\sigma} 2\pi F_{\boldsymbol{k}}^{\sigma}\, \delta\left(E_{\boldsymbol{p}+\boldsymbol{k}} - E_{\boldsymbol{p}} - \hbar\omega_{\boldsymbol{k}}^{\sigma}\right) \times \left[\left(N_{\boldsymbol{k},\sigma}+1\right) f_{\boldsymbol{p}+\boldsymbol{k}}\left(1-f_{\boldsymbol{p}}\right) - N_{\boldsymbol{k},\sigma} f_{\boldsymbol{p}}\left(1-f_{\boldsymbol{p}+\boldsymbol{k}}\right)\right] \quad \text{(C.1)}$$

in the notation introduced in chapter 4. We use the scattering strengths $F_{\boldsymbol{k}}^{\sigma}$ from section 3.1 because Peierls's equations were formulated for scattering with discrete modes. Let us keep in mind that we use Peierls's short convention [49], where negative values of σ mean a negative transferred energy $\hbar\omega_{\boldsymbol{k}}^{-|\sigma|} = -\hbar|\omega_{\boldsymbol{k}}^{\sigma}|$.

According to Peierls [49], the collective mode collisional integral for the mode σ is

$$\left(\frac{\partial N_{\boldsymbol{k},\sigma}}{\partial t}\right)_{\text{coll}} = 2\int_{\boldsymbol{p}} 2\pi F_{\boldsymbol{k}}^{\sigma}\, \delta\left(E_{\boldsymbol{p}+\boldsymbol{k}} - E_{\boldsymbol{p}} - \hbar\omega\right) \times \left[\left(N_{\boldsymbol{k},\sigma}+1\right) f_{\boldsymbol{p}+\boldsymbol{k}}\left(1-f_{\boldsymbol{p}}\right) - N_{\boldsymbol{k},\sigma} f_{\boldsymbol{p}}\left(1-f_{\boldsymbol{p}+\boldsymbol{k}}\right)\right]. \quad \text{(C.2)}$$

C.1.2 Detailed balance

The collision terms $\left(\frac{\partial N_{\boldsymbol{k},\sigma}}{\partial t}\right)_{\text{coll}}$ and $\left(\frac{\partial f_{\boldsymbol{p}}}{\partial t}\right)_{\text{coll}}$ vanish when $N_{\boldsymbol{k},\omega}$ is the Bose-Einstein distribution function N_{ω}^{0}, and $f_{\boldsymbol{p}}$ is the Fermi-Dirac distribution function, because

they fulfill equations of detailed balance:

$$\left[N^0_\omega \left(f^0_{E_{\boldsymbol{p}+\boldsymbol{k}}} - f^0_{E_{\boldsymbol{p}}}\right) + f^0_{E_{\boldsymbol{p}+\boldsymbol{k}}}\left(1 - f^0_{E_{\boldsymbol{p}}}\right)\right] \delta\left(E_{\boldsymbol{p}+\boldsymbol{k}} - E_{\boldsymbol{p}} - \hbar\omega\right) = 0 \tag{C.3a}$$

$$\left[(N^0_\omega + 1)\left(f^0_{E_{\boldsymbol{p}+\boldsymbol{k}}} - f^0_{E_{\boldsymbol{p}}}\right) + f^0_{E_{\boldsymbol{p}}}\left(1 - f^0_{E_{\boldsymbol{p}+\boldsymbol{k}}}\right)\right] \delta\left(E_{\boldsymbol{p}+\boldsymbol{k}} - E_{\boldsymbol{p}} - \hbar\omega\right) = 0 \tag{C.3b}$$

As the distribution of the collective excitations is already in equilibrium, the collective excitation decay term vanishes. Hence, the Bose-Einstein and Fermi-Dirac distribution function are the solution to the coupled system of Boltzmann equation in the absence of an external field.

Expressed in terms of the probabilities $P_{\boldsymbol{k},\omega}$ from chapter 3, the principle of detailed balance reads

$$P_{\boldsymbol{k},\omega}\delta\left(E_{\boldsymbol{p}+\boldsymbol{k}} - E_{\boldsymbol{p}} - \hbar\omega\right) = e^{\hbar\omega\beta} P_{-\boldsymbol{k},-\omega}\delta\left(E_{\boldsymbol{p}+\boldsymbol{k}} - E_{\boldsymbol{p}} - \hbar\omega\right), \tag{C.4}$$

see [32], and it requires that

$$\mathfrak{Im}\left(\frac{-1}{\varepsilon_{-\boldsymbol{k},-\omega}}\right) = -\mathfrak{Im}\left(\frac{-1}{\varepsilon_{\boldsymbol{k},\omega}}\right). \tag{C.5}$$

C.1.3 Linearization

In order to find the linearized versions of the collisional term in the collective mode and carrier Boltzmann equations, Eq. (C.1) and Eq. (C.2), we focus on the expression in square brackets which occurs in both of these equations, and which can be written as

$$\left[N_{\boldsymbol{k},\omega}\left(f_{\boldsymbol{p}'} - f_{\boldsymbol{p}}\right) + f_{\boldsymbol{p}'}\left(1 - f_{\boldsymbol{p}}\right)\right] \delta(E' - E - \hbar\omega). \tag{C.6}$$

We evaluate it under the assumption that the distribution functions are only slightly out of equilibrium. That means, we will replace the carrier distribution $f_{\boldsymbol{p}}$ in Eq. (C.6) with its first order correspondent $f^1_{\boldsymbol{p}}$ from Eq. (4.1), and the collective mode distribution $N_{\boldsymbol{k},\omega}$ with $N^1_{\boldsymbol{k},\omega}$ from Eq. (4.2). This results in expressions which only depend on the equilibrium distribution functions f^0 and N^0, and the non-equilibrium terms g and G, which we assume to be small compared to the former, $\beta G_{\boldsymbol{k},\omega} \ll N^0_{\boldsymbol{k},\omega}$ and $\beta g_{\boldsymbol{p}} \ll f^0_E$. (Here and in the following, we abbreviate $E_{\boldsymbol{p}}$ to E and $E_{\boldsymbol{p}'}$ to E'.) All expressions involving squares of g, G or mixed terms gG are hence very small, and we

can neglect them. Consequently, we find

$$\begin{aligned}\left[N_{\boldsymbol{k},\omega}\left(f_{\boldsymbol{p}'}-f_{\boldsymbol{p}}\right)+f_{\boldsymbol{p}'}\left(1-f_{\boldsymbol{p}}\right)\right]^1\delta(E'-E-\hbar\omega)=\\ \Bigg(N_\omega^0\left[1+(1+N_\omega^0)\beta G_{\boldsymbol{k},\omega}\right]\left\{f_{E'}^0\left[1+(1-f_{E'}^0)\beta g_{\boldsymbol{p}'}\right]\right.\\ \left.-f_E^0\left[1+(1-f_E^0)\beta g_{\boldsymbol{p}}\right]\right\}\\ +f_{E'}^0\left[1+\left(1-f_{E'}^0\right)\beta g_{\boldsymbol{p}'}\right]\left\{1-f_E^0\left[1+\left(1-f_E^0\right)\beta g_{\boldsymbol{p}}\right]\right\}\Bigg)\\ \times\delta(E'-E-\hbar\omega)\end{aligned}\tag{C.7}$$

where the superscript 1 indicates that the equation is true to first order. Sorting the orders of the g, G, using that the 0^{th} order equation vanishes, Eq. (C.3) and neglecting all second order terms leads to

$$\begin{aligned}&\left[N_{\boldsymbol{k},\omega}\left(f_{\boldsymbol{p}'}-f_{\boldsymbol{p}}\right)+f_{\boldsymbol{p}'}\left(1-f_{\boldsymbol{p}}\right)\right]^1\delta(E'-E-\hbar\omega)\\ &\quad=\Big\{\beta g_{\boldsymbol{p}'}\left(N_\omega^0+1-f_E^0\right)f_{E'}^0\left(1-f_{E'}^0\right)\\ &\qquad-\beta g_{\boldsymbol{p}}\left(N_\omega^0+f_{E'}^0\right)f_E^0\left(1-f_E^0\right)\\ &\qquad-\beta G_{\boldsymbol{k},\omega}N_\omega^0\left(N_\omega^0+1\right)\left(f_E^0-f_{E'}^0\right)\Big\}\delta(E'-E-\hbar\omega)\end{aligned}\tag{C.8}$$

Using the equations of detailed balance, Eq. (C.3) again shows that the coefficients of g',$-g$ and $-G$ are all equal, and equal to

$$\beta N_\omega^0 f_E^0\left(1-f_{E'}^0\right)=\beta N_\omega^0\left(N_\omega^0+1\right)\left(f_E^0-f_{E'}^0\right),\tag{C.9}$$

as long as $E'-E=\hbar\omega$. Therefore,

$$\begin{aligned}&\left[N_{\boldsymbol{k},\omega}\left(f_{\boldsymbol{p}'}-f_{\boldsymbol{p}}\right)+f_{\boldsymbol{p}'}\left(1-f_{\boldsymbol{p}}\right)\right]^1\delta(E'-E-\hbar\omega)=\\ &\left[g_{\boldsymbol{p}'}-g_{\boldsymbol{p}}-G_{\boldsymbol{k},\omega}\right]\beta N_\omega^0 f_E^0\left(1-f_{E'}^0\right)\delta(E'-E-\hbar\omega)\end{aligned}\tag{C.10}$$

and

$$\begin{aligned}&\left[N_{\boldsymbol{k},\omega}\left(f_{\boldsymbol{p}'}-f_{\boldsymbol{p}}\right)+f_{\boldsymbol{p}'}\left(1-f_{\boldsymbol{p}}\right)\right]^1\delta(E'-E-\hbar\omega)=\\ &\qquad\left(g_{\boldsymbol{p}'}-g_{\boldsymbol{p}}-G_{\boldsymbol{k},\omega}\right)\beta N_\omega^0\left(N_\omega^0+1\right)\left(f_E^0-f_{E'}^0\right)\delta(E'-E-\hbar\omega)\end{aligned}\tag{C.11}$$

both hold, see [49]. Plugging Eq. (C.10) and Eq. (C.11) into Eq. (C.6) yields a first order term. Consequently, when we substitute Eq. (C.6) for the brackets in the collisional term of the carrier Boltzmann equation Eq. (C.1) and the collective mode Boltzmann equation Eq. (C.1) we get second order terms if the scattering rate $W_{\boldsymbol{k},\sigma}$ is of first order. Setting the scattering rate to its equilbrium term $W_{\boldsymbol{k},\sigma}^0$, yields the desired collisional terms of the carrier and collective mode Boltzmann equation to

first order, Eq. (4.19) and Eq. (4.6).

C.2 Equivalence of carrier–carrier Boltzmann equation with coupled carrier and plasmon Boltzmann equations

In this appendix, we show that, to first order, the description of carrier–carrier scattering with a single Boltzmann equation [49, chapter 6.5] and with two coupled Boltzmann equation, one for the carriers and one for the plasmons, are equivalent. See also appendix C.2, where we showed that the energy relaxation time for carrier-plasmon scattering and carrier–carrier scattering are equivalent.

We start with the latter desription. The first order collision term for the carriers thus is Eq. (4.19)

$$\left(\frac{\partial f_{\boldsymbol{p}}}{\partial t}\right)^1_{\text{coll}} = \iint\limits_{\boldsymbol{k}\ \hbar\omega} \frac{2\nu_k}{\hbar} \frac{\mathfrak{Im}\left(\varepsilon^c_{\boldsymbol{k},\omega}\right)}{\left|\varepsilon^c_{\boldsymbol{k},\omega}\right|^2} \delta\left(E_{\boldsymbol{p}+\boldsymbol{k}} - E_{\boldsymbol{p}} - \hbar\omega\right) f^0_{\boldsymbol{p}+\boldsymbol{k}} \left(1 - f^0_{\boldsymbol{p}}\right) \beta \left(N^0_\omega + 1\right) \times \left(g_{\boldsymbol{p}+\boldsymbol{k}} - g_{\boldsymbol{p}} - G_{\boldsymbol{k},\omega}\right) \quad \text{(C.12)}$$

Here, we have substituted the carrier-plasmon equilibrium scattering rate Eq. (3.13) Using the definition Eq. (2.41) of the imaginary part of the dielectric function in the RPA, Eq. (C.12) becomes

$$\left(\frac{\partial f_{\boldsymbol{p}}}{\partial t}\right)^1_{\text{coll}} = \int\limits_{\hbar\omega} \iint\limits_{\boldsymbol{k}\ \boldsymbol{q}} \frac{4\pi\beta\nu_k^2}{\hbar \left|\varepsilon^c_{\boldsymbol{k},\omega}\right|^2} \delta\left(E_{\boldsymbol{p}+\boldsymbol{k}} - E_{\boldsymbol{p}} - \hbar\omega\right) \delta\left(E_{\boldsymbol{q}+\boldsymbol{k}} - E_{\boldsymbol{q}} - \hbar\omega\right) \times \left(f^0_{\boldsymbol{q}} - f^0_{\boldsymbol{q}+\boldsymbol{k}}\right) f^0_{\boldsymbol{p}+\boldsymbol{k}} \left(1 - f^0_{\boldsymbol{p}}\right) \left(N^0_\omega + 1\right) \left(g_{\boldsymbol{p}+\boldsymbol{k}} - g_{\boldsymbol{p}} - G_{\boldsymbol{k},\omega}\right) \quad \text{(C.13)}$$

The Boltzmann equation for the plasmons yields

$$G_{\boldsymbol{k},\omega} = \frac{\int\limits_{\boldsymbol{q}} \delta\left(E_{\boldsymbol{q}+\boldsymbol{k}} - E_{\boldsymbol{q}} - \hbar\omega\right) \left(f^0_{\boldsymbol{q}} - f^0_{\boldsymbol{q}+\boldsymbol{k}}\right) \left(g_{\boldsymbol{q}+\boldsymbol{k}} - g_{\boldsymbol{q}}\right)}{\int\limits_{\boldsymbol{q}} \delta\left(E_{\boldsymbol{q}+\boldsymbol{k}} - E_{\boldsymbol{q}} - \hbar\omega\right) \left(f^0_{\boldsymbol{q}} - f^0_{\boldsymbol{q}+\boldsymbol{k}}\right)} \quad \text{(C.14)}$$

when it is solved for G(Eq. (4.40)). Substituting G in Eq. (C.13) yields

$$\left(\frac{\partial f_{\boldsymbol{p}}}{\partial t}\right)^1_{\text{coll}} = \int\limits_{\hbar\omega} \iint\limits_{\boldsymbol{k}\ \boldsymbol{q}} \frac{4\pi\beta\nu_k^2}{\hbar \left|\varepsilon^c_{\boldsymbol{k},\omega}\right|^2} \delta\left(E_{\boldsymbol{p}+\boldsymbol{k}} - E_{\boldsymbol{p}} - \hbar\omega\right) \delta\left(E_{\boldsymbol{q}+\boldsymbol{k}} - E_{\boldsymbol{q}} - \hbar\omega\right) \times \left(f^0_{\boldsymbol{q}} - f^0_{\boldsymbol{q}+\boldsymbol{k}}\right) f^0_{\boldsymbol{p}+\boldsymbol{k}} \left(1 - f^0_{\boldsymbol{p}}\right) \left(N^0_\omega + 1\right) \left(g_{\boldsymbol{p}+\boldsymbol{k}} - g_{\boldsymbol{p}} - g_{\boldsymbol{q}+\boldsymbol{k}} + g_{\boldsymbol{q}}\right) \quad \text{(C.15)}$$

Using the equation of detailed balance Eq. (C.3b), we can eliminate the plasmon

distribution N_ω^0 for carrier distribution functions. Moreover, we can carry out the integral over ω, thus eliminating the plasmon frequency from the equation. The resulting Boltzmann equation only contains carrier quantities. This is indeed the carrier–carrier scattering Boltzmann equation in first order.

$$\left(\frac{\partial f_{\boldsymbol{p}}}{\partial t}\right)^1_{\text{coll}} = \iint\limits_{\boldsymbol{k}\ \boldsymbol{q}} \frac{4\pi\beta\nu_k^2}{\hbar\left|\varepsilon^c_{\boldsymbol{k},(E_{\boldsymbol{p}+\boldsymbol{k}}-E_{\boldsymbol{p}})/\hbar}\right|^2}\delta\left(E_{\boldsymbol{p}+\boldsymbol{k}} - E_{\boldsymbol{p}} - E_{\boldsymbol{q}+\boldsymbol{k}} + E_{\boldsymbol{q}}\right) \times f^0_{\boldsymbol{p}+\boldsymbol{k}}\left(1-f^0_{\boldsymbol{p}}\right) f^0_{\boldsymbol{q}}\left(1-f^0_{\boldsymbol{q}+\boldsymbol{k}}\right)\left(g_{\boldsymbol{p}+\boldsymbol{k}} - g_{\boldsymbol{p}} - g_{\boldsymbol{q}+\boldsymbol{k}} + g_{\boldsymbol{q}}\right) \tag{C.16}$$

To highlight that this describes an interaction between two carriers of initial wave

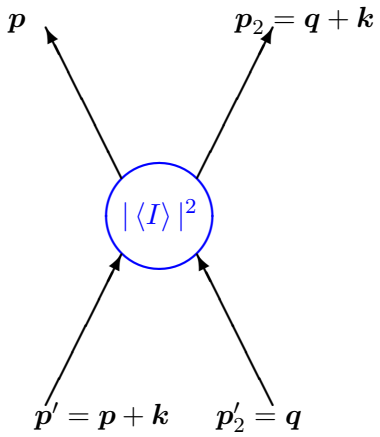

Figure C.1: Schematic explaining wave vector transfer between carriers in carrier carrier scattering. The blue circle stands for the carrier–carrier interaction Eq. (C.18).

vector $\boldsymbol{p}' = \boldsymbol{p} + \boldsymbol{k}$ and $\boldsymbol{p}_2' = \boldsymbol{q}$ and final wave vector $\boldsymbol{p}_2 = \boldsymbol{q} + \boldsymbol{k}$ and $\boldsymbol{p}$ (cf. Fig. C.1) for all possible sets of $\boldsymbol{k}$ and $\boldsymbol{q}$, we express Eq. (C.16) as

$$\left(\frac{\partial f_{\boldsymbol{p}}}{\partial t}\right)^1_{\text{coll}} = \iint\limits_{\boldsymbol{p}'}\iint\limits_{\boldsymbol{p}_2\,\boldsymbol{p}_2'} \frac{4\pi\beta\nu^2_{|\boldsymbol{p}'-\boldsymbol{p}|}}{\hbar\left|\varepsilon^c_{\boldsymbol{p}'-\boldsymbol{p},(E_{\boldsymbol{p}'}-E_{\boldsymbol{p}})/\hbar}\right|^2}\delta\left(E_{\boldsymbol{p}'} + E_{\boldsymbol{p}_2'} - E_{\boldsymbol{p}} - E_{\boldsymbol{p}_2}\right)\delta\left(\boldsymbol{p}' + \boldsymbol{p}_2' - \boldsymbol{p} - \boldsymbol{p}_2\right) \times f^0_{\boldsymbol{p}'}\left(1-f^0_{\boldsymbol{p}}\right) f^0_{\boldsymbol{p}_2'}\left(1-f^0_{\boldsymbol{p}_2}\right)\left(g_{\boldsymbol{p}'} + g_{\boldsymbol{p}_2'} - g_{\boldsymbol{p}} - g_{\boldsymbol{p}_2}\right) \tag{C.17}$$

This is becomes the expression Peierls gives [49, chapter 6.5] if one takes his matrix element $\langle I\rangle$ to be the screened carrier carrier scattering matrix element:

$$|\langle I\rangle|^2 = \frac{2\pi}{\hbar}\left|\frac{\nu_{|\boldsymbol{p}'-\boldsymbol{p}|}}{\varepsilon^c_{\boldsymbol{p}'-\boldsymbol{p},(E_{\boldsymbol{p}'}-E_{\boldsymbol{p}})/\hbar}}\right|^2 \delta\left(\boldsymbol{p}' + \boldsymbol{p}_2' - \boldsymbol{p} - \boldsymbol{p}_2\right) \tag{C.18}$$

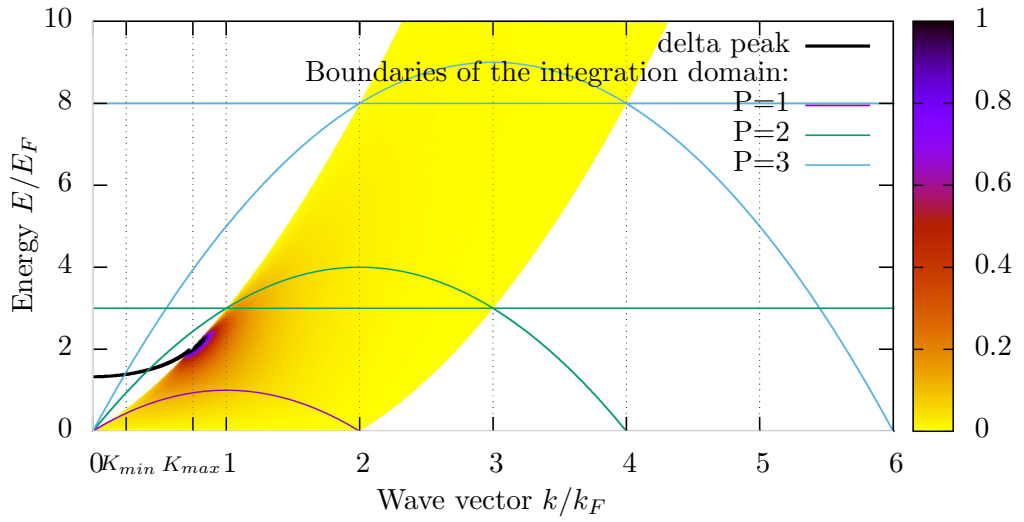

Figure C.2: Map plot of $\mathfrak{Im}\left(-\frac{1}{k\varepsilon_{k,\omega}}\right)$ inside the single pair excitation region, as a function of wave vector k and energy $E = \hbar\omega$, for $r_s = 2$ at zero temperature. Additionally, the thick black line indicates where $\mathfrak{Im}\left(-\frac{1}{k\varepsilon_{k,\omega}}\right)$ is a delta peak. The points marked K_{min} and K_{max} indicate the limits for the integration of the delta part of the self-energy integral for an initial momentum $P = \frac{p}{k_f} = 3$. The two-dimensional integration domains for different initial wave vectors lie between the k-axis and the lines in different colours. The horizontal lines are due to the distribution function, while the parabolas are due to energy-momentum conservation.

C.2.1 Quasiparticle excitation lifetime in a free electron gas in the RPA at zero temperature

The lifetime of a quasi-particle excitation of a free electron gas in the RPA [80, 118, 119] is a quantity which is closely related to the energy relaxation time Eq. (3.12) discussed in subsection 3.1.1. We discuss its detailed evaluation here, because it is similar, yet more simple, than some of the integrals we will have to evaluate in this thesis.

At $T = 0$, all states with $E < E_F$ are occupied, and all others unoccupied, see Fig. 2.1. An occupied state with $E > E_F$ is a quasi-particle excitation, and an unoccupied state with $E < E_F$ is a quasi-hole. Interaction with the electron gas gives the quasi-particle (and quasi-holes) a finite lifetime. Here, we only evaluate the quasi-particle lifetime (i.e., $p > k_F$, $P > 1$), and not the quasi-hole lifetime ($P < 1$), because the derivation of the latter is analogous to that of the former.

Quinn and Ferrell[80] originally calculated this lifetime by relating it to E^{im}_{corr}, the imaginary part of the self-energy

$$\tau_p^{\mathrm{QP}} = -\frac{2}{\hbar} E^{im}_{corr}(p). \tag{C.19}$$

This result can also be obtained directly from Fermi's Golden rule, as described in subsection 3.1.1 [22]. The only differences are that the term f_p^0 is not present, because we assume that the state with wave vector p is definitively occupied, and that we only consider emission processes, $\omega > 0$. (Absorption processes do not occur, because $N_\omega^0 = 0$ at zero temperature.) This yields

$$\frac{1}{\tau_p^{\mathrm{QP}}} = \frac{2}{\hbar} \int_{\boldsymbol{k}} \int_0^\infty \mathrm{d}\hbar\omega \, \nu_k \mathfrak{Im} \left\{ \frac{-1}{\varepsilon^c_{k,\omega}} \right\} \left(1 - f^0_{\boldsymbol{p}-\boldsymbol{k}}\right) \delta\left(E_{\boldsymbol{p}-\boldsymbol{k}} - E_{\boldsymbol{p}} + \hbar\omega\right) \quad \text{(C.20)}$$

Expression in 3d

In three dimensions, and with the scaled wave vector and frequencies Eq. (2.43) first introduced in section 2.2, Eq. (C.20) becomes

$$\begin{aligned} \frac{1}{\tau_P^{\mathrm{QP}}} &= \frac{2}{\hbar} k_F^3 \int_{\boldsymbol{K}} \int_0^\infty \mathrm{d}\Omega \, \nu_K \mathfrak{Im} \left\{ \frac{-1}{\varepsilon^c_{K,\Omega}} \right\} \left(1 - f^0_{\boldsymbol{P}-\boldsymbol{K}}\right) \delta\left((\boldsymbol{P}-\boldsymbol{K})^2 - P^2 + \Omega\right) \quad \text{(C.21)} \\ &= \frac{2}{\hbar} \frac{e^2 k_F}{\pi} \int_0^\infty \mathrm{d}K \int_0^\pi \mathrm{d}\theta \, \sin\theta \int_0^\infty \mathrm{d}\Omega \, \mathfrak{Im} \left\{ \frac{-1}{\varepsilon^c_{K,\Omega}} \right\} \left(1 - f^0_{\sqrt{P^2-\Omega}}\right) \delta\left(K^2 + \Omega - 2PK\cos\theta\right) \end{aligned}$$

Evaluating the theta integral using the delta-function yields

$$\frac{1}{\tau_P^{\mathrm{QP}}} = \frac{2}{\hbar} \frac{e^2 k_F}{2\pi P} \int_0^{2P} \frac{\mathrm{d}K}{K} \int_0^{K(2P-K)} \mathrm{d}\Omega \, \mathfrak{Im} \left\{ \frac{-1}{\varepsilon^c_{K,\Omega}} \right\} \left(1 - f^0_{\sqrt{P^2-\Omega}}\right) \quad \text{(C.22)}$$

For the ease of comparison with the literature[118, 80] we give the expression in terms of the imaginary part of the self-energy

$$\mathfrak{Im}\left\{E_p^{corr}\right\}/E_F = \frac{1}{\pi k_F a_0 P} \int_0^{2P} \frac{\mathrm{d}K}{K} \int_0^{K(2P-K)} \mathrm{d}\Omega \, \mathfrak{Im} \left\{ \frac{1}{\varepsilon^c_{K,\Omega}} \right\} \left(1 - f^0_{\sqrt{P^2-\Omega}}\right) \quad \text{(C.23)}$$

As discussed in subsubsection 2.2.2.2, at zero temperature, the wave vector – frequency plane splits into the single pair excitation region (SPER), $\mathfrak{Im}\{\varepsilon_{k,\omega}\} \neq 0$, and the rest where $\mathfrak{Im}\{\varepsilon_{k,\omega}\} = 0$ and where the plasma oscillations are undamped. Consequently, the integral Eq. (C.23) will have a SPER contribution, and an undamped plasma contribution. much the same way we evaluated the f-sum rule integral in section 2.2.3.2.

Delta peak contribution For $\Omega > K(K+2)$, we have can use Eq. (2.75) for the imaginary part of the inverse dielectric function. Hence the imaginary part of the

self-energy will be

$$\mathfrak{Im}\left\{E_p^{corr}\right\}/E_F = -\frac{1}{a_0 k_F K}\int_{K_{min}}^{K_{max}}\frac{\mathrm{d}K}{K}\frac{1}{\left|\frac{\partial}{\partial\Omega}\mathfrak{Re}\left\{\varepsilon_{K,\Omega_K}\right\}\right|} \tag{C.24}$$

with K_{min} and K_{max} from

$$0 < \Omega_K < K(2P-K) \quad \text{and} \tag{C.25}$$

$$0 < \Omega_K < P^2 - 1 \tag{C.26}$$

Note that we absorbed the factor $(1 - f^0_{\sqrt{P^2-\Omega}})$ into the definition of the domain Eq. (C.26). The restriction Eq. (C.25) stems from energy and momentum conservation. We included lines corresponding to Eq. (C.25) and Eq. (C.26) for several initial wave vectors P in Fig. C.2.

While there is an analytic expression for the real part of the Lindhard dielectric function $\frac{\partial}{\partial W}\mathfrak{Re}\{\varepsilon(Q, W_p(Q)\}$, cf. Eq. (2.73), K_{min} and K_{max} have to be determined numerically, or graphically - see Fig. C.2. Eq. (C.24) can be solved analytically when we replace $\varepsilon_{k,\omega}$ by its long-wavelength limit. The corresponding approximate delta peak contribution to $\mathfrak{Im}\{E_p^{corr}\}$ can be compared to the exact numerical solution in Fig. C.3.

SPER contribution The SPER contribution to $\mathfrak{Im}\left\{E_p^{corr}\right\}/E_F$ is

$$\mathfrak{Im}\left\{E_p^{corr}\right\}/E_F = \frac{1}{\pi a_0 k_F P}\int_0^{P+1}\frac{\mathrm{d}K}{K}\int_{\Omega_{min}(K)}^{\Omega_{max}(K,P)}\mathrm{d}\Omega\,\mathfrak{Im}\left\{\frac{1}{\varepsilon_{K,\Omega}}\right\} \tag{C.27}$$

with the integration limits (cf. Fig. C.2)

$$\Omega_{min}(Q) = \begin{cases} 0 & P \le 2 \\ K(K-2) & P > 2 \end{cases} \qquad \Omega_{max}(K,K) = \begin{cases} K(K+2) & K \le P-1 \\ P^2-1 & K > P-1 \end{cases} \tag{C.28}$$

Figure C.3 gives the imaginary part of the self-energy for $r_s = 2$. It includes the contribution to the imaginary self-energy due to the delta-peak and the finite part of $\mathfrak{Im}(\frac{1}{\varepsilon_{K,\Omega}})$, the approximations and calculations by Quinn[118], and compares the total imaginary self-energy to later and more numerically accurate results by Lundqvist[120].

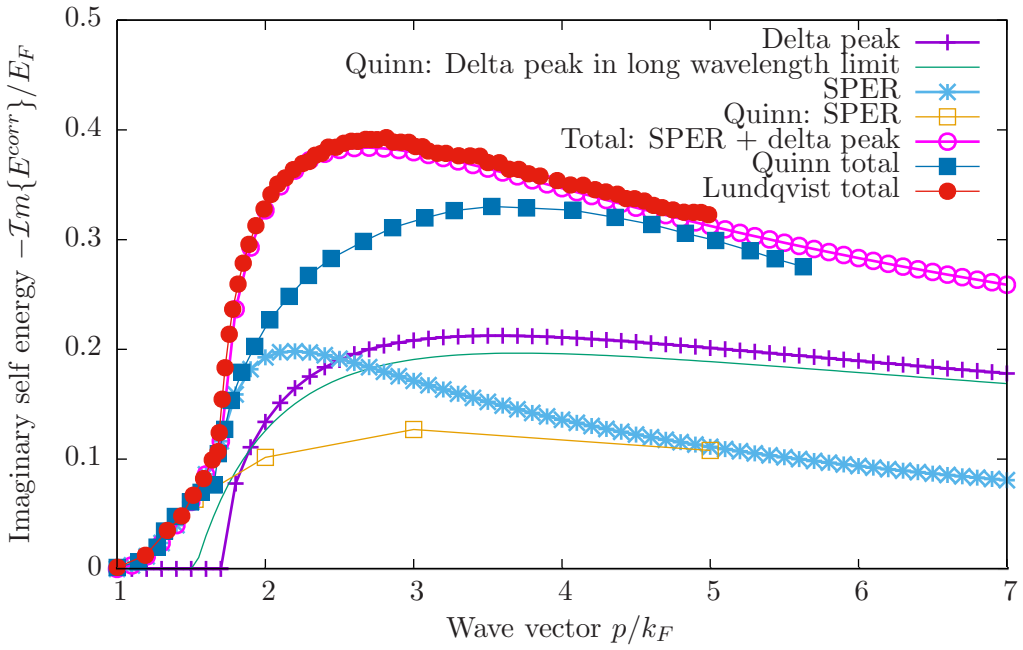

Figure C.3: Imaginary part of the self-energy $\mathfrak{Im}\left\{E_p^{corr}\right\}$ for $r_s = 2$ at T=0 as a function of wave vector p. Our calculations - the first three in the legend- are compared to the first calculations by Quinn[118], and later ones by Lundquist[120]. The data for the Quinn and Lundqvist plots was extracted from plots in[120, 118], and is therefore somewhat inaccurate. We give the contributions from the single pair excitation region (marked "SPER") and the delta peak separately, both for our calculations and the literature curves where available. Also given is the long wavelength limit of delta contribution as calculated by Quinn [118].

C.3 Integrals for the 3-d Boltzmann equation

The linearized collisional integral has been evaluated explicitly by Sanborn[48] for pure carrier–carrier scattering and in bulk semiconductors with spherical parabolic bands. Apart from the scattering rates, our expression is entirely equivalent to hers. However, we give the expression in terms of transferred energy and wave vector, while she uses bipolar coordinates [121].

We start by making the approximation of spherical parabolic bands, Eq. (2.22), from which follows $\boldsymbol{v_p} = \frac{\hbar}{m^*}\boldsymbol{p}$ for the group velocity, and $\tau_{\boldsymbol{p}} = \tau_p$. We scale all wave vectors with the Fermi wave vector $k_F = \sqrt[3]{3\pi^2 n}$ and all energies with the Fermi energy E_F from Eq. (2.27), to obtain the dimensionless wave vectors and energies Eq. (2.43) already used in section 2.2. Assuming all carriers are located in a single band, we can now specify the wave vector and frequency integrals as

$$\int_{\boldsymbol{k}} = k_F^3 \int \frac{\mathrm{d}^3\boldsymbol{K}}{(2\pi)^3} \quad \text{and} \quad \int_{\hbar\omega} = E_F \int \mathrm{d}\Omega\,. \tag{C.29}$$

C.3.1 Collective mode drag term $G_{\boldsymbol{k},\omega}$

With these approximation, we can use Eq. (4.12) to write $T_{\boldsymbol{K},\Omega}$ from Eq. (4.23) as

$$T_{\boldsymbol{K},\Omega} = \frac{8\pi^2 e^2/K^2}{\mathfrak{Im}\left(\varepsilon^{tot}_{\boldsymbol{K},\Omega}\right)} \frac{1}{(2\pi)^3} \frac{k_F}{E_F} \int \mathrm{d}^3\boldsymbol{Q}\, \delta(|\boldsymbol{Q}+\boldsymbol{K}|^2 - Q^2 - \Omega) \left(f^0_Q - f^0_{|\boldsymbol{Q}+\boldsymbol{K}|}\right) \times \frac{\left[\tau_{|\boldsymbol{Q}+\boldsymbol{K}|}(\boldsymbol{Q}+\boldsymbol{K}) - \tau_Q \boldsymbol{Q}\right] \cdot \boldsymbol{E}}{\boldsymbol{P}\cdot\boldsymbol{E}} \tag{C.30}$$

Here, we have used the Fourier transform of the Coulomb potential $\nu_k = \frac{4\pi e^2}{k_F^2 K^2}$. We evaluate the integral in Eq. (C.30) in spherical coordinates, with the polar axis parallel to the $\boldsymbol{K}$ direction and with the vectors $\boldsymbol{K}$ and $\boldsymbol{E}$ spanning the $x-z-$plane. That means that in Cartesian coordinates,

$$\boldsymbol{Q} = Q \begin{pmatrix} \sin\theta\cos\varphi \\ \sin\theta\sin\varphi \\ \cos\theta \end{pmatrix}, \boldsymbol{E} = E \begin{pmatrix} \sin\theta_{K,E} \\ 0 \\ \cos\theta_{K,E} \end{pmatrix}, \boldsymbol{K} = K \begin{pmatrix} 0 \\ 0 \\ 1 \end{pmatrix} \tag{C.31}$$

where Q, θ and φ are the spherical coordinates of $\boldsymbol{Q}$ and $\theta_{K,E}$ is the polar angle of $\boldsymbol{E}$, the angle between $\boldsymbol{K}$ and $\boldsymbol{E}$. As none of the other factors in the integral depend on the azimuthal angle φ, we can evaluate the φ-integral.

$$\frac{1}{2\pi}\int_0^{2\pi} \mathrm{d}\varphi\, \boldsymbol{Q}\cdot\boldsymbol{E} = \boldsymbol{E}\cdot\boldsymbol{K}\frac{Q}{K}\cos\theta \tag{C.32}$$

We use the energy conservation delta-function to evaluate the θ-integral, which means we can replace $\cos\theta$ by $\frac{\Omega - Q^2}{2QK}$, and eventually find

$$T_{\boldsymbol{K},\Omega} = \frac{1}{\mathfrak{Im}\left(\varepsilon^{tot}_{\boldsymbol{K},\Omega}\right)} \frac{e^2 k_F}{K^3 E_F} \int_{\frac{1}{2}|\frac{\Omega}{K}-K|}^{\infty} \mathrm{d}Q Q \left(f^0_Q - f^0_{\sqrt{Q^2+\Omega}}\right) \frac{\tau_{\sqrt{Q^2+\Omega}}\left(1+\frac{\Omega}{K^2}\right) + \tau_Q\left(1-\frac{\Omega}{K^2}\right)}{2} \tag{C.33}$$

We split the integral for T into four parts.

$$T_{\boldsymbol{K},\Omega} = \frac{1}{\mathfrak{Im}\left(\varepsilon^{tot}_{\boldsymbol{K},\Omega}\right)} \frac{e^2 k_F}{K^3 E_F} \frac{1}{2} \left[\left(1+\frac{\Omega}{K^2}\right)\left(I^1_{K,\Omega} - I^3_{K,\Omega}\right) + \left(1-\frac{\Omega}{K^2}\right)\left(I^2_{K,\Omega} - I^4_{K,\Omega}\right)\right] \tag{C.34}$$

with

$$I^1_{K,\Omega} = \int_{\frac{1}{2}|\frac{\Omega}{K}-K|}^{\infty} \mathrm{d}Q Q f^0_Q \tau_{\sqrt{Q^2+\Omega}} \qquad I^2_{K,\Omega} = \int_{\frac{1}{2}|\frac{\Omega}{K}-K|}^{\infty} \mathrm{d}Q Q f^0_Q \tau_Q \tag{C.35}$$

By making the substitution $Q \to \sqrt{Q^2+\Omega}$, we find that

$$I^3_{K,\Omega} = \int\limits_{\frac{1}{2}|\frac{\Omega}{K}-K|}^{\infty} \mathrm{d}QQ f^0_{\sqrt{Q^2+\Omega}} \tau_{\sqrt{Q^2+\Omega}} = I^2_{K,-\Omega} \tag{C.36}$$

$$I^4_{K,\Omega} = \int\limits_{\frac{1}{2}|\frac{\Omega}{K}-K|}^{\infty} \mathrm{d}QQ f^0_{\sqrt{Q^2+\Omega}} \tau_Q = I^1_{K,-\Omega} \tag{C.37}$$

We exclusively use the expressions $I^1_{K,\pm\Omega}$ and $I^2_{K,\pm\Omega}$, and find

$$T_{\boldsymbol{K},\Omega} = \frac{1}{\mathfrak{Im}\left(\varepsilon^{tot}_{\boldsymbol{K},\Omega}\right)} \frac{e^2 k_F}{K^3 E_F} \frac{1}{2} \Big\{ \left(I^1_{K,\Omega} - I^1_{K,-\Omega}\right) + \left(I^2_{K,\Omega} - I^2_{K,-\Omega}\right) \tag{C.38}$$

$$+ \frac{\Omega}{K^2} \left[\left(I^1_{K,\Omega} + I^1_{K,-\Omega}\right) - \left(I^2_{K,\Omega} + I^2_{K,-\Omega}\right) \right] \Big\} \tag{C.39}$$

which, together with the antisymmetry in Ω of $\mathfrak{Im}\left(\varepsilon^{tot}_{\boldsymbol{K},\Omega}\right)$ shows that $T_{K,-\Omega} = T_{K,\Omega}$.

C.3.2 Effective momentum relaxation time τ_p

Let us evaluate Eq. (4.24) for spherical parabolic bands. In the dimensionless variables from subsection C.3.1, the integral reads

$$\frac{1}{\tau_P} = \frac{k_F^3}{(2\pi)^3} \int \mathrm{d}^3\boldsymbol{K} \int \mathrm{d}\Omega\, W^0_{K,\Omega} \delta\left(|\boldsymbol{P}+\boldsymbol{K}|^2 - P^2 - \Omega\right) \frac{f^0_{|\boldsymbol{P}+\boldsymbol{K}|}}{f^0_P} \left(N^0_\Omega + 1\right) \tag{C.40}$$

$$\times \left[1 - \frac{\tau_{|\boldsymbol{P}+\boldsymbol{K}|}}{\tau_P} \frac{(\boldsymbol{P}+\boldsymbol{K})\cdot\boldsymbol{E}}{\boldsymbol{P}\cdot\boldsymbol{E}} + \frac{T_{\boldsymbol{K},\Omega}}{\tau_P} \frac{\boldsymbol{K}\cdot\boldsymbol{E}}{\boldsymbol{P}\cdot\boldsymbol{E}}\right]$$

As in subsection C.3.1, we will solve this integral in spherical coordinates. Alignment of the coordinate system is identical to that in subsection C.3.1, except for the naming to the vectors, i.e., Eq. (C.31) and C.32 hold, if we set $\boldsymbol{K} \to \boldsymbol{P}$ and $\boldsymbol{Q} \to \boldsymbol{K}$:

$$\frac{1}{2\pi} \int\limits_0^{2\pi} \mathrm{d}\varphi\, \boldsymbol{K}\cdot\boldsymbol{E} = \boldsymbol{E}\cdot\boldsymbol{P} \frac{K}{P} \cos\theta \tag{C.41}$$

We also need to assume that $T_{\boldsymbol{K},\Omega} = T_{K,\Omega}$, which is another way of requiring that $\mathfrak{Im}(\varepsilon^{tot}_{\boldsymbol{K},\Omega}) = \mathfrak{Im}(\varepsilon^{tot}_{K,\Omega})$. On inspecting Eq. (4.8), we see that this is consistent with our assumption of spherical bands. Furthermore, we need $W^0_{\boldsymbol{K},\Omega} = W^0_{K,\Omega}$, which means that the real part of the dielectric function cannot depend on the direction of the wave vector either, $\mathfrak{Re}(\varepsilon^{tot}_{\boldsymbol{K},\Omega}) = \mathfrak{Re}(\varepsilon^{tot}_{K,\Omega})$, see Eq. (3.4).

Hence, we can carry out the integral over the azimuthal and polar angles in

Eq. (C.40). Using the delta-function in Eq. (C.40), we can set $\cos\theta = \frac{\Omega - K^2}{2PK}$ yielding

$$\frac{1}{\tau_P} = \frac{k_F^3}{(2\pi)^2}\frac{1}{2P}\int_0^\infty \mathrm{d}K\, K \int_{K(K-2P)}^{K(K+2P)} \mathrm{d}\Omega\, W^0_{K,\Omega} \frac{f^0_{\sqrt{P^2+\Omega}}}{f^0_P}\left(N^0_\Omega + 1\right) \times \left[1 - \frac{\tau_{\sqrt{P^2+\Omega}}}{\tau_P}\left(1 + \frac{\Omega - K^2}{2P^2}\right) + \frac{T_{K,\Omega}}{\tau_P}\frac{\Omega - K^2}{2P^2}\right] \quad \text{(C.42)}$$

From Eq. (C.42) we can read that an infinite mobility solution of the type discussed in subsection 4.4.3 holds if $\tau_P = T_{K,\Omega}$ =const.

Quasi-elastic relaxation time approximation As discussed in subsection 4.4.3, for the initial step $n = 1$ in our iteration, we set $\tau^0_P = \tau$ =const, and we assume $|\boldsymbol{P} + \boldsymbol{K}| \approx P$ in the square bracket in Eq. (C.42), so that it will be replaced by $C_{K,\Omega}\left[1 - \frac{\cos\theta_{P+K,E}}{\cos\theta_{P,E}}\right]$ where $\theta_{A,B}$ is the angle between $\boldsymbol{A}$ and $\boldsymbol{B}$. This approximation is only made in this term, that is, Ω is not set to zero anywhere else in Eq. (C.42). When we integrate over the azimuthal angle,

$$\frac{1}{2\pi}\int_0^{2\pi} \mathrm{d}\varphi \left[1 - \frac{\cos\theta_{P+K,E}}{\cos\theta_{P,E}}\right] = 1 - \cos\theta_{P+K,P} \geq 0 \quad \text{(C.43)}$$

we see that the quasi-elastic scattering approximation ensures that τ^1_P is non-negative, independent of the particulars of the scattering mechanism. Consequently, the quasi-elastic relaxation time for materials with spherical parabolic bands reads

$$\frac{1}{\tau^{1,e}_P} = \frac{k_F^3}{(2\pi)^2}\frac{1}{2P}\int_0^\infty \mathrm{d}K\, K \int_{K(K-2P)}^{K(K+2P)} \mathrm{d}\Omega\, \frac{f^0_{\sqrt{P^2+\Omega}}}{f^0_P}\left(N^0_\Omega + 1\right) \times W^0_{K,\Omega}\left[1 - \frac{P}{\sqrt{P^2+\Omega}}\left(1 + \frac{\Omega - K^2}{2P^2}\right)\right]. \quad \text{(C.44)}$$

C.3.2.1 Example: Momentum relaxation due to carrier–LO-phonon scattering

We discuss carrier–LO-phonon scattering in the case of undamped LO-phonons explicitly, because all the integrals in the Boltzmann equation can be solved analytically in that case. As the LO-phonon frequency is independent of wave vector, Eq. (4.43) can be turned into a system of linear equations and solved without iteration [95, 94, 96]. We will not follow this path, because it is not straightforward to generalize to the more general cases treated in this work.

To calculate the momentum relaxation rate, we have to evaluate Eq. (C.42) with the

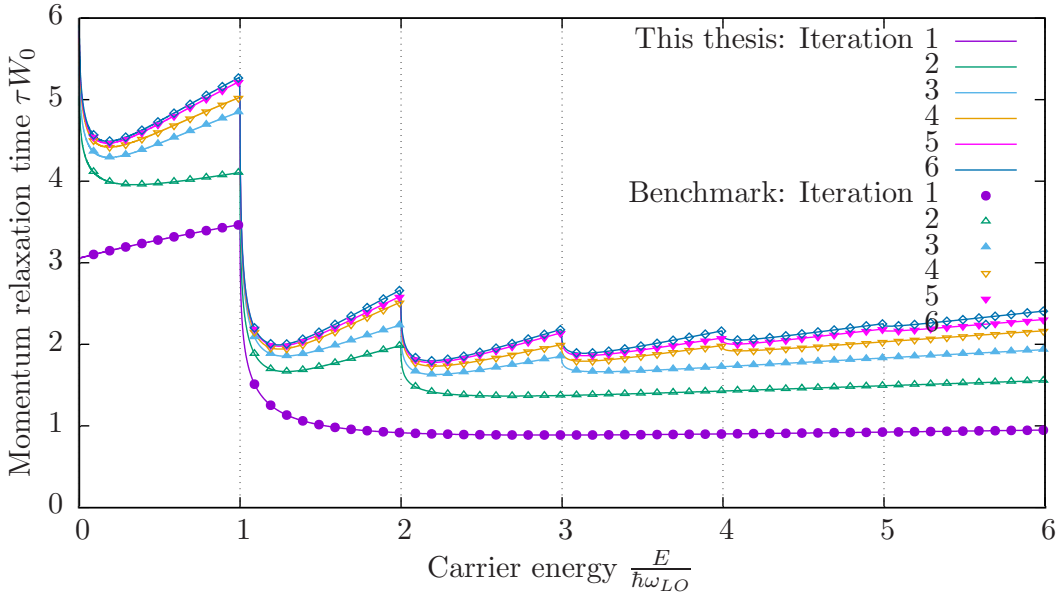

Figure C.4: Effective momentum relaxation rate τ as a function of carrier energy for GaAs at 300K and an electronic concentration of $10^{14}cm^{-3}$. τ is plotted in units of W_0^{-1} from Eq. (C.53) [26, 96]. For GaAs, $W_0 \approx 7.6GHz$. The first six steps of the iteration are shown. The benchmarks have been calculated with a code [122], which uses the Maxwell-Boltzmann distribution function. Our calculations use the Fermi-Dirac distribution function, which, however for GaAs at 300K and an electronic concentration of $10^{14}cm^{-3}$, at $\tilde{\mu}\beta \approx -8.4$ is far in the Maxwell-Boltzmann regime.

scattering rate Eq. (3.22). This scattering rate reads

$$W^0_{K,\Omega} = \frac{2\pi}{E_F} F^u_{k_F} \frac{1}{K^2} \left[\delta(\Omega - \Omega_{LO}) - \delta(\Omega - \Omega_{LO})\right] \tag{C.45}$$

in dimensionless units. We split up the integral Eq. (C.42) in two terms as in Eq. (5.5) which is described in subsection 5.3.2.

$$\frac{1}{\tau_P} = R_P^{1,+} + R_P^{1,-} - R_P^{2,+}\{\tau\}/\tau_P - R_P^{2,-}\{\tau\}/\tau_P \tag{C.46}$$

The first term $R_P^{1\pm}$ is

$$R_P^{1,\pm} = \frac{k_F^3}{4\pi E_F} \frac{F^u_{k_F}}{P} \frac{f^0_{\sqrt{P^2 \pm \Omega_{LO}}}}{f^0_P} \left[\pm\left(N^0_{\pm\Omega_{LO}} + 1\right)\right] \ln(K^{\pm}_{max}/K^{\pm}_{min}) \Theta(P^2 \pm \Omega_{LO}), \tag{C.47}$$

where Θ is the Heaviside stepfunction. This means that emission processes ("-"sign) only occur when $P^2 > \Omega_{LO}$, i.e., the kinetic energy has to be larger than the LO-phonon energy to emit an LO-phonon. The Bose-Einstein distribution function in $R_P^{1,-}$ is $-(N^0_{-\Omega_{LO}} + 1) = N^0_{\Omega_{LO}}$, so that $R^{1,\pm}$ are both positve.

The quantities $K^{\pm}_{min}$ and $K^{\pm}_{max}$ stem from energy-momentum conservation, and are

$$K^{\pm}_{max} = P + \sqrt{P^2 \pm \Omega_{LO}}\Theta(P^2 \pm \Omega_{LO}) \tag{C.48}$$

$$K^{\pm}_{min} = \left|P - \sqrt{P^2 \pm \Omega_{LO}}\Theta(P^2 \pm \Omega_{LO})\right| \tag{C.49}$$

The second term $R_P^{2,\pm}$ can be evaluated similarly to the first, yielding

$$R_P^{2,\pm} = \frac{k_F^3}{4\pi E_F}\frac{F^u_{k_F}}{P}\frac{f^0_{\sqrt{P^2\pm\Omega_{LO}}}}{f^0_P}\left[\pm\left(N^0_{\pm\Omega_{LO}}+1\right)\right]\frac{\tau_{\sqrt{P^2\pm\Omega_{LO}}}}{\tau_P}\Theta\left(P^2\pm\Omega_{LO}\right)\times \left[\ln(K^{\pm}_{max}/K^{\pm}_{min})\left(1\pm\frac{\Omega_{LO}}{2P^2}\right) - \frac{\sqrt{P^2\pm\Omega_{LO}}}{P}\right] \tag{C.50}$$

We see that if we solve equation Eq. (C.46) by iterating it to self-consistency

$$\frac{1}{\tau_P^{n+1}} = R_P^{1,+} + R_P^{1,-} - R_P^{2,+}\{\tau^n\}/\tau_P^n - R_P^{2,-}\{\tau^n\}/\tau_P^n, \tag{C.51}$$

each subsequent iteration τ_P^{n+1} only depends on its previous iteration value $\tau^n_{\sqrt{P\pm\Omega_{LO}}}$ at the energy plus or minus the LO-phonon energy. This is why Ridley has called his way of solving this equation the ladder method [96]. As there are no integrals to evaluate within each iteration, equation Eq. (C.51) can be iterated to self-consistency without large numerical effort.

Elastic limit of the LO-phonon momentum relaxation time For ease with comparison with the literature, e.g. [26, 106], we give the elastic limit of the carrier–LO-phonon momentum relaxation time, $\tau_p^{elastic}$ i.e., for when the LO-phonon energy is much smaller than the carrier energy E $\Omega_{LO} \ll P^2$, or $\hbar\omega_{LO} \ll E$.

$$\frac{1}{\tau_p^{elastic}} = \frac{k_F^4}{4\pi E_F}\frac{F^u_{k_F}}{p} = \left(1-\frac{\varepsilon^\infty}{\varepsilon^0}\right)\frac{\omega_{LO}}{pa_0^*}\left(2N^0_{\omega_{LO}}+1\right) \tag{C.52}$$

The momentum relaxation time is often given as a function of the carrier energy scaled by the LO-phonon energy [26],

$$\tau_E^{elastic} = \frac{2}{W_0(2N^0_{\omega_{LO}}+1)}\sqrt{\frac{E}{\hbar\omega_{LO}}} \quad \text{with} \quad W_0 = \left(\frac{1}{\varepsilon^\infty}-\frac{1}{\varepsilon^0}\right)\frac{e^2}{\hbar}\sqrt{\frac{2m^*\omega_{LO}}{\hbar}}, \tag{C.53}$$

where we introduce the frequency W_0 used by Ridley [26, 96].

We show the momentum relaxation times obtained after a small number of iterations in Fig. C.4.

C.4 Integrals for the 2-d Boltzmann equation

C.4.1 Transport and screening due to multiple valleys

As we want to describe transport and screening in MoS_2, which has two equivalent conduction band minima, we have to account for multiple equivalent valleys in our equations for the coupled Boltzmann equations, and the carrier dielectric functions.

Being able to capture this was one of the reasons why we wrote the integrals over the carrier wave vector symbolically as $\int_{\boldsymbol{p}}$. If we now write these integrals as

$$\int_{\boldsymbol{p}} = \sum_{i=1}^{M_v} \int \frac{\mathrm{d}^2\boldsymbol{p}_i}{(2\pi)^2} = M_v \int \frac{\mathrm{d}^2\boldsymbol{p}}{(2\pi)^2} \tag{C.54}$$

we automatically obtain equations that hold for the case of M_v equivalent conduction band valleys. Explicitly, this means, that $n^{d=2} = M_v m_i^{d=2}$, i.e., that only a fraction of the total carrier sheet density is present in each valley, and that each of the valleys contributes to the susceptibility of the carrier gas. $\chi^c_{\boldsymbol{k},\omega} = M_v \chi^{c,\text{valley } i}_{\boldsymbol{k},\omega}$

As discussed in subsection C.5.3, we only need to consider the carriers in one of the valleys to calculate the total mobility due to all valleys. This means that all the carrier quantities ($f^0_{\boldsymbol{p}}$, $E_{\boldsymbol{p}}$ and n) in the integrals for the momentum relaxation time only pertain to one valley (We do not include a valley index for brevity, and because the equations are identical in all valleys.), but the dielectric functions and the integrals for the collective modes are sums over all valleys.

C.4.2 Integrals for momentum relaxation time

In two dimensions, the expression for the effective momentum relaxation time τ_p of a carrier due to interaction with coupled collective modes obeys

$$\frac{1}{\tau_p} = \frac{1}{(2\pi)^2} \int \mathrm{d}^2\boldsymbol{k} \int \mathrm{d}\hbar\omega \, W^0_{\boldsymbol{k},\omega} \delta\left(E_{\boldsymbol{p}+\boldsymbol{k}} - E_p - \hbar\omega\right) \left(N^0_\omega + 1\right) \frac{f^0_{E_{\boldsymbol{p}+\boldsymbol{k}}}}{f^0_{E_{\boldsymbol{p}}}} \times \left[1 - \frac{\tau_{\boldsymbol{p}+\boldsymbol{k}}}{\tau_p} \frac{(\boldsymbol{p}+\boldsymbol{k})\cdot\boldsymbol{E}}{\boldsymbol{p}\cdot\boldsymbol{E}} + \frac{T_{\boldsymbol{k},\omega}}{\tau_{\boldsymbol{p}}} \frac{\boldsymbol{k}\cdot\boldsymbol{E}}{\boldsymbol{p}\cdot\boldsymbol{E}}\right] \tag{C.55}$$

if we assume that all carriers are located in the $z = 0$ plane and hence all transferred wave vectors $\boldsymbol{k}$ are truly two-dimensional. We also neglect inter-valley scattering.

Here, $W_{\boldsymbol{k},\omega}$ is the equilibrium scattering rate between the carrier and the coupled collective mode, and $\boldsymbol{k}$ and $\hbar\omega$ are the transferred wave vector and energy in the scattering process. E_p is the energy of a carrier of wave vector $\boldsymbol{p}$, which we assume to be in a spherical, parabolic band, and f^0_E is their equilibrium distribution function,

the Fermi-Dirac distribution. N^0_ω is the distribution function of the coupled collective modes, the Bose-Einstein distribution. $T_{\boldsymbol{k},\omega}$ is the lifetime due to drag between the carriers and the coupled collective modes. We now scale all wave vectors with the Fermi wave vector $k_F = \sqrt[2]{2\pi n_S}$ (cf. Eq. (2.30)) , where n_S is the two-dimensional electron density, and all energies with the Fermi energy E_F from Eq. (2.27) to obtain the dimensionless wave vectors $K = \frac{k}{k_F}$, $P = \frac{p}{k_F}$ and $Q = \frac{q}{k_F}$, and the dimensionless energy $\Omega = \frac{\hbar\omega}{E_F}$.

In the dimensionless variables, the integral reads

$$\frac{1}{\tau_P} = \frac{k_F^2}{(2\pi)^2}\int \mathrm{d}^2\boldsymbol{K}\int \mathrm{d}\Omega\, W^0_{\boldsymbol{K},\Omega}\left(N^0_\Omega + 1\right)\delta\left(|\boldsymbol{P}+\boldsymbol{K}|^2 - P^2 - \Omega\right)\frac{f^0_{|\boldsymbol{P}+\boldsymbol{K}|}}{f^0_P} \times\left[1 - \frac{\tau_{|\boldsymbol{P}+\boldsymbol{K}|}}{\tau_P}\frac{(\boldsymbol{P}+\boldsymbol{K})\cdot\boldsymbol{E}}{\boldsymbol{P}\cdot\boldsymbol{E}} + \frac{T_{\boldsymbol{K},\Omega}}{\tau_P}\frac{\boldsymbol{K}\cdot\boldsymbol{E}}{\boldsymbol{P}\cdot\boldsymbol{E}}\right] \quad \text{(C.56)}$$

The quantities $W_{\boldsymbol{K},\Omega}$, f_P, τ_P and $T_{K,\Omega}$ have the same value (and unit) as $W_{\boldsymbol{k},\omega}$, f_{E_p}, τ_p and $T_{k,\omega}$. As τ appears on both sides of Eq. (C.56), we will solve it iteratively. In the following, we will discuss the evaluation of the integral for each iteration step. We

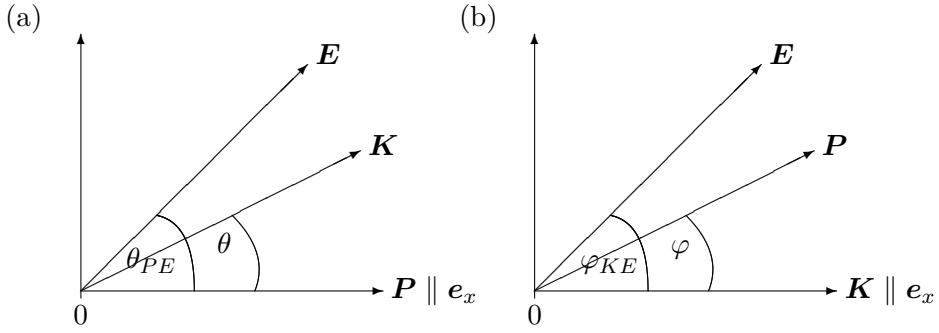

Figure C.5: Coordinate system for (a) $\boldsymbol{K}$ integral in $\tau_{\boldsymbol{P}}$, Eq. (C.56)f (b) $\boldsymbol{P}$ integral in $T_{\boldsymbol{K},\Omega}$, Eq. (C.70)f

carry out the integral over $\boldsymbol{K}$ in two-dimensional cylindrical coordinates with the x-axis aligned with $\boldsymbol{P}$, as in Fig. C.5a. The angle between $\boldsymbol{P}$ and $\boldsymbol{K}$ is the integration variable θ, and the angle between $\boldsymbol{P}$ and $\boldsymbol{E}$ is θ_{PE}.

$$\int \mathrm{d}^2\boldsymbol{K} = \int_0^\infty \mathrm{d}K\, K \int_{-\pi}^{\pi}\mathrm{d}\theta \quad \text{(C.57)}$$

Let us write the integrand in Eq. (C.56) in terms of K and θ. As in the three-dimensional case, we assume that $W_{\boldsymbol{K},\Omega} = W_{K,\Omega}$. The delta-function reads

$$\delta\left(|\boldsymbol{P}+\boldsymbol{K}|^2 - P^2 - \Omega\right) = \delta\left(K^2 + 2PK\cos\theta - \Omega\right) = \frac{1}{2PK}\delta\left(\cos\theta - \frac{\Omega - K^2}{2PK}\right),$$

and

$$|\boldsymbol{P}+\boldsymbol{K}| = \sqrt{P^2+K^2+2PK\cos\theta}.$$

So far, all terms have been symmetric in the angle θ. The terms

$$\frac{\boldsymbol{K}\cdot\boldsymbol{E}}{\boldsymbol{P}\cdot\boldsymbol{E}} = \frac{K}{P}\frac{\cos(\theta_{PE}-\theta)}{\cos\theta_{PE}} = \frac{K}{P}\cos\theta + \frac{K}{P}\tan\theta_{PE}\sin\theta \tag{C.58}$$

and

$$\frac{(\boldsymbol{P}+\boldsymbol{K})\cdot\boldsymbol{E}}{\boldsymbol{P}\cdot\boldsymbol{E}} = 1 + \frac{K}{P}\cos\theta + \frac{K}{P}\tan\theta_{PE}\sin\theta \tag{C.59}$$

have an antisymmetric contribution. Fortunately, the azimuthal integral over the antisymmetric summand vanishes:

$$\int_{-\pi}^{\pi}\mathrm{d}\theta\, h(\theta) = \int_{0}^{\pi}\mathrm{d}\theta\ [h(\theta)+h(-\theta)] = \begin{cases} 0 & h(-\theta) = -h(\theta) \\ 2\int_0^{\pi}\mathrm{d}\theta\, h(\theta) & h(-\theta) = h(\theta) \end{cases} \tag{C.60}$$

Eventually, this yields

$$\begin{aligned}\frac{1}{\tau_P} = \frac{k_F^2}{(2\pi)^2}\int_0^{\infty}\mathrm{d}K\,K\int_{K(K-2P)}^{K(K+2P)}\mathrm{d}\Omega\frac{2W^0_{K,\Omega}\left(N^0_\Omega+1\right)}{\sqrt{\Omega-K(K-2P)}\sqrt{K(K+2P)-\Omega}}\frac{f^0_{\sqrt{P^2+\Omega}}}{f^0_P} \\ \times\left[1-\frac{\tau_{\sqrt{P^2+\Omega}}}{\tau_P}\left(1+\frac{\Omega-K^2}{2P^2}\right)+\frac{T_{\boldsymbol{K},\Omega}}{\tau_P}\frac{\Omega-K^2}{2P^2}\right]\end{aligned} \tag{C.61}$$

Here we used that the integral over θ

$$\begin{aligned}2\int_0^{\pi}\mathrm{d}\theta\,\frac{1}{2PK}\delta\left(\cos\theta-\frac{\Omega-K^2}{2PK}\right) &= \frac{1}{PK}\int_0^{\pi}\mathrm{d}\theta\,\frac{1}{\sin\theta}\delta\left[\theta-\arccos\left(\frac{\Omega-K^2}{2PK}\right)\right] \\ &= \begin{cases}\frac{2}{\sqrt{\Omega-K(K-2P)}\sqrt{K(K+2P)-\Omega}} & K(K-2P)\le\Omega\le K(K+2P) \\ 0 & \text{else}\end{cases}\end{aligned} \tag{C.62}$$

For the quasi-elastic momentum relaxation time from Eq. (4.31), we have to replace the square bracket in Eq. (C.61) with its quasi-elastic, RTA limit. This bracket turns out to be identical to its 3d equivalent, so that Eq. (4.31) becomes

$$\begin{aligned}\frac{1}{\tau_P} = \frac{k_F^2}{(2\pi)^2}\int_0^{\infty}\mathrm{d}K\,K\int_{K(K-2P)}^{K(K+2P)}\mathrm{d}\Omega\frac{2\left(N^0_\Omega+1\right)}{\sqrt{\Omega-K(K-2P)}\sqrt{K(K+2P)-\Omega}}\frac{f^0_{\sqrt{P^2+\Omega}}}{f^0_P} \\ \times\left[1-\frac{P}{\sqrt{P^2+\Omega}}\left(1+\frac{\Omega-K^2}{2P^2}\right)\right]W^0_{K,\Omega}C_{K,\Omega}\end{aligned} \tag{C.63}$$

C.4.3 Integration of the singularities

As the reader might have noticed, the integrand of the Ω integral in Eq. (C.61) has inverse square root singularities at both the upper and the lower integration limits. However, integrals of the type

$$I = \int_{\Omega_{min}}^{\Omega_{max}} \mathrm{d}\Omega \, \frac{g(\Omega)}{\sqrt{\Omega - \Omega_{min}}\sqrt{\Omega_{max} - \Omega}} \tag{C.64}$$

are integrable unless the function $g(\Omega)$ introduces difficulties. (See, e.g.,[123].) To see this, we start by splitting I at some Ω_{mid} with $\Omega_{min} < \Omega_{mid} < \Omega_{max}$. For the lower part of the integral, we make the substitution $t = \sqrt{\Omega - \Omega_{min}}$

$$I_1 = \int_{\Omega_{min}}^{\Omega_{mid}} \mathrm{d}\Omega \, \frac{g(\Omega)}{\sqrt{\Omega - \Omega_{min}}\sqrt{\Omega_{max} - \Omega}} = \int_0^{\sqrt{\Omega_{mid} - \Omega_{min}}} \mathrm{d}t \, \frac{2\, g\left(\Omega_{min} + t^2\right)}{\sqrt{\Omega_{max} - \Omega_{min} - t^2}}. \tag{C.65}$$

Our choice of Ω_{mid} guarantees that the remaining inverse square root in Eq. (C.65) does not become singular.

Similarly, we make the substitution $t = \sqrt{\Omega_{max} - \Omega}$ for the upper part of the integral:

$$I_2 = \int_{\Omega_{mid}}^{\Omega_{max}} \mathrm{d}\Omega \, \frac{g(\Omega)}{\sqrt{\Omega - \Omega_{min}}\sqrt{\Omega_{max} - \Omega}} = \int_0^{\sqrt{\Omega_{max} - \Omega_{mid}}} \mathrm{d}t \, \frac{2\, g\left(\Omega_{max} - t^2\right)}{\sqrt{\Omega_{max} - \Omega_{min} - t^2}}. \tag{C.66}$$

The integral I is the sum of I_1 and I_2. [1]

C.4.3.1 Example: Integrals for carrier–LO-phonon-scattering

In the case of LO-phonon scattering, $W_{K,\Omega}$ in Eq. (C.61) is a delta function at the constant dimensionless LO-phonon frequency Ω_0, and hence $g^{\pm}(\Omega) = g^{\pm}\delta(\Omega - \Omega_0)$. $\Omega_0 > 0$ and g^+ stand for absorption, and $\Omega_0 < 0$ and g^- for emission. Using the delta function, we can carry out the Ω integral in Eq. (C.61) directly, yielding

$$R_P^{1,\pm} = \int_{K_{min}}^{K_{max}} \mathrm{d}K \, K \frac{g^{\pm}}{\sqrt{\Omega_0 - K(K-2P)}\sqrt{K(K+2P) - \Omega_0}} \tag{C.67}$$

for the first term in Eq. (C.61), compare Eq. (C.46). The integration domain is defined by the $K_{min/max}$ from Eq. (C.49). This integral also has inverse square root singularities at both the upper and the lower integration limit. Some elementary

[1] In principle, it would be possible to choose Ω_{mid} halfway between Ω_{min} and Ω_{max}, and combine I_1 and I_2 conveniently. However, as the integrand is also singular at $\Omega = 0$ because N_Ω^0 is, and $\Omega_{min} < 0$ for $K < 2P$, this is not very helpful in general.

algebra helps to make this more evident, yielding

$$R_P^{1,\pm} = \int_{K_{min}}^{K_{max}} \mathrm{d}K\, K \frac{g^{\pm}}{\sqrt{(K-K_{min})(K_{max}-K)}} \frac{1}{\sqrt{(K+K_{min})(K_{max}+K)}} \tag{C.68}$$

This is again an integral of the type Eq. (C.64) and can be solved in the same way as the former. Fig. C.6 shows how an integral of this type takes many more evaluations when done crude force rather than using a substitution of the type discussed here.

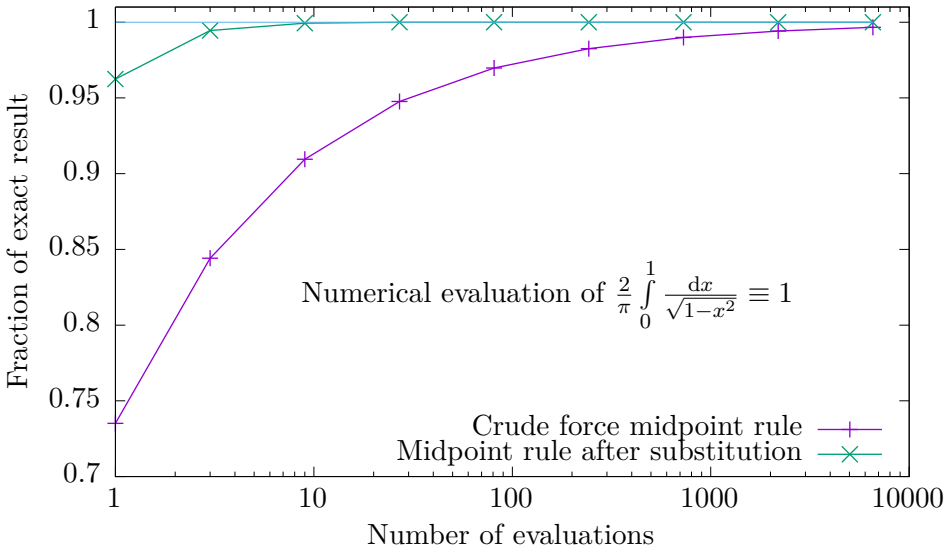

Figure C.6: Numerical evaluation of $\int_0^\infty \mathrm{d}x \frac{1}{1-x^2}$ with square root singularities at $x = \pm 1$ divided by the exact result, depending on the number of function evaluations. This corresponds to LO-phonon scattering as discussed in subsubsection C.4.3.1 with $P = \sqrt{\Omega_0}$, which makes Eq. (C.68) $R^{1\pm} = g^{\pm} \int_0^1 \frac{\mathrm{d}x}{\sqrt{1-x^2}}$. Numerical evaluation after substitution requires a lot fewer steps to achieve the same accuracy.

C.4.4 Integrals for phonon drag term

The phonon drag Eq. (4.23) defined in chapter 4 reads

$$T_{\boldsymbol{k},\omega} = \frac{2\pi\nu_k}{\mathfrak{Im}(\varepsilon^{tot}_{\boldsymbol{k},\omega})} \frac{M_v}{(2\pi)^2} \int \mathrm{d}\boldsymbol{p}^2\, \delta\left(E_{\boldsymbol{k}+\boldsymbol{p}} - E_{\boldsymbol{p}} - \hbar\omega\right) \left(f^0_{E_{\boldsymbol{p}}} - f^0_{E_{\boldsymbol{k}+\boldsymbol{p}}}\right) \times \frac{\tau_{\boldsymbol{p}+\boldsymbol{k}}(\boldsymbol{p}+\boldsymbol{k})\cdot\boldsymbol{E} - \tau_{\boldsymbol{p}}\boldsymbol{p}\cdot\boldsymbol{E}}{\boldsymbol{k}\cdot\boldsymbol{E}} \tag{C.69}$$

Here, $\nu_K = \frac{2\pi e^2}{k_F K}$ is the Fourier transform of the Coulomb integral in two-dimensional space, which we can use because we assume all carriers are located in the $z = 0$ plane. The factor M_v is a scalar accounting for the possibility of multiple degenerate valleys. With several degenerate valleys, there are n_S/M_v carriers in each valley, and the

carrier susceptibility is M_v times the contribution from a single valley. With the dimensionless variables from subsection C.4.2, this reads

$$T_{\boldsymbol{K},\Omega} = \frac{2\pi\nu_K k_F^2}{\mathfrak{Im}(\varepsilon^{tot}_{\boldsymbol{K},\Omega})E_F}\frac{M_v}{(2\pi)^2}\int \mathrm{d}\boldsymbol{P}^2\,\delta\left(|\boldsymbol{K}+\boldsymbol{P}|^2-|\boldsymbol{P}|^2-\Omega\right)\left(f^0_{|\boldsymbol{P}|}-f^0_{|\boldsymbol{K}+\boldsymbol{P}|}\right) \times \frac{\tau_{|\boldsymbol{P}+\boldsymbol{K}|}(\boldsymbol{P}+\boldsymbol{K})\cdot\boldsymbol{E}-\tau_{|\boldsymbol{P}|}\boldsymbol{P}\cdot\boldsymbol{E}}{\boldsymbol{K}\cdot\boldsymbol{E}} \tag{C.70}$$

We orient the coordinate system with $\boldsymbol{K}\parallel\boldsymbol{e}_x$, see Fig. C.5b. This means that

$$\frac{\boldsymbol{P}\cdot\boldsymbol{E}}{\boldsymbol{K}\cdot\boldsymbol{E}} = \frac{P}{K}\left(\cos\varphi+\sin\varphi\tan\varphi_E\right)$$

with φ and φ_E defined in Fig. C.5b. Consequently,

$$T_{\boldsymbol{K},\Omega} = \frac{2\pi\nu_K k_F^2}{\mathfrak{Im}(\varepsilon^{tot}_{\boldsymbol{K},\Omega})E_F}\frac{M_v}{(2\pi)^2}\int_0^\infty \mathrm{d}P\,P\int_{-\pi}^{\pi}\mathrm{d}\varphi\,\delta\left(K^2+2KP\cos\varphi+\Omega\right)\left(f^0_P-f^0_{\sqrt{P^2+\Omega}}\right) \times\left\{\tau_{\sqrt{P^2+\Omega}}\left[1+\frac{P}{K}\left(\cos\varphi+\sin\varphi\tan\varphi_E\right)\right]-\tau_P\left[\frac{P}{K}\left(\cos\varphi+\sin\varphi\tan\varphi_E\right)\right]\right\} \tag{C.71}$$

As the terms with $\sin\varphi$ cancel due to antisymmetry, we can write

$$T_{\boldsymbol{K},\Omega} = \frac{2\pi\nu_K k_F^2}{\mathfrak{Im}(\varepsilon^{tot}_{\boldsymbol{K},\Omega})E_F}\frac{2M_v}{(2\pi)^2}\int_0^\infty \mathrm{d}P\,P\int_0^{\pi}\mathrm{d}\varphi\,\frac{\delta\left(\varphi-\arccos\frac{\Omega-K^2}{2KP}\right)}{|2KP\sin\varphi|}\left(f^0_P-f^0_{\sqrt{P^2+\Omega}}\right) \times\left[\tau_{\sqrt{P^2+\Omega}}\left(1+\frac{P}{K}\cos\varphi\right)-\tau_P\frac{P}{K}\cos\varphi\right] \tag{C.72}$$

or

$$T_{\boldsymbol{K},\Omega} = \frac{2\pi M_v\nu_K k_F^2}{\mathfrak{Im}(\varepsilon^{tot}_{\boldsymbol{K},\Omega})E_F}\frac{1}{(2\pi)^2K}\int_{|\frac{\Omega-K^2}{2K}|}^\infty \mathrm{d}P\,P\frac{f^0_P-f^0_{\sqrt{P^2+\Omega}}}{\sqrt{P^2-(\frac{\Omega-K^2}{2K})^2}} \times\frac{1}{2}\left[\tau_{\sqrt{P^2+\Omega}}\left(1+\frac{\Omega}{K^2}\right)+\tau_P\left(1-\frac{\Omega}{K^2}\right)\right] \tag{C.73}$$

We define

$$I^1_{K,\Omega} = \int\limits_{|\frac{\Omega-K^2}{2K}|}^{\infty} \mathrm{d}P\, P \frac{f^0_P \tau_{\sqrt{P^2+\Omega}}}{\sqrt{P^2 - \left(\frac{\Omega-K^2}{2K}\right)^2}} \tag{C.74a}$$

$$I^2_{K,\Omega} = \int\limits_{|\frac{\Omega-K^2}{2K}|}^{\infty} \mathrm{d}P\, P \frac{f^0_P \tau_P}{\sqrt{P^2 - \left(\frac{\Omega-K^2}{2K}\right)^2}} \tag{C.74b}$$

$$I^3_{K,\Omega} = \int\limits_{|\frac{\Omega-K^2}{2K}|}^{\infty} \mathrm{d}P\, P \frac{f^0_{\sqrt{P^2+\Omega}} \tau_{\sqrt{P^2+\Omega}}}{\sqrt{P^2 - \left(\frac{\Omega-K^2}{2K}\right)^2}} \tag{C.74c}$$

$$I^4_{K,\Omega} = \int\limits_{|\frac{\Omega-K^2}{2K}|}^{\infty} \mathrm{d}P\, P \frac{f^0_{\sqrt{P^2+\Omega}} \tau_P}{\sqrt{P^2 - \left(\frac{\Omega-K^2}{2K}\right)^2}}, \tag{C.74d}$$

With the substitution $P \to P' = \sqrt{P^2 - \Omega}$, one can see that $I^3_{K,\Omega} = I^2_{K,-\Omega}$ and $I^4_{K,\Omega} = I^1_{K,-\Omega}$. Using $\nu_K = \frac{2\pi e^2}{k} = \frac{2\pi e^2}{K k_F}$ yields

$$T_{\boldsymbol{K},\Omega} = \frac{1}{\mathfrak{Im}(\varepsilon^{tot}_{\boldsymbol{K},\Omega})} \frac{e^2 M_v k_F}{E_F K^2} \frac{1}{2} \left[\left(I^1_{K,\Omega} - I^2_{K,-\Omega}\right) \left(1 + \frac{\Omega}{K^2}\right) \left(I^2_{K,\Omega} - I^1_{K,-\Omega}\right) \left(1 - \frac{\Omega}{K^2}\right) \right] \tag{C.75}$$

With $\frac{e^2 k_F}{E_F} = \frac{2}{k_F a_0}$ and after rearranging $T_{K,\Omega}$ to stress its symmetry, we get

$$\begin{aligned} T_{\boldsymbol{K},\Omega} &= \frac{M_v}{k_F a_0 K^2 \mathfrak{Im}(\varepsilon^{tot}_{\boldsymbol{K},\Omega})} \\ &\times \left\{ I^1_{K,\Omega} - I^1_{K,-\Omega} + I^2_{K,\Omega} - I^2_{K,-\Omega} + \frac{\Omega}{K^2} \left[I^1_{K,\Omega} + I^1_{K,-\Omega} - \left(I^2_{K,\Omega} + I^2_{K,-\Omega}\right) \right] \right\} \end{aligned} \tag{C.76}$$

The $I^i_{K,\Omega}$ are all integrals of the type of Eq. (C.65), that means the singularity at $P = P_{min} = |\frac{\Omega-K^2}{2K}|$ is integrable. Explicitly,

$$I^1_{K,\Omega} = 2 \int\limits_0^{\infty} \mathrm{d}t\, \frac{P_{min} + t^2}{\sqrt{2P_{min} + t^2}} \tau_{\sqrt{(P_{min}+t^2)^2+\Omega}} f^0_{P_{min}+t^2} \tag{C.77}$$

$$I^2_{K,\Omega} = 2 \int\limits_0^{\infty} \mathrm{d}t\, \frac{P_{min} + t^2}{\sqrt{2P_{min} + t^2}} \tau_{P_{min}+t^2} f^0_{P_{min}+t^2} \tag{C.78}$$

When implementing the numerical evaluation of these integrals, the value of $T_{K,\Omega}$ for constant τ,

$$T_{K,\Omega}|_{\tau=\mathrm{const}} = \frac{\mathfrak{Im}\left(\varepsilon^{e}_{\boldsymbol{K},\Omega}\right)}{\mathfrak{Im}\left(\varepsilon^{tot}_{\boldsymbol{K},\Omega}\right)} \tau \tag{C.79}$$

can be helpful as a test.

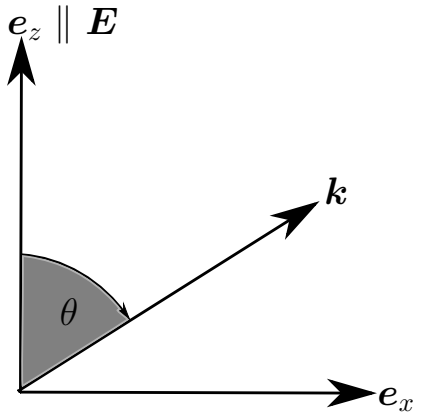

Figure C.7: Visualization of important angles for the three-dimensional drift velocity and mobility. We have chosen to depict the x-z plane. In the three-dimensional case, there is azimuthal symmetry, so that this picture could be rotated around the z-axis arbitrarily. In the two-dimensional case, there are only two axes present, the x- and the z-axis.

C.5 Calculation of carrier mobility

The calculation of the carrier mobility is textbook material. However, often only the expressions for the mobility in the Maxwell-Boltzmann limit are given, cf. [26]. We recommend, e.g., the brief description of the mobility in [98].

In weak field transport, where the perturbation in the distribution function is proportional to the applied field, the drift velocity also proportional to the applied field. The proportionality constant between the drift velocity and the applied field is called mobility.

Drift velocity in isotropic parabolic bands

We are only interested in longitudinal transport, i.e., along the field direction. The drift velocity arises from an average of the group velocity over the distribution function. For isotropic parabolic bands, $\boldsymbol{v}(\boldsymbol{k}) = \frac{\hbar}{m}\boldsymbol{k}$. The component of the average drift velocity in field direction $\boldsymbol{E}$, is

$$\langle \boldsymbol{v}_{\boldsymbol{E}} \rangle_{\boldsymbol{k}} = \langle \boldsymbol{v} \cdot \boldsymbol{e}_E \rangle_{\boldsymbol{k}} = \frac{\sum\limits_{\boldsymbol{k}} f_{\boldsymbol{k}} \frac{\hbar}{m} \boldsymbol{k} \cdot \boldsymbol{e}_{\boldsymbol{E}}}{\sum\limits_{\boldsymbol{k}} f_{\boldsymbol{k}}} \tag{C.80}$$

This way of defining averages is useful, because they are insensitive to scaling factors in the distribution function.

Table C.1: The four lowest order Legendre polynomials, see [4]

n	$P_n(x)$
0	1
1	x
2	$\frac{1}{2}(3x^2-1)$
3	$\frac{1}{2}(5x^3-3x)$

We transform the sum into an integral using the notation first introduced in Eq. (2.40), which holds for 2d- and 3d-integrals equally. Moreover, we write the integral in terms of scaled, dimensionless wave vectors. With the vector $\boldsymbol{K} = \frac{\boldsymbol{k}}{k_F}$, a dimensionless wave vector scaled by the Fermi wave vector, the drift velocity now reads

$$\langle \boldsymbol{v}_{\boldsymbol{E}} \rangle_{\boldsymbol{k}} = \frac{\hbar}{m} \frac{\int \mathrm{d}\boldsymbol{k}\, f_{\boldsymbol{k}} \boldsymbol{k} \cdot \boldsymbol{e}_{\boldsymbol{E}}}{\int \mathrm{d}\boldsymbol{k}\, f_{\boldsymbol{k}}} = v_F \frac{\int \mathrm{d}\boldsymbol{K}\, f_{\boldsymbol{K}} \boldsymbol{K} \cdot \boldsymbol{e}_{\boldsymbol{E}}}{\int \mathrm{d}\boldsymbol{K}\, f_{\boldsymbol{K}}}. \tag{C.81}$$

The evaluation of this integral will be different but similar in three or two dimensions.

C.5.1 Carrier mobility in semiconductors with spherical parabolic bands in three dimensions

Let us use a spherical coordinate system with the z-axis aligned with the field direction $\boldsymbol{e}_{\boldsymbol{E}} = \boldsymbol{e}_z$, so that the angle between $\boldsymbol{k}$ and $\boldsymbol{E}$ is the polar angle θ, see Fig. C.7. If our system is isotropic the distribution function is independent of the azimuth angle φ.

$$\langle \boldsymbol{v}_{\boldsymbol{E}} \rangle_{\boldsymbol{k}} = v_F \frac{\int_0^\infty \mathrm{d}K \int_0^\pi \mathrm{d}\theta\, K^3 \sin\theta f_{\boldsymbol{K}} \cos\theta}{\int_0^\infty \mathrm{d}K \int_0^\pi \mathrm{d}\theta\, K^2 \sin\theta f_{\boldsymbol{K}}} \tag{C.82}$$

We can expand the distribution function into Legendre polynomials[4]:

$$f_{\boldsymbol{K}} = \sum_{n=0}^{\infty} f_K^n P_n(\cos\theta) \tag{C.83}$$

The zeroth and first order coefficients of this expansion are the distribution functions f_K^0 and f_K^1, cf. chapter 4. Legendre polynomials obey the orthogonality relation[4]

$$\int_{-1}^{1} \mathrm{d}x\, P_i(x) P_j(x) = \frac{2}{2j+1}\delta_{ij} \text{ or } \int_0^\pi \mathrm{d}\theta\, \sin\theta P_i(\cos\theta)\, P_j(\cos\theta) = \frac{2}{2j+1}\delta_{ij} \tag{C.84}$$

The lowest order Legendre polynomials are listed in table C.1. Taking advantage of $P_1(\cos\theta) = \cos\theta$ and $P_0(\cos\theta) = 1$, we can apply the orthogonality relation to the

drift velocity

$$\langle \boldsymbol{v}_{\boldsymbol{E}} \rangle_{\boldsymbol{k}} = v_F \frac{\sum_{n=0}^{\infty} \int_0^{\infty} \mathrm{d}K \int_0^{\pi} \mathrm{d}\theta \, K^3 \sin\theta f_K^n P_n(\cos\theta) P_1(\cos\theta)}{\sum_{n=0}^{\infty} \int_0^{\infty} \mathrm{d}K \int_0^{\pi} \mathrm{d}\theta \, K^2 \sin\theta f_K^n P_n(\cos\theta) P_0(\cos\theta)} = \frac{v_F}{3} \frac{\int_0^{\infty} \mathrm{d}K \, K^3 f_K^1}{\int_0^{\infty} \mathrm{d}K \, K^2 f_K^0} \tag{C.85}$$

This shows that the drift velocity only depends on the first two coefficients of the distribution function when expanded into Legendre polynomials. Explicitly, this means that, as long as the proportionality between the applied field and the distribution function holds, the drift velocity only depends on the linear contributions to the distribution function, and no higher terms are necessary.

Mobility The longitudinal mobility is the proportionality constant between the drift velocity in field direction and an applied electric field $|\boldsymbol{E}|$.

$$\langle \boldsymbol{v}_{\boldsymbol{E}} \rangle_{\boldsymbol{k}} = \mu |\boldsymbol{E}| \tag{C.86}$$

The first term of the expansion into the Legendre polynomials from our calculations above is

$$f_K^1 \cos\theta = f_K^0 \left(1 - f_K^0\right) g_{\boldsymbol{k}} \beta = v_F e \beta f_K^0 \left(1 - f_K^0\right) \tau_K K |\boldsymbol{E}| \cos\theta, \tag{C.87}$$

see Eq. (4.1).

This gives the expression

$$\mu = \frac{e\beta v_F^2}{3} \frac{\int_0^{\infty} \mathrm{d}K \, K^4 f_K^0 \left(1 - f_K^0\right) \tau_K}{\int_0^{\infty} \mathrm{d}K \, K^2 f_K^0} \tag{C.88}$$

for mobility, or, equivalently,

$$\mu = -\frac{e}{3m*} \frac{\int_0^{\infty} \mathrm{d}K \, K^3 \left(\frac{\partial}{\partial K} f_K^0\right) \tau_K}{\int_0^{\infty} \mathrm{d}K \, K^2 f_K^0} \tag{C.89}$$

After a partial integration of the integral in the denominator, we find

$$\mu = \frac{e}{m*} \frac{\int_0^{\infty} \mathrm{d}K \, K^3 \left(\frac{\partial}{\partial K} f_K^0\right) \tau_K}{\int_0^{\infty} \mathrm{d}K \, K^3 \left(\frac{\partial}{\partial K} f_K^0\right)} = \frac{e}{m*} \frac{\int_0^{\infty} \mathrm{d}K \, K^4 f_K^0 \left(1 - f_K^0\right) \tau_K}{\int_0^{\infty} \mathrm{d}K \, K^4 f_K^0 \left(1 - f_K^0\right)}. \tag{C.90}$$

This makes it clear that the mobility is proportional to an average over the

momentum relaxation time,

$$\mu = \frac{e}{m^*} \langle \tau \rangle \tag{C.91}$$

with

$$\langle \tau \rangle = \frac{\int_0^\infty \mathrm{d}K \, K^3 \left(\frac{\partial}{\partial K} f_K^0 \right) \tau_K}{\int_0^\infty \mathrm{d}K \, K^3 \left(\frac{\partial}{\partial K} f_K^0 \right)}. \tag{C.92}$$

Note that mobility is usually given in units of $\frac{cm^2}{Vs}$, which is neither cgs nor SI. As mentioned in the preliminary, all the equations in this thesis are in Gaussian cgs units. This means that Eq. (C.90) yields a mobility in $\frac{cm^2}{statV\ s}$, which then has to be converted as described in the preliminary.

Mobility from integration over energy While the formula above is useful when the effective momentum relaxation time τ_E is calculated as a function of momentum, transforming the integrals into integrals over energy allows the denominator integral to be evaluated semi-analytically. From Eq. (C.90), we find

$$\mu = \frac{e}{m*} \frac{\int_0^\infty \mathrm{d}E \, E^{\frac{3}{2}} \left(\frac{\partial}{\partial E} f_E^0 \right) \tau_E}{\int_0^\infty \mathrm{d}E \, E^{\frac{3}{2}} \left(\frac{\partial}{\partial E} f_E^0 \right)} = \frac{e}{m*} \frac{\int_0^\infty \mathrm{d}E \, E^{\frac{3}{2}} f_E^0 \left(1 - f_E^0\right) \tau_E}{\int_0^\infty \mathrm{d}E \, E^{\frac{3}{2}} f_E^0 \left(1 - f_E^0\right)} \tag{C.93}$$

The integral in the denominator is proportional to a Fermi-Dirac integral

$$\mathfrak{F}_{\frac{1}{2}}(\tilde{\mu}\beta) = \frac{1}{\Gamma(\frac{3}{2})} \frac{x^{\frac{1}{2}}}{\exp(x - \tilde{\mu}\beta) + 1} \quad \text{with} \quad \Gamma\left(\frac{3}{2}\right) = \frac{\sqrt{\pi}}{2} \tag{C.94}$$

and the chemical potential $\tilde{\mu}$, and can be found tabulated, along with the Gamma function, see [4].

This yields,

$$\mu = \frac{e}{m^*} \frac{4\beta^{\frac{3}{2}}}{3\sqrt{\pi}\mathfrak{F}_{\frac{1}{2}}(\tilde{\mu}\beta)} \int_0^\infty \mathrm{d}E \, E^{\frac{3}{2}} f_E^0 \left(1 - f_E^0\right) \tau_E \tag{C.95}$$

3-d mobility in the Boltzmann limit

In the classical limit, i.e., $\tilde{\mu}\beta \to -\infty$

$$f_E^0 = \frac{1}{1 + \exp(E\beta - \tilde{\mu}\beta)} \approx \exp(-E\beta + \tilde{\mu}\beta) \quad \text{and} \quad 1 - f_E^0 = \frac{\exp(E\beta - \tilde{\mu}\beta)}{1 + \exp(E\beta - \tilde{\mu}\beta)} \approx 1 \tag{C.96}$$

so that the mobility Eq. (C.93) can be expressed as

$$\begin{aligned}\mu &\approx \frac{e}{m^*}\frac{\int_0^\infty \mathrm{d}E\, E^{\frac{3}{2}}\tau_E f_E^0}{\int_0^\infty \mathrm{d}E\, E^{\frac{3}{2}} f_E^0} = \frac{e}{m^*}\frac{\int_0^\infty \mathrm{d}E\, E^{\frac{3}{2}}\tau_E e^{-E\beta}}{\int_0^\infty \mathrm{d}E\, E^{\frac{3}{2}} e^{-E\beta}} \\ &= \frac{e}{m^*}\frac{1}{\Gamma\left(\frac{5}{2}\right)}\int_0^\infty \mathrm{d}x\, x^{\frac{3}{2}}\tau_{x/\beta}e^{-x} = \frac{e}{m^*}\frac{4}{3\sqrt{\pi}}\int_0^\infty \mathrm{d}x\, x^{\frac{3}{2}}\tau_{x/\beta}e^{-x}\end{aligned} \tag{C.97}$$

Thus, the mobility in the Boltzmann limit is proportional to an average over the effective momentum relaxation time weighted with the Boltzmann distribution times the energy to the $\frac{3}{2}$, cf., e.g. [26, page 129].

C.5.2 Carrier mobility in semiconductors with spherical parabolic bands in two dimensions

Expanding Eq. (C.81) in polar coordinates with the z direction aligned with the electric field yields

$$\langle \boldsymbol{v_E}\rangle_{\boldsymbol{k}} = v_F \frac{\int_0^\infty \mathrm{d}K \int_0^{2\pi} \mathrm{d}\theta\, K^2 f_{\boldsymbol{K}} \cos\theta}{\int_0^\infty \mathrm{d}K \int_0^{2\pi} \mathrm{d}\theta\, K f_{\boldsymbol{K}}} \tag{C.98}$$

θ is the angle between the wave vector $\boldsymbol{k}$ and the field, see Fig. C.7. As we assume $f_{-\boldsymbol{K}} = f_{\boldsymbol{K}}$ and $f_{K,\theta+2\pi} = f_{K,\theta}$, we can express $f_{\boldsymbol{K}}$ through a Fourier-Cosine expansion

$$f_{\boldsymbol{K}} = \sum_{n=0}^{\infty} f_K^n \cos(n\theta). \tag{C.99}$$

The zeroth and first order coefficients of this expansion are the distribution functions f_K^0 and f_K^1, cf. chapter 4. The drift velocity thus becomes

$$\langle \boldsymbol{v_E}\rangle_{\boldsymbol{k}} = v_F \frac{\int_0^\infty \mathrm{d}K \sum_{n=0}^{\infty} f_K^n K^2 \int_0^{2\pi} \mathrm{d}\theta\, \cos(n\theta)\cos\theta}{\int_0^\infty \mathrm{d}K \sum_{n=0}^{\infty} f_K^n K \int_0^{2\pi} \mathrm{d}\theta\, \cos(n\theta)} \tag{C.100}$$

Evaluating the θ integral in the denominator yields

$$\int_0^{2\pi} \mathrm{d}\theta\, \cos(n\theta) = \frac{1}{n}\sin(2\pi n) = 2\pi\delta_{n,0}. \tag{C.101}$$

Using $\cos(n\theta)\cos(\theta) = \frac{1}{2}\left\{\cos\left[(n-1)\theta\right] + \cos\left[(n+1)\theta\right]\right\}$ and the denominator integral

yields the numerator integral as

$$\int_0^{2\pi} \mathrm{d}\theta\, \cos(n\theta)\cos\theta = \frac{1}{2}\left\{\int_0^{2\pi} \mathrm{d}\theta\, \cos\left[(n-1)\theta\right] + \int_0^{2\pi} \mathrm{d}\theta\, \cos\left[(n+1)\theta\right]\right\} \tag{C.102}$$

$$= \pi\left(\delta_{n,1} + \delta_{n,-1}\right). \tag{C.103}$$

Consequently,

$$\langle \boldsymbol{v}_{\boldsymbol{E}} \rangle_{\boldsymbol{k}} = v_F \frac{\int_0^\infty \mathrm{d}K\, K^2 f_K^1}{2\int_0^\infty \mathrm{d}K\, K f_K^0} \tag{C.104}$$

With Eq. (C.86) and Eq. (C.87), which also holds in the 2-d case, we can express the mobility as

$$\mu = -\frac{e}{2m*} \frac{\int_0^\infty \mathrm{d}K\, K^2 \left(\frac{\partial}{\partial K} f_K^0\right) \tau_K}{\int_0^\infty \mathrm{d}K\, K f_K^0} \tag{C.105}$$

which which partial integration can be written as

$$\mu = \frac{e}{m*} \frac{\int_0^\infty \mathrm{d}K\, K^2 \left(\frac{\partial}{\partial K} f_K^0\right) \tau_K}{\int_0^\infty \mathrm{d}K\, K^2 \left(\frac{\partial}{\partial K} f_K^0\right)} = \frac{e}{m*} \frac{\int_0^\infty \mathrm{d}K\, K^3 f_K^0 \left(1 - f_K^0\right) \tau_K}{\int_0^\infty \mathrm{d}K\, K^3 f_K^0 (1 - f_K^0)} \tag{C.106}$$

Note that the only formal difference to Eq. (C.90) is the exponent of K.

Mobility from integration over energy When the momentum relaxation time τ_E is given as a function of energy, we can express the mobility as

$$\mu = \frac{e}{m*} \frac{\int_0^\infty \mathrm{d}E\, E \left(\frac{\partial}{\partial E} f_E^0\right) \tau_E}{\int_0^\infty \mathrm{d}E\, E \left(\frac{\partial}{\partial E} f_E^0\right)} = \frac{e}{m*} \frac{\int_0^\infty \mathrm{d}E\, E f_E^0 \left(1 - f_E^0\right) \tau_E}{\int_0^\infty \mathrm{d}E\, E f_E^0 \left(1 - f_E^0\right)} \tag{C.107}$$

As the denominator integral

$$\int_0^\infty \mathrm{d}E\, E \left(\frac{\partial}{\partial E} f_E^0\right) = -\int_0^\infty \mathrm{d}E\, f_E^0 = k_B T \ln\left(1 + e^{\tilde{\mu}\beta}\right), \tag{C.108}$$

we can write the mobility as

$$\mu = \frac{e}{m^*} \frac{\beta^2}{\ln\left(1 + e^{\tilde{\mu}\beta}\right)} \int_0^\infty \mathrm{d}E\, E f_E^0 \left(1 - f_E^0\right) \tau_E \tag{C.109}$$

2-d mobility in the Boltzmann limit In the classical limit Eq. (C.96), the mobility can be written as

$$\mu = \frac{e}{m*} \frac{\int_0^\infty \mathrm{d}E\, E e^{-E\beta} \tau_E}{\int_0^\infty \mathrm{d}E\, E e^{-E\beta}} = \frac{e}{m*} \int_0^\infty \mathrm{d}x\, x e^{-x} \tau_{x/\beta} \tag{C.110}$$

C.5.3 Carrier mobility in semiconductors with multiple equivalent valleys

If the conduction bands of n-type semiconductors (or valence bands of p-type semiconductors) have M_v equivalent minima (maxima), low-field transport in that semiconductors takes place in M_v so-called valleys in reciprocal space. This scenario occurs for the n-type transport in MoS_2, which has two equivalent valleys at the K-points, cf. Fig. 1.4.

We take this into account for the mobility calculation by considering the fraction $\frac{1}{M_v}$ of the carriers concentration $n_i = \frac{n}{M_v}$ in each of the valleys. The total drift velocity will be

$$\langle \boldsymbol{v}_{\boldsymbol{E}} \rangle_{\boldsymbol{k}} = \frac{\hbar}{m} \frac{\sum_i \sum_{\boldsymbol{k}_i} f_{\boldsymbol{k}_i} \boldsymbol{k}_i \cdot \boldsymbol{e}_{\boldsymbol{E}}}{\sum_i \sum_{\boldsymbol{k}_i} f_{\boldsymbol{k}_i}} = \frac{\hbar}{m} \frac{\sum_{\boldsymbol{k}_i} f_{\boldsymbol{k}_i} \boldsymbol{k}_i \cdot \boldsymbol{e}_{\boldsymbol{E}}}{\sum_{\boldsymbol{k}_i} f_{\boldsymbol{k}_i}}. \tag{C.111}$$

This expression is formally identical to Eq. (C.80), we only sum over one of several equivalent valleys rather than multiple ones [107]. In the classical limit, where the mobility does not depend on the chemical potential, the distribution of the carriers into multiple valleys has no effect on the mobility. This of course assumes that the effect of the multiple valleys on the momentum relaxation time is already taken into account.

C.5.4 Approximate account of the effect of the occupation of satellite valleys on the carrier mobility

This section discusses the occupation of satellite valleys in semiconductors with parabolic bands. The phrase comes from situations like in bulk GaAs, where the lowest lying conduction band is at the Γ point, and the next higher conduction band minima are in the 8 equivalent L points on the edges of the Brilloin zone. In a 3d plot of the occupied states in reciprocal space, the electrons in the L point ellipsoids resemble stellites in an orbit around the electrons at Γ, cf., e.g., [24].

In chapter 2, we calculated the occupation of a parabolic conduction band with a minimum at $E = 0$, compare Eq. (2.24) and Eq. (2.26). These formulas still holds for the situation with multiple valleys present, but we have to include the energy at the

bottom of each band for reference, and we must account for the fact that the satellite valleys are not necessarily spherical.

The occupation of the bands i at the energy E_i consequently is

$$n_i \propto M_i \left(m_i^{DOS}\right)^{\frac{d}{2}} \mathfrak{F}_{\frac{d}{2}-1}\left(\tilde{\mu}\beta - E_i\beta\right) \tag{C.112}$$

Here, $d \in \{2, 3\}$ is the dimension of the semiconductor, and $\mathfrak{F}_n$ is the Fermi-Dirac integal. M_i is the valley degeneracy of the satellite valleys. For example, in GaAs, there are conduction band valleys in 8 equivalent [111] directions, at the edge of the Brillouin zone. This yield $M_L = 8 \cdot \frac{1}{2} = 4$ L valley minima per Brillouin zone. So, in our notation, n_L is the carrier concentration in all 4, not only a single L valley, and equivalently for other valleys.

m_i^{DOS} is the density of states effective mass of the conduction band minima. This accounts for the fact that the equi-energy surfaces for parabolic bands can be ellipsoids [107]. In our examples, the GaAs L bands, the equi-energy surfaces are rotationally symmetric ellipsoids along the [111] directions, and hence

$$m_L^{DOS} = \left(m_l m_t^2\right)^{\frac{1}{3}} \tag{C.113}$$

where m_l and m_t are the effective masses along and perpendicular to the rotational axis.

We can express the relative occupation in the conduction bands of type i as

$$\frac{n_i}{n_{tot}} = \frac{M_i \left(m_i^{DOS}\right)^{\frac{d}{2}} \mathfrak{F}_{\frac{d}{2}-1}\left(\tilde{\mu}\beta - E_i\beta\right)}{\sum_i M_i (m_i^{DOS})^{\frac{d}{2}} \mathfrak{F}_{\frac{d}{2}-1}(\tilde{\mu}\beta - E_i\beta)} \tag{C.114}$$

In the $d = 2$ case, the Fermi-Dirac integral can be evaluated analytically, and we have

$$\frac{n_i}{n_{tot}}|_{d=2} = \frac{M_i m_i^{DOS} \ln\left(1 + e^{\tilde{\mu}\beta - E_i\beta}\right)}{\sum_i M_i m_i^{DOS} \ln\left(1 + e^{\tilde{\mu}\beta - E_i\beta}\right)}. \tag{C.115}$$

Calculating the fraction of the total occupation in the lowest conduction band lets us see at what point the approximation that only the lowest conduction band is occupied starts to fail. This is important, because unoccupied bands cannot contribute to transport, but occupied ones might.

Maxwell Boltzmann limit In the Maxwell Boltzmann limit, $\tilde{\mu}\beta \to -\infty$, the relative occupation is independent of the chemical potential, and in consequence,

independent of the absolute occupation:

$$\frac{n_i}{n_{tot}}|_{\tilde{\mu}\beta\to-\infty} = \frac{M_i \left(m_i^{DOS}\right)^{\frac{d}{2}} e^{-E_i\beta}}{\sum_i M_i \left(m_i^{DOS}\right)^{\frac{d}{2}} e^{-E_i\beta}} \tag{C.116}$$

This limit holds for low carrier concentrations or high temperatures.

Degenerate limit For high carrier concentrations, or low temperatures, the degenerate limit can be applied,

$$\frac{n_i}{n_{tot}}|_{\tilde{\mu}\beta\to\infty} = \frac{M_i \left(m_i^{DOS}\right)^{\frac{d}{2}} (E_F - E_i\beta)^{\frac{d}{2}}}{\sum_i M_i \left(m_i^{DOS}\right)^{\frac{d}{2}} (E_F - E_i\beta)^{\frac{d}{2}}} \tag{C.117}$$

where, the relative occupation of the bands is independent of temperature.

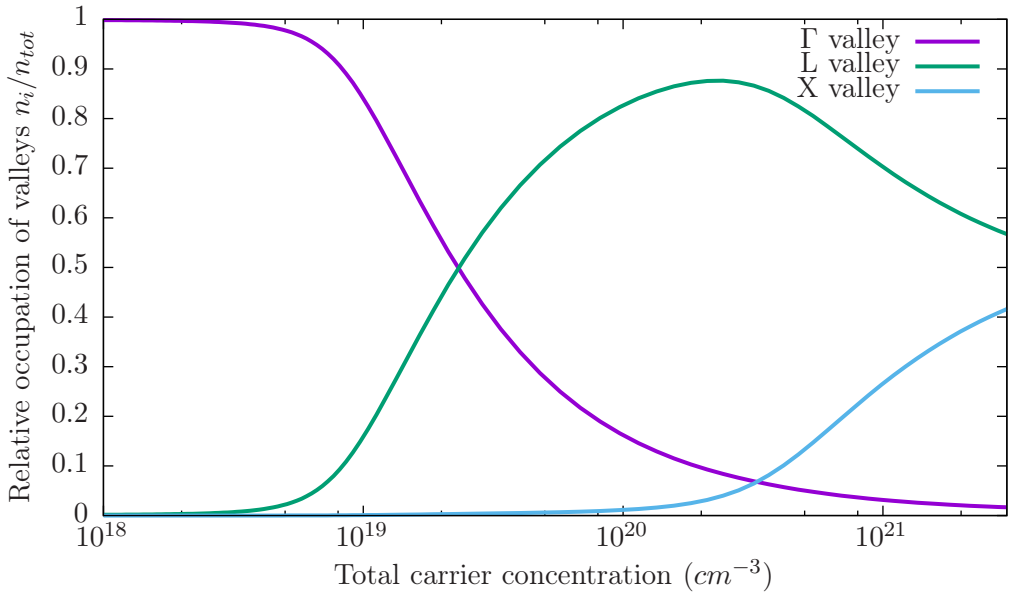

Figure C.8: Relative occupation of the lowest conduction bands in room temperature GaAs, as a function of the total carrier concentration. For the multiply degenerate L and X valleys, n_i is the carrier concentration in all equivalent L or X valleys.

Relative occupation of parabolic conduction bands in 3d GaAs For this calculation, we take the 4 equivalent L valleys and the 3 equivalent X valleys into account. We set the energy to zero at the bottom of the Γ valley. The parameters for this calculation are given in Tab. C.5.4. The relative occupation of these three different types of bands is plotted against the total carrier concentration in all three bands in bulk GaAs in Fig. C.8.

Table C.2: Effective masses, valley degeneracy number M and energies of the satellite conduction bands in bulk GaAs relative to the lowest conduction band at Γ. All constant energy surfaces are rotational ellipsoids and the corresponding effective masses are given in multiples of the electron mass m_e.

	E (meV)	M	m_t/m_e	m_l/m_e	m^{DOS}/m_e	m^{opt}/m_e
Γ	0	1	0.067	0.067	0.067	0.067
L	330	4	0.13	1.54	0.30	0.19
X	440	3	0.23	1.98	0.47	0.33

C.5.4.1 Effect of satellite valley occupation on the total mobility

When satellite valleys are occupied, they open up a new channel for transport. The total mobility becomes

$$\mu_{tot} = \sum_i \frac{n_i}{n_{tot}} \mu_i \tag{C.118}$$

with the μ_i calculated with in each satellite band according to section C.5. As discussed by Herring and Vogt [107], in materials with ellipsoidal equi-energy surfaces, a coordinate transformation can be made, so that the expressions for spherical bands can be used for the calculation of the momentum relaxation time, except for the fact that the density of states effective mass Eq. (C.113) has to be substituted for the scalar effective mass.

The mobility in each valley is, averaged over reciprocal space,

$$\mu_i = \frac{e}{m^{opt}{}_i} \langle \tau \rangle_i \tag{C.119}$$

where m^{opt} is the optical, or conductivity effective mass [107]. In a 3d material like GaAs, where the equi-energy surfaces of the satellite valleys are rotational ellipsoids, the optical effective mass is

$$m^{opt} = \frac{3}{\frac{2}{m_t} + \frac{1}{m_l}}, \tag{C.120}$$

see Tab. C.5.4.

Approximate treatment of the effect of the satellite valleys on the carrier mobility in GaAs If we make certain assumptions, we can estimate the effect on the satellite valleys on the total mobility without calculating the mobility in the satellite valleys explicitly. These approximations can be quite good if the occupation of the satellite valleys is not too high.

If we assume that the mobility in the Γ valley is much higher than in the L or X valleys, $\mu_\Gamma \gg \mu_L$, $\mu_\Gamma \gg \mu_X$, Eq. (C.118) simplifies to

$$\mu_{tot} \approx \frac{n_\Gamma}{n_{tot}} \mu_\Gamma. \tag{C.121}$$

Another possible approximation is that the averaged momentum relaxation time $\langle\tau\rangle$ is roughly the same in all the valleys: $\langle\tau\rangle_\Gamma \approx \langle\tau\rangle_L \approx \langle\tau\rangle_X \approx \langle\tau\rangle$. Consequently, the mobility becomes

$$\mu_{tot} \approx \frac{n_\Gamma}{n_{tot}}\mu_\Gamma \sum_i \frac{n_i}{n_\Gamma}\frac{m_\Gamma^{opt}}{m_i^{opt}}, \tag{C.122}$$

which, again, leads to Eq. (C.121), if the relative occupation of the satellite valleys is not too high. Fig. C.9 shows the effect of the satellite valleys on the mobility in room

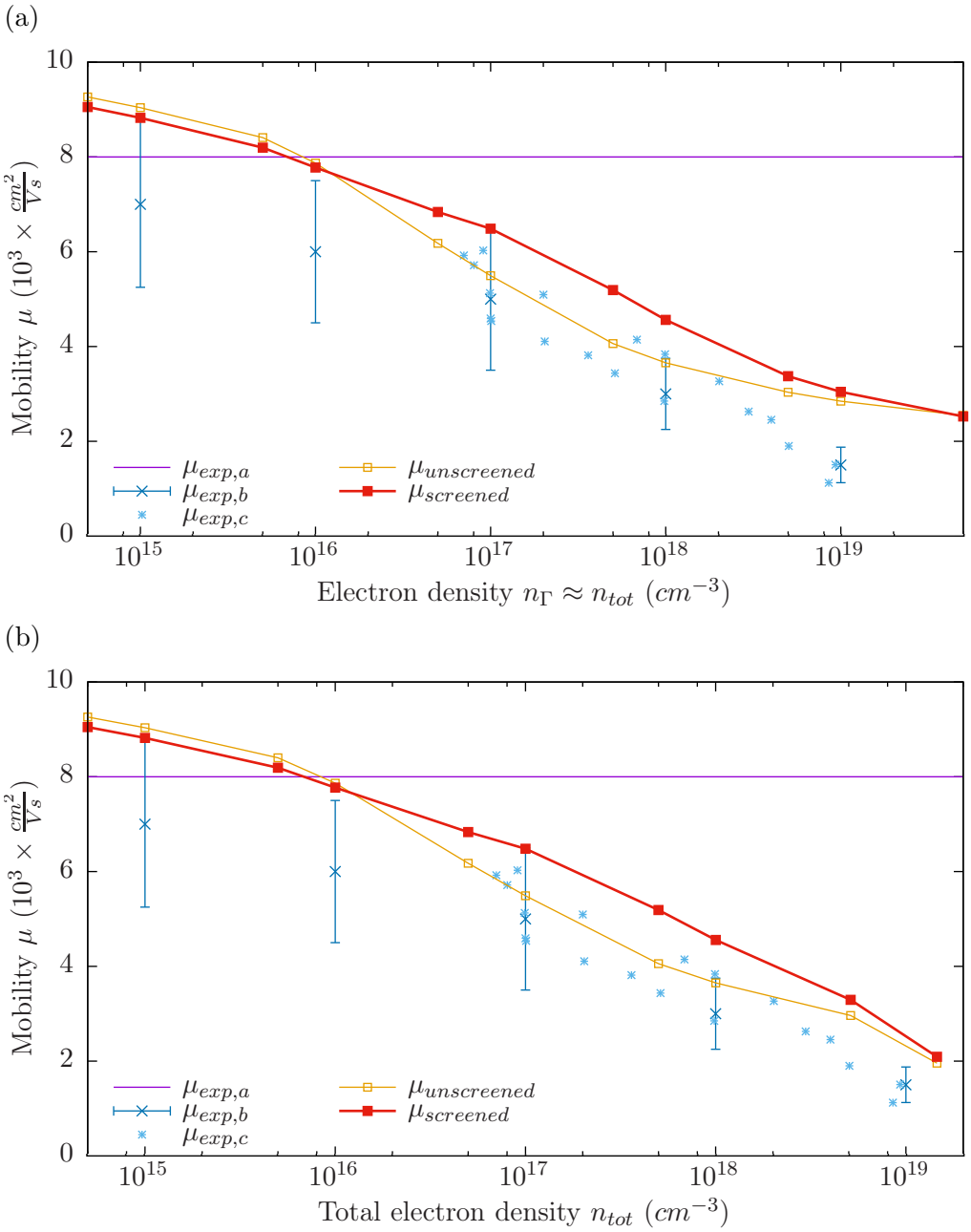

Figure C.9: Mobility in room temperature GaAs as a function of the total carrier concentration, see chapter 5. (a) Neglecting the effect of satellite valleys, i.e., assuming all carriers are in the Γ valley. (b) Treating the effect of the satellite valleys approximately with Eq. (C.121)

temperature GaAs. Up until $n = 10^{18} cm^{-3}$, the approximation that all carriers are in the Γ valley is excellent, see Fig. C.8. We only consider total carrier concentrations up to about $n_{tot} = 2 \times 10^{19} cm^{-3}$, where still more than 70% of the carriers are in the Γ band. Treating the occupation of the satellite bands approximately with Eq. (C.121), gives improved agreement with experiment over the case where the satellite bands are ignored.

C.6 Numerical implementation

This section gives some information on the numerical implementation of the expressions which need to be evaluated in order to calculate the momentum relaxation due to carrier –coupled collective mode scattering. Some of the choices concerning the numerical implementation were already made in appendix C.3 and appendix C.4, e.g., explicitly using the energy-conservation delta-function to eliminate the integral over the polar angle rather than the integral over the transferred wave vector.

The numerical calculations in this thesis, and also the data to create plots of dielectric functions and scattering rates were created with two codes, which were written for this purpose. One code treats bulk semiconductors (3d-code) and one the semiconductor heterostructures (2d-code). These codes have a largely identical structure, and share certain modules and data structure, though the expressions which had to be implemented differ somewhat.

These codes were written in C and have been run on Linux operating systems. Workhorse functions for root-finding and integrations, or for special functions were either taken from the Gnu Scientific Library [124] or modified from Numerical Recipes [123]. An implementation of the derivatives of certain Fermi-Dirac integrals written in FORTRAN was also used [125, 126, 127, 128].

The codes are most easily run with an input file, but can be run interactively. The code takes options for what type of bulk material (3d-code) or heterostructure (2d-code) is to be used, and what approximations are to be used (concerning the treatment of screening, neglecting either the LO-phonons or the plasmons, RTA or iteration to self-consistent solution, etc.). Other options set the temperature and the carrier concentration, and a maximal number of iterations to be used for the iteration to self-consistency, and the neglect or inclusion of other scattering mechanisms beside screened carrier–polar phonon scattering. The codes can be run in different modes, calculating some or all of the following quantities: the dielectric functions, zeros of the real part of the dielectric functions, sum rule integrals, energy relaxation times, momentum relaxation times with or without drag term (including carrier mobilities and the Seebeck coefficient).[2]

[2]Not all permutations of these options and parameters are implemented in the codes. The codes

The codes discussed here were not written with distribution in mind. At the time of the publication of this thesis, they are hosted in a private bitbucket.org repository. Should they be distributed in the form they were in at the time of publication of the thesis, they would have to be distributed under the GNU general public license (GPL) [124], due to their use of GSL library functions.

For the calculations in this thesis, the codes were run with parameter ranging from the classical limit to the degenerate limit, and choosing appropriate grid sizes, target accuracies for adaptive integrations and integrations was challenging. We generally carried out convergence tests for certain parameters and then erred on the side of over-convergence for subsequent calculations. For the 2-d code, the convergence criteria were relaxed carefully in order to allow faster calculations.

We will give details for the numerical parameters used to numerically determine the quantities discussed below for one 2-d example and one 3-d example. The 3-d example is room temperature GaAs with a carrier concentration of $n = 5 \times 10^{17} cm^{-3}$. The 2-d example is for a HfO_2-MoS_2-SiO_2-heterostructure at room temperature and a carrier concentration of $n_S = 2 \times 10^{12} cm^{-2}$. In both cases we calculate the fully-self consistent momentum relaxation time for carrier–coupled plasmon–LO-phonon scattering, including the drag term.

Initial wave vector grid Each of the steps in the iteration of the momentum relaxation time to self-consistency involved calculating the momentum relaxation τ_p depending on the previous step, cf. Eq. (4.24). To this end, integrals of the form

$$\int_{K_1(P)}^{K_2(P)} \mathrm{d}K \int_{\Omega_1(K,P)}^{\Omega_2(K,P)} \mathrm{d}\Omega \, \mathfrak{Im}\left(\frac{1}{\varepsilon_{K,\Omega}}\right) f(K,\Omega,P)\{\tau\}, \tag{C.123}$$

where f is some function of the scaled frequency Ω, the scaled wave vectors P and K (cf. Eq. (2.43)) and a functional of the momentum relaxation time τ, have to be evaluated. We calculated τ on a uniform wave vector grid. As each step in the iteration involves an integral over a previous iteration of τ cf. Eq. (4.24), we have to interpolate between the tabulated values as necessary.

We carried out calculations with widely varying temperatures and carrier densities, putting us in the classical limit, the highly degenerate limit, or anywhere in between. Consequently, there are multiple length scales determining the size and spacing of the wave vector grid. We chose the maximal wave vector in the grid to be several times the maximum of Fermi-wave vector or the Debye wave vector, and the spacing to be a fraction of their minimum. Consequently, this approach fails when one goes very far into either the degenerate or the classical limit. In the 3-d example, we used a grid

have not been tested extensively beyond the examples presented in this thesis.

with $0 < P < 10$ with 100 points for the scaled initial wave vector P (cf. Eq. (2.43)). In the 2-d example, we used a grid with $0.026 < P < 5.2$ with 200 points for the scaled initial wave vector P.

Dielectric functions As discussed in chapter 2, the imaginary parts of the carrier dielectric functions can be expressed in terms of Fermi-Dirac integrals. In the 2-d case, this involves a Fermi-Dirac integral which has to be evaluated numerically, but which has been implemented previously. [125, 126, 127, 128]. The real parts of the carrier dielectric functions cannot in general be expressed analytically, or even in terms of special functions. We tabulate the functions I_x^d from Eq. (2.54) on a fine grid to calculate the polarizability Eq. (2.55) and eventually the real part of the dielectric function in two or three dimensions. The functions implementing the real parts of the dielectric functions call the tabulated values and return an interpolated value. The grid size is determined by the values at which the dielectric function will have to be evaluated later in the code. See subsubsection 2.2.2.1 for some details on the integral $I_x^{d=3}$ from Eq. (2.62) which determines the carrier dielectric function in the 3d-case.

In the 3-d example, $I_x^{d=3}$ is tabulated on a $0 < x < 26.353$ grid with 52707 points. In the 2-d example, $I_x^{d=2}$ is tabulated on a $0 < x < 20$ grid with 400000 points.

Zeros of the dielectric functions We calculate the -in general- multiple roots of the real part of the dielectric function by first looking for sign-changes on a dense frequency grid for each wave vector, and subsequently bisecting the interval with the sign change. We check the amplitude of the real part of the dielectric function and the imaginary part of the inverse dielectric function to distinguish between zeros and poles.

In the 2-d example, we used a $0 < \Omega < 40.38$ grid with 4038 points for the initial discretization for the scaled frequency Ω (cf. Eq. (2.43)). In the 3-d example, we used a $0 < \Omega < 10$ grid for with 1000 points the initial discretization.

Frequency integrals We carried out the frequency integrals needed to calculate the f-sum rule, quasi-particle lifetimes and energy momentum relaxation times as described in appendix C.3, appendix C.4 and appendix C.2.1. We split the frequency integration domain between the sign changes of the real part of the dielectric function. In each of these domains, we carry out the integration with an adaptive open Simpson's rule [123]. This integration function increases the number of equally spaced grid points until the integral reaches a target relative accuracy. In the 3-d example, the target relative accuracy was 10^{-3}. In the 2-d example, the target relative accuracy was 10^{-2}.

If these integrals do not converge in this way, we treated sections of the integrand around the zeros of the real part of the dielectric function (which are delta peaks for undamped oscillations, and can be very sharp peaks if the anharmonic damping is small) explicitly as delta-functions, cf. Eq. (2.75). This allows us to calculate the $T = 0$ or $k = 0$ limits of sum rule integrals, energy and momentum relaxation time, but becomes rather cumbersome for the 2-d case, where the effective dielectric function is quite a complicated function, cf. subsection 3.2.2. Consequently, this explicit treatment of delta-peaks has not been implemented for the general 2-d case, and we always assumed sufficiently large anharmonic damping for the frequency integrals to converge. As discussed in appendix C.4.3, it helps to use a certain substitution to remove inverse square root singularities from the integrands of the 2-d integrals for the momentum relaxation and drag term.

The f-sum rule described in subsection 2.2.3 can be used as a test of the implementation of the frequency integrals.

Transferred wave vector integrals The wave vector integrals for the momentum relaxation time in the 3-d case were calculated on a uniform grid. We used a grid with the same spacing as the initial wave vector grid, but with twice the number of points, to allow for back-scattering. In the 3-d example, we used a grid with $0 < K < 20$ with 200 points for the transferred wave vector K (cf. Eq. (2.43)).

We found that in the two-dimensional case, wave vector integrals needed a much denser wave vector grid to converge than in the three-dimensional case. We consequently implemented an adaptive integration in the wave vector domain, using the gsl qag function [124]. In the 2-d example, we calculated the wave vector integrals with a target relative accuracy of 5%. As the 2-d calculations were carried out after the 3-d calculations, the adaptive wave vector integration was not implemented for the bulk case, though, in hindsight this would be beneficial.

Evaluation of drag term The calculation of the drag term $T_{K,\Omega}$, Eq. (C.39) in 3-d, and Eq. (C.76) in 2-d can be a bottleneck if the integrations are carried out explicitly within the wave vector and frequency integral. Therefore we tabulated $T_{K,\Omega}$ on a two-dimensional grid, and wrote a function which interpolated from this table on each call. This two-dimensional wave vector grid is determined by the largest relevant wave vector as described in the paragraph on wave vector integration above. The largest relevant frequencies follow from the larges zeros of the real part of the dielectric function. In the 2-d example, we used the Ω-grid discussed above, with $0 < \Omega < 40.38$ with 4038 points, and a transferred wave vector grid with $0.0026 < K < 10.41$ with 400 points. The drag term integral was calculated as on a grid with $0 < Q < 5.2$ with 200 points. In the 3-d example, we used the K- and

Ω-grids discussed above, with a $0 < \Omega < 10$ grid for with 1000 points and a grid with $0 < K < 20$ with 200 points, and the drag term integral was calculated as on a grid with $0 < Q < 10$ with 1000 points.

Convergence criteria for iterating the momentum relaxation time to self-consistency We used the carrier mobility as a convergence criterion when we iterated the momentum relaxation to self-consistency. We broke off the iteration when the mobility changed less than a certain value for a set number of iterations. For the 2-d calculations, the iteration was considered converged if the mobility had changed by less than 10^{-5} for 10 iterations. This meant that the 2-d example took 56 iterations to converge. For the 3-d calculations, the iteration was considered converged if the mobility had changed by less than 10^{-4} for 10 iterations. This meant that the code considered the 3-d example converged after 30 iterations.

Iterations in the bulk case, and without a drag term typically needed only a couple of tens of iterations, while calculations with a drag term could require many hundreds of iterations, especially in the classical or degenerate limits.

Parallelization We parallelized the calculation of the momentum relaxation time over initial wave vector points within each iteration. These calculations are independent, so that the parallelization is very efficient. The 3-d example took 57min to run on 8 processors. The 2-d example took 51min to run on 8 processors. Calculations without a drag term run much faster.

Outlook It was not the aim of this thesis to develop efficient code for distribution, and all the code written for this thesis is for proof of concept. The methods in this thesis could doubtlessly be implemented to allow the examples discussed in this section to run within a couple of minutes on a single processor. We recommend integrating on adaptive grids throughout. For the calculation of carrier mobilities on a dense grid of carrier densities, or temperatures, we discourage iterating the relaxation time approximation momentum relaxation time to self-consistency independently for each point. Instead, one should iterate from the self-consistent momentum relaxation time for the previous point.

Appendix D

Seebeck coefficient

We only give a crude introduction into the Seebeck coefficient here, closely following [24].

Applying a voltage to a material can not only give rise to an electric, but also a thermal current. The latter effect is called Thomson effect (or Peltier effect under certain conditions)[24]. The inverse effect is know as the Seebeck effect and the proportionality constants between the applied fields and currents are related to each other.

Starting from the thermodynamic relation for the change in heat,

$$dQ = TdS = dU - \tilde{\mu}dN \tag{D.1}$$

with the chemical potential $\tilde{\mu}$, the temperature T and the change in entropy dS and number N, we write

$$\boldsymbol{j}_Q = T\boldsymbol{j}_S = \boldsymbol{j}_E - \tilde{\mu}\boldsymbol{j}_N \tag{D.2}$$

for the heat current $\boldsymbol{j}_Q$. In an isotropic electron gas, its two contributions are from the particle current j_N

$$\boldsymbol{j}_N = \frac{2}{(2\pi)^3}\int \mathrm{d}^3\boldsymbol{k}\, n\boldsymbol{v}_{\boldsymbol{k}} f_{\boldsymbol{k}} = n\mu\boldsymbol{E}, \tag{D.3}$$

with the mobility μ and the applied external field $\boldsymbol{E}$ (see section C.5, Eq. C.88), and from the energy current

$$\boldsymbol{j}_E = \frac{2}{(2\pi)^3}\int \mathrm{d}^3\boldsymbol{k}\, n\boldsymbol{v}_{\boldsymbol{k}}\boldsymbol{E}_{\boldsymbol{k}} f_{\boldsymbol{k}} = nc\boldsymbol{E}, \tag{D.4}$$

where we have introduced the shorthand c. This means that the electronic

contribution to the heat current is

$$\boldsymbol{j}_Q = n(c - \tilde{\mu}\mu)\boldsymbol{E}. \tag{D.5}$$

The Peltier coefficient connects the heat current with the electric current $\boldsymbol{j}_e = e\boldsymbol{j}_N$ which is proportional to the particle current:

$$\boldsymbol{j}_Q = \Pi \boldsymbol{j}_e \tag{D.6}$$

Hence we can express it as

$$\Pi = \frac{1}{e}\left(\frac{c}{\mu} - \tilde{\mu}\right). \tag{D.7}$$

The Seebeck coefficient is connected to the Peltier coefficient by

$$S = \frac{\Pi}{T} = \frac{1}{eT}\left(\frac{c}{\mu} - \tilde{\mu}\right). \tag{D.8}$$

Here we have only considered the contribution from electrons to the Peltier and Seebeck coefficients. In semiconductors, there is also a contributions from holes, with opposite sign due to its opposite charge. As we consider highly n-doped semiconductors, it should be permissible to neglect the hole contribution.

As the expression for the heat current only differs by the one for the particle current by a factor of $E_{\boldsymbol{k}}$ in the integral, we can get the expression for c by comparison with the one for μ from Eq. C.89

$$\mu = -\frac{e}{3m*}\frac{\int_0^\infty \mathrm{d}K\, K^3 \left(\frac{\partial}{\partial K} f_K^0\right)\tau_K}{\int_0^\infty \mathrm{d}K\, K^2 f_K^0} \qquad c = -\frac{eE_F}{3m*}\frac{\int_0^\infty \mathrm{d}K\, K^5 \left(\frac{\partial}{\partial K} f_K^0\right)\tau_K}{\int_0^\infty \mathrm{d}K\, K^2 f_K^0} \tag{D.9}$$

and their quotient is

$$\frac{c}{\mu} = \frac{\int_0^\infty \mathrm{d}K\, K^5 \left(\frac{\partial}{\partial K} f_K^0\right)\tau_K}{\int_0^\infty \mathrm{d}K\, K^3 \left(\frac{\partial}{\partial K} f_K^0\right)\tau_K} E_F = \frac{\int_0^\infty \mathrm{d}K\, K^6 f_K^0 \left(1 - f_K^0\right)\tau_K}{\int_0^\infty \mathrm{d}K\, K^4 f_K^0 \left(1 - f_K^0\right)\tau_K} E_F \tag{D.10}$$

Limits In the case of high degeneracy the derivative of the distribution function will be a delta function at the Fermi wave vector $K = 1$, so that $\frac{c}{\mu} \to E_F$ as the degenerate limit is reached, and the Peltier coefficient $\Pi \to \frac{1}{e}(E_F - \tilde{\mu}) \to 0$ will go to zero.

If we assume a constant momentum relaxation time, the Peltier coefficient will be independent of the momentum relaxation time, and hence any details of the scattering process.

In the classical limit, with constant momentum relaxation time, we can evaluate $\frac{c}{\mu}$

analytically

$$\frac{c}{\mu} = \frac{\int_0^\infty \mathrm{d}K\, K^6 f_K^0}{\int_0^\infty \mathrm{d}K\, K^4 f_K^0} E_F = k_B T \frac{\Gamma(7/2)}{\Gamma(5/2)} = \frac{5}{2} k_B T \tag{D.11}$$

(see, e.g., [25, chapter X]) and find

$$\Pi_{classical} = \frac{1}{e}\left(\frac{5}{2} k_B T - \tilde{\mu}\right). \tag{D.12}$$

We use the momentum relaxation times calculated in section 5.3 above to calculate the Seebeck coefficient in room temperature GaAs Eq. D.8 with Eq. D.10. In

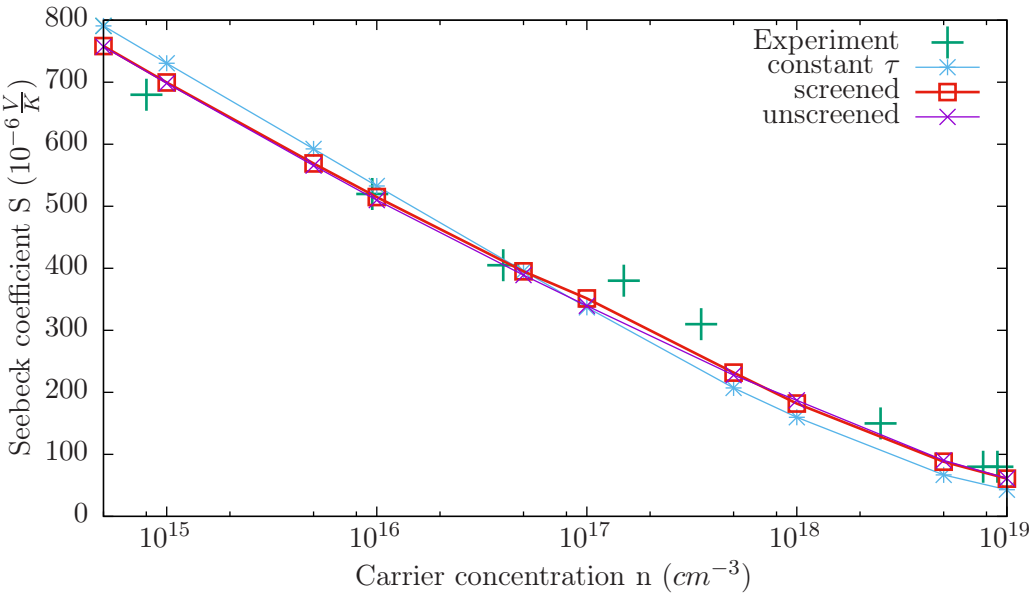

Figure D.1: Seebeck coefficient in n-GaAs at $T = 300K$ as a function of carrier concentration. The line marked "constant τ"is calculated total momentum relaxation time Eq. D.8 with Eq. D.10 with a constant momentum relaxation time, and is hence independent of the momentum relaxation time. The line marked "unscreened" is calculated from the total momentum relaxation time due to unscreened LO-phonon scattering, charged impurity scattering and LA-phonon scattering. The line marked "screened" is calculated from the total momentum relaxation time due to unscreened LO-phonon scattering, charged impurity scattering and LA-phonon scattering. Experimental values are taken from [129].

Fig. D.1, we show the room temperature Seebeck coefficient as a function of the carrier concentration. The Seebeck coefficient is calculated from the total momentum relaxation times calculated in section 5.3, which were plotted in Fig. 5.7c. The Seebeck coefficient is not suitable for experimental testing of the effect of screening on the momentum relaxation time, because the Seebeck coefficients calculated with and without screening differ barely from each other. In fact, we see that these two calculations for the Seebeck coefficient do not even differ strongly from the Seebeck

coefficient for an arbitrary constant momentum relaxation time.

Our calculation shows that drag between coupled plasmon–LO-phonon modes and carriers is not important for the Seebeck coefficient of room temperature GaAs. Phonon drag can however strongly affect the Seebeck coefficients, especially at low temperatures – compare calculations by Mahan et al. [50] which explained some striking peaks in the experimental data for the Seebeck coefficient in silicon [130] by taking phonon drag into account.

Appendix E

Other scattering mechanisms

E.1 Other scattering mechanisms in bulk GaAs

E.1.1 LA phonon scattering

We include scattering due to longitudinal accoustic phonon with the momentum relaxation time [3, chapter 5]

$$\frac{1}{\tau_p^{LA}} = \frac{\sqrt{2}\,(a_c)^2\,(m^*)^{3/2}\,k_B T\sqrt{E_p}}{\pi\hbar^4\rho v_s^2} \tag{E.1}$$

and the parameters are given for GaAs in Tab. 2.1.

E.1.2 Charged impurity scattering

Charged impurity scattering is calculated in the Brooks-Herring model, as described in[98, chapter IIIB]. In the Brooks-Herring model, the Coulomb potential screened by the carriers is assumed to have to form of a Yukawa potential, with the inverse screening length

$$\beta_s = \frac{1}{l_{Debye}}\sqrt{\frac{\mathfrak{F}_{-1/2}(\nu)}{\mathfrak{F}_{1/2}(\nu)}}. \tag{E.2}$$

Here, l_{Debye} is the Debye screening length, $\mathfrak{F}_{\mathrm{i}}(\nu)$ are the Fermi-Dirac integrals and ν is the chemical potential. The factor involving the Fermi-Dirac integrals takes into account that the screening length varies depending on the degree of degeneracy of the carrier distribution [98].

We use the relaxation time τ_{BH} from [98, Eq. 34], but calculate the mobility using the proper Fermi-Dirac distribution function (Eq. (5.4)), not the non-degenerate Boltzmann distribution function in [98, Eq. 36]. This is necessary, because we

consider rather high electron concentrations.

We make the assumption that the carrier density equals the impurity concentration, $n = N_I$, i.e., firstly, all donors are ionized, secondly, there are many more donors than acceptors, and thirdly, the impurity concentration is much larger than the intrinsic carrier concentration. In order to get a better estimation of the carrier density, we would need not only the donor and acceptor concentration, but also the impurity energy levels. That means that we can only make a more accurate mobility calculation if we know which and how many dopants were used for each sample. We will forgo such a detailed description and only show that the mobilities we calculate are in accordance with existing measurements, and that, in principle, one should be able to distinguish carrier coupled mode scattering from carrier-LO-phonon scattering in certain parameter ranges.

E.2 Other scattering mechanisms in MoS_2-heterostructures

Other than interface phonon-plasmon scattering, we consider scattering mechanisms which are intrinsic to the investigated structure, that is, acoustic and optical deformation potential scattering (ADP and ODP) and piezoelectric scattering (PE). We use parameters for relaxation times Kaasbjerg et al. [57, 5] calculated for a monolayer of MoS_2 in a vacuum.

E.2.1 Acoustic deformation potential scattering and piezoelectric scattering

We treat ADP scattering and PE scattering as elastic processes. We also neglect interference term between ADP and PE, so that each process has an independent momentum relaxation time [5, appendix C2]. For a carrier with momentum p, the momentum relaxation rate is[57, 5]

$$\frac{1}{\tau_p} = \frac{\Xi^2 m^* k_B T}{\hbar^3 \rho c} \frac{1}{\pi} \int_0^\pi \mathrm{d}\varphi \, \frac{1 - \cos\varphi}{\left|\tilde{\varepsilon}_{k(\varphi),\omega=0}\right|^2} \tag{E.3}$$

where $k(\varphi) = \sqrt{2p\,(1 - \cos\varphi)}$ is the magnitude of the transferred wave vector if the angle between the initial and final wave vector is φ. m^* and ρ are the effective mass and ion mass sheet density of MoS_2 c is the speed of sound of the TA or LA phonon, and Ξ is the corresponding ADP, or effective long wavelength piezoelectric potential. (See [5, Eq. (15)]).

$\tilde{\varepsilon}_{k,\omega}$ is the free carrier contribution to the static dielectric function of the structure.

The screening due to the valence electrons is already taken into account in the deformation potential [5, appendix C2]. Hence

$$\tilde{\varepsilon}_{k,\omega=0} = 1 + \frac{\chi^{free}_{k,\omega=0}}{\varepsilon^{interface}_{k,\omega=0}} \tag{E.4}$$

where $\varepsilon^{interface}_{k,\omega}$ is the static dielectric function of the structure, Eq. (3.57) and $\chi^{free}_{k,\omega}$ is the free electron susceptibility Eq. (3.61). As $\varepsilon^{interface}_{k,\omega}$ enters, the screening is different for different structures, see Fig. E.1b. Ma and Jena, Kaasbjerg et al., and Bogulsawski et al. [54, 5] agree that the TA ADP should have $\tilde{\varepsilon} = 1$. Kaasbjerg et al. make the argument that this is because TA ADP scattering is dominated by Umklapp processes, which should be unscreened by free carriers. Bogulsawski et al.[131, 132] argue that in the long wavelength limit, this result follows from the symmetry of the TA ADP matrix element in a semiconductor with multiple spherical valleys like MoS_2.

E.2.2 Optical deformation potential scattering

ODP scattering is an inelastic process. The momentum relaxation time is[57, Eq. 31][1]

$$\frac{1}{\tau_p} = \frac{m^* D^2}{2\hbar^2 \rho \omega} \left[N^0_\omega + \left(N^0_\omega + 1 \right) \Theta \left(E_p - \hbar\omega \right) \right] \tag{E.5}$$

Here D is the zeroth order ODP due to the LO or homopolar mode of constant frequency ω. The Heaviside step function Θ makes sure the emission term vanishes when the electron energy is smaller than the phonon energy.

First order ODP and intervalley ADP has been found to be insignificant for low field transport [57] and will be neglected.

E.2.3 LO-phonon scattering

The scattering due to the Fröhlich interfaction Kaasbjerg et al.[57] is of an interface phonon type, not of a confined phonon type, as can be seen from their discussion in [57, appendix B].

Ma and Jena [54] include Frölich scattering of the interface or remote phonon type and of the confined phonon type (which they refer to as LO-phonon scattering).[2] This is not double counting. In fact, the Poisson equation has solutions of confined and of interface type [86, 133]. However, we think that the confinement in a slab of MoS_2 with a thickness of a=6.145Åis so strong that confined solutions do not contribute to

[1] ODP is not screened by free carriers in MoS_2 due to the symmetry of the ODP [131].

[2] However, despite the confined nature of these modes, Ma and Jena [54] screen them as if they were interface type modes.

Table E.1: Material parameters for MoS_2, from Ref. [5] unless a different reference is given. m_e is the electron mass. The effective acoustic deformation potential for piezoelectric scattering was calculated with [5, Eq. (15)].

Quantity	symbol	value
Effective mass	m^*	0.35 m_e (Ref. [52])
Ion mass sheet density	ρ	$3.17 \times 10^{-7} \frac{g}{cm^2}$
LA speed of sound	c_{LA}	$6.7{\times}10^5 \frac{cm}{s}$
TA speed of sound	c_{TA}	$4.2{\times}10^5 \frac{cm}{s}$
LA ADP	Ξ_{LA}	2.4 eV
TA ADP	Ξ_{LA}	1.5 eV
PE effective ADP	Ξ_{PE}	2.39 eV (Ref. [57])
LO-phonon energy	$\hbar\omega_{LO}$	47.9 meV (Ref. [7])
Homopolar phonon energy	$\hbar\omega_{HP}$	50.0 meV
LO ODP	D_{LO}	$2.6{\times}10^8 \frac{eV}{cm}$ (Ref. [57])
HP ODP	D_{HP}	$4.1{\times}10^8 \frac{eV}{cm}$ (Ref. [57])

low-field transport. The discretized wave vectors allowed for the confined modes would be $k_n = n\frac{\pi}{a} \approx n\ 5.1 \times 10^7 cm^{-1}$, which means that even k_1 is roughly three times larger than the Fermi wave vector for the largest carrier concentrations considered, $k_F(n_s = 10^{14} cm^{-1}) \approx 1.8 \times 10^7 cm^{-1}$.

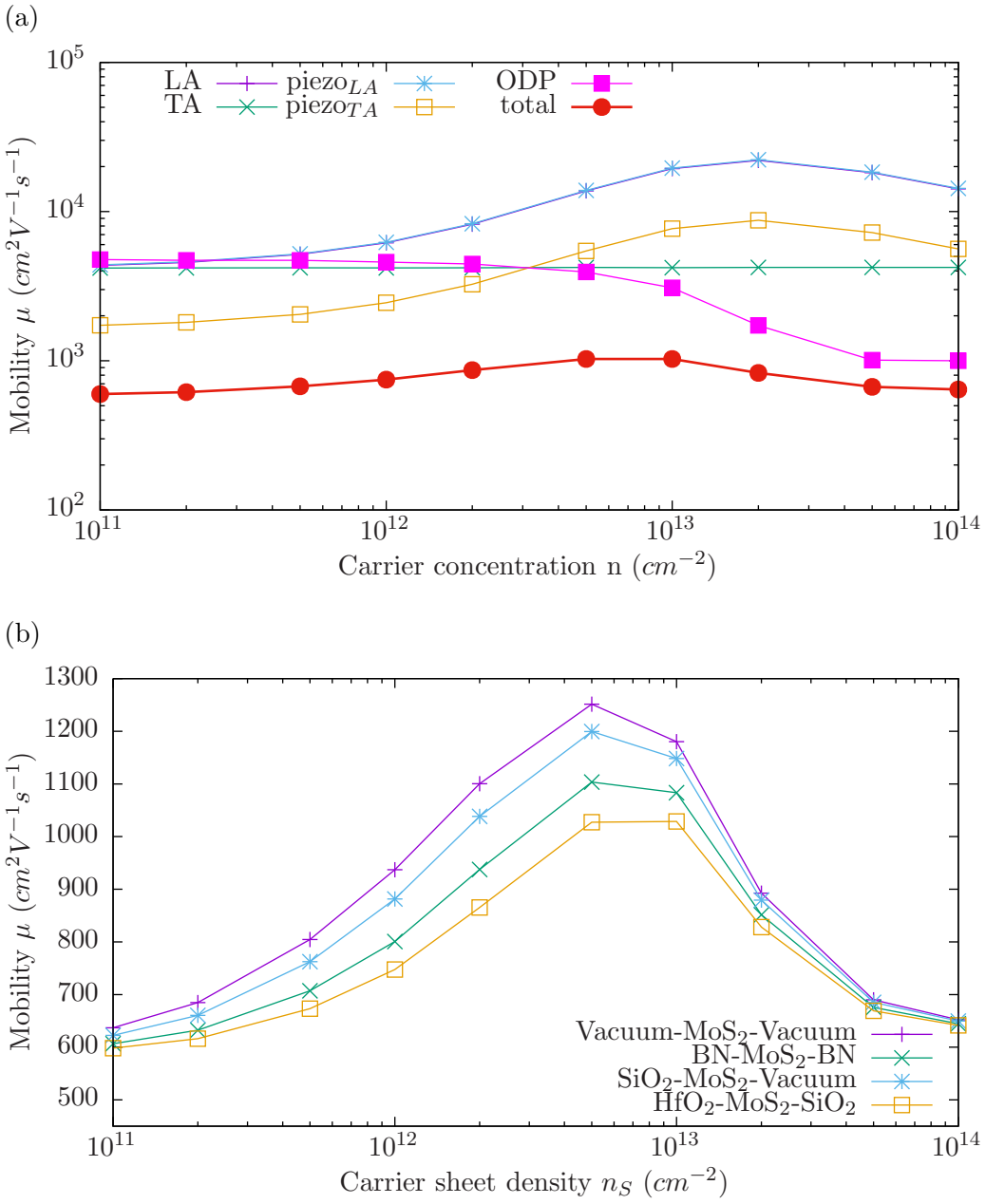

Figure E.1: Room temperature mobility as a function of carrier sheet density with all intrinsic scattering mechanisms considered, except for interface phonon-plasmon scattering. (a) Room temperature mobility due to acoustic deformation potential scattering of the LA and TA modes, piezoelectric scattering of the LA and TA modes, and zero order optical deformation potential scattering, and the total mobility resulting from all these scattering mechanisms for the HfO_2-MoS_2-SiO_2-structure. (b) Total room temperature mobility due to acoustic and optical deformation potential scattering and piezoelectric scattering in the different investigated structures marked.

Bibliography

[1] M. V. Fischetti, D. A. Neumayer and E. A. Cartier. Effective electron mobility in Si inversion layers in metal–oxide–semiconductor systems with a high-kappa insulator: The role of remote phonon scattering. *J. Appl. Phys.*, 2001. vol. 90, pages 4587 . URL http://dx.doi.org/10.1063/1.1405826.

[2] L. Landau. On the vibrations of the electronic plasma. *JETP*, 1946. vol. 16, page 574. Translated from Russian by E. Lifschitz, URL http://www.sciencedirect.com/science/book/9780080105239.

[3] P. Yu and M. Cardona. *Fundamentals of Semiconductors: Physics And Materials Properties*. Springer, third edn., 2005. URL http://books.google.ie/books?id=W9pdJZoAeyEC.

[4] M. Abramowitz and I. Stegun. *Handbook of mathematical functions with formulas, graphs, and mathematical tables*. No. v. 55, no. 1972 in Applied mathematics series. U.S. Govt. Print. Off., 1964. URL http://books.google.ie/books?id=MtU8uP7XMvoC.

[5] K. Kaasbjerg, K. S. Thygesen and A.-P. Jauho. Acoustic phonon limited mobility in two-dimensional semiconductors: Deformation potential and piezoelectric scattering in monolayer MoS_2 from first principles. *Phys. Rev. B*, Jun 2013. vol. 87, page 235312. URL http://dx.doi.org/10.1103/PhysRevB.87.235312.

[6] J. D. Jackson. *Classical Electrodynamics*. New York: Wiley, third edn., 1999.

[7] T. J. Wieting and J. L. Verble. Infrared and Raman Studies of Long-Wavelength Optical Phonons in Hexagonal MoS_2. *Phys. Rev. B*, Jun 1971. vol. 3, pages 4286. URL http://dx.doi.org/10.1103/PhysRevB.3.4286.

[8] R. Geick, C. H. Perry and G. Rupprecht. Normal Modes in Hexagonal Boron Nitride. *Phys. Rev.*, Jun 1966. vol. 146, pages 543. URL http://dx.doi.org/10.1103/PhysRev.146.543.

[9] F. Gervais and B. Piriou. Temperature dependence of transverse and longitudinal optic modes in the α and β phases of quartz. *Phys. Rev. B*, May

1975. vol. 11, pages 3944. URL http://dx.doi.org/10.1103/PhysRevB.11.3944.

[10] S. Sze. *Modern semiconductor device physics*. AWiley-Interscience publication. Wiley, 1998. URL https://books.google.ie/books?id=urfvAAAAMAAJ.

[11] M. Fukuda. *Optical Semiconductor Devices*. A Wiley Interscience publication. Wiley, 1999. URL https://books.google.ie/books?id=I_J5uyUxOu4C.

[12] L. Esaki. The Birth of the Semiconductor Superlattice. In *Fundamentals of Semiconductors: Physics And Materials Properties* [3], chap. Pioneers of Semiconductor Physics Remember, page 578, 2005. URL http://books.google.ie/books?id=W9pdJZoAeyEC.

[13] J. Faist. *Quantum Cascade Lasers*. EBSCO ebook academic collection. OUP Oxford, 2013. URL https://books.google.ie/books?id=tPHoMxFn5iMC.

[14] P. D.-C. Marisol Martin-Ganzalez, O. Caballero-Calero. Nanoengineering thermoelectrics for 21st century: Energy harvesting and other trends in the field. *Renewable and Sustainable Energy Reviews*, 2013. vol. 24, pages 288 . URL http://dx.doi.org/10.1016/j.rser.2013.03.008.

[15] K. S. Novoselov, D. Jiang, F. Schedin, T. J. Booth, V. V. Khotkevich, S. V. Morozov and A. K. Geim. Two-dimensional atomic crystals. *Proceedings of the National Academy of Sciences of the United States of America*, 2005. vol. 102, pages 10451. URL http://dx.doi.org/10.1073/pnas.0502848102.

[16] B. Radisavljevic, A. Radenovic, J. Brivio, V. Giacometti and A. Kis. Single-layer MoS2 transistors. *Nat Nano*, mar 2011. vol. 6, pages 147. 10.1038/nnano.2010.279, URL http://dx.doi.org/10.1038/nnano.2010.279.

[17] B. Radisavljevic and A. Kis. Mobility engineering and a metal - insulator transition in monolayer MoS2. *Nat Mater*, 2013. vol. 12, page 815. URL http://dx.doi.org/10.1038/nmat3687.

[18] A. Molina-Sánchez and L. Wirtz. Phonons in single-layer and few-layer MoS_2 and WS_2. *Phys. Rev. B*, Oct 2011. vol. 84, page 155413. URL http://dx.doi.org/10.1103/PhysRevB.84.155413.

[19] Y. Cai, J. Lan, G. Zhang and Y.-W. Zhang. Lattice vibrational modes and phonon thermal conductivity of monolayer MoS_2. *Phys. Rev. B*, Jan 2014. vol. 89, page 035438. URL http://dx.doi.org/10.1103/PhysRevB.89.035438.

[20] R. Downs and M. Hall-Wallace. The American Mineralogist crystal structure database. *American Mineralogist*, 1 2003. vol. 88, pages 247. Retrieved September24, 2016, URL http://rruff.geo.arizona.edu/AMS/amcsd.php.

[21] B. Mills. Ball-and-stick model of the part of the crystal structure of molybdenite. https://upload.wikimedia.org/wikipedia/commons/5/5d/Molybdenite-3D-balls.png, 2007. Retrieved September 24, 2016.

[22] D. Pines. *Elementary Excitations in Solids: Lectures on Protons, Electrons, and Plasmons*. W. A. Benjamin, Inc., New York, 1964.

[23] D. Pines and D. Bohm. A Collective Description of Electron Interactions: II. Collective vs Individual Particle Aspects of the Interactions. *Phys. Rev.*, Jan 1952. vol. 85, pages 338. URL http://dx.doi.org/10.1103/PhysRev.85.338.

[24] N. W. Ashcroft and N. D. Mermin. *Solid State Physics*. Saunders College, Philadelphia, 1976.

[25] J. Ziman. *Electrons and Phonons: The Theory of Transport Phenomena in Solids*. The international series of monographs on physics. Oxford University Press, Incorporated, 1962. URL http://books.google.ie/books?id=hpVRcAAACAAJ.

[26] B. K. Ridley. *Quantum processes in semiconductors*. Clarendon Press, Oxford, 4th edn., 1999.

[27] R. A. Cowley and G. Dolling. Conduction Electrons and Optic Modes of Ionic Crystals. *Phys. Rev. Lett.*, Apr 1965. vol. 14, pages 549. URL http://dx.doi.org/10.1103/PhysRevLett.14.549.

[28] A. Mooradian and G. B. Wright. Observation of the Interaction of Plasmons with Longitudinal Optical Phonons in GaAs. *Phys. Rev. Lett.*, May 1966. vol. 16, pages 999. URL http://dx.doi.org/10.1103/PhysRevLett.16.999.

[29] G. C. Cho, T. Dekorsy, H. J. Bakker, R. Hövel and H. Kurz. Generation and Relaxation of Coherent Majority Plasmons. *Phys. Rev. Lett.*, Nov 1996. vol. 77, pages 4062. URL http://dx.doi.org/10.1103/PhysRevLett.77.4062.

[30] B. B. Varga. Coupling of Plasmons to Polar Phonons in Degenerate Semiconductors. *Phys. Rev.*, Mar 1965. vol. 137, pages A1896. URL http://dx.doi.org/10.1103/PhysRev.137.A1896.

[31] L. Landau, E. Lifshitz and L. Pitaevskiĭ. *Electrodynamics of continuous media*. Pergamon international library of science, technology, engineering, and social studies. Pergamon, 1984. URL https://books.google.ie/books?id=j7nvAAAAMAAJ.

[32] P. Nozieres and D. Pines. *Theory Of Quantum Liquids*. Advanced Books Classics Series. Westview Press, 1999. URL http://books.google.ie/books?id=q3wCwaV-gmUC.

[33] H. Ehrenreich. Electron scattering in InSb. *Journal of Physics and Chemistry of Solids*, 1957. vol. 2, pages 131 . URL http://dx.doi.org/10.1016/0022-3697(57)90099-9.

[34] H. Ehrenreich. Screening effects in polar semiconductors. *Journal of Physics and Chemistry of Solids*, 1959. vol. 8. URL http://dx.doi.org/10.1016/0022-3697(59)90297-5.

[35] C. M. Wolfe, G. E. Stillman and W. T. Lindley. Electron Mobility in High-Purity GaAs. *Journal of Applied Physics*, 1970. vol. 41, pages 3088. URL http://dx.doi.org/10.1063/1.1659368.

[36] M. E. Kim, A. Das and S. D. Senturia. Electron scattering interaction with coupled plasmon-polar-phonon modes in degenerate semiconductors. *Phys. Rev. B*, Dec 1978. vol. 18, pages 6890. URL http://dx.doi.org/10.1103/PhysRevB.18.6890.

[37] A. I. Kasiyan and P. I. Russu. The Effect of Collective Electron-Hole Plasma Modes on Charge Carrier Mobility in Polar Semiconductors. *physica status solidi (b)*, 1985. vol. 128, pages 243. URL http://dx.doi.org/10.1002/pssb.2221280129.

[38] L. Van Hove. Correlations in Space and Time and Born Approximation Scattering in Systems of Interacting Particles. *Phys. Rev.*, Jul 1954. vol. 95, pages 249. URL http://dx.doi.org/10.1103/PhysRev.95.249.

[39] D. Pines. *The Role of Plasma Oscillations in Electron Interactions.* Ph.D. thesis, Princeton University, 1950.

[40] D. Bohm and D. Pines. A Collective Description of Electron Interactions: III. Coulomb Interactions in a Degenerate Electron Gas. *Phys. Rev.*, Nov 1953. vol. 92, pages 609. URL http://dx.doi.org/10.1103/PhysRev.92.609.

[41] J. Lindhard. On the properties of a gas of charged particles. *Det Kongelige Danske Videnskabernes Selskab*, 1954. vol. 28, pages 1.

[42] R. H. Lyddane, R. G. Sachs and E. Teller. On the Polar Vibrations of Alkali Halides. *Phys. Rev.*, Apr 1941. vol. 59, pages 673. URL http://dx.doi.org/10.1103/PhysRev.59.673.

[43] B. Y.-K. Hu and S. Das Sarma. Inelastic scattering in a doped polar semiconductor at finite temperature. *Phys. Rev. B*, Oct 1991. vol. 44, pages 8319. URL http://dx.doi.org/10.1103/PhysRevB.44.8319.

[44] B. A. Sanborn, B. Y.-K. Hu and S. Das Sarma. Correction to the decay rate of nonequilibrium carrier distributions due to scattering-in processes. *Phys. Rev.*

B, Mar 1994. vol. 49, pages 7767. URL http://dx.doi.org/10.1103/PhysRevB.49.7767.

[45] D. L. Maslov. Mutual drag of two- and three-dimensional electron gases: A collective-collisions approach. *Phys. Rev. B*, Jan 1992. vol. 45, pages 1911. URL http://dx.doi.org/10.1103/PhysRevB.45.1911.

[46] F. Stern. Polarizability of a Two-Dimensional Electron Gas. *Phys. Rev. Lett.*, Apr 1967. vol. 18, pages 546. URL http://dx.doi.org/10.1103/PhysRevLett.18.546.

[47] B. A. Sanborn. Nonequilibrium total-dielectric-function approach to the electron Boltzmann equation for inelastic scattering in doped polar semiconductors. *Phys. Rev. B*, May 1995. vol. 51, pages 14247. URL http://dx.doi.org/10.1103/PhysRevB.51.14247.

[48] B. A. Sanborn. Electron-electron interactions, coupled plasmon-phonon modes, and mobility in n-type GaAs. *Phys. Rev. B*, May 1995. vol. 51, pages 14256. URL http://dx.doi.org/10.1103/PhysRevB.51.14256.

[49] R. Peierls. *Quantum Theory of Solids*. Clarendon Press, 1955.

[50] G. D. Mahan, L. Lindsay and D. A. Broido. The Seebeck coefficient and phonon drag in silicon. *Journal of Applied Physics*, 2014. vol. 116, 245102. URL http://dx.doi.org/10.1063/1.4904925.

[51] K. Hess and P. Vogl. Remote polar phonon scattering in silicon inversion layers. *Solid State Communications*, 1979. vol. 30, pages 797 . URL http://dx.doi.org/10.1016/0038-1098(79)90051-6.

[52] T. Cheiwchanchamnangij and W. R. L. Lambrecht. Quasiparticle band structure calculation of monolayer, bilayer, and bulk MoS_2. *Phys. Rev. B*, May 2012. vol. 85, page 205302. URL http://dx.doi.org/10.1103/PhysRevB.85.205302.

[53] K. F. Mak, C. Lee, J. Hone, J. Shan and T. F. Heinz. Atomically Thin MoS_2: A New Direct-Gap Semiconductor. *Phys. Rev. Lett.*, Sep 2010. vol. 105, page 136805. URL http://dx.doi.org/10.1103/PhysRevLett.105.136805.

[54] N. Ma and D. Jena. Charge Scattering and Mobility in Atomically Thin Semiconductors. *Phys. Rev. X*, Mar 2014. vol. 4, page 011043. URL http://dx.doi.org/10.1103/PhysRevX.4.011043.

[55] L. Zeng, Z. Xin, S. Chen, G. Du, J. Kang and X. Liu. Remote phonon and impurity screening effect of substrate and gate dielectric on electron dynamics in single layer MoS2. *Applied Physics Letters*, 2013. vol. 103, 113505. URL http://dx.doi.org/10.1063/1.4821344.

[56] Z.-Y. Ong and M. V. Fischetti. Mobility enhancement and temperature dependence in top-gated single-layer MoS_2. *Phys. Rev. B*, Oct 2013. vol. 88, page 165316. URL http://dx.doi.org/10.1103/PhysRevB.88.165316.

[57] K. Kaasbjerg, K. S. Thygesen and K. W. Jacobsen. Phonon-limited mobility in n-type single-layer MoS_2 from first principles. *Phys. Rev. B*, Mar 2012. vol. 85, page 115317. URL http://dx.doi.org/10.1103/PhysRevB.85.115317.

[58] S. M. Sze. *Physics of Semiconductor Devices*. Wiley-Interscience, 2 edn., Nov 1981. URL http://www.worldcat.org/isbn/0471056618.

[59] N. R. Arista and W. Brandt. Dielectric response of quantum plasmas in thermal equilibrium. *Phys. Rev. A*, Mar 1984. vol. 29, pages 1471. URL http://dx.doi.org/10.1103/PhysRevA.29.1471.

[60] K. Flensberg and B. Y.-K. Hu. Plasmon enhancement of Coulomb drag in double-quantum-well systems. *Phys. Rev. B*, Nov 1995. vol. 52, pages 14796. URL http://dx.doi.org/10.1103/PhysRevB.52.14796.

[61] M. Bleicher. *Halbleiter-Optoelektronik*. Uni-Taschenbücher. Hüthig, 1986. URL https://books.google.ie/books?id=9J1KAAAACAAJ.

[62] S. Perkowitz. Free carriers, coupled modes, and the generalized dielectric function in PbTe. *Phys. Rev. B*, Oct 1975. vol. 12, pages 3210. URL http://dx.doi.org/10.1103/PhysRevB.12.3210.

[63] G. Mahan. *Many Particle Physics*. Physics of Solids and Liquids. Springer, 2000. URL http://books.google.ie/books?id=xzSgZ4-yyMEC.

[64] M. Gell-Mann and K. A. Brueckner. Correlation Energy of an Electron Gas at High Density. *Phys. Rev.*, Apr 1957. vol. 106, pages 364. URL http://dx.doi.org/10.1103/PhysRev.106.364.

[65] M. Gell-Mann. Specific Heat of a Degenerate Electron Gas at High Density. *Phys. Rev.*, Apr 1957. vol. 106, pages 369. URL http://dx.doi.org/10.1103/PhysRev.106.369.

[66] K. Sawada, K. A. Brueckner, N. Fukuda and R. Brout. Correlation Energy of an Electron Gas at High Density: Plasma Oscillations. *Phys. Rev.*, Nov 1957. vol. 108, pages 507. URL http://dx.doi.org/10.1103/PhysRev.108.507.

[67] J. Hubbard. The Description of Collective Motions in Terms of Many-Body Perturbation Theory. *Proceedings of the Royal Society of London A: Mathematical, Physical and Engineering Sciences*, 1957. vol. 240, pages 539. URL http://dx.doi.org/10.1098/rspa.1957.0106.

[68] H. Ehrenreich and M. H. Cohen. Self-Consistent Field Approach to the Many-Electron Problem. *Phys. Rev.*, Aug 1959. vol. 115, pages 786. URL http://dx.doi.org/10.1103/PhysRev.115.786.

[69] J. Goldstone and K. Gottfried. Collective excitations of fermi gases. *Il Nuovo Cimento (1955-1965)*, 1959. vol. 13, pages 849. URL http://dx.doi.org/10.1007/BF02726371.

[70] G. Manfredi. How to model quantum plasmas. *Fields Institute Communications Series*, 2005. vol. 46, page 263. URL https://arxiv.org/abs/quant-ph/0505004.

[71] A. L. Fetter. Electrodynamics and thermodynamics of a classical electron surface layer. *Phys. Rev. B*, Nov 1974. vol. 10, pages 3739. URL http://dx.doi.org/10.1103/PhysRevB.10.3739.

[72] P. F. Maldague. Many-body corrections to the polarizability of the two-dimensional electron gas. *Surface Science*, 1978. vol. 73, pages 296 . URL http://dx.doi.org/10.1016/0039-6028(78)90507-1.

[73] B. Mihaila. Lindhard function of a d-dimensional Fermi gas. *ArXiv e-prints*, Nov 2011. https://arxiv.org/abs/1111.5337.

[74] N. Iwamoto. Sum rules and static local-field corrections of electron liquids in two and three dimensions. *Phys. Rev. A*, Dec 1984. vol. 30, pages 3289. URL http://dx.doi.org/10.1103/PhysRevA.30.3289.

[75] P. A. M. Dirac. The Quantum Theory of the Emission and Absorption of Radiation. *Proceedings of the Royal Society of London. Series A, Containing Papers of a Mathematical and Physical Character*, 1927. vol. 114, pages pp. 243. URL http://www.jstor.org/stable/94746.

[76] H. B. Callen and T. A. Welton. Irreversibility and Generalized Noise. *Phys. Rev.*, Jul 1951. vol. 83, pages 34. URL http://dx.doi.org/10.1103/PhysRev.83.34.

[77] H. Nyquist. Thermal Agitation of Electric Charge in Conductors. *Phys. Rev.*, Jul 1928. vol. 32, pages 110. URL http://dx.doi.org/10.1103/PhysRev.32.110.

[78] R. Kubo. The fluctuation-dissipation theorem. *Reports on Progress in Physics*, 1966. vol. 29, page 255. URL http://stacks.iop.org/0034-4885/29/i=1/a=306.

[79] P. Nozières and D. Pines. A dielectric formulation of the many body problem: Application to the free electron gas. *Il Nuovo Cimento (1955-1965)*, 1958. vol. 9, pages 470. URL http://dx.doi.org/10.1007/BF02725103.

[80] J. J. Quinn and R. A. Ferrell. Electron Self-Energy Approach to Correlation in a Degenerate Electron Gas. *Phys. Rev.*, Nov 1958. vol. 112, pages 812. URL http://dx.doi.org/10.1103/PhysRev.112.812.

[81] H. Fröhlich. Electrons in lattice fields. *Advances in Physics*, 1954. vol. 3, pages 325. URL http://dx.doi.org/10.1080/00018735400101213.

[82] B. Laikhtman and P. M. Solomon. Electron-drag effect in Si metal-oxide-semiconductor devices with thin oxide layers. *Phys. Rev. B*, Sep 2005. vol. 72, page 125338. URL http://dx.doi.org/10.1103/PhysRevB.72.125338.

[83] B. Laikhtman and P. M. Solomon. Remote phonon scattering in field-effect transistors with a high kappa insulating layer. *J. Appl. Phys.*, 2008. vol. 103, page 014501. URL http://dx.doi.org/10.1063/1.2826951.

[84] S. Yu, K. W. Kim, M. A. Stroscio, G. J. Iafrate, J.-P. Sun and G. I. Haddad. Transfer matrix method for interface optical-phonon modes in multiple-interface heterostructure systems. *J. Appl. Phys.*, 1997. vol. 82, pages 3363 . URL http://dx.doi.org/10.1063/1.365649.

[85] R. Sauer. *Halbleiterphysik: Lehrbuch für Physiker und Ingenieure*. Oldenbourg, 2009. URL https://books.google.ie/books?id=_pxcHH4uDz4C.

[86] K. J. Nash. Electron-phonon interactions and lattice dynamics of optic phonons in semiconductor heterostructures. *Phys. Rev. B*, Sep 1992. vol. 46, pages 7723. URL http://dx.doi.org/10.1103/PhysRevB.46.7723.

[87] M. V. Fischetti and S. E. Laux. Long-range Coulomb interactions in small Si devices. Part I: Performance and reliability. *J. Appl. Phys.*, 2001. vol. 89, pages 1205 . URL http://dx.doi.org/10.1063/1.1332423.

[88] M. V. Fischetti. Long-range Coulomb interactions in small Si devices. Part II. Effective electron mobility in thin-oxide structures. *J. Appl. Phys.*, 2001. vol. 89, pages 1232 . URL http://dx.doi.org/10.1063/1.1332424.

[89] Z.-Y. Ong and M. V. Fischetti. Theory of interfacial plasmon-phonon scattering in supported graphene. *Phys. Rev. B*, Oct 2012. vol. 86, page 165422. URL http://dx.doi.org/10.1103/PhysRevB.86.165422.

[90] Z.-Y. Ong and M. V. Fischetti. Erratum: Theory of interfacial plasmon-phonon scattering in supported graphene [Phys. Rev. B 86, 165422 (2012)]. *Phys. Rev. B*, Nov 2012. vol. 86, page 199904. URL http://dx.doi.org/10.1103/PhysRevB.86.199904.

[91] A. Konar, T. Fang and D. Jena. Effect of high-κ gate dielectrics on charge transport in graphene-based field effect transistors. *Phys. Rev. B*, Sep 2010.

vol. 82, page 115452. URL http://dx.doi.org/10.1103/PhysRevB.82.115452.

[92] T. P. O'Regan, M. V. Fischetti, B. Sorée, S. Jin, W. Magnus and M. Meuris. Calculation of the electron mobility in III-V inversion layers with high-κ dielectrics. *Journal of Applied Physics*, 2010. vol. 108, 103705. URL http://dx.doi.org/10.1063/1.3500553.

[93] C. Kittel. *Introduction to Solid State Physics*. Wiley, 1996. URL https://books.google.ie/books?id=1X8pAQAAMAAJ.

[94] K. Fletcher and P. N. Butcher. An exact solution of the linearized Boltzmann equation with applications to the Hall mobility and Hall factor of n-GaAs. *Journal of Physics C: Solid State Physics*, 1972. vol. 5, page 212. URL http://stacks.iop.org/0022-3719/5/i=2/a=010.

[95] R. T. Delves. Theoretical Transport Coefficients for Polar Semiconductors. *Proceedings of the Physical Society*, 1959. vol. 73, page 572. URL http://stacks.iop.org/0370-1328/73/i=4/a=305.

[96] B. K. Ridley. Polar-optical-phonon and electron-electron scattering in large-bandgap semiconductors. *Journal of Physics: Condensed Matter*, 1998. vol. 10, page 6717. URL http://stacks.iop.org/0953-8984/10/i=30/a=011.

[97] B. Y.-K. Hu and K. Flensberg. Electron-electron scattering in linear transport in two-dimensional systems. *Phys. Rev. B*, Apr 1996. vol. 53, pages 10072. URL http://dx.doi.org/10.1103/PhysRevB.53.10072.

[98] D. Chattopadhyay and H. J. Queisser. Electron scattering by ionized impurities in semiconductors. *Rev. Mod. Phys.*, Oct 1981. vol. 53, pages 745. URL http://dx.doi.org/10.1103/RevModPhys.53.745.

[99] A. Matthiessen. *Rep. Brit. Ass.*, 1862. vol. 32, page 144.

[100] D. L. Rode. Electron Mobility in Direct-Gap Polar Semiconductors. *Phys. Rev. B*, Aug 1970. vol. 2, pages 1012. URL http://dx.doi.org/10.1103/PhysRevB.2.1012.

[101] S. Sze and J. Irvin. Resistivity, mobility and impurity levels in GaAs, Ge, and Si at 300°K. *Solid-State Electronics*, 1968. vol. 11, pages 599 . URL http://dx.doi.org/10.1016/0038-1101(68)90012-9.

[102] E. J. Moore. Quantum-Transport Theories and Multiple Scattering in Doped Semiconductors. II. Mobility of n-type Gallium Arsenide. *Phys. Rev.*, Aug 1967. vol. 160, pages 618. URL http://dx.doi.org/10.1103/PhysRev.160.618.

[103] T. Gunst, T. Markussen, K. Stokbro and M. Brandbyge. First-principles method for electron-phonon coupling and electron mobility: Applications to

two-dimensional materials. *Phys. Rev. B*, Jan 2016. vol. 93, page 035414. URL http://dx.doi.org/10.1103/PhysRevB.93.035414.

[104] D. Y. Qiu, F. H. da Jornada and S. G. Louie. Optical Spectrum of MoS_2: Many-Body Effects and Diversity of Exciton States. *Phys. Rev. Lett.*, Nov 2013. vol. 111, page 216805. URL http://dx.doi.org/10.1103/PhysRevLett.111.216805.

[105] E. O. Kane. Band structure of indium antimonide. *Journal of Physics and Chemistry of Solids*, 1957. vol. 1, pages 249 . URL http://dx.doi.org/10.1016/0022-3697(57)90013-6.

[106] Y. I. Ravich, B. A. Efimova and V. I. Tamarchenko. Scattering of Current Carriers and Transport Phenomena in Lead Chalcogenides. *Physica Status Solidi B Basic Research*, Jan 1971. vol. 43, pages 11. URL http://dx.doi.org/10.1002/pssb.2220430102.

[107] C. Herring and E. Vogt. Transport and Deformation-Potential Theory for Many-Valley Semiconductors with Anisotropic Scattering. *Phys. Rev.*, Mar 1957. vol. 105, pages 1933. URL http://dx.doi.org/10.1103/PhysRev.105.1933.

[108] R. Bhatt and P. Lee. Low temperature conductivity of doped semiconductors: Mass anisotropy and intervalley effects. *Solid State Communications*, 1983. vol. 48, pages 755 . URL http://dx.doi.org/10.1016/0038-1098(83)91011-6.

[109] J. Hubbard. The Description of Collective Motions in Terms of Many-Body Perturbation Theory. *Proceedings of the Royal Society of London A: Mathematical, Physical and Engineering Sciences*, 1957. vol. 240, pages 539. URL http://dx.doi.org/10.1098/rspa.1957.0106.

[110] K. S. Singwi, M. P. Tosi, R. H. Land and A. Sjölander. Electron Correlations at Metallic Densities. *Phys. Rev.*, Dec 1968. vol. 176, pages 589. URL http://dx.doi.org/10.1103/PhysRev.176.589.

[111] T. Boyd and J. Sanderson. *The physics of plasmas*. Cambridge University Press, 2003. URL http://books.google.ie/books?id=DDJkQgAACAAJ.

[112] J. Bittencourt. *Fundamentals of Plasma Physics*. Springer, 2004. URL http://books.google.ie/books?id=qCA64ys-5bUC.

[113] A. Vlasov. On Vibration Properties of Electron Plasma [sic]. *JETP*, 1938. vol. 8, page 291.

[114] K. S. Thorne and R. D. Blandford. Applications of Classical Physics, 2012-2013. Unpublished textbook from lecture notes, retrieved 2013, URL http://www.pma/caltech.edu/Courses/ph136/yr2012/.

[115] J. Bak and D. Newman. *Complex Analysis*. Undergraduate Texts in Mathematics. Springer New York, 1999. URL https://books.google.ie/books?id=JX2YSgfZwbYC.

[116] J. H. Malmberg and C. B. Wharton. Collisionless Damping of Electrostatic Plasma Waves. *Phys. Rev. Lett.*, Aug 1964. vol. 13, pages 184. URL http://dx.doi.org/10.1103/PhysRevLett.13.184.

[117] J. H. Malmberg and C. B. Wharton. Dispersion of Electron Plasma Waves. *Phys. Rev. Lett.*, Jul 1966. vol. 17, pages 175. URL http://dx.doi.org/10.1103/PhysRevLett.17.175.

[118] J. J. Quinn. Range of Excited Electrons in Metals. *Phys. Rev.*, May 1962. vol. 126, pages 1453. URL http://dx.doi.org/10.1103/PhysRev.126.1453.

[119] R. H. Ritchie. Interaction of Charged Particles with a Degenerate Fermi-Dirac Electron Gas. *Phys. Rev.*, May 1959. vol. 114, pages 644. URL http://dx.doi.org/10.1103/PhysRev.114.644.

[120] B. I. Lundqvist. Some Numerical Results on Quasiparticle Properties in the Electron Gas. *Phys. Status. Solidi.*, 1969. vol. 32, page 273.

[121] M. Combescot and R. Combescot. Conductivity relaxation time due to electron-hole collisions in optically excited semiconductors. *Phys. Rev. B*, May 1987. vol. 35, pages 7986. URL http://dx.doi.org/10.1103/PhysRevB.35.7986.

[122] M. P. Vaughan. Inelastic Scattering, December 2011. Numerical code and documentation from private communication.

[123] W. H. Press, S. A. Teukolsky, W. T. Vetterling and F. B.P. *Numerical recipes in C: The art of scientific computing*. Cambridge University Press, New York, 2nd edn., 1992. URL http://numerical.recipes/.

[124] GSL - GNU Scientific Library. www.gnu.org/software/gsl. Retrieved September 24, 2016.

[125] F. X. Timmes. http://cococubed.asu.edu/code_pages/fermi_dirac.shtml. Fortran code for the calculation of Fermi-Dirac integrals, retrieved 4/10/16.

[126] J. M. Aparicio. A Simple and Accurate Method for the Calculation of Generalized Fermi Functions. *The Astrophysical Journal Supplement Series*, 1998. vol. 117, page 627. URL http://stacks.iop.org/0067-0049/117/i=2/a=627.

[127] L. D. Cloutman. Numerical Evaluation of the Fermi-Dirac Integrals. *The Astrophysical Journal Supplement Series*, Nov 1989. vol. 71, page 677. URL http://dx.doi.org/10.1086/191393.

[128] H. M. Antia. Rational Function Approximations for Fermi-Dirac Integrals. *The Astrophysical Journal Supplement Series*, Jan 1993. vol. 84, page 101. URL http://dx.doi.org/10.1086/191748.

[129] Gallium arsenide (GaAs), Seebeck coefficient. In O. Madelung, U. Rössler and M. Schulz (editors), *Group IV Elements, IV-IV and III-V Compounds. Part b - Electronic, Transport, Optical and Other Properties*, vol. 41A1b of *Landolt-Börnstein - Group III Condensed Matter*, pages 1–8. Springer Berlin Heidelberg, 2002. URL http://dx.doi.org/10.1007/10832182_207.

[130] T. H. Geballe and G. W. Hull. Seebeck Effect in Silicon. *Phys. Rev.*, May 1955. vol. 98, pages 940. URL http://dx.doi.org/10.1103/PhysRev.98.940.

[131] P. Boguslawski. Screening of the deformation potential by free electrons in the multivalley conduction band. *Journal of Physics C: Solid State Physics*, 1977. vol. 10, page L417. URL http://stacks.iop.org/0022-3719/10/i=15/a=005.

[132] P. Bogulsawski and J. Mycielski. Is the deformation potential in semiconductors screened by free carriers? *Journal of Physics C: Solid State Physics*, 1977. vol. 10, page 2413. URL http://stacks.iop.org/0022-3719/10/i=13/a=015.

[133] M. A. Stroscio and M. Dutta. *Phonons in Nanostructures*. Cambridge University Press, first edn., 2001. URL http://dx.doi.org/10.1017/CBO9780511534898.